

Aus dem Institut für Prophylaxe und Epidemiologie der Kreislaufkrankheiten  
des Klinikums der Ludwig-Maximilians-Universität München



Dissertation

zum Erwerb des Doctor of Philosophy (Ph.D.) an der

Medizinischen Fakultät der

Ludwig-Maximilians-Universität zu München

# **Single-cell Transcriptome Analyses of Dorsal Root Ganglia in Aged Hyperlipidemic Mice**

vorgelegt von:

Shu Lu

.....

aus:

Lianyungang, China

.....

Jahr: 2023

Mit Genehmigung der Medizinischen Fakultät der  
Ludwig-Maximilians-Universität zu München

**First evaluator (1. TAC member):** *Prof. Dr. Andreas Habenicht*

**Second evaluator (2. TAC member):** *Dr. Sarajo Mohanta*

**Third evaluator:** *Prof. Dr. Gunnar Schotta*

**Fourth evaluator:** *Prof. Dr. Martin Dichgans*

**Dean: Prof. Dr. med. Thomas Gudermann**

Date of the defense:

13.07.2023

---

# TABLE OF CONTENTS

## TABLE OF CONTENTS

TABLE OF CONTENTS.....	1
ZUSAMMENFASSUNG .....	1
ABSTRACT .....	2
LIST OF TABLES.....	3
LIST OF ABBREVIATIONS .....	4
<b>1 INTRODUCTION .....</b>	<b>6</b>
<b>1.1 Atherosclerosis.....</b>	<b>6</b>
1.1.1 Initiation, progression, and complications of atherosclerosis.....	6
1.1.2 Immune cells in atherosclerosis .....	7
1.1.3 Adventitial layer and artery tertiary lymphoid organ (ATLO) neogenesis in atherosclerosis .....	8
<b>1.2 The nervous system (NS) .....</b>	<b>9</b>
1.2.1 Anatomy of the NS.....	10
1.2.2 The peripheral NS (PNS) ganglia .....	11
1.2.3 Neurons in dorsal root ganglia (DRG) .....	12
1.2.4 Glial cells in DRGs .....	13
1.2.5 Other cell types in DRGs .....	14
<b>1.3 NS and cardiovascular diseases (CVDs) .....</b>	<b>15</b>
1.3.1 Neuroimmune interaction .....	15
1.3.2 The PNS in neuroimmune interactions.....	15
1.3.3 Neuroimmune regulation of immune cells.....	16
1.3.4 Neuroimmune interactions in CVDs .....	16
<b>1.4 Single-cell RNA sequencing (scRNA-seq) technology .....</b>	<b>17</b>
1.4.1 ScRNA-seq provides transcriptome information at the single-cell level .....	18
1.4.2 ScRNA-seq in neuroscience research.....	20
1.4.3 DRG neuron subtype identification using scRNA-seq .....	21
1.4.4 ScRNA-seq in cardiovascular research.....	23
1.4.5 Defining neuroimmune interactions by scRNA-seq .....	23
<b>1.5 Aims .....</b>	<b>24</b>
<b>2 MATERIALS AND METHODS.....</b>	<b>25</b>
<b>2.1 Materials.....</b>	<b>25</b>
2.1.1 Mice .....	25
2.1.2 Standard solutions and buffers.....	25
2.1.3 Antibodies.....	27
2.1.4 Equipment .....	28
2.1.5 10x Genomics scRNA-seq reagent kits, accessories, and equipment .....	28
2.1.6 Software and algorithms .....	29
<b>2.2 Methods.....</b>	<b>30</b>
2.2.1 Spinal cord (SC), meninges, and DRG isolation.....	30
2.2.2 Preparation of single-cell suspensions from spleen and LN .....	30
2.2.3 Preparation of single-cell suspensions from SC, meninges, and DRG .....	31
2.2.4 Flow cytometry.....	31
2.2.5 CD45 tail vein injection .....	32
2.2.6 FACS sorting of total live cells for scRNA-seq .....	32
2.2.7 Construction of scRNA-seq libraries .....	33
2.2.8 Sequencing raw data processing .....	33
2.2.9 Standard cell quality control and clustering via Seurat .....	34
2.2.10 Integration of reference DRG scRNA-seq data and aged DRGs dataset .....	35
2.2.11 Evaluation of gene signatures in single-cell datasets using scoring value .....	36
2.2.12 Gene set enrichment analysis (GSEA).....	37
2.2.13 Cell-cell interaction analysis .....	37
2.2.14 Immunofluorescence staining .....	38
2.2.15 Statistical analyses .....	38

## TABLE OF CONTENTS

<b>3</b>	<b>RESULTS</b>	<b>39</b>
<b>3.1</b>	<b>Immune cell infiltration in the NS during aging</b>	<b>39</b>
3.1.1	Establishment of FACS protocols for DRGs and SCs	39
3.1.2	Immune cell infiltration in the NS during aging	41
3.1.3	Immune cells in the NS during atherosclerosis progression	44
<b>3.2</b>	<b>Aged DRG single cell atlas</b>	<b>47</b>
3.2.1	Construction of DRG atlases	48
3.2.2	Transcriptional characteristics of cell types in aged DRGs	50
3.2.3	Macrophages in aged DRGs	53
<b>3.3</b>	<b>Neuron subtype composition in aged DRGs</b>	<b>57</b>
3.3.1	Integrated analysis of DRG neurons	57
3.3.2	CGRP-alpha PEP neuron subtypes in aged WT DRGs	61
3.3.3	Transcriptional profiles of CGRP-alpha neurons in aged DRG	62
3.3.4	Cell-cell interactions in aged WT DRG	65
<b>3.4</b>	<b>Molecular changes of DRGs during atherosclerosis progression</b>	<b>67</b>
3.4.1	Changes of Apoe expression and Apoe-associated genes	67
3.4.2	Transcriptome differences in aged WT versus Apoe <sup>-/-</sup> DRGs	70
3.4.3	Transcriptome changes of each cell type in aged WT versus Apoe <sup>-/-</sup> DRGs	73
3.4.4	CGRP-alpha2 neuron transcriptional profiles in aged WT versus Apoe <sup>-/-</sup> DRGs	77
3.4.5	Cell-cell interactions in aged WT versus Apoe <sup>-/-</sup> CGRP-alpha2 neurons	78
3.4.6	Predicted neuroimmune interactions among DRGs and ATLOs/renal lymph nodes (RLNs)	81
<b>3.5</b>	<b>Effect of resiniferatoxin (RTX) treatment on CGRP-alpha2-associated changes</b>	<b>85</b>
3.5.1	Trpv1 <sup>+</sup> neurons in aged DRGs	85
3.5.2	ScRNA-seq of control and RTX-treated DRGs	87
3.5.3	Effects of RTX treatment on T6-T13 DRGs	89
3.5.4	Transcriptome changes after RTX treatment	91
3.5.5	Potential CGRP-alpha2-associated neuroimmune pathways during atherosclerosis progression	93
<b>4</b>	<b>DISCUSSION</b>	<b>97</b>
4.1	Outlook	102
	<b>REFERENCES</b>	<b>104</b>
	<b>APPENDIX</b>	<b>115</b>
	<b>ACKNOWLEDGEMENTS</b>	<b>141</b>
	<b>AFFIDAVIT</b>	<b>142</b>
	<b>CONFIRMATION OF CONGRUENCY</b>	<b>143</b>
	<b>CURRICULUM VITAE</b>	<b>144</b>
	<b>LIST OF PUBLICATIONS</b>	<b>145</b>

## ZUSAMMENFASSUNG

### ZUSAMMENFASSUNG

Atherosklerose, die der Pathologie der Mehrzahl der Herz-Kreislauf-Erkrankungen mit den meisten Todesursachen weltweit zugrunde liegt, ist mit einer umfassenden Umstrukturierung des peripheren Nervensystems (PNS) assoziiert. Kürzlich wurde von unserer Arbeitsgruppe eine direkte Nervenverschaltung erkrankter Arterien mit dem Gehirn entdeckt, die wir als *artery brain circuit* (ABC) bezeichnet haben. Der murine ABC-Sensor, d.h. der afferente Arm des ABC, verbindet erkrankte Arterien mit dorsalen Wurzelganglien (DRGs), die in das Rückenmark (SC) eintreten, um höhere Hirnregionen zu erreichen, in denen die elektrischen Signale, die von den erkrankten Arterien erzeugt werden, von sensorischen Hirnneuronen entlang des Schmerzwegs empfangen werden. Das Hauptziel dieser Arbeit bestand darin, das unerforschte Gebiet der PNS-Entzündung bei Atherosklerose mittels Einzelzellsequenzierung (scRNA-seq) des ABC-Sensors als Modell bei atherosklerotischen Mäusen zu untersuchen. Der erste und mühsame Teil der Arbeit bestand darin, Methoden zum Ausschluss von Artefakten wie Blutkontamination und Gewebekontamination aus umliegenden Blutgefäßen und Meningen zu entwickeln, um bona fide Einzelzellsuspensionen hoher Qualität zu präparieren. Anschließend wurden Protokolle zur Herstellung von Einzelzellpräparationen von Wurzelganglien und Rückenmark etabliert. Nach Erreichen dieses Meilensteins als Voraussetzung für scRNA-seq-Analysen des ABC-Sensors ergaben FACS-Analysen in Kombination mit immunhistochemischen Analysen eine Reihe von bedeutenden Ergebnissen. Es wurde beobachtet, dass das Altern bei gesunden Mäusen zur Infiltration von Immunzellen in Wurzelganglien und Rückenmark bereits ohne Atherosklerose führte, aber die Entwicklung von fortgeschrittener Atherosklerose in alten Mäusen zu einer signifikanten weiteren Zunahme von Immunzellen führte. Die scRNA-seq-Daten wurden anschließend mit einer Vielzahl von Algorithmen analysiert, einschließlich der Zelltyp-Clustering und der Vorhersage von Zell-Zell-Interaktionen durch Ligand-Rezeptor-Identifikation *in silico* zwischen Neuronen und nicht-neuronalen Zellen wie Endothelzellen, Fibroblasten, Schwann-Zellen und Leukozyten, die im PNS während der Atherosklerose-Progression zu beobachten sind. Diese Daten ermöglichten die Erstellung von Transkriptomkarten der verschiedenen Neuronen- und Immunzelltypen zusammen mit anderen nicht-neuronalen Zellen des ABC-Sensors. Eine Einschränkung dieser Arbeit bestand darin, dass einige Neuronensubpopulationen, die im Nervensystem identifiziert wurden, selten waren und diese Zellen - obwohl potenziell wichtig - nicht mehreren Algorithmustypen unterzogen werden konnten. Insgesamt haben unsere Daten bedeutende Voraussetzungen geschaffen, das gesamte Nervensystem während des Alterns und in Abhängigkeit der Atherosklerose zu kartieren. Die hier berichteten Daten bilden die Grundlage für funktionelle Untersuchungen in der Maus und im Menschen, um die Interaktionen zwischen dem Nervensystem und der Atherosklerose zu definieren.

## ABSTRACT

### ABSTRACT

Atherosclerosis is the pathology underlying most causes of death worldwide and has been shown to be associated with a major restructuring of the peripheral nervous system (PNS) that initiates an artery brain circuit (ABC). The murine ABC sensor, i.e. the afferent arm of the ABC, connects diseased arteries with dorsal root ganglia (DRGs) that enter the spinal cord (SC) to reach higher brain areas where the electrical signals derived from the diseased arteries are received by sensory brain neurons along the pain pathway. However, the molecular alterations and restructuring of the ABC sensor during atherosclerosis remain unknown. The major goal of this thesis was to explore the uncharted territory of PNS inflammation in atherosclerosis by using single-cell sequencing (scRNA-seq) of the ABC sensor as a model in atherosclerotic mice. The first and painstaking part of the thesis consisted of setting up methods to rule out artifacts, such as blood contamination and tissue contamination from surrounding blood vessels and meninges. Subsequently, faithful and controlled protocols to prepare single cell preparations of DRGs and SCs were established. After achieving this milestone as a requirement for scRNA-seq analyses of the ABC sensor, FACS analyses of the DRGs and SCs combined with immunohistochemical analyses were shown to yield a series of major results. It was found that aging in healthy mice led to immune cell infiltration of DRGs and SCs in the absence of atherosclerosis, but the development of advanced atherosclerosis led to a significant further increase of immune cells in the DRGs and the SCs when young, adult and aged mice were compared. Concurrently, the scRNA-seq body of data were analyzed by a variety of algorithms including cell type clustering and the prediction of cell-cell interactions through ligand-receptor pairs between neurons and non-neuronal cells, such as endothelial cells, fibroblasts, Schwann cells, and leukocytes that emerge in the PNS during atherosclerosis progression. These data allowed to construct transcriptome maps of the multiple neuron and immune cell types together with other non-neuronal cells of the ABC sensor. However, given that a variety of neurons identified in DRGs were rare, a limitation of this work was that these cells - while potentially important - could not be subjected to several types of algorithms. When taken together, our data have revealed major aging- and atherosclerosis-associated changes in neurons and non-neuronal cell transcriptomes of the initial portions of the ABC sensor. We propose that this data provides a solid foundation to define the role of atherosclerosis in shaping the ABC during aging and atherosclerosis. Such future studies together with the current data will enable us to address the long-term goal as physicians to develop new therapeutic approaches to prevent and treat this treacherous and deadly disease.

## LIST OF TABLES

### LIST OF TABLES

Table 1 List of reagents.....	25
Table 2 List of buffers .....	26
Table 3 Digestion cocktail for SC and DRGs.....	26
Table 4 List of antibodies for FACS analyses.....	27
Table 5 List of immunofluorescence primary antibodies .....	27
Table 6 List of immunofluorescence secondary antibodies .....	27
Table 7 List of equipment.....	28
Table 8 10x Genomics scRNA-seq reagent kits, accessories, and equipment .....	28
Table 9 Software and algorithms (under macOS 13.1).....	29
Table 10 Marker genes of aged DRG cell types .....	34

## LIST OF ABBREVIATIONS

### LIST OF ABBREVIATIONS

<b>Abbreviation</b>	<b>Full form</b>
ABC	Artery-brain circuit
ApoE	Apolipoprotein E
ANOVA	Analysis of variance
ATLO	Artery tertiary lymphoid organ
ATP	Adenosine triphosphate
App	Amyloid beta precursor protein
BF	Brightfield
BCL	Binary base call file
CNS	Central nervous system
CGRP	Calcitonin gene-related peptide
CVD	Cardiovascular disease
C-LTMR	C low-threshold mechanoreceptors
Calca	Calcitonin/calcitonin-related polypeptide alpha
DC	Dendritic cell
DRG	Dorsal root ganglion
DEG	Differentially expressed gene
DAPI	4',6-diamidino-2-phenylindole
EC	Endothelial cell
ECM	Extracellular matrix
FVD	Fixable viability dye
FACS	Fluorescence-activated cell sorting
GO	Gene ontology
GSEA	Gene set enrichment analysis
GPCR	G-protein-coupled receptors
i.v.	Intravenous
IL	Interleukin
LN	Lymph node
LDL	Low density lipoprotein
KEGG	Kyoto encyclopedia of genes and genomes
MHC	Major histocompatibility complex
mSch	Myelinating Schwann cell
NS	Nervous system
NF	Neurofilament
NES	Normalized enrichment score

## LIST OF ABBREVIATIONS

NP	Non-peptidergic nociceptors
Ncam	Neural cell adhesion molecule
nmSch	Non-myelinating Schwann cell
PEP	Peptidergic nociceptors
PNS	Peripheral nervous system
PBS	Phosphate-buffered saline
P0	Postnatal day 0
RTX	Resiniferatoxin
Sch	Schwann cell
Sst	Somatostatin
SGC	Satellite glial cell
Spp1	Secreted phosphoprotein 1
SNS	Somatosensory nervous system
scRNA-seq	Single-cell RNA sequencing
T <sub>reg</sub>	Regulatory T cell
T <sub>EM</sub>	Effector memory T cell
T <sub>CM</sub>	Central memory T cell
TH	Tyrosine hydroxylase
Trpv1	Transient receptor potential cation channel subfamily V member 1
TrpM8	Transient receptor potential cation channel subfamily M member 8
Trem2	Triggering receptor expressed on myeloid cells 2
Trem2 <sup>hi</sup>	Trem2 high
tSNE	T-distributed stochastic neighbor embedding
UMAP	Uniform manifold approximation and projection
WT	Wild-type

# 1 INTRODUCTION

## 1.1 Atherosclerosis

Mortality linked to cardiovascular diseases (CVD) has experienced a continuous rise, becoming the primary cause of fatalities globally [1]. Atherosclerosis serves as the prevalent underlying factor for major CVDs, such as ischemic heart conditions and cerebrovascular diseases [2, 3]. Characterized as a chronic inflammatory disorder affecting arterial walls, atherosclerosis contributes to the development of atherosclerotic plaques within the intimal layer of the arterial wall. This process results in the constriction of the arterial lumen, consequently decreasing blood flow and oxygen supply to vital organs, leading to tissue ischemia, myocardial infarctions, and strokes, among other complications. It is the main pathology of cardiovascular disease, claiming ~ 3.9 million lives annually in Europe alone. The conventional target of atherosclerosis research over the past eight decades has been the intima. However, it is well established that the disease involves all three arterial wall layers including the media layer and the adventitia layer also being severely affected [4]. Our group focuses on the adventitia during aging. Our studies have shown that the majority of immune cells in murine atherosclerosis accumulate in the lamina adventitia rather than in intima plaques [5]. And both the innate and adaptive immune systems play roles in the progression of atherosclerosis [6].

The characteristics of atherosclerotic inflammation can be described as a gradual accumulation of lipids and inflammatory cells, i.e. macrophages and T cells, in the developing atherosclerotic intima lesions though the adventitia contain additional leukocyte subtypes such as mast cells and B cells which may play major roles in disease progression as well [7, 8]. Atherosclerosis is associated with multiple risk factors: It emerges in response to a combination of genetic factors such as those described for the low density lipoprotein receptor, apolipoprotein B, and the ATP-binding cassette transporter family of membrane proteins, and other factors such as diabetes, obesity, aging, smoking, physical inactivity, and high fat diets [9].

### 1.1.1 Initiation, progression, and complications of atherosclerosis.

Atherosclerosis was first discovered by Jean Lobstein in 1829 [10]. However, even two centuries after its first description, the exact cause for the initiation of atherosclerosis is still unclear. Various theories have emerged to explain the initiation of this condition, with a focus on inflammatory and immune responses. These theories include the oxidized low-density lipoprotein hypothesis, the autoimmune hypothesis, and the response to injury hypothesis [11-13].

## INTRODUCTION

Atherosclerosis inflammation predominantly occurs at sites of the arterial wall with disturbed blood flow at arterial branching points and bifurcations. In hyperlipidemic mice, it emerges at the aortic root, then gradually progresses along the aortic tree involving adjacent media and adventitia at later stages [9, 14-16]. Although atherosclerosis begins in early childhood, the buildup of atherosclerotic plaques in the sub-endothelial space of the arterial wall takes years to decades through a complex series of cellular events within the arterial wall and becomes clinically overt in most cases in old age [17].

Advanced atherosclerotic plaques are composed of a fibrous cap covering a lipid-rich core, infiltrations of innate and adaptive immune cells including monocytes, macrophages, lipid-laden foam cells, dendritic cells, T cells, extracellular lipid, and smooth muscle cells at various stages of atherosclerotic lesion development [9, 18-21]. Inflammatory immune reactions are involved in the initiation, progression, and complications in atherosclerosis. Oxidation of LDL is considered as one of the triggering events in the initiation of atherosclerotic lesion formation. Numerous immune cells including dendritic cells, macrophages, and T cells have been observed at the site of atherosclerotic lesions in the intima during the initial stages of the disease, but their abundance decreases with time. Atherosclerotic plaques generate various mediators secreted by the plaque cells including pro-atherogenic and anti-atherogenic cytokines and chemokines contribute to disease progression and tissue damage [22, 23]. Eventually, plaque growth, and plaque rupture with subsequent thrombus formation results in lumen narrowing, flow-limiting stenosis, tissue ischemia, and finally tissue infarcts. The thrombus can provoke ischemic insults such as acute coronary syndromes and stroke [24-27].

### 1.1.2 Immune cells in atherosclerosis

Recent advances in research have led to the view that atherosclerosis is a chronic inflammatory condition initiated by the immune system and targeting the arterial wall [3, 12, 28]. Numerous evidences point to the role of chronic inflammation in attracting and/or activating various immune cells, such as monocytes, macrophages, dendritic cells (DCs), and T cells including anti-inflammatory regulatory T cells (Tregs) [12, 18, 25, 29]. Inflammatory processes are also responsible for the creation of macrophage-foam cells [9, 19], naïve T cell conversion into effector T cells and memory T cells [20, 30, 31], and both pro-inflammatory and anti-inflammatory macrophages [32, 33]. Atherosclerotic plaques contain macrophages/foam cells, DCs, and T cells but rarely B cells. The chronic inflammation process involves both innate and adaptive immune responses, characterized by a complex interplay between different cell types and their products. These immune cells exert pro- or anti-inflammatory responses through different cytokine-mediated pathways [22, 34]. Moreover, immune cells undergo recruitment, migration, proliferation, survival or apoptosis within the arterial wall during atherosclerosis development [35-38]. Due to the application of newly

## INTRODUCTION

developed single-cell transcript and protein technologies, such as scRNA-seq and mass cytometry [39, 40], other immune cell subtypes were observed in plaques, including several DC subtypes and T cell subpopulations, which are presumed to play distinct roles in arterial wall inflammation [28, 35, 36, 41]. Importantly, scRNA-seq of the atherosclerotic aorta demonstrated the presence of M1 macrophage, M2 macrophage, and a new subtype triggering receptor expressed on myeloid cells 2 (Trem2)<sup>hi</sup> macrophages, which highly express Trem2 and osteopontin encoding genes: CD9 antigen (Cd9), and secreted phosphoprotein 1 (Spp1), cathepsin genes including Cathepsin B (Ctsb), Cathepsin D (Ctsd) [39]. Interestingly, evidence indicates that the endothelium, smooth muscle cells and immune cells in the plaque release different neuronal guidance molecules including netrins, semaphorins, and ephrins in atherogenesis [42-45], indicating that some molecules traditionally thought to be expressed in the nervous system (NS) can also be produced by immune cells [46, 47].

### 1.1.3 Adventitial layer and artery tertiary lymphoid organ (ATLO) neogenesis in atherosclerosis

The adventitia recently emerged as a focus of atherosclerosis research, as it is a highly active and dynamic compartment of the arterial wall. Researchers have postulated that the adventitia may play a role in the advancement of the disease [41, 48]. The normal arterial adventitia layer consists of an extracellular matrix (ECM) scaffold containing various cells, including fibroblasts, fibrocytes, and immunomodulatory cells (DCs and macrophages), resident progenitor cells and structures including vasa vasora, lymph vessels, and nerve fibers [49]. The adventitia of atherosclerotic arteries contains a specific set of innate and adaptive immune cells including monocytes / macrophages, various DC subtypes, T and B cells [50, 51] (**Figure 1**). Thus, the adventitia is the most complex and heterogeneous compartment of both the normal and the diseased artery.

In earlier research conducted by our group, we discovered that during plaque progression, leukocyte aggregates containing T/B cell clusters and other immune cells develop in the arterial adventitia adjacent to the atherosclerotic lesions in aged Apoe<sup>-/-</sup> mice. We termed these leukocyte aggregates ATLOs. ATLOs exhibit comparable cellularity and structural features to lymph nodes and are predominantly observed in the aortal abdominal segment. However, they are not present in aged wild-type mice, young mice, or only infrequently in the aorta thoracic segment of aged Apoe<sup>-/-</sup> mice. These data indicate that ATLOs form in a territorially-defined and age-dependent manner. The well-developed stage III of ATLOs consists of distinct T cell regions and activated B cell follicles with functional germinal centers, where follicular dendritic cells (FDCs) can be detected. ATLOs share significant resemblances with TLOs in classic organ-specific autoimmune diseases, offering indirect evidence of an autoimmune reaction during the advanced stages of atherosclerosis development [13]. Crucially, and similar to lymph nodes, this evidence implies that ATLOs may orchestrate both pro- and anti-atherogenic immune responses in a strictly segmental manner and that ATLOs can

## INTRODUCTION

facilitate a highly localized T/B cell-dependent autoimmune reaction targeting unknown arterial wall-derived autoantigens [13]. In recent experiments, we observed that nerve axons are increased in ATLOs in multiple arterial segments independent of ATLOs of *Apoe*<sup>-/-</sup> mice and in human atherosclerotic arterial segments including coronary arteries. These studies further revealed that the atherosclerotic arterial wall is directly connected to the brain via peripheral NS (PNS) ganglia including dorsal root ganglia (DRGs) and sympathetic ganglia by forming a previously unknown artery-brain circuit [52].

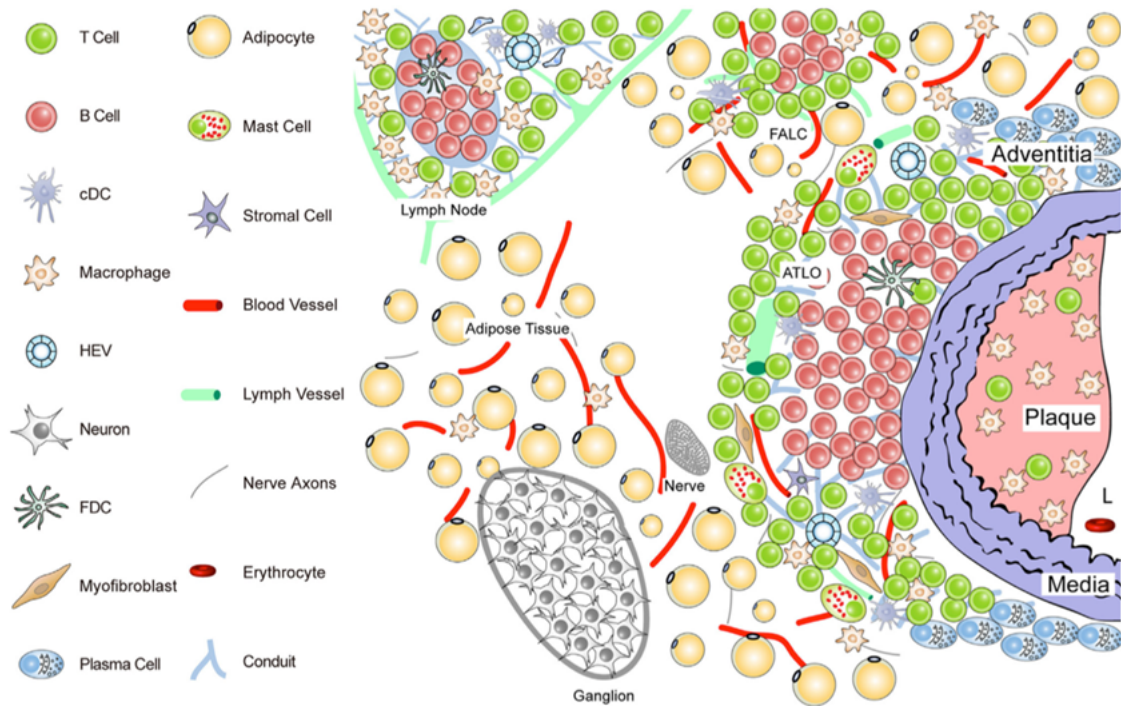


**Figure 1 Aged *Apoe*<sup>-/-</sup> aorta and the surrounding periarterial tissues exhibit a unique anatomy.** In aged *Apoe*<sup>-/-</sup> mice, ATLO formation occurs within the aortic adventitia layer, particularly adjacent to atherosclerotic plaques, with a preference for the abdominal aorta segment. ATLO development progresses through stages, including small T/B-cell aggregates (stage I) and well-organized TLOs with separate T and B cell areas (stages II and III). The advanced ATLOs consist of B cell follicles containing FDCs, newly formed conduits, high endothelial venules, and atypical lymph vessels. Adapted from *Yin et al.* [41].

## 1.2 The nervous system (NS)

The NS serves as a highly complex component of the organism that coordinates its actions and integrates the sensory information by conveying messages between various body regions to preserve homeostasis. The NS is the complex network of nerves and accessory neuronal cells that originate from neural ectoderm during embryonic development.

## INTRODUCTION

### 1.2.1 Anatomy of the NS

The NS consists of two main components i.e. the central NS (CNS) and the PNS. During development, the CNS and the PNS originate from the central neural plate/tube and the peripheral neuronal crest/placode of the neural ectoderm, respectively. The CNS is composed of two primary and major tissues, i.e. the brain and spinal cord (SC). The CNS integrates all afferent inputs, coordinates and impacts the body's activity via efferent polysynaptic connections. The PNS mainly consists of nerves including cranial / spinal / peripheral nerves and their ganglia outside the brain and the SC (**Figure 2**). The main function of the PNS is to connect the CNS with all peripheral tissues. The PNS can be divided into three separate sub-systems outside the CNS, i.e. its somatosensory NS (SNS), the autonomic NS and the enteric NS components. The PNS also includes the intrinsic NS of the heart and possibly other peripheral organs contain similar relatively independently acting components. The SNS contains sensory and motor nerves of the PNS with cell bodies are located in the DRGs or - with its CNS components - in the ventral horn of the SC and in the somatic motor nuclei of the brainstem, respectively. The SNS innervates somatic tissues including skin, skeletal muscle, and joints, and is responsible for controlling voluntary activities. The autonomic NS is a principle and major part of the PNS that innervates all tissues. Based on physiological and anatomical differences, the autonomic NS is further divided into the sympathetic NS and the parasympathetic NS. The sympathetic NS arises from the cervical and thoracolumbar regions of the SC. Most sympathetic ganglia are located close to the SC forming two chains on both sides. The sympathetic NS functions to convey stress signals amounting to a fight and flight response. In contrast, the parasympathetic NS manages the body's rest and digestive processes. The enteric NS is dedicated to regulating the gastrointestinal system and operates as a relatively independent component of the PNS, despite its connections to other PNS elements [53]. Within the NS, nerves that convey information from the body to the CNS are referred to as sensory or afferent nerves, while those transmitting signals from the CNS are named as motor or efferent nerves.

## INTRODUCTION

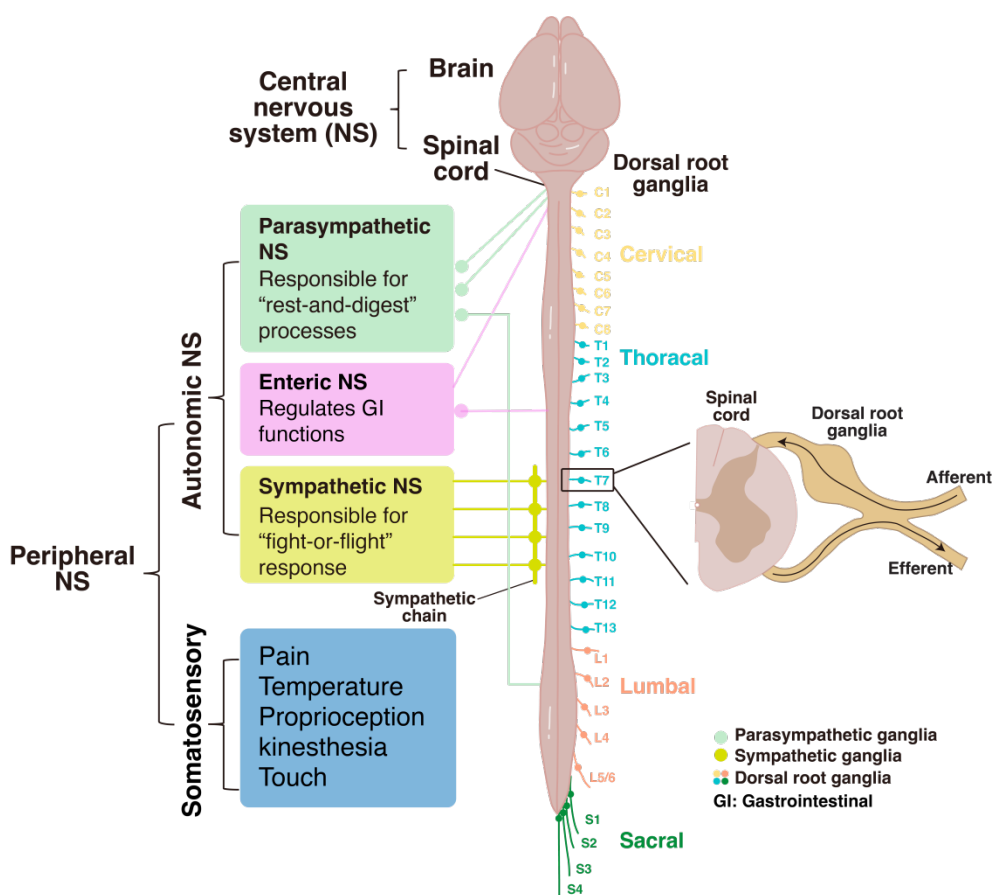


**Figure 2 Anatomy of the NS.** The NS encompasses the PNS and the CNS. The CNS comprises the brain and the SC while the PNS consists of the autonomic and somatosensory NS. The autonomic NS is subdivided into the sympathetic, parasympathetic, and enteric NS. The somatosensory NS is further classified into efferent and afferent subdivisions. Within the afferent division of the somatosensory NS, DRG harbors a variety of principal sensory neurons.

### 1.2.2 The peripheral NS (PNS) ganglia

PNS ganglia are specialized communication hubs of the PNS containing a group of neurons with long axons, where the preganglionic axons synapse with postganglionic neurons that innervate the target tissues. Depending on their functions, PNS ganglia are divided into sensory ganglia and autonomic efferent ganglia. Sensory ganglia contain unipolar or pseudounipolar neurons, whereas autonomic efferent ganglia contain multipolar neurons. The PNS ganglia have a dense connective tissue capsule called epineurium, and the neuronal cell bodies are surrounded by satellite glial cells (SGCs).

The SNS processes information that organisms receive and sends them to the CNS. The SNS includes cranial trigeminal ganglia, peripheral nodose ganglia, and DRGs. The trigeminal ganglia are located in the head region, the nodose ganglia are located in the neck region, and DRGs are located in the trunk. The DRGs are the most common type of sensory ganglia and are present in intervertebral foramina along the spinal cord. The neurons in the DRG are first-order neurons of

## INTRODUCTION

sensory neurons and belong to pseudounipolar type neurons having a cell body and two axonal branches: the peripheral one extends to the peripheral organs, including internal and somatic organs to detect various sensory modalities, and the central one extends to the SC dorsal columns to transmit peripheral signals to the CNS. These primary sensory neurons commonly terminate with second-order sensory neurons in the CNS.

### 1.2.3 Neurons in dorsal root ganglia (DRG)

Neurons serve as the fundamental and functional components of the NS, playing critical roles in receiving information, integrating, sending motor commands, transforming, and relaying electrical signals. They exhibit significant variations in size, shape, and structure based on their function, type, and distribution in the NS. However, most neurons possess three key elements: a cell body, axons, and dendrites. The cell body is the neuron's center, axons are tail-like structures that arise from the cell body at specialized locations called axon hillocks, and dendrites are specialized extensions of the neuronal cell body. The classifications of neurons are complex because of the complex molecular, morphological, connectional, and functional properties. Neurons are broadly classified into three types, although, there are still major technical and conceptual obstacles for neuronal classification: (i) Sensory neurons, which relay signals from peripheral regions to the CNS; (ii) motor neurons, which transmit signals from the CNS to peripheral organs; (iii) interneurons, which connect different types of neurons. Neurons have different shapes depending on their functions and types. For example, motor neurons are multipolar neurons having a cell body with multiple dendrites and a long axon, whereas sensory neurons are pseudounipolar having a cell body without any dendrite and a bifurcated long axon [54].

Neurons in DRGs are sensory neurons responsible for detecting and transmitting peripheral stimuli and sensations. Since different types of DRG neurons can reflect different stimuli, identifying the various types of DRG neurons can enhance our understanding of their roles in both physiological and pathological conditions. Sensory neurons are categorized into four primary classes based on the level of myelination and action potential conduction velocity of action potential and/or nerve activity: heavily myelinated A $\alpha$  fibers, moderately myelinated A $\beta$  fibers, thinly myelinated A $\delta$  fibers, and unmyelinated C fibers. The extent of myelination significantly influences action potential conduction rates. Furthermore, sensory neurons can be classified by their specific stimulus types and intensities, such as nociceptors, which response predominantly to noxious stimuli. Moreover, technological advances of new technologies, such as scRNA-seq enables identification of transcriptionally distinct neuronal populations (described below).

## INTRODUCTION

### 1.2.4 Glial cells in DRGs

Neurons and glial cells are two major classes of cell populations in the NS, which form the structural basis for the main function of the NS in coordinating actions and transmitting signals. Glial cells primarily serve to modulate the functions of neurons that generate and propagate electrical and chemical signals. First discovered in the 1800s, glial cells are an essential component of the NS. Within the CNS, glial cells are comprised of microglia, astrocytes, and oligodendrocytes. On the other hand, the PNS contains SGCs, myelinating Schwann cells (mSchs), non-myelinating Schwann cells (nmSchs), and enteric glial cells. The various glial cell types exhibit associations with distinct neuronal types [55-57].

Schwann cells, the primary glial cells of the PNS nerves and ganglia, arise from neural crest cells and differentiate into either myelinating or non-myelinating cells during development. Myelinating Schwann cells wrap around single large axons along their lengths and form a multilayer myelin structure, which comprises various lipids and proteins, and provide electrical insulation to the axon. Unlike mSch, nmSch cells do not wrap around axons, rather they embed multiple axons by forming a groove like structure (**Figure 3**). These two types of Schwann cells play important roles in neuron development and maintenance, and in regulating their functions [58]. To understand and identify different stages of Schwann cell development, several molecular differentiation markers are used to characterize them including transcription factor SOX-10 (Sox10) expressed at all stages, transcription factor AP-2-alpha (Tfap2a) with higher expression in neural crest cells, fatty acid-binding protein brain (Fabp7) having higher expression level in Schwann cell precursor and immature Schwann cells, glial fibrillary acidic protein (GFAP) and protein S100 (S100), which are specifically expressed in immature Schwann cells [57]. Immature Schwann cells develop into pro-myelin Schwann cells and become myelinating Schwann cells. Multiple transcription factors and pathways, like E3 SUMO-protein ligase EGR2 (Egr2), POU domain class 3 transcription factor 1 (Pou3f1), and Phosphatidylinositol 3-kinase (Pi3k) signaling pathways are associated with mSch cells [57, 59]. But the detailed characteristics of Schwann cells, especially in DRGs, remains poorly understood.

## INTRODUCTION

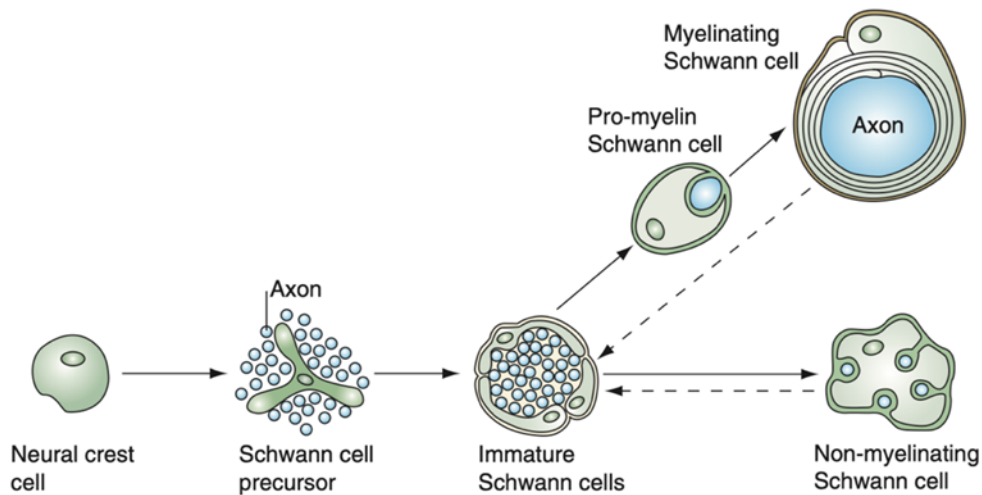


**Figure 3 An overview of Schwann cell maturation.** The developmental stage of Schwann cells can be categorized into three distinct cell clusters: migrating cells from the neural crest, Schwann cell precursors that express a range of differentiation markers, and immature Schwann cells. Myelination takes place exclusively by Schwann cells that surround the axons with large diameter, while Schwann cells enclosing the axons with small diameter evolve into non-myelinating cells. The broken arrows signify the potential for reversibility during the last stage, predominantly occurring in the postnatal phase. Adopted from *Jessen et al. [57]*.

SGC is another major glial cell type in DRGs. The cell body and axon hillock (initial segment) of neurons are tightly enveloped by a basal lamina sheath of the SCG. This structure makes the neurons and their associated SGCs act as “neuron-glia units” where both cells closely interact [60, 61]. During the initial phase of SGCs development, they appeared as star-shaped, nucleated cells with several attenuated cytoplasmic expansions located in the center of several immature neurons. Under normal physiological conditions, SGCs can control the traffic of all substances from the blood to ganglia neurons due to the envelope structure, and thereby play an important role in maintaining the homeostasis of the perineuronal microenvironment and support neuroprotection. Under pathological conditions, SGCs were reported to contribute to neuropathic pain by expressing both neurotrophic factors, like interleukin (IL)-1 $\beta$ , IL-6, tumor necrosis factor and fractalkine [62-64], and their receptors [65]. In addition, SGCs are involved in regulating ATP levels in DRGs by releasing Ecto-ATPases in pain pathways [60].

### 1.2.5 Other cell types in DRGs

Although research on neurons and glial cells has been conducted for many years, a comprehensive understanding of other cell types within ganglia is still needed. In a newly reported study, some other types of cells from the PNS were defined, including nerve-associated fibroblasts and nerve-resident homeostatic myeloid cells using scRNA-seq technology. For example, in the brachial plexus and sciatic nerves, 65% of the total individual cells were assigned to Schwann cells and fibroblasts, while the remaining cells were assigned to hematopoietic and vascular cell types [66]. In DRGs, Schwann

## INTRODUCTION

cells, smooth muscle cells, and endothelial cells were identified using single-cell mass cytometry technology [67]. In addition, our group found immune cells including T cells, macrophages, and mast cells in DRGs [52]. The development of cutting-edge techniques, including scRNA-seq, has enabled the identification of multiple cell types in DRGs, the analysis of their transcriptomic features under both healthy and diseased states, and a deeper comprehension of each cell type's role in the DRG.

### 1.3 NS and cardiovascular diseases (CVDs)

#### 1.3.1 Neuroimmune interaction

Traditionally, the NS and the immune system were thought to work independently. The interactions of these two systems are, however, recognized in some NS inflammatory diseases like multiple sclerosis [68]. In recent years, growing research has focused on exploring the detailed interactions between these two systems. For example, many immune cells and cytokines were demonstrated to affect the functions of NS including memory [69], psychiatric diseases [70], and Alzheimer's disease [71, 72]. Moreover, there is also increasing evidence indicating that the NS can affect immunity. For example, hepatic invariant natural killer T cells in mice were demonstrated to be affected by stroke [73]. Nav1.8-expressing (Nav1.8<sup>+</sup>) neurons have been shown to release calcitonin gene-related peptide (CGRP), which can inhibit the infiltration of monocytes and neutrophils during subcutaneous *S. aureus* infections in mice [74, 75]. In DRGs, a distinct population of sensory neurons were demonstrated to monitor and regulate the gene expressions in peripheral LNs [76].

#### 1.3.2 The PNS in neuroimmune interactions

The PNS actively participates in neuroimmune interactions. Afferent nerves within the PNS connect to various tissues such as lymph nodes and spleen, and function as essential pathways for conveying immune system signals to the NS. The immune molecules and pathogens can activate sensory neurons in DRGs and subsequently project the signals to the SC. From the SC, these neurons interact with spinal interneurons and relay neurons that project to the brain. For instance, in the context of pain pathways, nociceptors (nociceptive neurons) exhibit receptors for various immune mediators such as cytokines, lipids, proteases, and growth factors. These receptors can be activated by immune molecules like IL-1 $\beta$ , IL-6, IL-5, 5-hydroxytryptamine, histamine, nerve growth factor, prostaglandin E2, which originate from mast cells, neutrophils, macrophages, and T cells [77]. Upon activation by these immune mediators, sensory neurons can release neuromodulators such as substance P, CGRP, and other molecules that can influence and interact with nearby endothelial cells and additional immune cells [75, 78]. In another neuroimmune pathway, afferent neurons of the vagus nerve, which have cell bodies located in nodose and jugular ganglia complex in mice.

## INTRODUCTION

These neurons convey peripheral immune information to the brain and can be stimulated by various factors during bacterial or viral infections, as well as cellular damage. Activation occurs in response to molecules such as tumor necrosis factor, IL-1 $\beta$  and others released by immune cells [79, 80].

### 1.3.3 Neuroimmune regulation of immune cells

Neuroimmune interactions involve communication pathways between the NS and immune system components in a bidirectional manner. Recent evidence demonstrated that both the parasympathetic and the sympathetic NS can regulate inflammation in inflammatory diseases, such as sepsis, inflammatory bowel disease, arthritis, hypertension, obesity, and other diseases [81, 82].

The sympathetic NS can - among multiple other types of interactions - affect immune cells via  $\alpha$ -adrenergic and  $\beta$ -adrenergic receptors, which are the targets for noradrenaline and adrenaline. These mediators can also influence the activity of immune cells, particularly their migration, cellular activation, and cytokine production [83]. For example, CD4<sup>+</sup> T cell proliferation and cytokine production can be enhanced by the activation of  $\beta$ -adrenergic receptors [84]. Sympathetic neurons can affect macrophages and switch their transcriptome to a more pro-inflammatory state; promote browning of white adipose tissue, mediate an increase of brown adipose tissue content and thermogenesis; and initiate weight loss in obese mice [85]. The parasympathetic NS also plays important roles in regulating functions of the immune system. The most crucial component of the parasympathetic NS is the vagus nerve. For instance, the vagus nerve regulates inflammation through what is known as the cholinergic anti-inflammatory pathway [86-88]. In inflammation conditions, cytokines can stimulate an afferent arc at the site of inflammation, while the efferent arc releases acetylcholine (ACh) to modulate inflammation, such as inhibiting immune responses during sepsis or suppressing cytokine release via the  $\alpha 7$  nicotinic ACh receptor on immune cells [89]. Furthermore, in barrier tissues like skin, lung, and gut, sensory neurons can interact with immune cells [90, 91]. For example, Trpv1<sup>+</sup> sensory neurons can inhibit the recruitment of neutrophils to infection sites such as skin and lung via CGRP secretion [90, 92]. These data demonstrate that the sensory nervous system is involved in multiple neuroimmune interactions.

### 1.3.4 Neuroimmune interactions in CVDs

CVDs and their relationship with the immune system have been a topic of research for numerous years. Hypertension, a signature risk factor for CVDs, is linked to an imbalance in the neural autonomic modulation of the cardiovascular system [93, 94]. The association between the autonomic NS and the immune system appears to play important roles in hypertension [82, 95]. Pivotal research findings indicate that during myocardial infarction, the sympathetic NS can prompt the migration of bone marrow stem and progenitor cells, eventually leading to their differentiation into various cell

## INTRODUCTION

types such as endothelial progenitor cells (EPCs), inflammatory cells, and brain microglia [82, 96, 97].

Atherosclerotic plaques are devoid of innervation, and the effects of neuronal control on atherosclerosis had largely been unexplored until recently. In a study recently published by our group [52], we identified neuroimmune cardiovascular interfaces (NICIs), which emerged in atherosclerosis-affected adventitia segments and displayed expanded axon networks, including growth cones at axon termini near immune cells and media smooth muscle cells. We also discovered that NICIs formed a structural ABC: abdominal adventitia nociceptive afferents entered the SC through T6-T13 DRGs and could be traced to the brain, including the parabrachial nucleus and central amygdala neurons. Sympathetic efferent neurons projected from medullary and hypothalamic neurons to the adventitia via spinal intermediolateral neurons and both coeliac and sympathetic chain ganglia (**Figure 4**). Additionally, during atherosclerosis progression, ABC PNS components were activated. These findings illustrated the neuroimmune interactions between immune cells in the arterial wall and the NS, forming a structural ABC, and therapeutic intervention into the ABC attenuates atherosclerosis. However, functional impacts of the sensory NS to affect atherosclerosis remain to be elucidated.

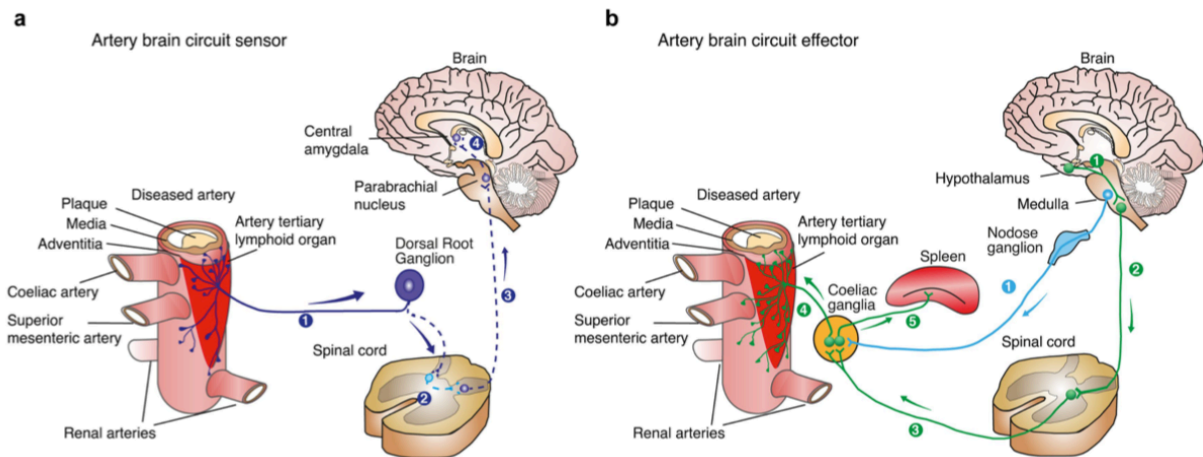


**Figure 4 Schematics of the ABC sensor and the ABC effector. A,** Aortic adventitia NICIs initiate the ABC using sensory neurons originating in the DRGs to enter the CNS via the SC dorsal horn and projects to the brain stem medulla oblongata. **B,** SNS efferent projection stem from hypothalamic and brainstem nuclei, extending to the SC and to the adventitia through the CG. Vagal efferent originates in the medulla oblongata project to the CG to form an ABC effector. Adopted from *Mohanta et al., 2022 [52]*.

### 1.4 Single-cell RNA sequencing (scRNA-seq) technology

Cells have traditionally been studied in the past regarding single genes but information on the single-cell transcriptome was lacking. The development of single-cell technology revolutionized transcript and protein expression allowing insights into the physiology and aberrant disease-related changes

## INTRODUCTION

to an unprecedented level. ScRNA-seq technology was first reported in 2009 [98], and has become increasingly refined during the last years as the state-of-the-art technology for providing unprecedented insights into the cellular diversity of individual cell transcriptomes [99].

### 1.4.1 ScRNA-seq provides transcriptome information at the single-cell level

High-throughput RNA-seq has become a reliable method for quantitative total transcriptome identification at the single-cell level [100]. Over the past few years, various scRNA-seq technologies have been established, including single-cell tagged reverse transcription-seq [101], single-cell RNA barcoding-seq [102], Smart-seq [103], Smart-seq2 [104], Drop-seq [105], and 10x Genomics platform based scRNA-seq [106]. All these improvements make scRNA-seq a powerful tool for cell transcriptome research at the single-cell level. In scRNA-seq, the individual cells are labelled using a unique label before high-throughput RNA-seq. For example, in the molecular crowding SCRBS-seq protocol, a lysis buffer including barcoded oligo-dT primers was put in each well of 96 well plate and the individual cells were sorted into each well, followed by creation of the library of each cell in a separate well [107]. In the Drop-seq protocol, a microfluidic device was designed to rapidly separate thousands of individual cells into nanoliter-sized aqueous droplets and binding distinct barcodes with each cell's RNAs [105]. The biggest advantage of drop-seq is the ability to sequence even more than several thousands of cells at one time. Based on this technology, the 10x Genomics chromium controller, IX and X series devices were introduced for single-cell partitioning and barcoding, multiplexing, fixed-RNA profiling of live and fixed cells respectively.

## INTRODUCTION

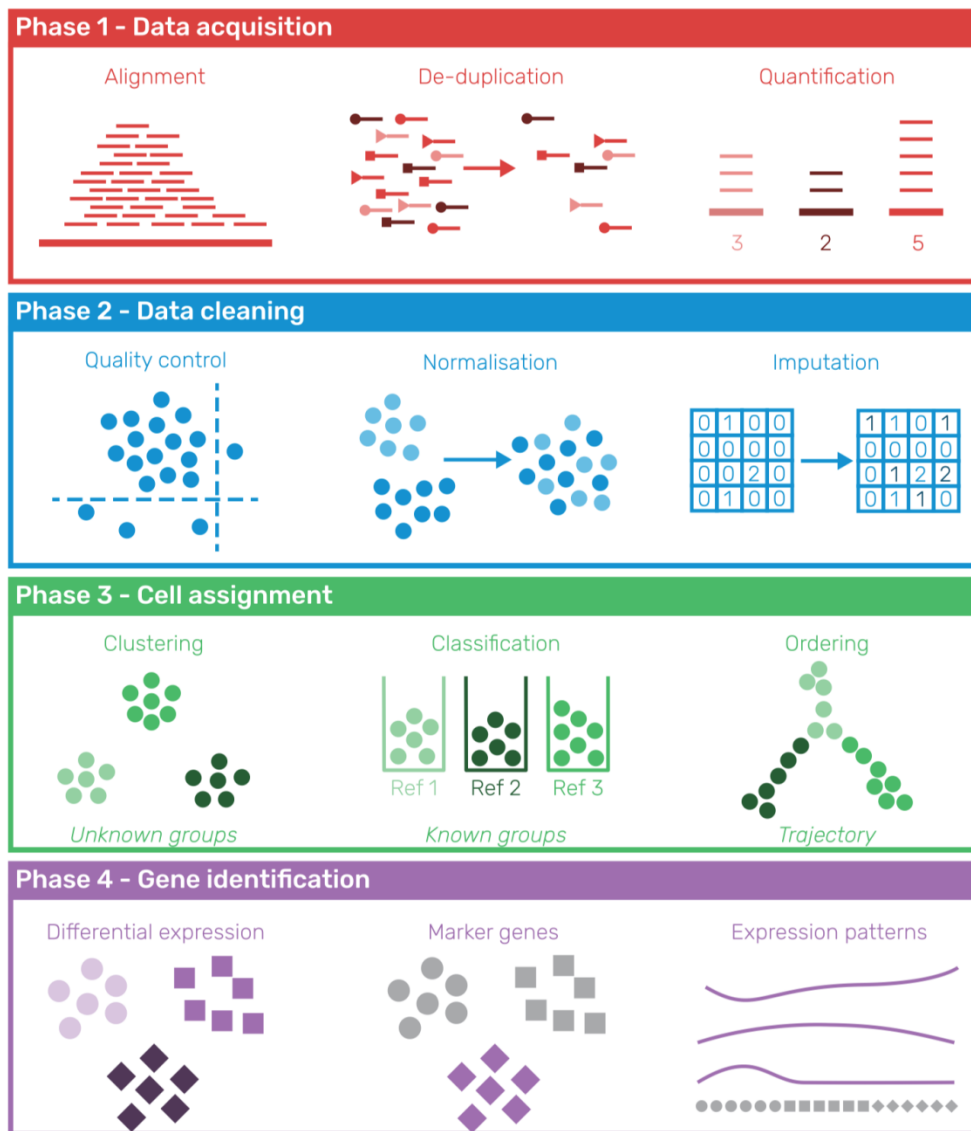


**Figure 5 Steps of a standard scRNA-seq data analysis workflow.** During the initial stage (data acquisition), samples undergo pre-processing and are aligned to the genome, resulting in the generation of expression count matrices. Subsequently, in the second stage (data cleaning), quality control measures and filtering are applied. In the third stage (cell assignment), cells are grouped into subpopulations based on their gene expression profiles. While the fourth stage (gene identification), involves the computation of differentially expressed genes (DEGs) and the identification of marker genes to provide meaningful insights into the sequencing data. Adopted from Zappia et al. [108].

After the single-cell capture and RNA-seq, the next step is data analysis (**Figure 5**). With the development of scRNA-seq, a standard analytical workflow for the data analysis has been established [109-111]. The workflow can be divided into several steps, including pre-processing and quality control, normalization, identification, clustering into subpopulations, and gene identification. Most scRNA-seq analyses were performed using published tools. Currently, there are more than four hundred published tools, with R being the most popular programming platform [108]. The tools are divided into several categories based on their tasks or functions, including visualization,

## INTRODUCTION

clustering, dimension reduction, ordering, normalization, differential expression, interactive, quality control, gene networks among others.

### 1.4.2 ScRNA-seq in neuroscience research

The NS in adult mammals is extremely complex and its molecular architecture has not systematically delineated before the application of scRNA-seq (**Figure 6**). Zeisel et al. performed a systematic and comprehensive survey of mouse NS by analyzing 500,000 cells from 19 different adolescent mouse NS regions including different brain regions and the SC in the CNS; and the enteric NS, the sensory DRGs and the sympathetic chain ganglia in the PNS via scRNA-seq technology using the 10x Genomics Chromium protocol [112]. After a multistage analysis pipeline, 265 clusters were obtained from 160,796 high-quality single-cell transcriptomes and these were assigned to seven major clusters based on their gene expression signatures: neurons, oligodendrocytes, astrocytes, ependymal cells, peripheral glia, immune cells, and vascular cells. The gene expression also showed area-specific gene expression patterns of some cell classes. For example, PNS neurons were separated from the CNS neurons in scRNA-seq data, reflecting the different origins, i.e. PNS neurons were mostly neural-crest-derived, while CNS neurons were neural tube-derived. The peripheral neurons were then classified into sensory, sympathetic, and enteric subdivisions, corresponding to their functional, anatomical, and developmental gene expression profiles. ScRNA-seq of numerous neuronal cells offers a powerful resource and initial insights into molecular diversity and composition of the mouse NS. The resulting transcriptomic atlas facilitates the identification of several cell type-specific genes, thereby enhancing our understanding of their functions.

ScRNA-seq was not only used to define the transcriptomic atlas of normal NS, but also used to identify the disease-associated transcriptional changes. For instance, scRNA-seq was utilized to examine peripheral nerve cells in both healthy conditions and chronic autoimmune neuritis, leading to the identification and independent validation of nmSch and nerve-associated fibroblast markers [66]. Intriguingly, homeostatic myeloid cells were outnumbered by infiltrating lymphocytes, which altered the local cell-cell interaction and prompted a specific transcriptional response in glial cells. This research uncovered a partially preserved autoimmunity module induced in glial cells during disease progression [66]. In another study, scRNA-seq of uninjured, injured, and developing sciatic nerve cells to identify the ligands expressed by different injured rodent nerve cell types and their association with peripheral neurons [113]. This study provided a different approach to use scRNA-seq to search for the functional differences among different treatments.

## INTRODUCTION

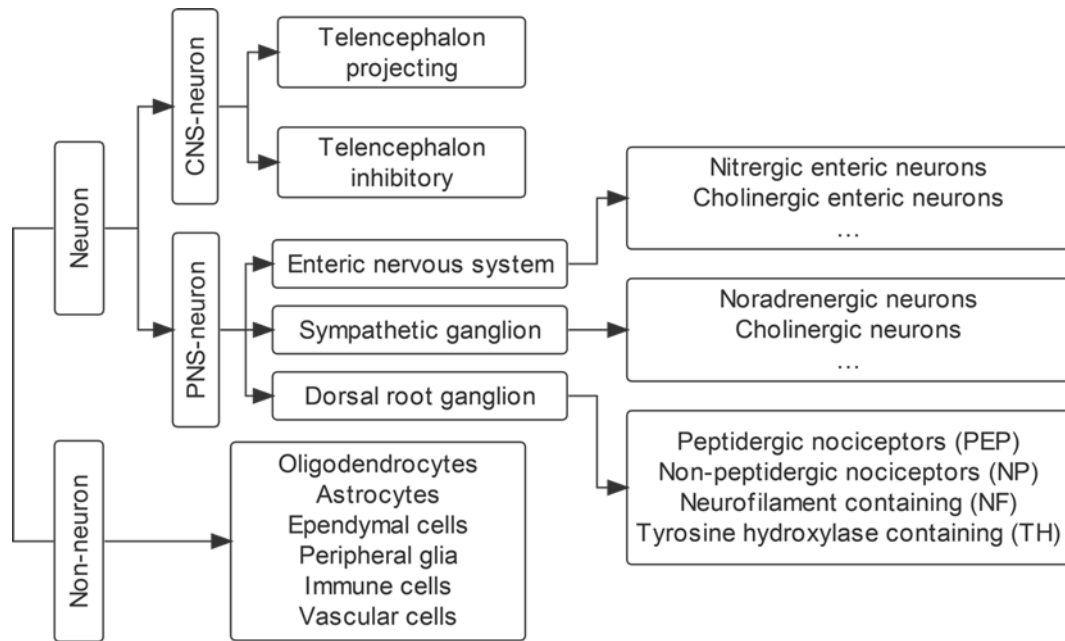


**Figure 6 Molecular survey of the mouse NS using scRNA-seq technology.** Using scRNA-seq, mouse NS cells are identified as neurons and non-neuronal cells. Based on their locations, neurons are classified into central NS neurons and peripheral NS neurons. In CNS, two types of neurons, telencephalon projecting neurons and telencephalon inhibitory neurons, can be identified. In the PNS, neurons are classified into three types by their locations. Within DRGs, four distinct neuronal classifications can be identified: peptidergic nociceptors (PEP), non-peptidergic nociceptors (NP), neurofilament heavy chain containing (NF), and tyrosine hydroxylase containing (TH) neurons. Non-neuronal cells in the NS encompass glial cells, ependymal cells, immune cells, and vascular cells. Adapted from *Zeisel et al., 2018 [112]*.

### 1.4.3 DRG neuron subtype identification using scRNA-seq

As previously detailed, NS cells were categorized into seven principal groups according to their gene expression profiles: neurons, oligodendrocytes, astrocytes, ependymal cells, peripheral glia, immune cells, and vascular cells [112]. DRG neurons can be divided into two major subtypes: myelinated large size neurofilament heavy chain (Nefh) positive neurons, and unmyelinated Nefh<sup>-</sup> small size nociceptive C neurons [114]. Proprioceptive neurons were identified by their expression of TrkC (Ntrk3) and the calcium-binding protein parvalbumin (Pvalb) [115]. These neurons innervate Golgi tendon organs and muscle spindles. In nociceptors, a major division is PEP and NP neurons. Using scRNA-seq, neurochemicals of sensory neurons have been extensively studied and correlated to functional properties [116-118]. In the first systemically scRNA-seq survey of DRG neurons subtypes, 799 individual cells were collected from mouse lumbar DRGs, the non-peptidergic neurons were excluded using beta-2-microglobulin (B2m) and vimentin (Vim), and the neurons were grouped into PEP, NP, NF and TH neurons at the single-cell level [119]. In this study, the PEP neuron cluster was defined by neuropeptides coding genes such as tachykinin 1 (Tac1) and calcitonin / calcitonin-related polypeptide alpha (Calca), and neurotrophic tyrosine kinase receptor type 1 (Ntrk1). The NP cluster was defined using key genes mas-related G-protein coupled receptor

## INTRODUCTION

member (Mrgprd) and P2X purinoceptor 3 (P2rx3). The NF cluster was defined using genes *Nefh* and *Pvalb*. The TH cluster was defined by the marker gene tyrosine 3-monooxygenase (*Th*). The definition of DRG neurons using scRNA-seq differs from traditional immune staining-based classifications and this provides considerably more information, but it also allows for definition of neuron and nonneuron cell subtypes. Meanwhile, different scRNA-seq datasets defined the DRG neurons using different criteria. For example, somatostatin (*Sst*) was used to define PEP neurons [120, 121]; NP neurons were defined by the expression of the neurotrophic factor receptor *Ret* along with the coreceptors *GFRα1* (*Gfra1*) and *GFRα2* (*Gfra2*) [122]. In another study, 197 single DRG neurons were picked from dissociated DRG cells, including IB4-positive neurons, IB4-negative small neurons, and large neurons. These neurons were separated into 17 different types by high-coverage scRNA-seq ( $10950 \pm 1218$  genes per neuron) [123]. In a scRNA-seq survey of newborn and young mouse DRG neurons [124], it was observed that the DRG neurons were named differently according to a previous study but exhibited consistency in gene expression (**Figure 7**) [112, 119, 124-126].

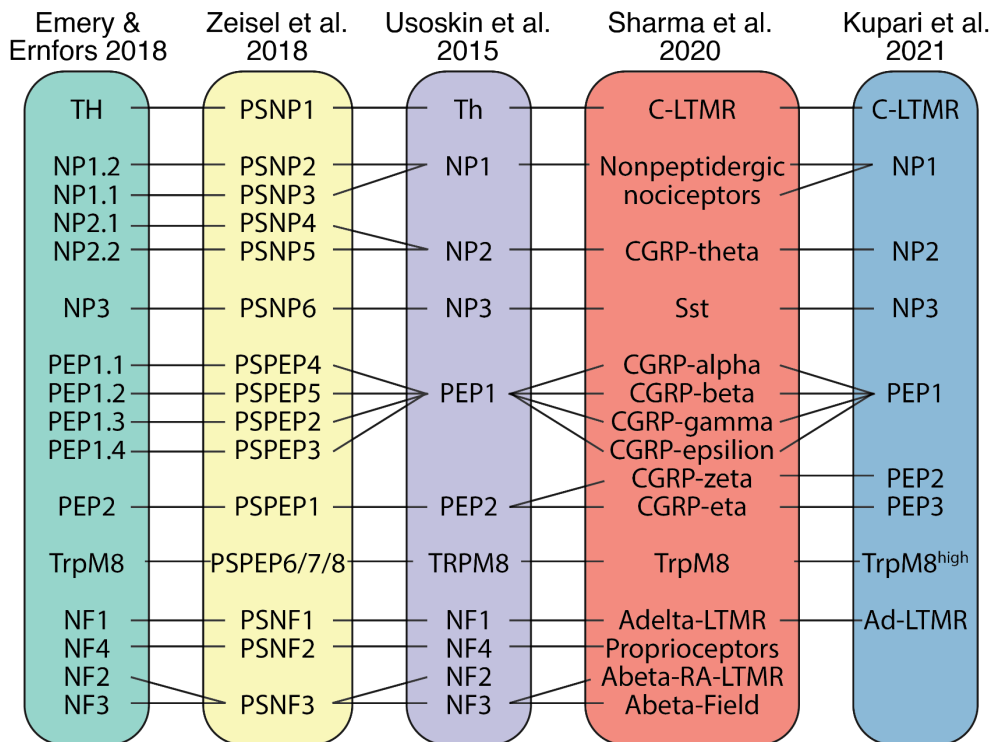


**Figure 7 Synopsis of the DRG neuron subtypes.** A comparative analysis was conducted on the DRG neuron subtypes present in the mouse and macaque datasets to establish a comprehensive understanding of the similarities and differences in terms of classification and nomenclature. This examination aimed to facilitate a better interpretation of the research findings and their implications across different studies. The overview presented here serves as a foundation for further exploration and discussion of the respective DRG neuron subtypes and their corresponding terminology [112, 119, 124-126]. Adopted from *Kupari et al.* [126].

## INTRODUCTION

### 1.4.4 ScRNA-seq in cardiovascular research

In cardiovascular research, scRNA-seq technology has been employed. Profiling the transcriptional heterogeneity of the cells in atherosclerotic plaques has enabled a deeper understanding of disease pathogenesis and progression. Using the scRNA-seq of aortic leukocytes from various atherosclerosis mouse models, 11 distinct leukocyte types were defined; surface markers, gene programs, and cytokine secretion were examined; and DEGs were identified in healthy and atherosclerotic arteries [40]. Consistent with histological previous histological findings, transcriptomic profiling showed that macrophages, T cells, monocytes and various DC subtypes constituted the main cellular components in both mouse and human atherosclerotic arteries [40]. A comparison between non-diseased and atherosclerotic aorta transcriptomes revealed 13 distinct aortic cell clusters and 3 distinct types of macrophages. A novel macrophage type i.e. Trem2<sup>hi</sup> macrophages, were found in the arterial wall that are specialized in lipid metabolism and catabolic processes [39]. Furthermore, scRNA-seq was utilized to characterize modulated vascular smooth muscle cells (SMCs) in the aortic root and ascending aorta during atherosclerosis progression. Transcription factor 21 (TCF21) was found to be strongly associated with SMC phenotypic modulation in diseased human coronary arteries [127]. In a recent study on human heart development, scRNA-seq was performed on 3717 individual cells from human embryonic cardiac samples [128]. Cell atlases of the embryonic heart at three developmental stages were studied and the cell-type distribution and spatial organization in the human embryonic heart were mapped. Potential roles of diverse cell types during human embryonic heart development were identified. This study provides a publicly available resource of the human embryonic heart network using scRNA-seq technology. Additionally, cell-cell communication mediated by ligand-receptor pairs or complexes is crucial for understanding biological processes, and scRNA-seq makes it possible to analyze the intercommunications among different single cells [129-131]. Recently, 10519 nucleated non-myocyte cells from heart ventricles were investigated using scRNA-seq [132], defining 12 distinct cell clusters and describing the transcriptional heterogeneity of major cell types. It also defined parallel intercellular cell-cell communications within the cardiac cellular network called cardiac cellulome using a dataset of 2009 ligand-receptor pairs.

### 1.4.5 Defining neuroimmune interactions by scRNA-seq

Research on cellular functions is increasingly used to understand the collective context of each cell. Interactions between cells involve a diverse array of molecules, such as ions, metabolites, integrins, receptors, junction proteins, structural proteins, ligands, and proteins secreted by the extracellular matrix [133]. Among the NS and the immune system, the phenotypes of neurons, as well as non-neuronal cells such as immune and stromal cells, are influenced by the local tissue environment during aging and chronic inflammatory diseases. Consequently, transcriptome analysis of individual

## INTRODUCTION

cells may help to identify critical pathways within neuroimmune circuits. scRNA-seq is the state-of-the-art technology to address these issues: i) it opens the opportunity to identify new subtypes of immune cells based in their native tissue environment, e.g. as activated in response to their interaction with the NS in atherosclerosis; and ii) it has the ability to define specifically expressed mRNAs in the neuronal cells due to pathological neuroimmune interactions [39, 134].

Innate immune cell compartments are highly diverse. Using scRNA-seq on microglia and macrophages from several brain compartments, a comprehensive molecular census of hematopoietic cells was detected during neuroinflammation in different brain compartments, and specific cell types were defined for each compartment. From the scRNA-seq results, it was found that MHC-II<sup>+</sup> circulating myeloid cells may play an important role in neuroinflammation in the brain [135]. In another study, microglia from multiple anatomical structures of the CNS were characterized in multiple sclerosis indicating that demyelinating and neurodegenerative diseases can be associated with a specific subtype of microglia with distinct hallmark genes, including Apoe, insulin-like growth factor I (Igf1r), Lysozyme C-2 (Lyz2), integrin alpha-x (Itgax), Cytochrome b-245 heavy chain (Cybb), and the MHC-II genes [136]. In the PNS, molecularly distinct LN-innervating sensory neuron subtypes were found to express several specific inflammatory molecules and receptors including Toll-like receptor 4 (TLR4), which is a well-known receptor for lipopolysaccharide [124, 137].

### 1.5 Aims

We previously identified a direct neuronal connection between arteries and the brain that we have termed the ABC. However, much needs to be learned about the molecular mechanisms of the ABC and its potential impacts to control atherosclerosis progression. Here, we focus on the sensory part of the ABC, i.e. the ABC sensor [52]. The core experiments to understand the ABC sensor better used scRNA-seq. For this purpose, several method-related techniques had to be established including the preparation of DRGs and the SC to avoid blood contamination, remove meninges before preparing single-cell suspension, establish quality controls and apply various algorithms for data analyses. Yet, the major aim of this thesis was to address the question whether DRG cells show changes of transcriptomes in neuronal and non-neuronal cells during atherosclerosis progression in aged mice. The following questions were addressed:

1. Is atherosclerosis associated with changes in immune cells in DRGs and the SC?
2. Is atherosclerosis associated with changes in transcriptome profiles in DRG neurons and in non-neuronal cells?
3. What are the effects of chemical denervation on DRGs at single-cell resolution?
4. What are the potential DRG-associated atherosclerosis-specific neuroimmune interactions?

## 2 MATERIALS AND METHODS

### 2.1 Materials

#### 2.1.1 Mice

C57BL/6J WT and Apoe<sup>-/-</sup> mice with a C57BL/6J genetic background were acquired from the Jackson Laboratories. Both WT and Apoe<sup>-/-</sup> mice were bred and housed in Munich University's specific pathogen-free animal facility, adhering to a 12-hour light/dark cycle. Mice employed in this project were young (8 weeks), adult (24 - 32 weeks), and aged (more than 78 weeks) and sustained on a standard chow diet. The animal procedures were approved by the Regierung Oberbayern in accordance with the local Animal Use and Care Committee's guidelines and the National Animal Welfare Laws.

#### 2.1.2 Standard solutions and buffers

The subsequent tables encompass of reagents, equipment, and scRNA-seq data analyzing packages utilized in the study:

**Table 1 List of reagents**

Reagents	Company	Cat#	Storage
PBS	Sigma-Aldrich	P4417-100TAB	4 °C
DPBS	Gibco	14190-094	4 °C
PFA	Sigma-Aldrich	P-6148	RT
EDTA	Roth	8040.1	RT
Hematoxylin	Dako	S2020	RT
10% BSA	Aurion	70411/1	4 °C
Acetone	Merck	K40718714	RT
Ethanol	VWR	18k144019	RT
Tissue Tec	Sakura	0827400006	RT
Fluoromount G	Dako	S3023	4 °C
Eosin	Roth	X883.1	RT
Sirius red	Waldeck	1A-280	RT
Roti-Histokitt-II	Roth	T160.1	RT
DMSO	PanReac AppliChem	A3672,0100	RT
Tween 80	Sigma-Aldrich	P1754	RT

## MATERIALS AND METHODS

Percoll	Sigma-Aldrich	GE17-0891-01	4 °C
Compensation Beads	Thermo Fisher	01-2222-42	4 °C
Ketamin 10%	Medistar	799-762	RT
Xylazin 2%	Ecuphar	797-469	RT

**Table 2 List of buffers**

Solution	Composition	Storage
PBS (10 x)	1.37 M NaCl, 27 mM KCl, 0.1 M Na <sub>2</sub> HPO <sub>4</sub> , 17.6 mM KH <sub>2</sub> PO <sub>4</sub> , adjust pH to 7.2 - 7.4	RT
PBS (1 x)	1-part 10 x PBS with 9 parts waters	RT
4% PFA	40g paraformaldehyde in 980 ml PBS, adjust pH to 7.2 - 7.4 with NaOH; Filter before use;	4 °C
10 x EDTA buffer	Na <sub>2</sub> EDTA·2H <sub>2</sub> O 18.61 g, dH <sub>2</sub> O 1000 ml, PH 8.4	RT
FACS buffer	PBS with 2% fetal calf serum (FCS; Lonza);	4 °C
ACK lysis buffer	0.15 mM NH <sub>4</sub> Cl, 1 mM KHCO <sub>3</sub> , 0.1 mM Na <sub>2</sub> EDTA, pH 7.2-7.4	RT
SIP (standard isotonic percoll)	9 parts percoll with 1-part 10 x PBS	Freshly prepared RT
70% percoll	70 ml SIP mix with 30 ml 1 x PBS	RT
37% percoll	37 ml SIP mix with 63 ml 1 x PBS	RT
30% percoll	30 ml SIP mix with 70 ml 1 x PBS	RT
50% Glycerol	Mix an equal volume of water and 99% glycerol, through a 0.2 µm filter	-20 °C

**Table 3 Digestion cocktail for SC and DRGs**

Digestion cocktail	Final concentration	Company
DPBS	1 x	Gibco
DNase I	60 U/mg	Sigma, 2000 U/mg
Hepes	20 mM	Sigma, MW 238.30
Collagenase I	450 U/ml	Sigma, 125 CDU/mg
Hyaluronidase	60 U/mg	Sigma, 400 – 1000 U/mg
Collagenase XI	125 U/ml	Sigma, 1200 CDU/mg

## MATERIALS AND METHODS

### 2.1.3 Antibodies

**Table 4 List of antibodies for FACS analyses**

Antibody	Clone	Format	Dilution	Company
Fixable Viability Dye (FVD)	-	eFluor 780	1:1000	eBioscience
		eFluor 660	1:1000	eBioscience
		eFluor 506	1:1000	eBioscience
Anti-CD45	30-F11	Percp-cy5.5	1:200	eBioscience
	30-F11	V500	1:200	eBioscience
Anti-CD16/32	93	Purified	1:300	BioLegend
Anti-TCRb	H57-597	BV605	1:200	eBioscience
Anti-B220	RA3-6B2	V500	1:200	eBioscience
Anti-CD4	GK1.5	PE-cy7	1:200	BioLegend
Anti-CD8	53-6.7	V450	1:200	BioLegend
Anti-CD11b	M1/70	BV711	1:200	BioLegend
Anti-CD11c	N418	FITC	1:200	BD
Anti-CD44	IM7	APC-cy7	1:200	BioLegend
Anti-CD62L	MEL-14	FITC	1:200	BioLegend
Anti-NeuN	A60	Alexa Fluor488	1:100	Millipore

**Table 5 List of immunofluorescence primary antibodies**

Antibody	Cat#/Clone	Cell/Structure	Host	Dilution	Company
Anti-CD3e	145-2C11	Pan-T cell	Hamster	1:100	BD
Anti-B220	RA3-6B2	Pan-B cell	Rat	1:200	BD

**Table 6 List of immunofluorescence secondary antibodies**

Antibody	Host	Format	Dilution	Company
Anti-rabbit IgG	Goat	Cy3; Cy5	1:300	Invitrogen
Anti-FITC IgG	Mouse	Cy3	1:300	Invitrogen
Anti-rabbit IgG	Goat	Alexa 488	1:200	Invitrogen
Anti-rabbit IgG	Donkey	Cy3; Cy5	1:300	Dianova
Anti-rabbit IgG	Goat	Cy3; Cy5	1:300	Invitrogen
Anti-rat IgG	Donkey	Cy3; Cy5	1:300	Dianova

## MATERIALS AND METHODS

### 2.1.4 Equipment

**Table 7 List of equipment**

Name	Company	Model/Type
Dissection stereomicroscope	Leica	Stemi 2000
Fluorescence microscope	Leica	DM 6000 B
Cryostat microtome	Leica Biosystems	Leica RM2235
Automated Cell Counter	Thermo Fisher	Countess 3 FL
Centrifuge	Eppendorf	5810R
Refrigerated centrifuge	Thermo Fisher	Megafuge™ 40R
ThermoMixer	Eppendorf	ThermoMixer® C
Flow cytometer	BD	Canto-II
		LSRFortessa
Automated cell counter	Bio-Rad	TC20™
Light microscope	Leica	DM LB

### 2.1.5 10x Genomics scRNA-seq reagent kits, accessories, and equipment

**Table 8 10x Genomics scRNA-seq reagent kits, accessories, and equipment**

Reagent Kits	Cat#	Company	Storage
Chromium Next GEM Single Cell 5' Library & Gel Bead Kit v1.1, 16 rxns	1000165	10x Genomics	-20 °C
Chromium i7 sample index plate	220103	10x Genomics	-20 °C
Fragment Analyzer Qualitative DNA kits	DNF-0910-k0500	Agilent	4 °C
Next GEM chip G single cell kit	1000127	10x Genomics	RT
Buffer EB	19086	Qiagen	RT
Nuclease-free water	129115	Qiagen	RT
Ethanol, Pure	E7023	Millipore	RT
Tween 20 80%	1662404	Bio-Rad	RT
Qubit™ dsDNA HS and BR Assay Kits	Q32854	Thermo Fisher	4 °C
SPRIselect for Size Selection	B23318	Beckman Coulter	4 °C
<b>Accessories</b>			
Chromium Next GEM Secondary Holder	3000332	10x Genomics	RT
MicroAmp™ 8-Cap Strip, clear	N8010580	Thermo Fisher	RT
10x Magnetic Separator	230003	10x Genomics	RT

## MATERIALS AND METHODS

<b>Equipment</b>			
Chromium controller	1000202	10x Genomics	/
C1000 Thermal Cycler with 96-Well Fast Reaction Module	1851196	Bio-Rad	/
Qubit 4 Fluorometer	Q33238	Thermo Fisher	/
Vortex Mixer	10153-838	VWR	/
5200 Fragment Analyzer System	M5310AA	Agilent	/

### 2.1.6 Software and algorithms

**Table 9 Software and algorithms (under macOS 13.1)**

<b>Software and algorithms</b>	<b>Source</b>	<b>Identifier</b>
R (v 4.2.1)	R Core Team	<a href="https://www.r-project.org/">https://www.r-project.org/</a>
RStudio (v 1.4)	RStudio Team	<a href="https://rstudio.com/">https://rstudio.com/</a>
R – tidyr (v 1.1.3)	RStudio	<a href="https://tidyr.tidyverse.org/">https://tidyr.tidyverse.org/</a>
R – ggplot2 (v 3.3.3)	RStudio	<a href="https://ggplot2.tidyverse.org/">https://ggplot2.tidyverse.org/</a>
R – dplyr (v 1.0.5)	RStudio	<a href="https://dplyr.tidyverse.org/">https://dplyr.tidyverse.org/</a>
R – Seurat (v 4.3.0)	Satija lab	<a href="https://satijalab.org/seurat/index.html">https://satijalab.org/seurat/index.html</a>
R – clusterProfiler (v 4.8)	Guangchuang Yu Lab	<a href="https://bioconductor.org/packages/clusterProfiler/">https://bioconductor.org/packages/clusterProfiler/</a>
R – DESeq2 (v 3.12)	Bioconductor	<a href="https://bioconductor.org/packages/DESeq2/">https://bioconductor.org/packages/DESeq2/</a>
R – affy (v 1.68.0)	Bioconductor	<a href="https://bioconductor.org/packages/affy/">https://bioconductor.org/packages/affy/</a>
R – gcrma (v 2.62.0)	Bioconductor	<a href="https://bioconductor.org/packages/gcrma/">https://bioconductor.org/packages/gcrma/</a>
R – RCy3 (v 2.10.2)	Bioconductor	<a href="https://bioconductor.org/packages/RCy3/">https://bioconductor.org/packages/RCy3/</a>
R – biomaRt (v 2.46.3)	Bioconductor	<a href="https://bioconductor.org/packages/biomaRt/">https://bioconductor.org/packages/biomaRt/</a>
R – ComplexHeatmap (v 2.6.2)	Bioconductor	<a href="https://bioconductor.org/packages/ComplexHeatmap/">https://bioconductor.org/packages/ComplexHeatmap/</a>
R – EnhancedVolcano (v 1.10.0)	Bioconductor	<a href="https://bioconductor.org/packages/EnhancedVolcano/">https://bioconductor.org/packages/EnhancedVolcano/</a>
org.Mm.eg.db (v 3.13.0)	Bioconductor	<a href="https://bioconductor.org/packages/org.Mm.eg.db/">https://bioconductor.org/packages/org.Mm.eg.db/</a>
mouse430a2.db (v 3.13.0)	Bioconductor	<a href="https://bioconductor.org/packages/mouse430a2.db/">https://bioconductor.org/packages/mouse430a2.db/</a>
R – patchwork (v 1.1.0)	Thomas LinPedersen	<a href="https://github.com/thomasp85/patchwork/">https://github.com/thomasp85/patchwork/</a>
R – igraph (v 1.2.6)	igraph core team	<a href="https://igraph.org/r/">https://igraph.org/r/</a>
R – monocle2 (v 1.2.6)	Trapnell lab	<a href="https://github.com/cole-trapnell-lab/">https://github.com/cole-trapnell-lab/</a>
R – UCell (v 1.1)	Github/carmonalab	<a href="https://github.com/carmonalab/UCell">https://github.com/carmonalab/UCell</a>

## MATERIALS AND METHODS

R – CellChat (v 1.4)	Github/sqjin	<a href="https://github.com/sqjin/CellChat">https://github.com/sqjin/CellChat</a>
CellRanger (v 5)	10x Genomics	<a href="https://www.10xgenomics.com/">https://www.10xgenomics.com/</a>
Metascape (Enrichment webtool)	Zhou et al., Nat. Com., 2019	<a href="https://metascape.org/">https://metascape.org/</a>
Cytoscape (v 3.8.2)	Cytoscape Consortium	<a href="https://cytoscape.org/">https://cytoscape.org/</a>
FlowJo (v 10.7.1)	BD	<a href="https://www.flowjo.com/">https://www.flowjo.com/</a>
Prism (v 9.0.2)	GraphPad	<a href="https://www.graphpad.com/">https://www.graphpad.com/</a>
Adobe Illustrator (v 25.0)	Adobe	<a href="https://www.adobe.com/products/illustrator.html">https://www.adobe.com/products/illustrator.html</a>

## 2.2 Methods

### 2.2.1 Spinal cord (SC), meninges, and DRG isolation

Mice were anesthetized with Ketamine-Xylazine. After intracardial blood collection, intracardiac perfusion of the mouse vasculature was using 10 ml of 0.5 mM EDTA/PBS, then by 20 ml chilled PBS and 20 ml chilled FACS buffer as described before. Mouse tissues including spleen, inguinal lymph node and renal lymph node (RLN), aorta and heart were isolated and in tissue blocks were prepared in Tissue-Tek(Sakura Finetek) [52, 138, 139]. After isolation of these tissue, the whole spine was isolated by resecting the discs and connective tissues between the base of the skull and first cervical vertebrae (c1) for isolation of SC and DRGs. For the SC isolation, the SC was segmentally removed from the vertebrae without damaging the vertebral bone marrow to avoid B cell contamination (around 5 - 7 vertebrae per segment) by manual breaking of the intervertebral ligaments, discs, and other connective tissues. The SC was put in cold DPBS on 35 mm petri dishes, the connected nerve fibers were removed; meninges were separated from SC as an individual sample.

DRGs were isolated after isolation of the spinal cord. For DRG isolation, the last rib was kept intact for the identification of T13 ganglia which is located in the intervertebral foramen below the last rib. DRGs were isolated from the intervertebral foramens in both sides of the vertebral column using special forceps such as Dumont forceps and Vannas spring scissors, the connected nerve fibers were trimmed, and DRGs were collected into 1.5 ml Eppendorf tubes containing FACS buffer.

### 2.2.2 Preparation of single-cell suspensions from spleen and LN

Mouse spleens (halved) and lymph nodes were minced into tiny pieces utilizing fine scissors. The tissues were then placed in a 70 µm cell strainer positioned atop a on a 50 ml Falcon tube. The cell

## MATERIALS AND METHODS

suspension was generated by softly mashing the tissue with a syringe-piston and by periodically adding FACS buffer, followed by centrifuged at 400 x g 5 minutes at 4 °C. For splenic cell suspension, the pellet was re-suspended in 8 ml ACK lysis buffer and incubated for 5 minutes at RT to eradicate red blood cells. Next, 5 ml of FACS buffer was added, and centrifugation process was repeated at 400 × g for 5 minutes at 4 °C. The pellet was then re-suspended in 5 ml of chilled FACS buffer, passed through a 50 µm strainer filled with the cell suspension solution, and washed again before suspending the splenocytes in 1 ml FACS buffer. Regarding lymph nodes, the pellet was resuspended in 200 µl FACS buffer after centrifugation. The cells were subsequently counted using an automated cell counter [138, 139].

### 2.2.3 Preparation of single-cell suspensions from SC, meninges, and DRG

SC, meninges, and DRGs were transferred into a new 1.5 ml Eppendorf tube with DPBS and centrifugation was carried out at 400 × g for 30 seconds at 4 °C, 4 °C to wash the tissues. The SC and meninges were dissected into small pieces and incubated in 1 ml of 1 x DPBS enzyme mix solution (450 U/ml collagenase type I, 125 U/ml Collagenase XI, 60 U/mg Hyaluronidase, 60 U/mg DNase I, and 20 mM HEPES) at 37 °C for 30 minutes on a Eppendorf thermomixer. DRGs were put into 1 ml of 1 x DPBS enzyme mix solution directly without any mincing and incubated at 37 °C for 45 minutes on a Eppendorf thermomixer. Percoll (GE Healthcare) was diluted with PBS to prepare different concentrations of percoll solutions i.e. SIP, 70%, 37%, and 30% percoll solutions [140, 141]. After digestion, tissues were homogenized by pipetting up and down using 1 ml pipette, filtered through 70 µm strainer into a 50 ml tube, and centrifuged at 400 x g for 7 minutes at 4 °C. Percoll density gradient was used to separate nucleated cells from myelin and debris. For this purpose, the SC pellet was resuspended in 5 ml of 70% percoll and transferred into a 15 ml tube followed by sequential addition of 4 ml of 30% percoll and 4 of ml 37% percoll using disposable glass Pasteur pipettes. The tube was centrifuged at 500 x g for 30 minutes at RT without brakes. After centrifugation, top myelin layer was aspirated, the white ring at the interface between 70% percoll and 37% percoll containing lymphocytes, microglia and neurons was carefully isolated into a 50 ml tube. The tube containing cells was diluted with DPBS to 30 ml and centrifuged at 500 x g for 10 minutes at 4 °C to remove any percoll in the solution. The supernatant was discarded after centrifugation, and pellet was resuspended in 200 µl FACS buffer for further use. For meninges and DRGs, the pellet was resuspended in 200 µl FACS buffer after centrifugation without any percoll density gradient step.

### 2.2.4 Flow cytometry

For FACS staining of single cell suspension, samples were transferred into 96 well V-bottom plate, washed twice with FACS buffer, and incubated with fixable viability dye (FVD) for 20 minutes at 4 °C

## MATERIALS AND METHODS

to irreversibly label dead cells. After incubation, cells were centrifuged, washed twice with FACS buffer and further incubated with Fc blocker CD16/32 for 10 minutes, and with antibody cocktail in FACS buffer for 30 minutes at 4 °C. The cell samples were then centrifuged, washed twice with FACS buffer, and either measured the same day or stained for intracellular antibodies. Following surface staining, the cells were fixed with 200 µl of freshly prepared fixation/permeabilization working solution (1 : 3) for 50 minutes at 4 °C. The cells were centrifuged and washed with 200 µl of 1 × permeabilization buffer (prepared by diluting 10 × permeabilization buffer with sterile water). After another centrifugation, the cells were re-suspended with 250 µl FACS buffer and employed for FACS analysis. Splenocytes and compensation beads (Thermo Fisher) were used as single staining controls, while the staining procedure was operated as described above with only one antibody. FACS measurements were performed using the BD Canto II or BD Fortessa (BD Biosciences) system and analyzed using FlowJo (v.10.6, BD). Total cell numbers were recorded for DRG, SC and meninges.

Cell populations were first gated based on the absence of fluorescence viability dye (FVD<sup>-</sup>) live cells and then classified as follows: T cells (CD45<sup>+</sup> TCRβ<sup>+</sup>); B cells (CD45<sup>+</sup> B220<sup>+</sup>); CD4<sup>+</sup> T cells (CD45<sup>+</sup> TCRβ<sup>+</sup> CD4<sup>+</sup>); CD4<sup>+</sup> naïve T cells (CD45<sup>+</sup> TCRβ<sup>+</sup> CD4<sup>+</sup> CD44<sup>-</sup> CD62L<sup>+</sup>); CD4<sup>+</sup> central memory T cells (T<sub>CM</sub>) (CD45<sup>+</sup> TCRβ<sup>+</sup> CD4<sup>+</sup> CD44<sup>+</sup> CD62L<sup>+</sup>); CD4<sup>+</sup> effector memory T cells (T<sub>EM</sub>) (CD45<sup>+</sup> TCRβ<sup>+</sup> CD4<sup>+</sup> CD44<sup>+</sup> CD62L<sup>-</sup>); CD8<sup>+</sup> T cells (CD45<sup>+</sup> TCRβ<sup>+</sup> CD8<sup>+</sup>); CD8<sup>+</sup> T<sub>CM</sub> (CD45<sup>+</sup> TCRβ<sup>+</sup> CD8<sup>+</sup> CD44<sup>+</sup> CD62L<sup>+</sup>); CD8<sup>+</sup> T<sub>EM</sub> (CD45<sup>+</sup> TCRβ<sup>+</sup> CD8<sup>+</sup> CD44<sup>+</sup> CD62L<sup>-</sup>); CD11b<sup>+</sup> myeloid cells (CD45<sup>+</sup> TCRβ<sup>-</sup> B220<sup>-</sup> SSC<sup>low</sup> CD11b<sup>+</sup>); CD11c<sup>+</sup> myeloid cells (CD45<sup>+</sup> TCRβ<sup>-</sup> B220<sup>-</sup> SSC<sup>low</sup> CD11c<sup>+</sup>). FACS data were reported as the percentages of specific cell populations.

### 2.2.5 CD45 tail vein injection

For each mouse, 37.5 µl CD45-APC-cy7 was diluted in 300 µl DPBS and kept on ice, the mouse was placed in the restrainer, the other side of the restrainer was blocked by a holder cover to prevent the mouse from escaping. The tail was held with thumb and first finger, and one of the two lateral tail veins was located, the syringe was lined up exactly in line with the vein, and the needle was inserted into the vein, 300 µl diluted antibody was injected via tail vein, the mouse relocated back to the ventilated cage. 3 minutes after antibody injection mice were sacrificed as described above.

### 2.2.6 FACS sorting of total live cells for scRNA-seq

For DRG scRNA-seq, T6-T13 DRGs were isolated separately in cold DMEM media and single cell suspension was prepared as described above. Single DRG cells were transferred to 96 well plate, stained with FVD for 20 minutes, and washed twice. BD FACSAria™ III was used to exclude low FSC and SSC debris and FVD<sup>+</sup> dead cells. Total live cells were sorted into FBS pre-wetted 1.5 ml

## MATERIALS AND METHODS

Eppendorf tube and counted using automated cell counter (Bio-Rad). The densities of sorted total live cells were adjusted to 500 - 2000 cells/ $\mu$ l via centrifugation. In addition, part of the total live cells were also sorted onto the slides and stored at -20 °C after air dry for immunostaining.

### 2.2.7 Construction of scRNA-seq libraries

The amount of sample required for scRNA-seq was determined based on the density of live cell suspension in the DRGs and a cell suspension volume calculator table (found in the Chromium next GEM single cell reagent kits v1.1 user guide), with a target cell recovery of 10,000. The methodology strictly adhered to the 10x Genomics official user guide (Chromium Next GEM Single Cell Reagent Kits v1.1). The appropriate aliquot of the cell suspension was employed to generate Gel Beads-in-emulsion (GEMs) on Chromium Next GEM Chip (10x Genomics) using Chromium controller (10x Genomics). Immediately after GEM creation, the Gel Bead was dissolved, and any co-partitioned cell was lysed. Oligonucleotides, containing Illumina R1 10x Barcode, unique molecular identifier (UMI), and 13 nucleotide template switch oligo (TSO) were released and mixed with the cell lysate and a master mix containing reverse transcription (RT) reagents and poly (dT) RT primers. Incubation of the GEMs produced barcoded full-length cDNA from polyadenylated mRNA. GEMs were disrupted and pooled following the recovery of GEM-RT reaction mixtures. Silane magnetic beads were utilized to purify the 10x Barcoded first-strand cDNA from the post-GEM-RT reaction mixture, which includes residual biochemical reagents and primers. Enzymatic fragmentation and size selection were used to optimize the cDNA amplicon size prior to 5' Gene Expression library construction. P5, P7, a sample index, and Illumina R2 sequence (read 2 primer sequence) were added via end repair, A-tailing, adaptor ligation, and sample index PCR. The final libraries contain the P5 and P7 priming sites used in Illumina sequencers. The illumina-ready libraries were sequenced at the recommended depth and run parameters using NovaSeq 6000 platforms (Illumina).

### 2.2.8 Sequencing raw data processing

The raw binary base call (BCL) files from sequencing were completely demultiplexed using the standard 10x Genomics 'Cell Ranger' pipeline (v 5.0.1) in the Ubuntu system (Version 20.04.1 LTS). Demultiplexed raw BCL files generated by Illumina sequencers were converted to FASTQ files using the 'cellranger mkfastq' function. The 'cellranger count' procedure was then performed, utilizing FASTQ files from 'cellranger mkfastq', followed by alignment, filtering, barcode counting, and UMI counting. Chromium cellular barcodes were employed to generate feature-barcode matrices, determine clusters, and conduct gene expression analysis. All arguments for 'cellranger mkfastq' and 'cellranger count' used default parameters. Through this pipeline, single-cell raw data were mapped to the mouse genome reference consortium mouse build 38 (GRCm38).

## MATERIALS AND METHODS

### 2.2.9 Standard cell quality control and clustering via Seurat

The output files from Cell Ranger were imported into RStudio (version 4.0.4), and analyzed using the standard procedures available in the Seurat package (version 4.0.0). As the most prevalent package for scRNA-seq data analysis, Seurat offers a wide range of functions such as FindMarkers for identifying signature genes or DEGs, IntegrateData for integrating multiple scRNA-seq datasets, and various visualization functions. Upon loading the output files into Seurat and generating a Seurat object, cells with fewer than 200 detected genes and genes identified in less than three cells were excluded from the analysis. Low-quality cells (i.e., low detected genes or high percentage of mitochondrial genes) or duplicates (i.e., a high number of genes per cell) were filtered out following these criteria: detected genes per cell < 200 or detected genes per cell > 8000 (for plaque: detected genes per cell > 5000), and the percentage of mitochondrial genes > 10% (for neurons: mitochondrial genes > 30%). After the quality control process, data were merged using the Seurat integration strategy, using the top 2000 highly variable genes.

To characterize the transcriptional profiles of DRG scRNA-seq data and compare the differences between aged WT and Apoe<sup>-/-</sup>, further processing of the DRG scRNA-seq data was performed. We employed 2000 highly variable genes to perform principal component analysis (PCA), using significant PCs to perform t-distributed stochastic neighbor embedding (tSNE) and uniform manifold approximation and projection (UMAP) for dimensionality reduction. We identified cell type-specific marker genes with the Seurat 'FindAllMarkers' function, and determined DEGs using 'FindMarkers' with an adjusted p-value threshold of 0.05 and a log2 fold change value of 0.25. We classified DRG cell types based on well-established key marker genes, dividing them into five functional classes: neurons, immune cells, vascular cells, fibroblasts, and glial cells. We further clustered these five classes into 13 distinct cell types (**Table 10**). To understand the potential functions of each cell type in aged DRG, the top 200 DEGs (ranked by adjusted p-value) for each cell type were used to perform gene ontology (GO) enrichment analysis using the Metascape enrichment analysis website tool (<https://metascape.org/>). In the GO enrichment analysis, the KEGG pathways were excluded. Subsequently, the enriched pathways were visualized using the R package ggplot2 (v 3.3.5) and Cytoscape software (v 3.8.2). Top non-redundant enriched GO terms (ranked by negative log p-value) were displayed in bar plots.

**Table 10 Marker genes of aged DRG cell types**

Class	Cell type	Marker genes	References
Neurons	Neuron	Tubulin beta 3 class III (Tubb3), peripherin (Prph), tachykinin 1 (Tac1), stathmin-2 (Stmn2), small nucleolar RNA host gene 11 (Snhg11)	[112, 119, 142-148]

## MATERIALS AND METHODS

Immune cells	T cell	Protein tyrosine phosphatase receptor type C (Ptprc), CD3 antigen delta polypeptide (Cd3d), CD3 antigen epsilon polypeptide (Cd3e), TNF receptor superfamily member 18 (Tnfrsf18)	[149]
	Macrophage	chemokine (C-X3-C motif) receptor 1 (Cx3cr1), Mannose receptor C type 1 (Mrc1), platelet factor 4 (Pf4), colony stimulating factor 1 receptor (Csf1r)	[39, 150-154]
	Trem2 <sup>hi</sup> macrophage	Trem2, secreted phosphoprotein 1 (Spp1), CD72 antigen (Cd72), CD9 antigen (Cd9)	[39, 151, 155]
	Neutrophil	S100 calcium binding protein A8 (S100a8), S100a9, resistin like gamma (Retnlg), secretory leukocyte peptidase inhibitor (Slpi)	[156-160]
Vascular cells	Endothelial cell (EC)	Lymphocyte antigen 6 complex locus C1 (Ly6c1), Claudin 5 (Cldn5), endothelial Cell adhesion molecule (Esam), endomucin (Emcn)	[112, 161, 162]
	Pericyte	Vitronectin (Vtn), NADH: ubiquinone oxidoreductase subunit A4 like 2 (Ndufa4l2), potassium inwardly rectifying channel subfamily J member 8 (Kcnj8), regulator of G protein signaling 5 (Rgs5)	[112, 163-170]
Fibroblasts	Fibroblast1	decorin (Dcn), lumican (Lum), Apolipoprotein D (Apod), collagen type I alpha 1 (Col1a1), collagen type I alpha 2 (Col1a2)	[162, 171, 172]
	Fibroblast2	Claudin 1 (Cldn1), claudin 22 (Cldn22), solute carrier family 6 neurotransmitter transporter member 13 (Slc6a13), Kruppel-like factor 5 (Klf5), Kcn J member 13 (Kcnj13)	[162, 164]
	Fibroblast3	Peptidase inhibitor 16 (Pi16), C-type lectin domain family 3 member b (Clec3b), secreted frizzled-related protein 4 (Sfrp4), collagen type XIV alpha 1 (Col14a1),	[162, 173, 174]
Glial cells	Satellite glial cell (SGC)	Fatty acid-binding protein 7 (Fabp7), Kcn J member 10 (Kcnj10), aldolase C fructose-bisphosphate (Aldoc), endothelin receptor type B (Ednrb), brevican (Bcan)	[112, 126, 162, 175, 176]
	Myelinating Schwann cell (mSch)	Myelin protein zero (Mpz), noncompact myelin-associated protein (Ncmmap), peripheral myelin protein 22 (Pmp22), claudin 19 (Cldn19), myelin basic protein (Mbp)	[55, 112, 147, 162, 177]
	Non-myelinating Schwann cell (nmSch)	L1 cell adhesion molecule (L1cam), Sodium channel voltage-gated type VII alpha (Scn7a), a disintegrin and metallopeptidase domain 23 (Adam23), cell adhesion molecule with homology to L1CAM (Chl1)	[177-180]

### 2.2.10 Integration of reference DRG scRNA-seq data and aged DRGs dataset

Due to the limited number of neurons from aged WT and Apoe<sup>-/-</sup> DRG, it was difficult to characterize the precise transcription of neuron subtypes, so a reference was necessary for subclustering aged DRG neurons. To identify the expression patterns of neuron subtypes, a published young DRG neurons scRNA-seq dataset [124] was used as a reference. The young DRG neurons scRNA-seq dataset was generated from 10,922 cells from cervical, thoracic, and lumbar parts, revealing at least

## MATERIALS AND METHODS

15 transcriptionally distinct DRG neuron subclusters or states. The Seurat scRNA-seq integration strategy was employed for the young and aged DRG neurons scRNA-seq datasets. First, the original young DRG neurons scRNA-seq dataset was downloaded from the Gene Expression Omnibus (GEO) dataset with accession code GSE139088. The downloaded series matrix files were trimmed using the R package dplyr (v 1.0.5) to create count matrices and meta data. This was followed by the creation of the Seurat object and standard analysis workflow for young DRG neurons. The Seurat function IntegrateData was used to integrate the data and create a new integrated Seurat object. After integrating the young and aged DRG neuron, the Seurat function CellSelector was used to choose clusters based on the young DRG neurons scRNA-seq dataset meta data, and we assigned the same cluster names to aged DRG neurons. UMAP was used to check the clustering results of the DRG neurons scRNA-seq data. To further examine the transcriptional profiles of aged DRG neurons, the expression similarity between aged DRG neurons and 'Sharma Atlas' neurons was calculated using a reported method [76]. Firstly, the top 50 genes (ranked by adjusted p-value) of each cluster in the young DRG neurons scRNA-seq dataset were used to create a gene list, including 700 unique total genes. Then, the average expressions of these selected genes in each cell type in aged DRG data were checked. The Spearman correlation between aged DRG neurons and pseudo-population averages was calculated. The heatmaps were used to show the expression similarity between aged DRG data and young DRG neuron subtypes.

### 2.2.11 Evaluation of gene signatures in single-cell datasets using scoring value

To examine the effects of the Apoe gene in aged DRGs in the comparison between WT and Apoe<sup>-/-</sup> mice, we calculated the Pearson correlation coefficient of the Apoe gene with all genes in aged DRGs. First, we isolated the normalized Apoe gene expressions of all cells and compared the expressions of the Apoe gene with all other genes one by one during using the basic R function cor. The results were ranked by the Pearson correlation coefficient. All genes with a correlation coefficient greater than 0 were defined as Apoe gene positively-associated genes, while those with a correlation coefficient less than 0 were defined as negatively-associated genes. The top 500 genes and bottom 500 genes were separately used for GO terms enrichment analysis.

To identify and compare the differences in certain biological functions or cell type-specific marker genes of scRNA-seq dataset, all cells were scored for their expression of gene signatures predicting distinct biological functions or sets of marker genes using the R package UCell. UCell is a powerful R package designed to scoring gene signatures within single-cell datasets [181]. For all signatures except neutrophil aging, functional scores were defined as the average normalized expression of corresponding genes. To identify the characteristics of different macrophage types, score values of brain macrophages, brain microglia, DRG macrophages, and LN macrophages were calculated using the top 100 marker genes. To examine the functional differences, score values of the selected

## MATERIALS AND METHODS

functions using expressed GO term genes were calculated, including antigen processing via MHC class I (GO:0019886), antigen processing via MHC class II (GO:0002474), and phagocytosis (GO:0006911).

### 2.2.12 Gene set enrichment analysis (GSEA)

The GSEA is a computational technique employed to evaluate whether a predefined group of genes exhibits statistically significant and consistent variations between two distinct biological conditions. To ascertain whether there are significantly concordant differences in a predefined gene set between aged WT and *Apoe*<sup>-/-</sup> in total DRG or specific cell types, we used R package clusterProfiler (v 4.0.2) gseGO function performed GSEA. After calculating Seurat function FindMarkers between the two biological states (aged WT and *Apoe*<sup>-/-</sup>), the genes were ranked by fold change values, followed by GSEA calculation using the clusterProfiler function gseGO. The results were visualized using dot plots, based on p-value, gene count, and gene ratio (count/setSize), and bar plots, based on normalized enrichment scores. The GSEA enrichment network overview was visualized using the emaplot function. Specific enriched pathways were visualized using gseaplot. In the enrichment analysis of *Apoe*-associated genes, the genes were ranked by correlation coefficient with the *Apoe* gene. Genes with a correlation coefficient greater than zero were considered as *Apoe* gene positively-associated genes, while those with a correlation coefficient less than zero were considered negatively-correlated genes. GSEA enrichment of positively-associated and negatively-associated genes was performed separately via gseGO, and the results were visualized using clusterProfiler and ggplot2.

### 2.2.13 Cell-cell interaction analysis

We hypothesized that cells in DRGs and ATLOs would express proteins facilitating neuroimmune communications during atherosclerosis. As we generated unbiased DRG scRNA-seq data, we incorporated databases of ligand and receptor pairs to determine if any of the DRG cell types expressed cognate molecules and thus may be poised to interact with ATLO during atherosclerosis. To predict potential cell-cell interactions between different cell types among DRGs and ATLOs, we employed CellChat (v 1.4.0) to identify potentially significant ligand-receptor pairs within DRG neuron subtypes and ATLO immune cells. In CellChat calculation, we utilized Seurat objects to create CellChat objects with the function createCellChat, followed by a CellChat calculation step using the functions computeCommunProb and computeCommunProbPathway. To check the neuroimmune interaction differences between aged WT and *Apoe*<sup>-/-</sup> datasets, we merged CellChat objects using the functions mergeCellChat and compareInteractions, following the published protocol [182]. We then visualized the results with functions netVisual\_diffInteraction, netVisual\_heatmap,

## MATERIALS AND METHODS

netVisual\_bubble, and ggplot2. Some of the graphs were further visualized using R packages that combined DEGs and enrichment results.

### 2.2.14 Immunofluorescence staining

The frozen tissue sections were quickly thawed on a hot plate setting 37 °C for one minute. Then, the sections were air dried for 30 minutes. The sections were fixed with 4% PFA or with 4 % PFA-acetone combination, then rehydrated with PBS at RT for 10 minutes. The 4% PFA-sucrose pretreated fixed frozen tissue sections were directly rehydrated with PBS at RT for 10 minutes. Then, the sections were blocked for 60 minutes and incubated with primary antibody overnight (>10 hours). For the extracellular protein antibodies, the sections were blocked with 2.5% BSA and 5% serum in PBS, whereas for intranuclear and intracellular protein antibodies, Triton X-100 was added to the blocking solution for permeabilization. The information for each primary antibody is listed in table 2.5. After washing in PBS and the slides were incubated with secondary antibody and 4', 6-diamidino-2-phenylindole (DAPI) diluted in 2.5 % BSA in PBS for 1 hour. For neuronal cell staining, NeuN was added into the secondary antibody for neuronal nuclei staining. The information for each secondary antibody is listed in table 2.6. After final PBS washing the slides were mounted in Fluoromount-G mounting media (Dako) and kept in 4 °C until imaging. For negative controls, the immunostaining procedure was performed without primary antibodies.

### 2.2.15 Statistical analyses

Measurements were expressed as mean  $\pm$  standard error of the mean (SEM). The statistical significance of FACS data was assessed using GraphPad prism 9, employing either a two-tailed unpaired t-test or one-way or two-way ANOVA for repeated measures, followed by Bonferroni's multiple comparisons test. P-values < 0.05 were considered statistically significant. The statistical significance of DEGs in scRNA-seq data was examined using Seurat or R-based functions. For comparisons involving discrete variables, the data distribution was tested using the Shapiro-Wilk test. For normality distributed data, a one-way analysis of variance accompanied by a Bonferroni post hoc test was employed to perform statistical analyses among multiple groups. In the case of non-normal distribution data, a two-sided Wilcoxon rank-sum test was employed for comparing differences between two groups, while the non-parametric Kruskal-Wallis H test, followed by Dunn's post hoc test for pairwise comparisons, was used for analyzing differences among three or more groups. Regarding categorical variables, the significance of comparisons was computed using Pearson's Chi-square test if the cell type numbers were greater than 5, or using Fisher's exact test if the cell type numbers were less than 5, Benjamini-Hochberg corrections were subsequently applied to reduce the inflation of the alpha error. A two-tailed p-value < 0.05 was deemed significant for differences.

### 3 RESULTS

#### 3.1 Immune cell infiltration in the NS during aging

##### 3.1.1 Establishment of FACS protocols for DRGs and SCs

To examine immune cells in the NS, we first established the protocols to isolate DRGs, SCs, and meninges (**Figure 8 A**). Next, we examined the locations of immune cells in SC. Immunostaining of CD3e<sup>+</sup> T cells and B200<sup>+</sup> B cells showed that T cells and B cells were largely located in meninges, but not in the SC parenchyma (**Figure 8 B**). We next examined the percentages of T cells and B cells in SC and meninges separately using FACS, and found more B cells in the meninges, but very few B cells in the SC (**Figure 8 C**).

To validate if these T cells and B cells are intravascular circulating immune cells or extravascular infiltrated immune cells in the tissues, fluorescent labelled CD45 monoclonal antibody (CD45 APC-Cy7) was injected intravenously (i.v.) via the tail vein and the percentages of CD45 intravascular cells in DRG, SC, and meninges were determined (**Figure 8 D**). FACS analysis showed that injected CD45 i.v. stained almost all (95%) circulating leukocytes in blood indicating specificity of the approach. The percentages of intravascular T cells among CD45 i.v.<sup>+</sup> leukocytes in DRG, SC, and meninges were below 20%, indicating that majority of T cells in these tissues were extravascular infiltrating T cells (**Figure 8 E**). However, intravascular B cells among CD45 i.v.<sup>+</sup> leukocytes in meninges were 2-fold higher than in DRG and SC i.e. ~ 40% in meninges compared to ~ 20% in DRG and SC (**Figure 8 E**). These data indicated that the immune cell composition of SC and meninges were different, and that meninges contained more intravascular circulating B cells. To minimize the effects of circulating immune cells and to study extravascular immune cell infiltration in the NS, we therefore removed meninges from SC in the further experiments.

## RESULTS

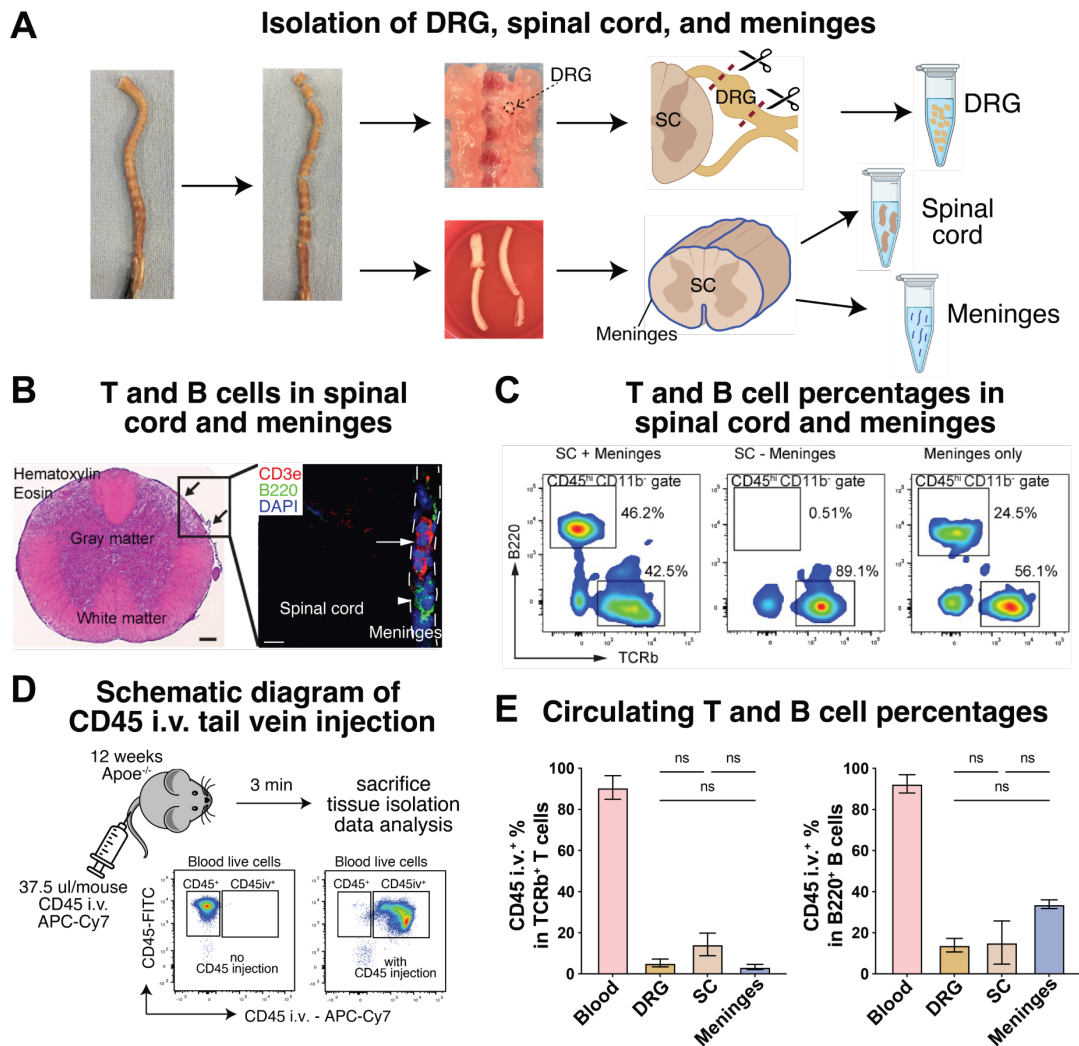


**Figure 8 Establishment of isolation protocols for DRGs, SC, and meninges.** **A**, Schematic workflow of DRGs, SC, and meninges isolation from the vertebrae. **B**, Images show the detection of CD3e<sup>+</sup> T cells (arrows) and B220<sup>+</sup> B cells (arrowhead) in aged WT meninges. Scale bar: 50  $\mu$ m for SC hematoxylin and eosin staining (left), 10  $\mu$ m for SC immunostaining (right). **C**, FACS scatter plots show the percentages of TCRb<sup>+</sup> T cell and B220<sup>+</sup> B cell in aged WT SC with or without meninges, and meninges only (n = 4 Apoe<sup>-/-</sup> mice). **D**, Schematic diagram of CD45 i.v. vein injection. 3 minutes after CD45 i.v. injection mice were sacrificed. FACS scatter plots show the gating strategy for CD45<sup>+</sup> leukocytes with or without CD45 i.v. injection from total live cells in blood. **E**, Bar plots show the percentages of circulating CD45<sup>+</sup> intravascular TCRb<sup>+</sup> T cells and B220<sup>+</sup> B cells in different tissues. Data are reported as mean  $\pm$  SEM, n denote biologically independent animals. The p-value was calculated using a one-way ANOVA test and adjusted for multiple comparisons using Bonferroni's correction method. ns: not significant.

This data established important controls to define where in the NS immune cells are located. Moreover, they helped our morphometry studies to quantify distinct immune cell subsets that we wished to analyze within neural and extra neuronal tissues versus those in the circulation.

## RESULTS

### 3.1.2 Immune cell infiltration in the NS during aging

We next examined lymphocytes and myeloid cells in the isolated DRGs and SC using FACS. For this purpose, we excluded doublets and dead cells using side scatter (SSC) and a fixable viability dye (FVD<sup>+</sup>). Then, we gated CD45<sup>hi</sup> cells from the CD45<sup>+</sup> gate to determine TCRb<sup>+</sup> T cells, B220<sup>+</sup> B cells, SSC-A<sup>low</sup>CD11b<sup>+</sup> and SSC-A<sup>low</sup>CD11c<sup>+</sup> myeloid cells, and T cell subtypes, including CD4<sup>+</sup> T cells, CD8<sup>+</sup> T cells, naïve T cells, central memory T cells (T<sub>CM</sub>), and effector memory T cells (T<sub>EM</sub>) (Figure 9).

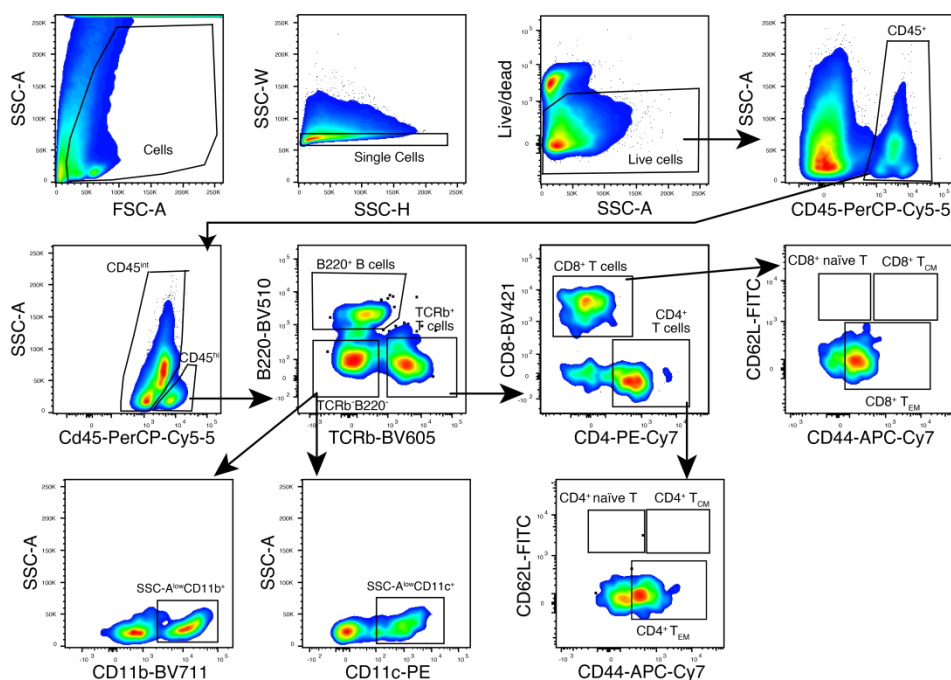


**Figure 9 FACS gating strategy of DRG immune cells.** Scatter plots show the gating strategy of DRG immune cells from aged WT mice. After exclusion of doublets and dead cells, CD45<sup>hi</sup> leukocytes and CD45<sup>int</sup> population were gated separately from CD45<sup>+</sup> cells. Then, TCRb<sup>+</sup> T cells, B220<sup>+</sup> B cells, and T cells subtypes, including CD4<sup>+</sup> T cells, CD8<sup>+</sup> T cells, CD62L<sup>+</sup>CD44<sup>-</sup> naïve T cells, CD62L<sup>+</sup>CD44<sup>+</sup> T<sub>CM</sub> and CD62L<sup>-</sup>CD44<sup>+</sup> T<sub>EM</sub> were gated from CD45<sup>hi</sup> cells. Side scatter (SSC-A) was used to exclude SSC-A<sup>hi</sup> granulocytes, and SSC-A<sup>low</sup>CD11b<sup>+</sup> and SSC-A<sup>low</sup>CD11c<sup>+</sup> myeloid cells were gated separately from non-T cell and non-B cell populations (TCRb<sup>+</sup>B220<sup>-</sup>). Labels in X- and Y-axes designate fluorescent primary antibodies/dye, and labels in scatter plots designate cell populations.

To examine immune cell infiltration in the DRG during aging, we determined different leukocyte populations in young (8 weeks), adult (32 weeks), and aged (> 78 weeks) WT mice using FACS. We found that the percentages of total CD45<sup>hi</sup> leukocytes significantly increased in aged DRGs compared to young and adult WT mice (Figure 10 A). Within the CD45<sup>hi</sup> population, TCRb<sup>+</sup> T cells were significantly increased in aged versus adult or young DRGs, whereas the changes B220<sup>+</sup> B cell numbers in aged DRGs were not significant compared to other age groups mostly due to large variability of B cells (Figure 10 B). To detail the changes in T cells, we next analyzed the T cell

## RESULTS

subpopulations, including CD4<sup>+</sup> T cells and CD8<sup>+</sup> T cells. CD4<sup>+</sup> T cells were significantly increased in aged mice compared to young mice, while CD8<sup>+</sup> T cells were significantly increased in aged mice compared to both young and adult mice (**Figure 10 C**). It is important to note that naïve T cells and T<sub>CM</sub> cells were rare among CD4<sup>+</sup> T cells and CD8<sup>+</sup> T cells (**Figure 9**). Interestingly, the numbers of both CD4<sup>+</sup> T<sub>EM</sub> and CD8<sup>+</sup> T<sub>EM</sub> were significantly increased in aged mice compared to young mice (**Figure 10 D**). These data indicated that the majority of CD4<sup>+</sup> T cells and CD8<sup>+</sup> T cells in DRGs were activated T<sub>EM</sub> cells, and their numbers increased during aging. In addition, FACS analyses of SSC-A<sup>low</sup>CD11b<sup>+</sup> and SSC-A<sup>low</sup>CD11c<sup>+</sup> myeloid cells in DRGs showed CD11c<sup>+</sup> myeloid cells were increased in aged versus young DRGs, while CD11b<sup>+</sup> myeloid cells did not change during aging.

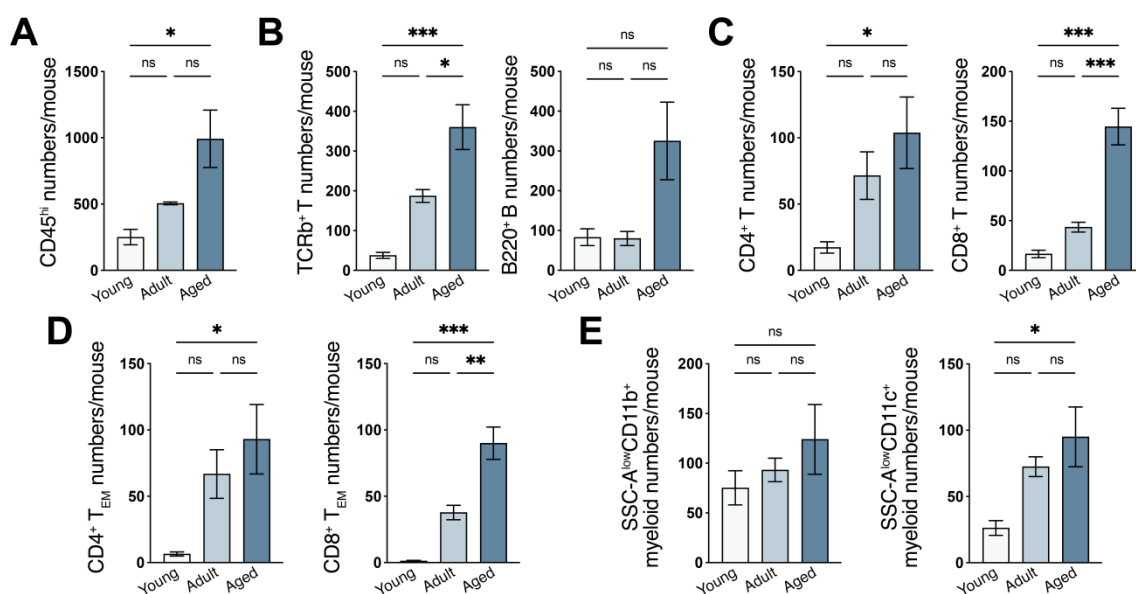


**Figure 10 Immune cell infiltration in WT DRG during aging.** **A**, Bar plots show CD45<sup>hi</sup> leukocytes of young (n = 4 mice), adult (n = 4 mice), and aged WT (n = 5 mice) DRGs. **B**, Bar plots show T and B cells of young, adult, and aged WT DRGs. **C**, Bar plots show CD4<sup>+</sup> and CD4<sup>+</sup> T<sub>EM</sub> T cells of young, adult, and aged WT DRGs. **D**, Bar plots show CD8<sup>+</sup> and CD8<sup>+</sup> T<sub>EM</sub> T cells of young, adult, and aged WT DRGs. **E**, Bar plots show SSC-A<sup>low</sup>CD11b<sup>+</sup> and SSC-A<sup>low</sup>CD11c<sup>+</sup> myeloid cells of young, adult, and aged WT DRGs. Data are reported as mean ± SEM, n represent biologically independent animals. The p-values are calculated using a one-way ANOVA test and adjusted for multiple comparisons using Bonferroni's correction method: \*p < 0.05, \*\*p < 0.01, \*\*\*p < 0.001, ns: not significant.

To examine immune cell infiltration in the CNS, we next performed FACS analysis of leukocytes in the SC, which is connected to the DRG. For this purpose, we removed the meninges from the SC (**Figure 8**), and analyzed total leukocytes including T cells, B cells, and myeloid cells using the following gating strategy (**Figure 11**).

## RESULTS

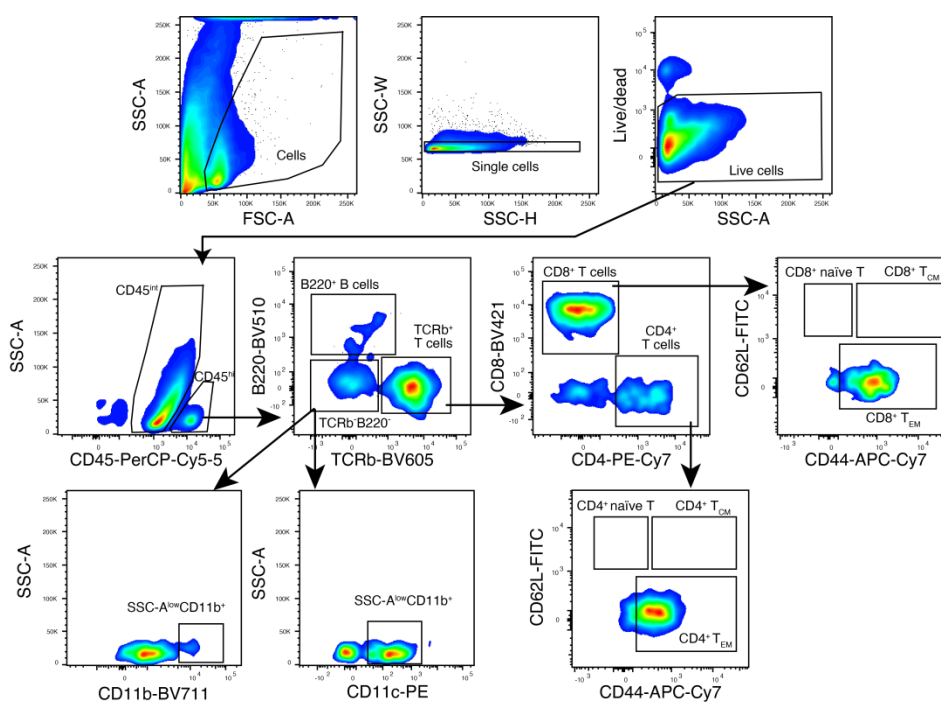


**Figure 11 FACS gating of SC immune cells.** Scatter plots show the gating strategy of SC immune cells from aged WT mice. After exclusion of doublets and dead cells, CD45<sup>hi</sup> leukocytes and CD45<sup>int</sup> cells were gated separately from the CD45<sup>+</sup> population. Then, TCRb<sup>+</sup> T cells, B220<sup>+</sup> B cells, and T cell subtypes, including CD4<sup>+</sup> T cells, CD8<sup>+</sup> T cells, CD62L<sup>+</sup>CD44<sup>-</sup> naïve T cells, CD62L<sup>+</sup>CD44<sup>+</sup> central and CD62L<sup>-</sup>CD44<sup>+</sup> effector memory T cells (T<sub>CM</sub> and T<sub>EM</sub>) were gated from CD45<sup>hi</sup> cells. SSC-A is used to exclude SSC-A<sup>hi</sup> granulocytes, and SSC-A<sup>low</sup>CD11b<sup>+</sup> and SSC-A<sup>low</sup>CD11c<sup>+</sup> myeloid cells were gated separately from non-T cell and non-B cell populations (TCRb B220<sup>+</sup>). Labels in X- and Y-axes designate fluorescent-labelled primary antibodies/dye, and labels in scatter plots designate cell populations.

FACS analyses of SC showed that the percentages of total CD45<sup>hi</sup> leukocytes were significantly increased during aging while the leukocyte numbers were increased in aged compared to both young and adult WT mice (**Figure 12 A**). Within CD45<sup>hi</sup> cells, the numbers of TCRb<sup>+</sup> T were significantly increased in aged compared to both young and adult age groups, consistent with the changes of total CD45<sup>hi</sup> leukocytes. However, there were no significant changes of B220<sup>+</sup> B cell numbers during aging (**Figure 12 B**). Among the TCRb<sup>+</sup> T cells, the CD4<sup>+</sup> T cell numbers and CD8<sup>+</sup> T cell numbers were significantly increased in aged compared to both young and adult WT mice. Interestingly, the increase of CD8<sup>+</sup> T cells during aging was 6-fold higher than CD4<sup>+</sup> T cells (**Figure 12 C**). It is noteworthy that in CD4<sup>+</sup> and CD8<sup>+</sup> T cells, naïve T cells were rare and T<sub>EM</sub> T cells were abundant in the SC, and the numbers of both CD4 T<sub>EM</sub> and CD8 T<sub>EM</sub> were significantly higher in aged compared to both young and adult mice (**Figure 12 D**). In addition, SSC-A<sup>low</sup>CD11c<sup>+</sup> myeloid cells were significantly increased in aged versus young and adult mice (**Figure 12 E**). These results indicated that CD45<sup>hi</sup> leukocytes including CD4<sup>+</sup> T cells, CD8<sup>+</sup> T cells, T<sub>EM</sub>, and SSC-A<sup>low</sup>CD11c<sup>+</sup> myeloid cells increased in the SC during aging.

## RESULTS

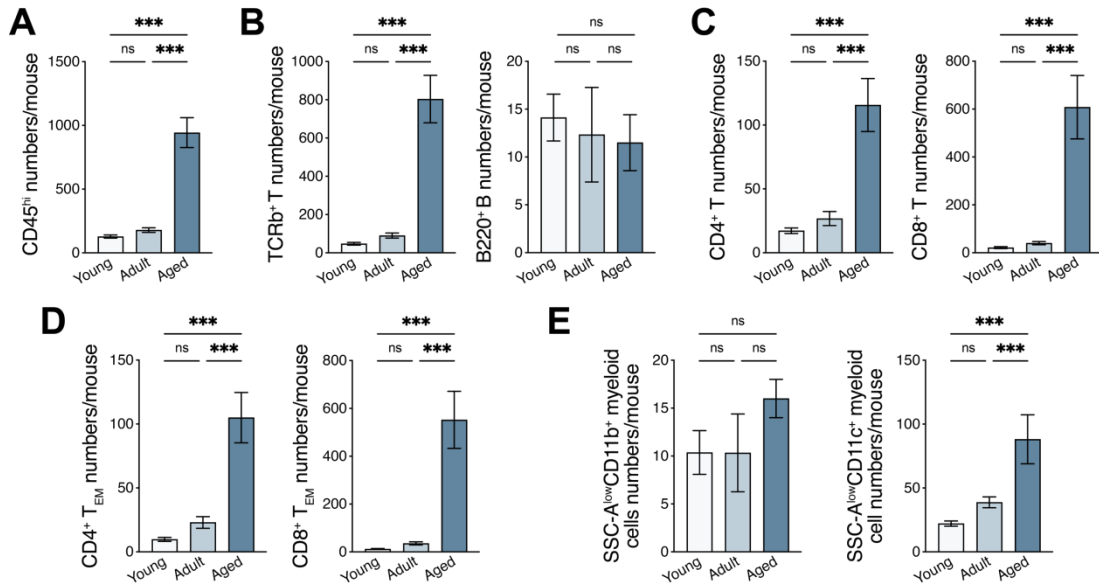


**Figure 12 Immune cells increase in the SC of WT mice during aging.** **A**, Bar plots show CD45<sup>hi</sup> leukocytes of young (n = 5 mice), adult (n = 7 mice), and aged WT (n = 5 mice) SCs. **B**, Bar plots show T and B cells of young, adult, and aged WT SCs. **C**, Bar plots show CD4<sup>+</sup> and CD4<sup>+</sup> T<sub>EM</sub> T cells of young, adult, and aged WT SCs. **D**, Bar plots show CD8<sup>+</sup> and CD8<sup>+</sup> T<sub>EM</sub> T cells of young, adult, and aged WT SCs. **E**, Bar plots show SSC-A<sup>low</sup>CD11b<sup>+</sup> and SSC-A<sup>low</sup>CD11c<sup>+</sup> myeloid cells of young, adult, and aged WT SCs. Data are reported as mean ± SEM, n represent biologically independent animals. The p-values are calculated using a one-way ANOVA test and adjusted for multiple comparisons using Bonferroni's correction method: \*p < 0.05, \*\*p < 0.01, \*\*\*p < 0.001, ns: not significant.

In summary, leukocyte infiltration in NS is increased during aging. The enhanced leukocyte infiltration was mainly due to an increase of TCRb<sup>+</sup> T cells including CD4<sup>+</sup> T cells, CD8<sup>+</sup> T cells, activated T<sub>EM</sub> cells, and SSC-A<sup>low</sup>CD11c<sup>+</sup> myeloid cells in both DRGs and SCs. B cells and SSC-A<sup>low</sup>CD11c<sup>+</sup> myeloid cells remain unchanged during aging.

### 3.1.3 Immune cells in the NS during atherosclerosis progression

In our previous work, we observed increased T cells, macrophages, and mast cells in peripheral ganglia, including paraaortic ganglia and DRGs, in 78 weeks aged Apoe<sup>-/-</sup> mice compared to WT mice [52]. In addition, leukocyte density increased in the brain parenchyma in aged Apoe<sup>-/-</sup> mice [72]. However, analysis of different immune cell populations in peripheral ganglia and in the CNS in WT and Apoe<sup>-/-</sup> mice at different ages remained unknown. To study the association of atherosclerosis with immune cells in the NS, we analyzed the immune cells in DRGs and SC in WT versus Apoe<sup>-/-</sup> mice at different ages.

## RESULTS

FACS analyses of DRGs in WT versus *Apoe*<sup>-/-</sup> mice showed that total CD45<sup>hi</sup> leukocyte numbers were not significantly different between two genotypes, although leukocytes in aged *Apoe*<sup>-/-</sup> mice showed a tendency to increase compared to age-matched WT mice (**Figure 13 A**). However, TCRb<sup>+</sup> T cells were significantly increased in aged *Apoe*<sup>-/-</sup> mice compared to aged WT mice, but there were no significant changes in B220<sup>+</sup> B cells between *Apoe*<sup>-/-</sup> and age-matched WT mice (**Figure 13 B**). To determine the association of atherosclerosis and T cell subpopulations, we examined CD4<sup>+</sup> T cells, CD8<sup>+</sup> T cells, naïve T cells, and T<sub>EM</sub> cells. We found that CD4<sup>+</sup> T cells were significantly increased, while CD4<sup>+</sup> T<sub>EM</sub> T cells showed a tendency to increase in aged *Apoe*<sup>-/-</sup> mice compared to aged WT mice, and CD4<sup>+</sup> naïve T cells and T<sub>CM</sub> T cells were rarely present (**Figure 13 C, D**). Similarly, CD8<sup>+</sup> T cells and CD8<sup>+</sup> T<sub>EM</sub> T cells were significantly increased in aged *Apoe*<sup>-/-</sup> versus WT mice (**Figure 13 C, D**). Among the myeloid cells, there were no significant changes in both SSC-A<sup>low</sup>CD11b<sup>+</sup> and SSC-A<sup>low</sup>CD11c<sup>+</sup> myeloid cells between two genotypes at different ages (**Figure 13 E**). These results indicated that the lymphocytes infiltration was enhanced in aged *Apoe*<sup>-/-</sup> versus WT DRGs, mainly by CD4<sup>+</sup>, CD8<sup>+</sup> and CD8 T<sub>EM</sub> T cells.

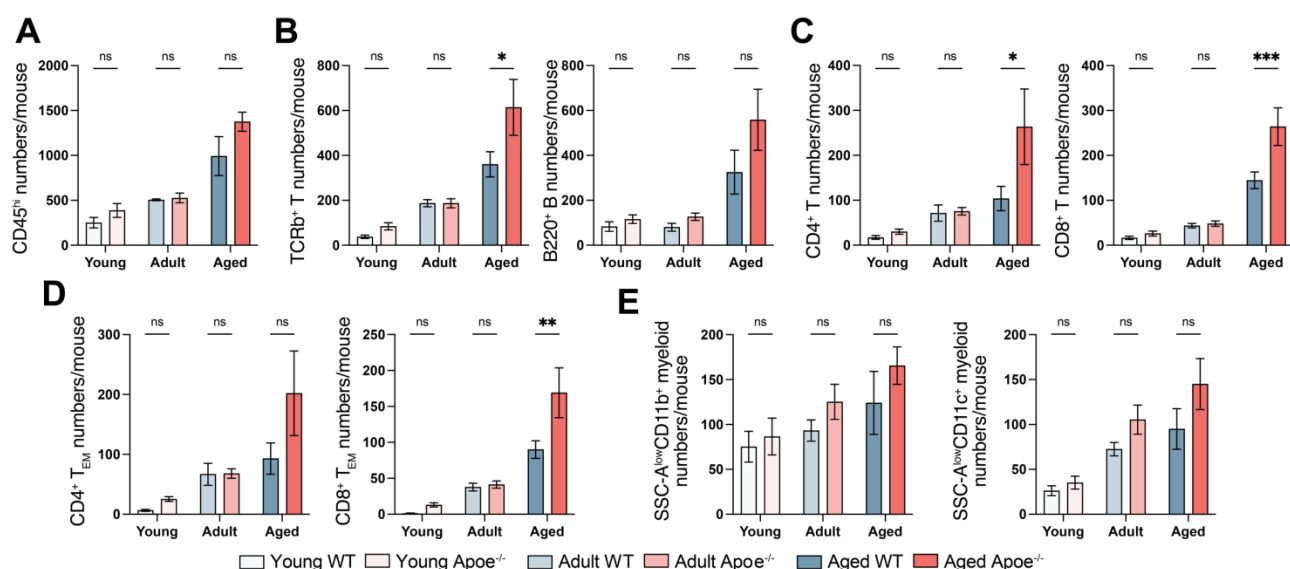


**Figure 13 Changes of DRG immune cells in WT versus *Apoe*<sup>-/-</sup> mice.** **A**, Bar plots show DRG CD45<sup>hi</sup> leukocytes of young (n = 4 WT, 5 *Apoe*<sup>-/-</sup>), adult (n = 4 WT, 7 *Apoe*<sup>-/-</sup>), and aged (n = 5 WT, 5 *Apoe*<sup>-/-</sup>) mice in WT versus *Apoe*<sup>-/-</sup> mice. **B**, Bar plots show T and B cells of young, adult, and aged DRGs in WT versus *Apoe*<sup>-/-</sup> mice. **C**, Bar plots show CD4<sup>+</sup> T cell and activated CD4<sup>+</sup> T<sub>EM</sub> cells of young, adult, and aged DRGs in WT versus *Apoe*<sup>-/-</sup> mice. **D**, Bar plots show CD8<sup>+</sup> T cells and activated CD8<sup>+</sup> T<sub>EM</sub> cells of young, adult, and aged DRGs in WT versus *Apoe*<sup>-/-</sup> mice. **E**, Bar plots show SSC-A<sup>low</sup>CD11b<sup>+</sup> and SSC-A<sup>low</sup>CD11c<sup>+</sup> myeloid cells of young, adult, and aged DRGs in WT versus *Apoe*<sup>-/-</sup>. Data are reported as mean ± SEM, n represent biologically independent animals, The p-values are calculated using a two-way ANOVA test and adjusted for multiple comparisons using Bonferroni's correction method: \*p < 0.05, \*\*p < 0.01, \*\*\*p < 0.001, ns: not significant.

FACS analyses of SCs show significantly increased CD45<sup>hi</sup> total leukocytes in aged *Apoe*<sup>-/-</sup> mice compared to WT mice (**Figure 14 A**), of which TCRb<sup>+</sup> T cells were significantly increased while

## RESULTS

B220<sup>+</sup> B cells showed no significant changes (**Figure 14 B**). Examination of different T cell subpopulation showed that CD4<sup>+</sup> T cells showed a tendency to increase, whereas CD8<sup>+</sup> T cells were significantly increased in aged Apoe<sup>-/-</sup> mice compared to aged WT mice (**Figure 14 C**). Interestingly, the number of CD8<sup>+</sup> T cells outnumbered CD4<sup>+</sup> T cells during aging in both genotypes (6- to 10-fold higher) (**Figure 14 C**). In SCs, naïve T cells of both CD4<sup>+</sup> T and CD8<sup>+</sup> T cell subsets were rarely observed. The numbers of CD4<sup>+</sup> T<sub>EM</sub> cells showed a tendency to increase, while CD8<sup>+</sup> T<sub>EM</sub> were significantly increased in aged Apoe<sup>-/-</sup> mice compared to aged WT mice, which was consistent with the changes of total CD4<sup>+</sup> and CD8<sup>+</sup> T cells (**Figure 14 D**). These results suggested that atherosclerosis is associated with enhanced infiltration of CD4<sup>+</sup> and CD8<sup>+</sup> T cells in SCs, i.e. CD4<sup>+</sup> T<sub>EM</sub> and CD8<sup>+</sup> T<sub>EM</sub>, with CD8<sup>+</sup> T cells predominating. In addition, SSC-A<sup>low</sup>CD11b<sup>+</sup> myeloid cells were increased in aged Apoe<sup>-/-</sup> versus WT mice and SSC-A<sup>low</sup>CD11b<sup>+</sup> myeloid cells showed a tendency to increase in Apoe<sup>-/-</sup> SC compared to age-matched WT mice (**Figure 14 E**).

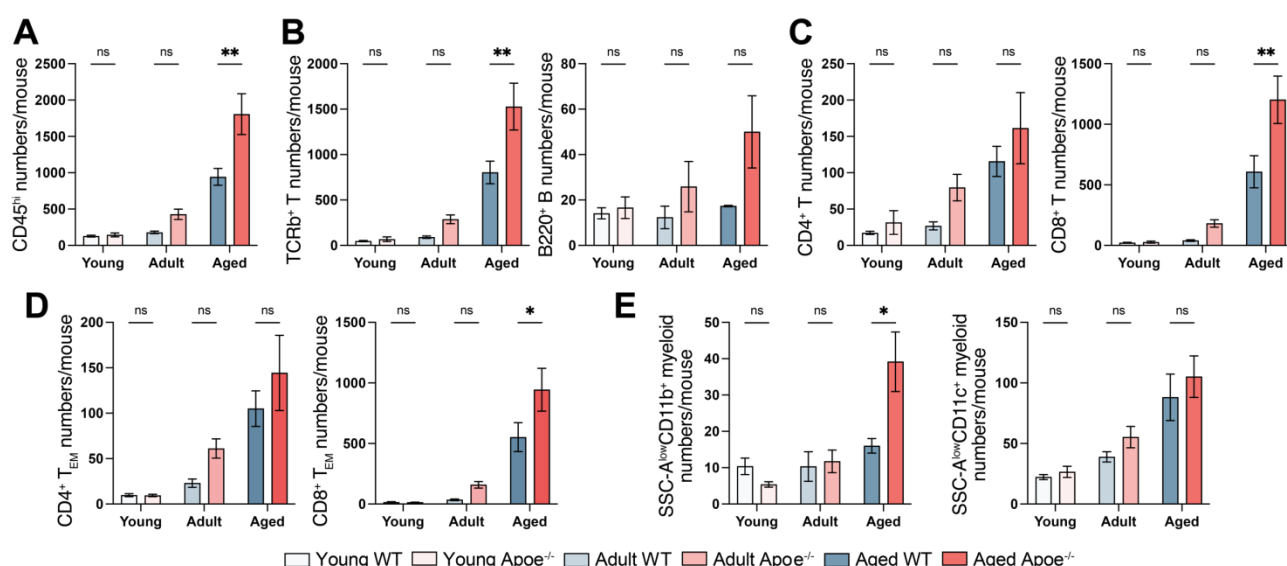


**Figure 14 Changes of SC immune cells in WT versus Apoe<sup>-/-</sup> mice.** **A**, Bar plots show CD45<sup>hi</sup> leukocytes of young (n = 4 WT, 5 Apoe<sup>-/-</sup>), adult (n = 4 WT, 7 Apoe<sup>-/-</sup>), and aged (n = 5 WT, 5 Apoe<sup>-/-</sup>) SC in WT versus Apoe<sup>-/-</sup> mice. **B**, Bar plots show T and B cells of young, adult, and aged SC in WT versus Apoe<sup>-/-</sup> mice. **C**, Bar plots show CD4<sup>+</sup> T cell and CD4<sup>+</sup> T<sub>EM</sub> cells of young, adult, and aged SC in WT versus Apoe<sup>-/-</sup> mice. **D**, Bar plots show CD8<sup>+</sup> T cell and CD8<sup>+</sup> T<sub>EM</sub> cells of young, adult, and aged SCs in WT versus Apoe<sup>-/-</sup> mice. **E**, Bar plots show SSC-A<sup>low</sup>CD11b<sup>+</sup> and SSC-A<sup>low</sup>CD11c<sup>+</sup> myeloid cells of young, adult, and aged SC in WT versus Apoe<sup>-/-</sup> mice. Data are reported as mean ± SEM, n represent biologically independent animals. The p-values are calculated using a two-way ANOVA test and adjusted for multiple comparisons using Bonferroni's correction method: \*p < 0.05, \*\*p < 0.01, \*\*\*p < 0.001, ns: not significant.

In summary, total leukocyte infiltration in the NS is increased in aged Apoe<sup>-/-</sup> versus WT mice, particularly in aged Apoe<sup>-/-</sup> mice with advanced atherosclerosis. There were no changes in DRGs and SCs of young and adult Apoe<sup>-/-</sup> mice compared to age-matched WT mice. Analyses of different leukocyte subtypes showed that enhanced leukocyte infiltration in NS during atherosclerosis

## RESULTS

progression was mainly due to an increase of TCRb<sup>+</sup> T cells including CD4<sup>+</sup> T cells, CD8<sup>+</sup> T cells and the activated T<sub>EM</sub> cells.

### 3.2 Aged DRG single cell atlas

To investigate the transcriptomic changes in peripheral ganglia in advanced atherosclerosis at single cell resolution, scRNA-seq of DRG cells was conducted using the 10x Genomics Chromium technology. For this purpose, single cell suspensions from the lower thoracic DRGs (T6 - T13), known to innervate the abdominal aorta [52], were isolated and barcoded. Subsequently, 5' gene expression libraries were constructed following the manufacturer's protocol, and next-generation sequencing and data analyses were carried out as described in methods. To improve the purity and remove the debris of the cell suspension, FACS sorting was employed during this procedure, resulting in a higher abundance of cells, i.e. CD45<sup>+</sup> leukocytes and NeuN<sup>+</sup> neurons in immunostaining (**Figure 15**).

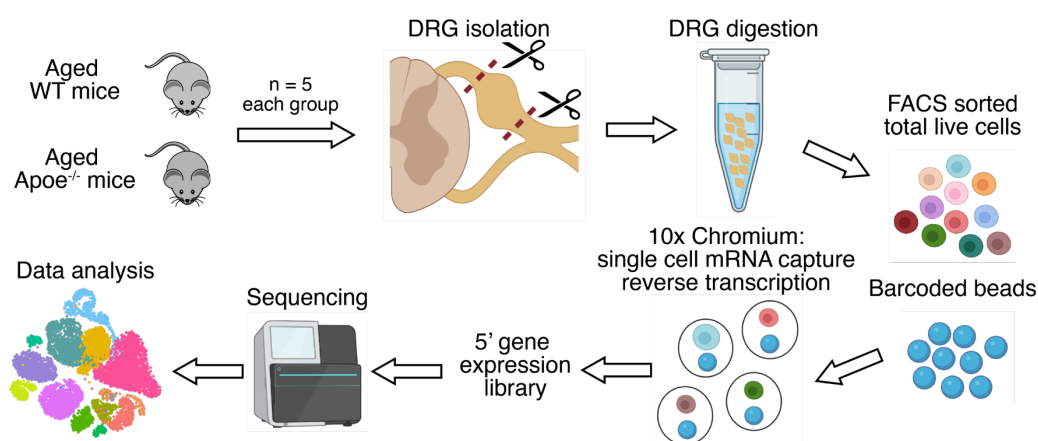


**Figure 15 Schematic of DRG scRNA-seq workflow.** Lower thoracic DRGs (T6-T13) are isolated and pooled from five mice per group. Total FVD<sup>-</sup> live cells are sorted by FACS, and individual cells are barcoded using the 10x genomics controller machine. Next, 5' gene expression libraries are constructed. Then, the libraries are subsequently sequenced and data are analyzed.

The raw scRNA-seq data were treated and analyzed following a standard 10x Genomics scRNA-seq analysis pipelines: raw data were aligned, and gene-cell matrices were generated using the Cell Ranger tool. The filtered matrices were further examined, and the batch effects between aged WT and Apoe<sup>-/-</sup> DRGs were removed using the Seurat R package [111, 183]. Pre-processing data quality control analyses were conducted to eliminate low-quality cells, including dead cells and those with high mitochondrial gene levels, cell debris with fewer total detected gene numbers per cell, and doublets having high total detected genes per cell. Cells with fewer than 200 or more than 8000 detected genes were excluded (**Figure 16**). Mitochondrial genes are associated with energy metabolism in cells, and higher percentages of these genes indicate increased energy metabolism

## RESULTS

activities, such as those found in heart cells [184]. Neurons are a high energy-demanding cell type; however, the precise percentages of mitochondrial genes in aged DRGs neurons have not been reported yet. In terms of filtering low quality cells with high mitochondrial genes in our aged DRGs scRNA-seq data, we set 10% mitochondrial genes threshold for non-neuronal cells and a 30% mitochondrial genes threshold for neurons, based on the reference reported in the scRNA-seq data analysis of the aged brain [185] (**Figure 16**). Following quality control, a total of 1563 cells (828 from WT and 735 from *Apoe*<sup>-/-</sup> mice) were obtained, with an average of 1415 detected genes per cell and a cumulative total of 32,502 detected genes from all captured cells.

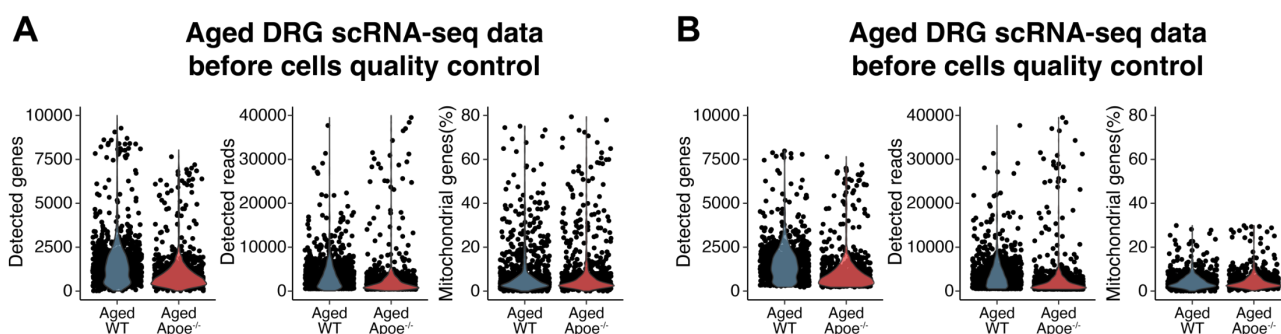


**Figure 16 Pre-processing scRNA-seq quality control criteria to remove low-quality cells and doublets.**

The characteristics of total number of mRNAs detected per cell (nFeatures), total number of reads detected per cell (nCounts) and mitochondrial gene percentage per cell before **A** and after **B** quality control in WT and *Apoe*<sup>-/-</sup> DRGs, respectively. Cells with fewer than 200 or more than 8000 detected genes, and more than 30% mitochondrial genes [185] were excluded.

During this single-cell transcriptome protocol, each mRNA was assigned a unique UMI, while each individual cell was given a unique barcode. The quality control results also demonstrated that low-quality cells were removed, and high-quality cells were obtained. By merging the UMI and cell barcodes of these high-quality cells, we were able to determine the number of cells and the expression levels of each gene.

### 3.2.1 Construction of DRG atlases

To determine the composition of DRG cell types and their gene expression patterns, an unbiased clustering procedure was performed using Seurat R package [183]. Initially, all 1563 DRG cells were classified into 13 distinct cell types based on their transcriptomic profiles and the expression of known key/signature genes. The cell types identified in aged DRG were neurons, T cells, macrophages, Trem2<sup>hi</sup> macrophages, neutrophils, endothelial cells (ECs), pericytes, fibroblast1, fibroblast2, fibroblast3, SGC, mSch, and nmSch as described in materials and methods (**Table 10**, **Figure 17 A, B**). To better understand the cell type composition, all thirteen cell types were broadly grouped into five classes based on marker gene expression and functions of marker genes: neurons

## RESULTS

(further classified in the neuron subclustering below), immune cells (T cells, macrophages, Trem2<sup>hi</sup> macrophages, neutrophils), vascular cells (ECs, pericytes), fibroblasts (fibroblast1, fibroblast2, fibroblast3), and glial cells (SGC, mSch and nmSch) (**Figure 16 C**).

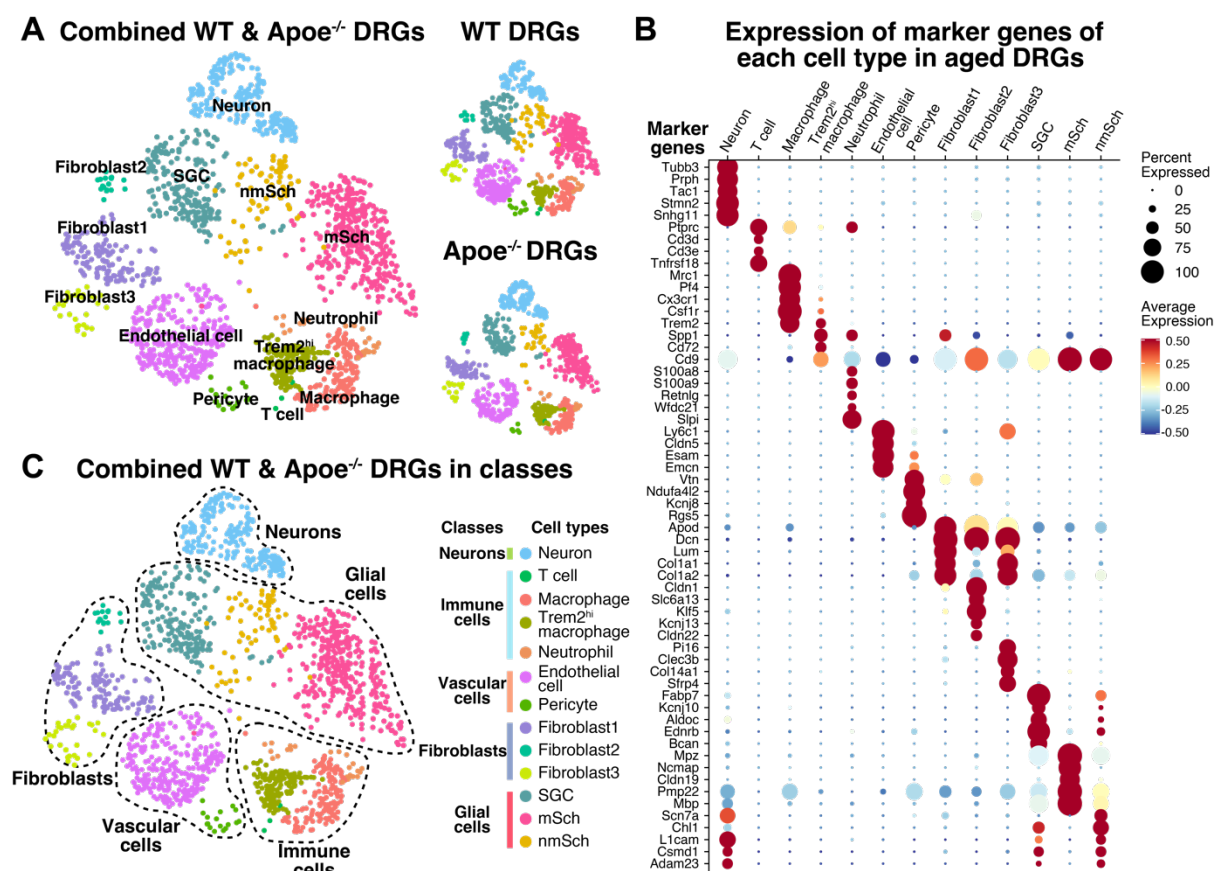


**Figure 17** ScRNA-seq of aged WT and Apoe<sup>-/-</sup> DRG cells identifies thirteen distinct cell types. **A**, UMAP plots depict all single-cell transcriptomes from aged WT (n = 5) and aged Apoe<sup>-/-</sup> (n = 5) DRG single cells. Each dot represents a single cell, 1563 individual cells obtained in total, dots are colored based on scRNA-seq clustering results, different colors represent different cell clusters. UMAPs of WT and Apoe<sup>-/-</sup> DRGs are shown separately at left. **B**, Bubble plots show expression of each cell type's marker genes in all DRG cells from both aged WT and Apoe<sup>-/-</sup> DRGs, the size of the bubble represents the percentage of cells expressing the marker genes in each cell type. The color depth corresponded to the average expression levels, red color means the highest expression levels, blue color designated low or no expression. **C**, UMAP shows the five main classes of aged WT and Apoe<sup>-/-</sup> DRGs. Each class is circled by dashed line. SGC, Satellite glial cell; mSch, myelinating Schwann cell; nmSch, non-myelinating Schwann cell.

Following the clustering of diverse cell types, supplementary UMAP analyses were executed to ascertain marker gene expressions corresponding to each cell type. The mean expression of all marker genes was computed and exhibited on the UMAPs, where the maximal expression of marker genes was reached within their respective cell types. These discoveries demonstrated that the marker genes were not only merely enriched, but also exclusively expressed in distinct cell types,

## RESULTS

mirroring their unique characteristics of each cell type on UMAP (**Figure 18**). Further investigation will be necessary to illustrate detailed transcriptional characteristics.

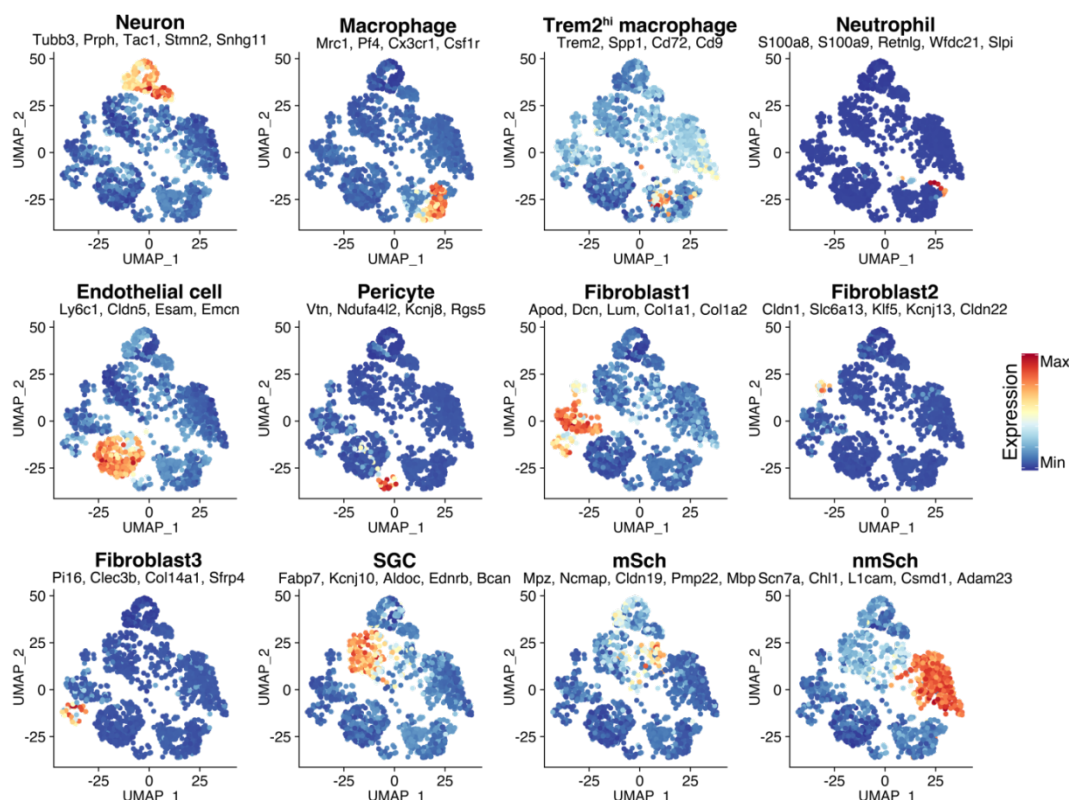


**Figure 18** Expression of marker genes in UMAPs of each cell type in aged DRGs. In aged WT DRGs, a known set of key marker genes for each cell type are selected and their average expression levels are projected onto the UMAPs to determine their cell-specific expression and confirm the clustering results. Red color represents the highest expression, blue color indicates low or no expression.

### 3.2.2 Transcriptional characteristics of cell types in aged DRGs

Recently, transcriptome profiles of young DRG cells including both neuronal and non-neuronal types have been reported using scRNA-seq [112, 119, 124, 162, 186]. However, the transcriptional profiles of aged DRG cells remained to be determined. To interpret and characterize these transcriptome profiles and explore the biological implications of all aged DRG cell types, we performed GO enrichment analyses on the top 200 highly expressed genes of each cell type using the Metascape web tool (<https://metascape.org>) [187]. The heatmap showed the cell type specific expression of top 10 marker genes, while the bubble plot displayed the enriched GO terms in each cell type (**Figure 19, top50 are shown in Appendix Table 1**).

Based on the enrichment results of neurons, synaptic function-associated pathways including vesicle-mediated transport in synapses (GO:0099003), and ion channel activity-associated pathways, such as regulation of ion transport (GO:0043269) and calcium-ion-regulated exocytosis

## RESULTS

(GO:0017156) were highly enriched in neurons compared to non-neuronal cells in aged WT DRGs (**Figure 19**). Notably, nociception (GO:0019233) and neuron projection-associated pathways were also enriched. These results indicated the enriched genes in aged WT DRG neurons were associated with distinct neuronal functions including synapse functions, ion channel activity, and neuron projection.

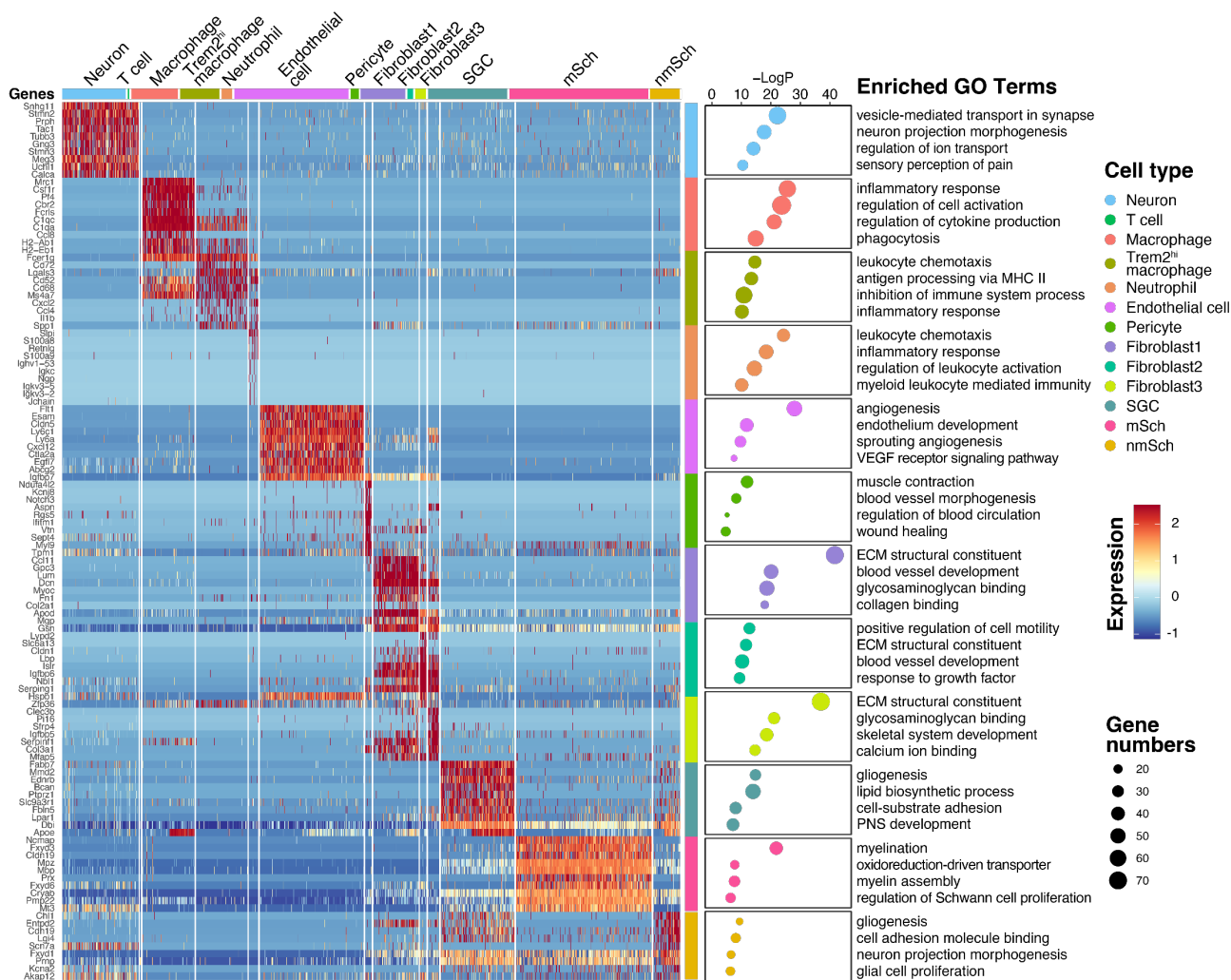


**Figure 19** Heatmap show the top 10 key genes of each cell type and associated enriched GO terms in aged WT DRGs. Left: Heatmap shows the top 10 highly expressed genes of each cell type in DRGs. Colors in the heatmap represent the expression level of each gene in individual cells, red and blue indicate highest and lowest expression, respectively. Color bar on top of the heatmap represent individual cell types, gene names for each cell type are shown at left. Right: The bubble plot shows the top 4 non-redundant enriched GO terms in each cell type. P-values ( $-\log P$ ) are depicted in X-axis, and the dot size represents number of genes associated with the GO terms in each cell type.

The GO enrichment analysis of immune cells in DRG revealed several shared pathways among macrophages, Trem2<sup>hi</sup> macrophages, and neutrophils. These pathways included leukocyte chemotaxis (GO:0030595) and inflammatory response (GO:0006954). However, the key associated genes differed among the cell types. For example, genes related to the inflammatory response such

## RESULTS

as Pf4 and Csf1r were specifically expressed in macrophages. In contrast, Trem2<sup>hi</sup> macrophages specifically expressed Cd14, Cyba, and Cybb, while neutrophils expressed S100a8 and S100a9, highlighting their distinct involvement in the DRG immune response. The shared GO terms may suggest specific functions for each of these three DRG immune cell types. Additionally, macrophages were associated with GO terms such as regulation of cell activation (GO:0006954), cytokine production (GO:0001817), and adaptive immune response (GO:0002250). Trem2<sup>hi</sup> macrophages were previously reported as anti-inflammatory macrophages in atherosclerosis [39] and myocardial infarction [188] since they expressed increased levels of Trem2, Spp1, and several cathepsins (Ctsb, Ctsd, and Ctsz) [39, 189-191]. Our data suggest that Trem2<sup>hi</sup> macrophages may possess anti-inflammatory functions in aged DRG, which are associated with leukocyte chemotaxis (GO:0030595), peptide antigen processing and presentation via MHC class II (GO:0002495), and negative regulation of immune system processes (GO:0002683) (**Figure 19**).

Vascular cells have recently been identified in PNS and CNS neuronal tissues through scRNA-seq analyses [112, 185]. DRG scRNA-seq GO analysis demonstrated that pathways related to blood vessel and lymph vessel development, as well as endothelial cell function were enriched in endothelial cells. Furthermore, pericytes exhibited enrichment in pathways related to blood vessel morphogenesis (GO:0048514), muscle contraction and wound healing (GO:0042060) (**Figure 19**).

In the PNS, fibroblasts contribute to the formation and turnover of the extracellular matrix (ECM) [171]. In aged DRGs, three fibroblast subtypes were identified based on their differential gene expression as described in methods (**Table 10**): Fibroblast1 (Apod, Dcn, Lum), Fibroblast2 (Cldn1, Slc6a1, Cldn22), and Fibroblast3 (Pi16, Clec3b). These findings were in line with recently reported DRG fibroblast classifications: Lum<sup>+</sup> fibroblast, Cldn1<sup>+</sup> fibroblast, and Sfrp4<sup>+</sup> fibroblast, respectively [162]. GO analysis revealed that ECM-associated pathways were highly enriched in all three fibroblast subtypes: blood vessel development (GO:0001568), glycosaminoglycan binding (GO:0005539), and collagen binding (GO:0005518) were highly expressed in fibroblast 1; whereas growth factor-associated pathway (GO:0070848), known to be linked with aging [192] and intracellular signaling [193, 194], was enriched in fibroblast2; and calcium ion binding (GO:0005509) was enhanced in fibroblast3. These results indicated the distinct transcriptional profiles of the three fibroblast subtypes (**Figure 19**).

As described above we identified three types of glial cells based on their distinct transcriptional profiles in aged DRGs in line with previously known glial cell types in young WT mice (Sharma et al. 2020): SGC, mSch, and nmSch. Our GO pathway enrichment analysis revealed that pathways associated with basic glial cell functions, such as gliogenesis and cell proliferation were enriched in all glial cell types (**Figure 19**). SGC wrap around sensory neuron somas. They have been reported to be involved in pain responses, particularly neuropathic and inflammatory pain [195]. Additionally,

## RESULTS

SGC have been found to play a role in lipid metabolism in nerve injury models. [162, 175, 195]. Our GO enrichment data from aged DRG revealed that the lipid biosynthesis process (GO:0008610) was enriched in SGC, suggesting the important role of SGC in lipid metabolism. This finding is consistent with the highest expression of the *ApoE* gene in SGC compared to all other DRG cell types. **(Figure 32 A)**. The mSch exhibited higher expression of genes related to myelination (GO:0042552), as well as structural constituents of myelin sheaths (GO:0042552) and pathways involved in myelin assembly (GO:0032288). In contrast, nmSch were enriched in gliogenesis, proliferation-associated pathways (GO:0042063, GO:0014009), and cell adhesion-related pathways (GO:0050839). Taken together, these enrichment analysis results depicted the distinct potential functions of each glial cell type in aged DRGs.

### 3.2.3 Macrophages in aged DRGs

To predict specific functions of the two types of macrophages in aged DRG, further comparisons of transcriptional differences between macrophage and Trem2<sup>hi</sup> macrophage were performed. Firstly, we found that the marker genes for these two types of macrophages in aged DRG were highly and specifically expressed **(Figure 20)**. The macrophage marker genes *Cx3cr1*, *Pf4*, macrophage mannose receptor 1 (*Mrc1*) and *Csf1r* were barely expressed in Trem2<sup>hi</sup> macrophages. Conversely, the Trem2<sup>hi</sup> macrophage marker gene, *Trem2*, was expressed at low levels in macrophages versus Trem2<sup>hi</sup> macrophages. These results were consistent with the definition of Trem2<sup>hi</sup> macrophages in published scRNA-seq datasets [39]. In addition, three other Trem2<sup>hi</sup> macrophage marker genes: *Spp1*, *Cd9*, and B-cell differentiation antigen *Cd72* were barely expressed in macrophages **(Figure 20 A)**. When we compared the expressions of all genes between macrophages versus Trem2<sup>hi</sup> macrophages, the *ApoE* gene and macrophage marker genes, including *Mrc1*, *Pf4*, *Csf1r*, were highly expressed in macrophages versus Trem2<sup>hi</sup> macrophages. The genes including *Cd9*, *Ctss*, *Ctsz*, *Ctsd*, which have been reported to be highly expressed in Trem2<sup>hi</sup> macrophages, were highly expressed in DRG Trem2<sup>hi</sup> macrophage versus macrophages **(Figure 19 B)**. We present a table to list the genes and putative cell types.

## RESULTS

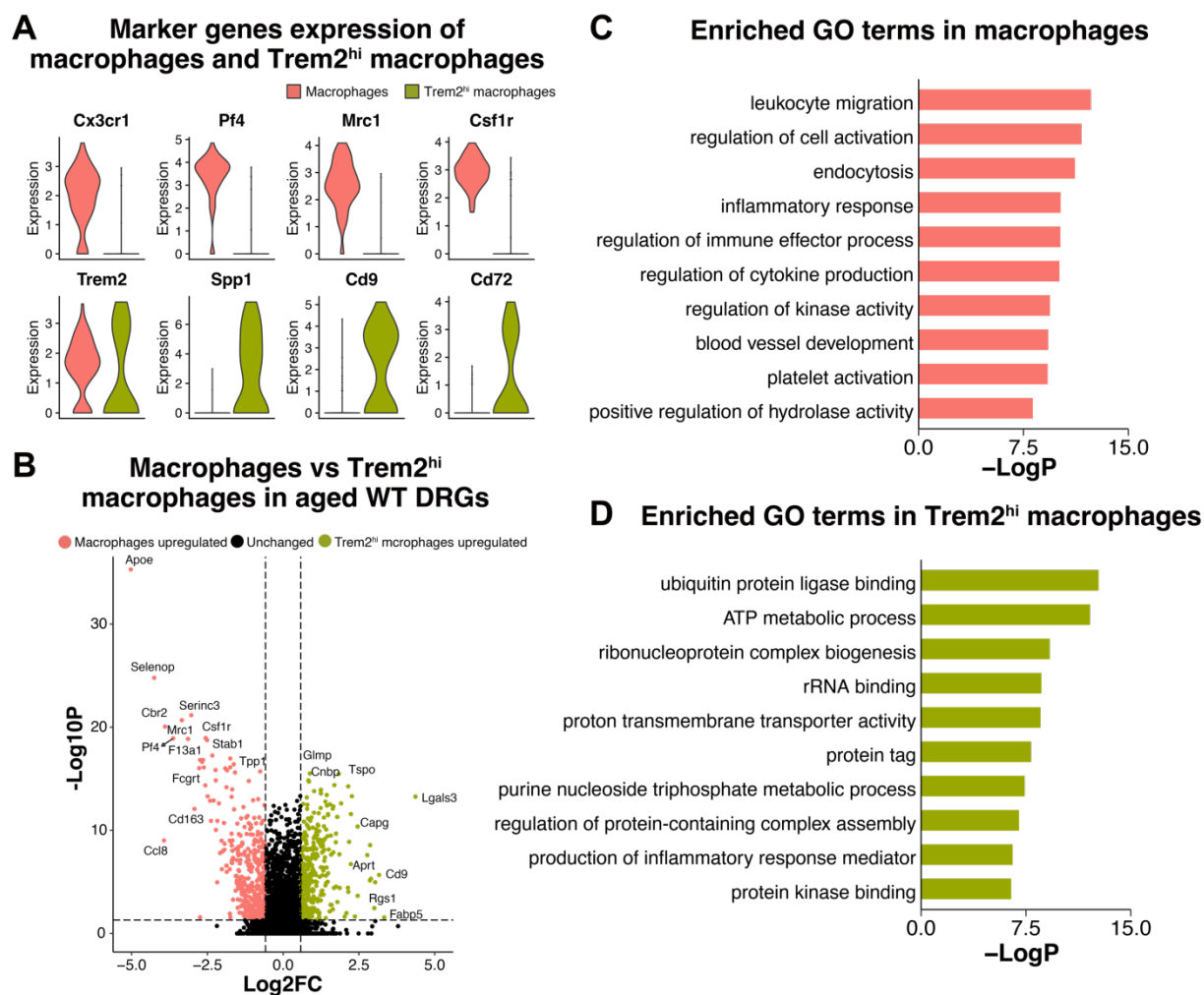


**Figure 20 Transcriptional identification of macrophage and Trem2<sup>hi</sup> macrophage in aged WT DRGs.** **A**, Violin plots show the gene expressions of DRG macrophages and Trem2<sup>hi</sup> macrophages in aged WT DRG, the genes at the upper plots are DRG macrophage marker genes, and the lower line are Trem2<sup>hi</sup> macrophage marker genes. **B**, Volcano plots show the differentially expressed genes between DRG macrophages and Trem2<sup>hi</sup> macrophages in aged WT mice. Each dot represent one gene, the genes with log2FC value greater than 0.58 and adjusted p-value less than 0.01 are considered as DEGs, the genes colored by red are the DEGs higher expressed in macrophages compared to Trem2<sup>hi</sup> macrophages, the genes colored by green are the DEGs higher expressed in Trem2<sup>hi</sup> macrophages compared to macrophages. **C**, Bar plot shows the top 10 non-redundant enriched GO terms in macrophages using higher expressed DEGs in macrophages compared to Trem2<sup>hi</sup> macrophages; **D**, Bar plot shows the top 10 non-redundant GO terms in Trem2<sup>hi</sup> macrophage using DEGs which higher expressed in Trem2<sup>hi</sup> macrophage compared to macrophage. Y-axis depict the full name of GO terms, X-axis depicted the p-values (-logP), and the length of the bar indicate the negative log p-value (-logP) of the GO term.

To understand the differences between two types of macrophages and Trem2<sup>hi</sup> macrophages, we performed enrichment analyses using total DEGs of both macrophages and Trem2<sup>hi</sup> macrophages. From the enrichment analyses, we discovered several immune-associated functions that were enriched in macrophages, such as leukocyte migration (GO:0050900), inflammatory response (GO:0006954), regulation of immune effector process (GO:0002697), and regulation of cytokine

## RESULTS

production (GO:0001817) (**Figure 20 C**). Conversely, multiple energy metabolism- and ribosome-associated pathways were enriched in Trem2<sup>hi</sup> macrophages, including ATP metabolic process (GO:0046034), ribonucleoprotein complex biogenesis (GO:0022613), proton transmembrane transporter activity (GO:0015078), purine nucleoside triphosphate metabolic process (GO:0009144), and rRNA binding (GO:0019843) (**Figure 20 D**). Since Trem2 was reported to maintain the metabolic process of brain microglia in Alzheimer's disease [196], enrichment of metabolic pathways in Trem2<sup>hi</sup> macrophages suggested that Trem2 may be associated with metabolic processes of Trem2<sup>hi</sup> macrophages in aged DRG. These findings illustrated the differences in the potential functions of these two types of macrophages.

Tissue-resident macrophages are a diverse population of immune cells that perform tissue-specific and niche-specific functions [197]. To investigate the transcriptomic profile of aged DRG macrophages, we integrated our DRG macrophages data with the genotype- (WT) and age-matched scRNA-seq data of brain microglia (GSE129788), brain macrophages (forebrain and midbrain, GSE129788) [185], and lymph node macrophages (RLN, <https://doi.org/10.6084/m9.figshare.21900735.v2>) [139]. We compared the differences between these macrophages originating from distinct tissues (**Figure 21**). UMAP showed that the brain macrophages and microglia were located separately in the distinct areas, while DRG macrophages were located at the similar location with brain macrophages (**Figure 21 A**). To assess the transcriptional similarity between DRG macrophages and macrophages from various tissues, we calculated the Spearman correlation coefficients as previously described [76]. We observed a higher correlation coefficient between DRG macrophages and brain macrophages compared to RLN macrophages or brain microglia. To quantify the similarity and differences between the macrophages from different tissues and the microglia, we calculated the score values for marker genes from brain macrophages and microglia. The box plots revealed that DRG macrophages had higher brain macrophage score values and lower microglia scores (**Figure 20 B**). Our data showed that DRG macrophages expressed the Fc receptor-like S (Fcrls) [137] and sialic acid binding Ig-like lectin H (Siglech) [198], both of which were reported to be associated with CNS and PNS resident macrophages. Moreover, DRGs did not express microglia marker genes like Sall1 [137] (**Figure 20 D**). These findings suggested that DRG macrophages exhibited a greater transcriptional similarity with brain macrophages, but neither with microglia nor with lymph node macrophages. Heatmap of highly expressed top 10 marker genes showed that the expression levels of key genes were different in these macrophages from different tissues and brain microglia (**Figure 20 C**). To investigate the potential biological functional differences of the macrophages from different tissues, we calculated score values for the selected GO terms, including antigen processing via MHC class I (GO:0019886), antigen processing via MHC class II (GO:0002474), and phagocytosis (GO:0006911). We observed higher score values for antigen processing via MHC class I and MHC class II in DRG macrophages compared to brain and lymph node macrophages. Macrophages have been reported to be essential

## RESULTS

for axon regeneration following nerve injury in the PNS [199]. Our results also revealed that DRG macrophages had higher phagocytosis score values compared to brain and lymph node macrophages (**Figure 20 E**).

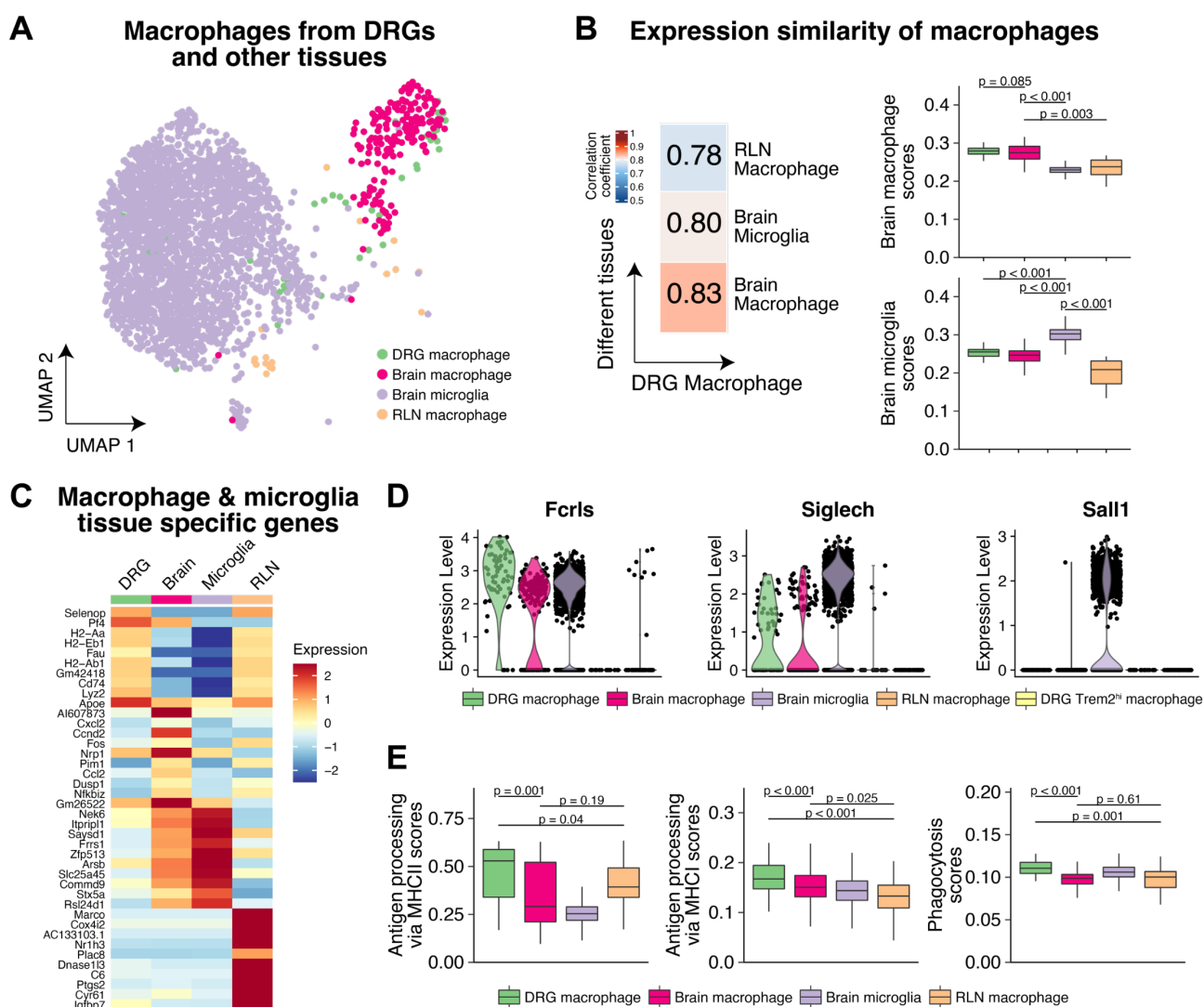


**Figure 21 Macrophages in aged DRGs are distinct from the macrophages in brain and lymphoid organs.**

**A**, UMAP shows the locations of macrophages from different tissues and microglia from brain. Colors of dots represent macrophages from different tissues and microglia from brain. **B**, Heatmap shows the correlation relationships of macrophages from aged WT DRGs and macrophages from lymph nodes and brain. Numbers in the blocks represent correlation coefficients. Boxplots show score values of brain macrophage and brain microglia. **C**, Heatmap shows the non-redundant top 10 marker genes of the macrophages from different tissues. Red color designates the highest expression, blue designates the lowest expression. **D**, Violin plots show the expression of *Fcrls*, *Siglech*, and *Sall1* in different macrophages and microglia. **E**, Boxplots show the score values of selected function-associated genes in different cell types. Kruskal-Wallis test is performed to determine the significance of the changes.

These data suggested that DRG macrophages might be involved in the axon regeneration process through phagocytosis. In summary, these findings indicated that DRG macrophages were distinct

## RESULTS

and potentially functionally different from other tissue macrophages, including brain or lymph node macrophages, and brain microglia.

### 3.3 Neuron subtype composition in aged DRGs

#### 3.3.1 Integrated analysis of DRG neurons

As mentioned below, the proportion of neurons in the total cell population of aged DRGs increased from 10.7% to 15% when comparing aged WT versus *Apoe*<sup>-/-</sup> DRGs (**Figure 35 A, B**). Moreover, we identified 99 DEGs in neurons of aged WT versus *Apoe*<sup>-/-</sup> DRGs (**Figure 36 C**). Additionally, we aimed to identify the neuron subtype composition in the aged DRGs. To uncover detailed transcriptional differences between aged WT and *Apoe*<sup>-/-</sup> mice at the single-cell resolution, we performed subclustering of neurons in aged DRGs and analyzed differential transcriptomes between aged WT and *Apoe*<sup>-/-</sup> neurons. Due to the limited number of aged DRG neurons, accurately classifying them into distinct neuron subtypes proved difficult. To address this issue, we employed a well-established neuron subclustering method from the literature to obtain precise information on neuron subtypes [76, 126]. In this neuron subclustering approach, we contextualized our aged WT and *Apoe*<sup>-/-</sup> DRG neuron scRNA-seq data with young WT DRG neuron scRNA-seq dataset (GSE139088) [76, 126]. After integrating the aged and young DRG neuron scRNA-seq datasets, the aged DRG neurons were mapped onto 15 existing neuron subtypes within young DRG neuron scRNA-seq dataset (**Figure 22 A, B**). From the UMAP, we classified the aged neurons into 10 subtypes: CGRP-alpha, CGRP-beta, CGRP-epsilon, CGRP-gamma, CGRP-zeta, C-LTMR, CGRP-theta, NP-nociceptor, Sst, and TrpM8 (**Figure 22 C**). These 15 existing neuron subtypes had been validated in young WT mice DRG using RNA fluorescent in situ hybridization (RNA-FISH) [124]. For instance, peptidergic nociceptor neuron subtype CGRP-alpha was found to express arginine vasopressin receptor 1A (*Apvr1a*) [119]. The C-low threshold mechanoreceptor C-LTMR was shown to express tyrosine hydroxylase (*Th*) [124]. The cold thermoreceptors TrpM8 was verified to express transient receptor potential cation channel member 8 (*Trpm8*) [124, 126]. However, the proportions and transcriptional profiles of these neuron subtypes in aged DRG remained unknown.

## RESULTS

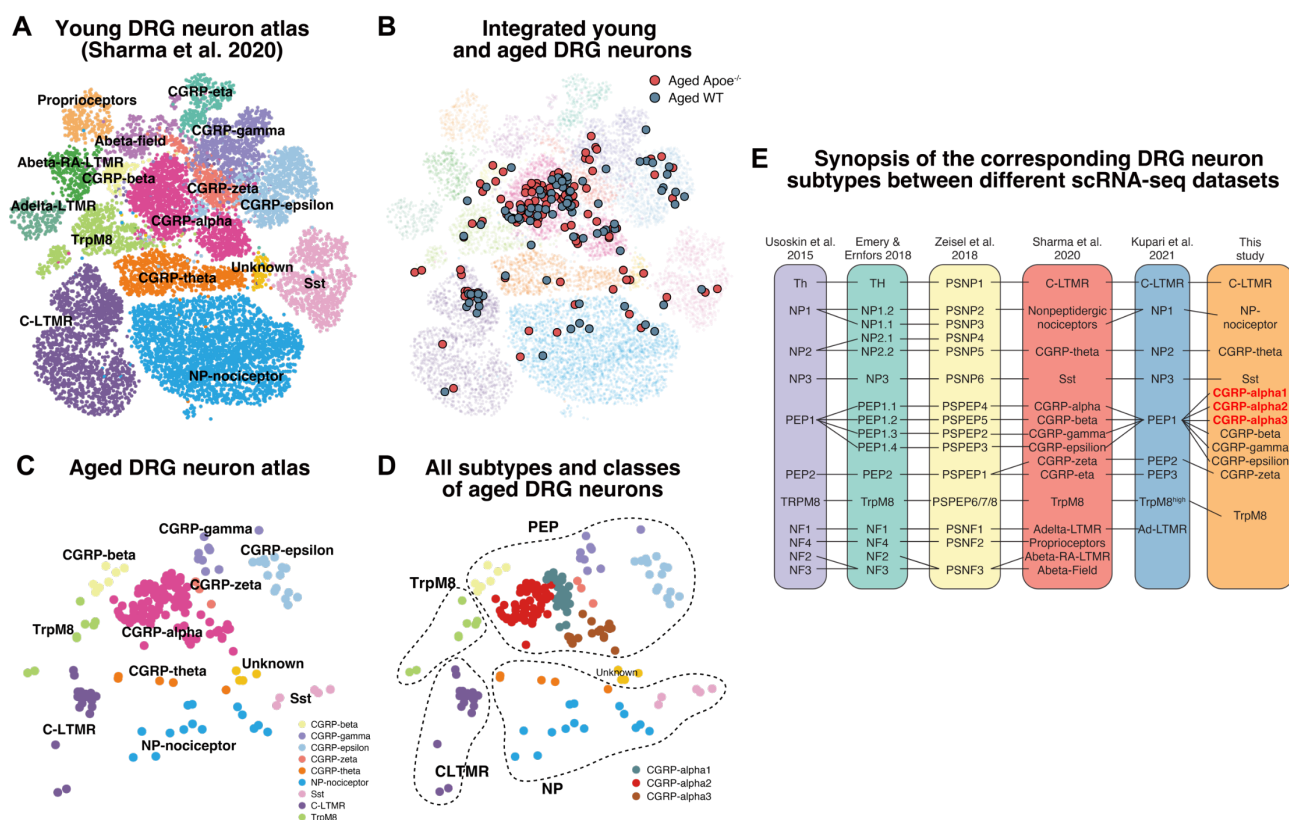


**Figure 22 Subclustering process of aged DRG neurons.** **A**, The UMAP shows the subcluster composition of the young (4-6 weeks) DRG neurons in published scRNA-seq dataset [124]. Each neuron subtype is colored and labelled by previously defined subtype names. **B**, The UMAP displays the integrated dataset of aged and young DRG neurons. Aged DRG neurons are projected against the young DRG neuron subtypes in background with higher transparency. Aged DRG neurons are highlighted with bigger size and black outlines and are colored by genotype. The red color represents aged *Apoe*<sup>-/-</sup> DRG neurons, while the blue color represents aged WT DRG neurons. **C**, The UMAP shows the aged DRG neuron atlas, colored by cell types, and labelled by cell type names. **D**, The UMAP shows the three subtypes of CGRP-alpha neurons with other neuron subtypes in aged DRG, colored by cell types, labelled by cell type names. **E**, Synopsis of the corresponding DRG neuron types of aged DRG neuron subtypes and with different DRG neuron scRNA-seq datasets.

Upon examining the UMAP of young DRG neurons, we noticed that CGRP-alpha neurons appeared as several distinct populations. To confirm and further investigate the transcriptional differences among CGRP-alpha neurons, we conducted additional subclustering of aged CGRP-alpha neurons. Our findings revealed that CGRP-alpha neurons were classified into three separate neuron populations. Consequently, we divided the total CGRP-alpha neurons into three neuron types based on their transcriptional differences: CGRP-alpha1, CGRP-alpha2, and CGRP-alpha3 neurons (**Figure 22 D, E**). Furthermore, due to the varying naming criteria for DRG neuron subtypes across different DRG neuron scRNA-seq studies, we aimed to simplify the understanding of neuron composition in aged DRGs. We next consolidated the 12 neuron subtypes into 5 neuron classes, as previously described [126]: CGRP-alpha1, CGRP-alpha2, CGRP-alpha3, CGRP-beta, CGRP-

## RESULTS

gamma, CGRP-epsilon, and CGRP-zeta were grouped as PEP neurons; CGRP-theta, NP-nociceptor, and Sst were categorized as NP neurons; and C-LTMR and TrpM8 neurons retained their original subtype names.

Although DRG neurons of different ages are distinct, the marker genes of neuron subtypes exhibited similar expression patterns [76]. To better define the predicted neuronal subtypes in aged DRG. We also assessed the expression similarity between each subtype of aged DRG neurons and those in the young DRG neuron dataset. From the heatmaps of Spearman correlation coefficient results between aged and young DRG neuron classes, the highest correlation coefficient for aged PEP neuron was observed with the young PEP neuron class (**Figure 23 A**). This finding suggests that aged DRG PEP neuron exhibited the closest transcriptional similarity to previously defined PEP neurons in the young DRG scRNA-seq dataset. When comparing aged PEP neurons to young DRG neuron subtypes, we found that all PEP neuron subtypes had the highest correlation coefficients with the corresponding subtypes in young DRG neurons (**Figure 23 B**). In comparison with young DRG scRNA-seq dataset, aged DRG neurons exhibited transcriptomic phenotypes consistent with previously defined neuronal classes in young DRGs, including C-LTMR, NP, and TrpM8 neurons, and their respective subtypes (**Figure 23 A, B**). As for NF neurons in aged DRG, the number was limited, and the Spearman correlation coefficient between aged and young DRG was low. To evaluate the gene expression similarities between individual aged DRG neurons and young DRG neurons, we examined the gene expression profiles of young DRG neuron subtypes. The resulting data illustrates that these genes are highly expressed in young DRG neuron subtypes. Furthermore, these neuron subtype-specific genes were also highly and distinctly expressed in aged DRG neurons (**Figure 23 C**). Several canonical marker genes of DRG neuron classes were examined further and are shown in a bubble plot (**Figure 23 D**). In summary, these integrated analyses helped us to accurately identify different neuron subtypes in aged DRG similar to the previously identified neuron subtypes in young DRG [119, 124, 126]. We observed that the gene expressions were similar but not identical suggesting that transcriptional profiling of aged DRG neuron subtypes requires further examination.

## RESULTS

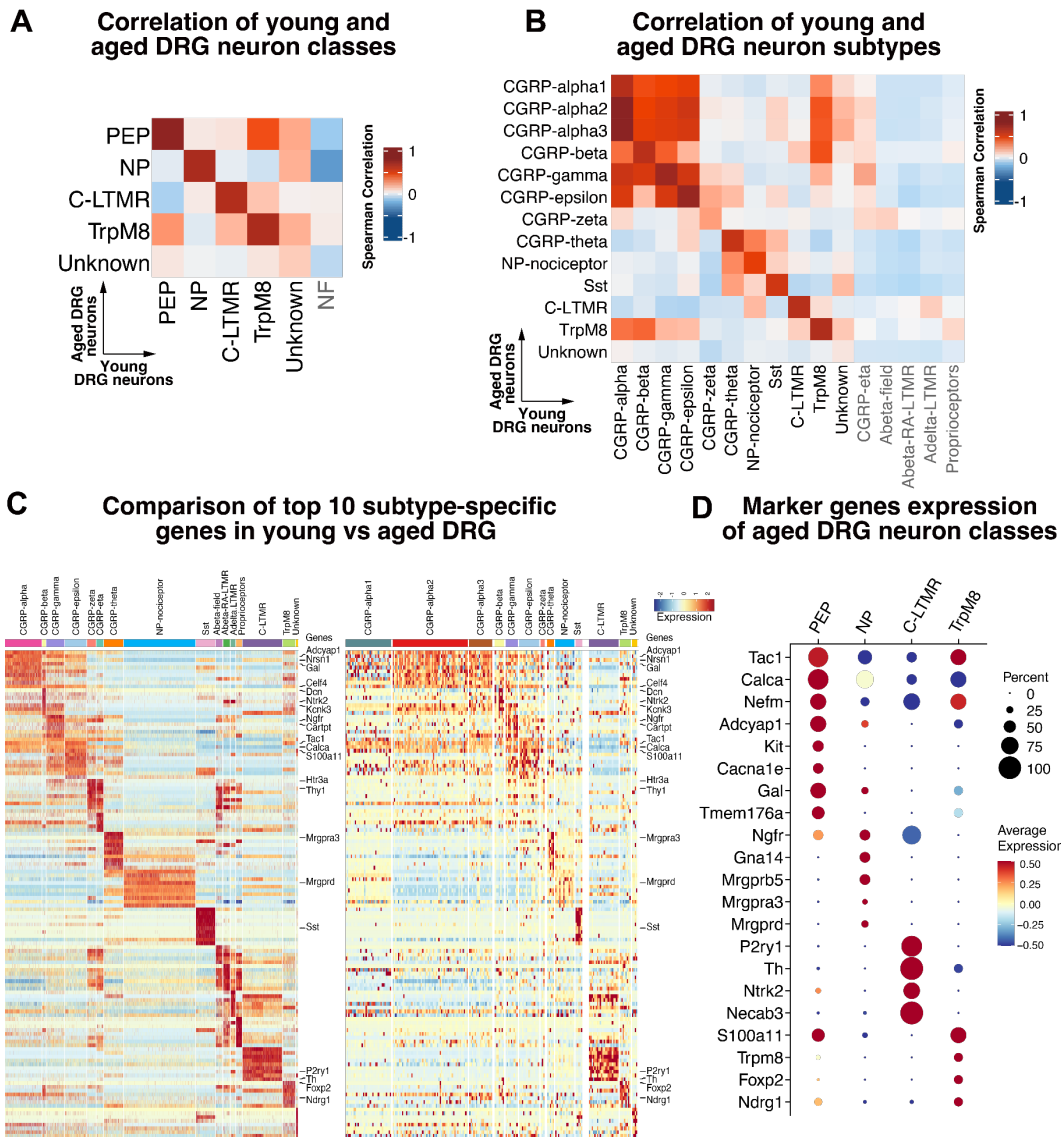


**Figure 23 Integration of aged DRG neuron cell types determination using public datasets.** **A**, Heatmap shows Spearman correlation between aged and young DRG neuron classes [124]. The names of columns are the clusters in young DRG neurons, the names of rows are classes in aged DRG neurons. **B**, Heatmap shows Spearman correlation of aged and young DRG neuron subtypes. Red color represents the highest correlation coefficient, and blue color represents the lowest correlation coefficient. **C**, Heatmap at left shows cell type-specific key genes within top 10 genes for each neuron subtype in previously defined young DRG neurons and their expressions in aged DRG neurons (heatmap at right). Red color represents the highest expression, and blue color represents the lowest expression. Neuron subtype names are listed on top and the key subtype-specific genes are listed at the left side of the heatmaps. Width of color bar for each subtype represents the number of neurons per subtype.

In summary, these findings demonstrated that the most neuron classes or subtypes in aged DRGs exhibited high transcriptional similarities with their corresponding classes or subtypes in previously defined young DRG neurons. Thus, utilization of young DRG neurons enabled us to accurately sub-cluster the limited number of aged DRG neurons.

## RESULTS

### 3.3.2 CGRP-alpha PEP neuron subtypes in aged WT DRGs

In aged DRGs, PEP neurons were the most abundant class in DRGs, and CGRP-alpha neurons were the most abundant neuron type in PEP neurons (**Figure 24 A, C**). These results indicated that PEP neurons, especially CGRP-alpha neurons, may play an important role in aged DRGs. To identify the transcriptional characteristics of PEP and CGRP-alpha neurons, a comparison between the PEP and CGRP-alpha neurons relative to all other neurons were performed in aged DRGs. GO term enrichment analysis of PEP neurons marker genes showed the neuropeptide signaling pathway (GO:0007218), corticosteroid hormone secretion regulation (GO:2000848), neuron projection (GO:0120035), and ion transport (GO:0098655) were enriched in PEP neurons in aged DRGs (**Figure 24 B**). The GO term enrichment analysis of CGRP-alpha neurons showed the enriched pathways were differed with the enriched pathways in PEP neurons, calcium channel activities (GO:0051592, GO:0043269), pain regulation (GO:0048265), and ATP metabolic process (GO:0046034) were enriched in CGRP-alpha neuron subtype (**Figure 24 D**). These results demonstrated that PEP neurons were the major neuron type in DRG and CGRP-alpha neurons were the major neuron subtype among PEP neurons. CGRP-alpha neurons may play important roles in aged DRGs including calcium channel activities, pain regulation, and energy metabolism.

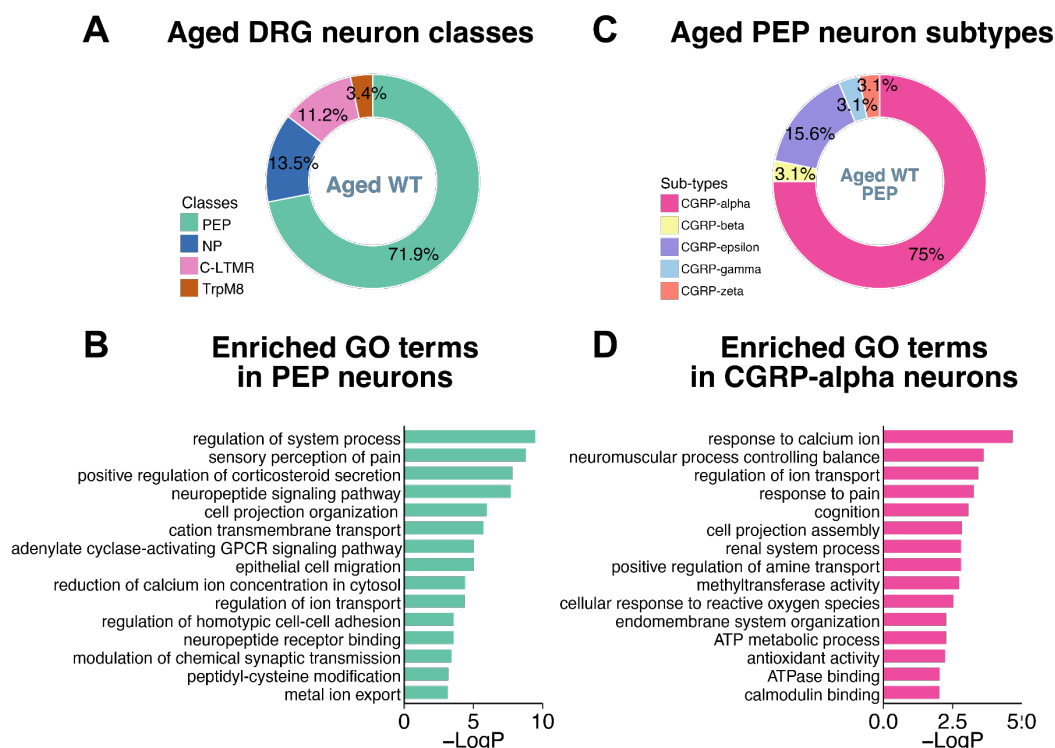


**Figure 24 CGRP-alpha neurons were major PEP neuron types in aged WT DRGs.** **A**, Donut plots show the percentages of the main classes in aged DRG neurons, the plots are colored by class, and labeled by percentages. **B**, Bar plot shows the top 15 non-redundant enriched GO terms of significant PEP neuron markers (adj.p < 0.05). **C**, Donut plots show the percentages of neuron subtypes in aged DRG PEP neurons, the plots are colored by class, and labeled by percentages. **D**, Bar plot shows the top 15 non-redundant

## RESULTS

enriched GO terms of CGRP-alpha neuron significant marker genes ( $\text{adj.p} < 0.05$ ). In the bar plots, the GO terms are ranked by p-value, the length of the bar designates negative log p-value. Adj.p, adjusted p-value.

### 3.3.3 Transcriptional profiles of CGRP-alpha neurons in aged DRG

As described above, we subclustered aged DRG neurons and confirmed our sub-clustering results using the previously defined young DRG neuron scRNA-seq datasets. During this analysis, we identified three subtypes of CGRP-alpha neurons, namely CGRP-alpha1, CGRP-alpha2, and CGRP-alpha3, which had not been reported before. In order to characterize the transcriptional profiles of these subtypes and define their potential functions, we evaluated the expression of marker genes. Additionally, we examined enriched GO terms related to biological functions.

Heatmap of top 10 highly expressed genes showed that the marker genes of CGRP-alpha subtypes were all expressed in each subtype (**Figure 25 A**). Several canonical genes, including *Arc3*, *Pomp*, *Malat1*, *Enox1*, *Atp1a2*, and *Ndr1* were selected and depicted in violin plots (**Figure 25 A, B, C**). To understand the potential biological implications of three CGRP-alpha subtypes, we performed GO enrichment analyses using the specific marker genes of each CGRP-alpha subtype. The enrichment bar plots revealed that molecular functions such as ubiquitin protein ligase binding and disordered domain-specific binding, along with biological processes such as response to nerve growth factor and regulation of cytoskeleton organization (GO:0031625, GO:0097718, GO:1990089, GO:0051493), were specifically enriched in CGRP-alpha1 neurons (**Figure 25 A**). In CGRP-alpha2 neurons, molecular functions like peptide binding and biological processes such as inorganic cation transmembrane transport, neuropeptide binding, and positive regulation of cell projection organization (GO:0042277, GO:0098662, GO:0042923, GO:0031346) were highly enriched (**Figure 25 A**). In CGRP-alpha3 neurons, biological processes including gliogenesis (GO:0042063) and glial cell development (GO:0021782) were enriched. By combining gene expression and GO enrichment analysis results, we observed that each CGRP-alpha subtypes exhibited distinct transcriptional profiles indicating potential functional differences among them. CGRP-alpha2 neurons were the most abundant subtype among three CGRP-alpha subtypes. Moreover, the pathways including neuropeptide-associated and ion channel activity-associated were enriched in CGRP-alpha2 neurons, which have been shown to play an important role in neuroimmune responses [200].

## RESULTS

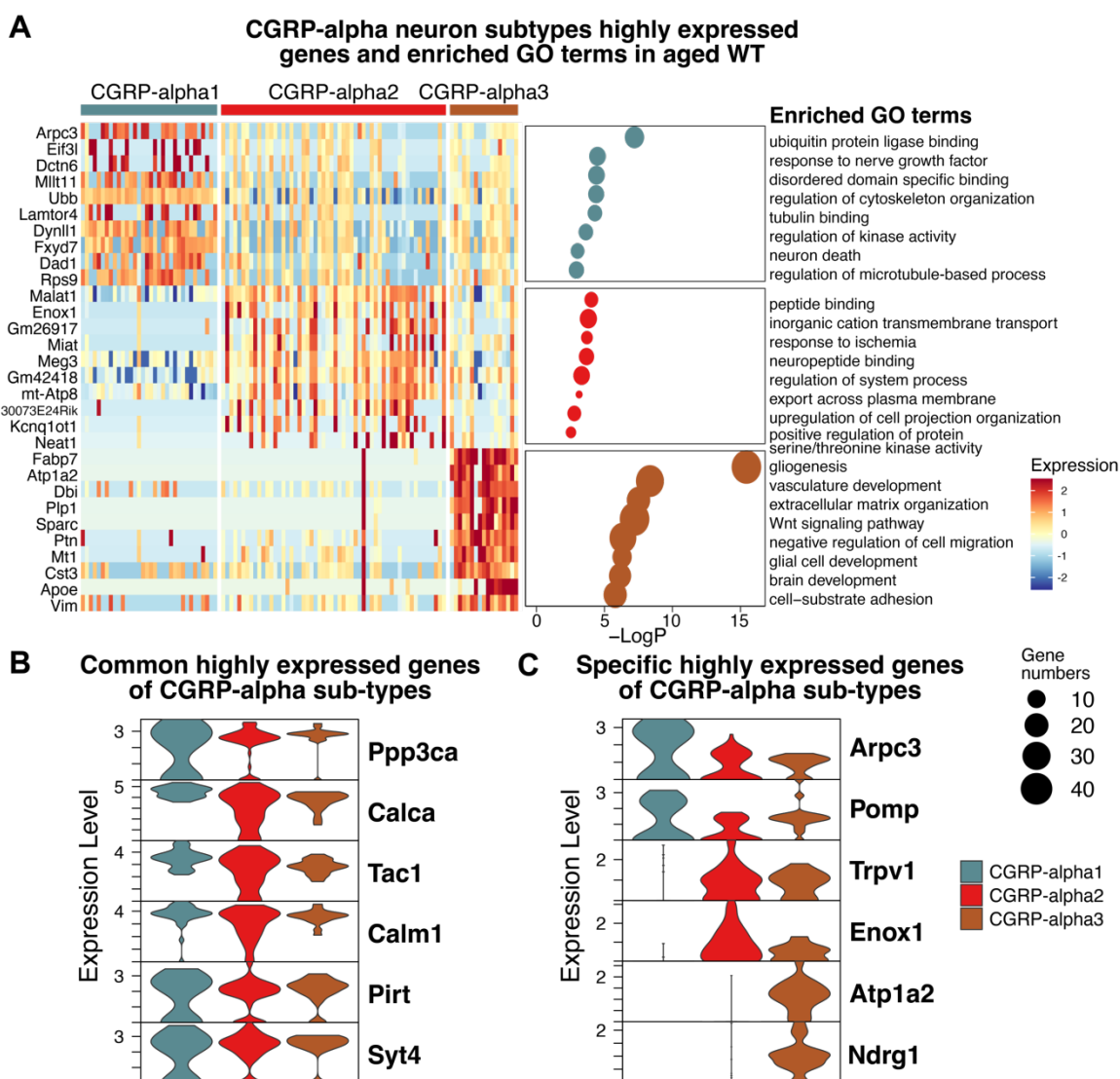


**Figure 25 Transcriptional profiles of CGRP-alpha neurons.** **A**, The heatmap (left) shows the marker genes of all CGRP-alpha neurons and their three subtypes. Red color represents the highest expression, and blue color represents the lowest expression. Gene names are shown at left, class names are shown above the heatmaps, colored by the same colors in UMAP, and the width of color bar above represents the cell numbers of each class. The bubble plot shows the top non-redundant enriched GO terms of each CGRP-alpha subtype. Y-axis designate GO terms, X-axis designate p-values (-logP). The dot sizes represent gene numbers which are associated with the respective GO term. The same color of each cell type in UMAP is used in bubble plots. **B**, Violin plots show the expression of selected CGRP-alpha common marker genes Ppp3ca, Calca, Tac1, Calm1, Pirt, and Syt4. **C**, Violin plots show the expression of CGRP-alpha1 neuron marker genes Arpc3 and Pomp, CGRP-alpha2 neurons marker genes Malat1 and Enox1, CGRP-alpha3 neuron marker genes Atp1a2 and Ndrgr1.

To further clarify the transcriptional differences among the three CGRP-alpha subtypes, we examined the expression of selected sensory neuron gene sets. These sets included ion channels, transcription factors, G-protein-coupled receptors (GPCRs), transient receptor potential (TRP) family members, neurotransmitters, neurotransmitter receptors, and neuropeptides. The heatmap and corresponding pie-chart results displayed increased expression of various ion channel genes in

## RESULTS

CGRP- $\alpha$ 2 neurons compared to CGRP- $\alpha$ 1 and CGRP- $\alpha$ 3 neurons (Figure 26 A, C). These genes included potassium voltage-gated channel genes *Kcna4*, *Kcnn2*, and *Kcng3* for action potential regulation and neurotransmitter release [201]. We also observed higher expression of TRP family member genes, including *Trpv1* and *Trpm8* responsible for nociception and inflammatory pain signaling [200]. GPCR genes such as G protein-coupled receptor 26 (*Gpr26*) and adhesion G protein-coupled receptor G3 (*Adgrg3*) showed increased expression as well, responsible for inter cellular signaling and neurotransmitter release [202, 203].

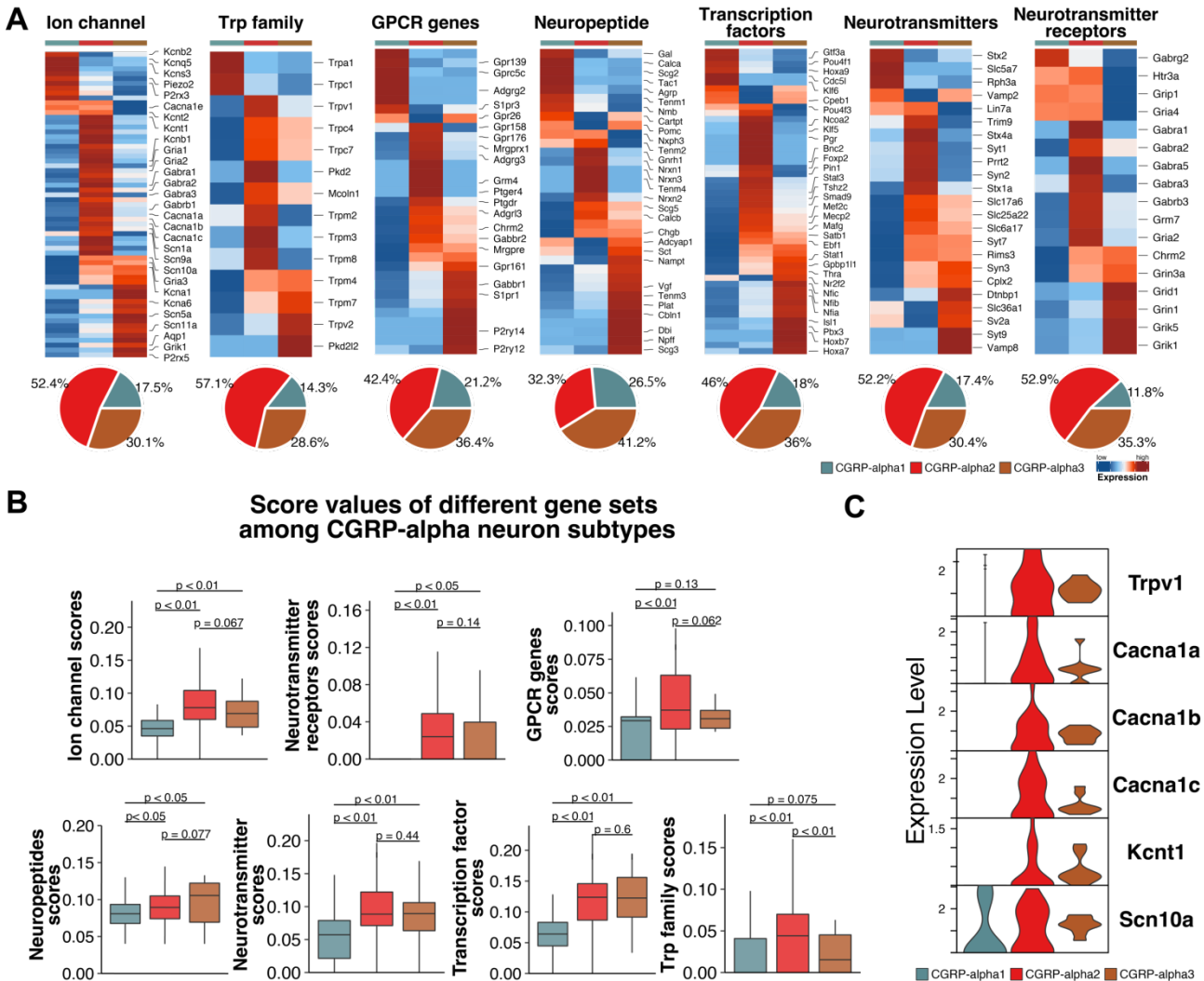


**Figure 26 Transcriptome differences among CGRP- $\alpha$  neurons.** **A**, Heatmaps display the average expression levels of several gene sets in CGRP- $\alpha$  neurons of aged WT DRGs. The key genes are listed on the left side of each heatmap, colors indicate the gene expression levels (red for highest and blue for lowest). **B**, Boxplots present the scoring values of the same gene sets for CGRP- $\alpha$  neuron subtypes in aged WT DRGs as shown in the heatmaps. The significances of changes are evaluated using the Wilcoxon test. **C**, Stacked violin plots illustrate the expression of selected genes in CGRP- $\alpha$  neuron subtypes of aged WT DRGs.

## RESULTS

To verify the changes in these gene sets, we computed score values by determining the average expression of genes in each set. The statistical analysis of score values corroborated the heatmap results: ion channel, TRP family, and GPCR genes' score values were significantly higher in CGRP-alpha2 neurons compared to CGRP-alpha1 and CGRP-alpha3 neurons. In contrast, the score values of neuropeptide genes, neuropeptide receptors, neurotransmitter genes, and transcription factor genes were significantly higher in CGRP-alpha2 and CGRP-alpha3 neurons compared to CGRP-alpha1 neurons (**Figure 26 B**). For more detailed information, we examined multiple canonical ion channel-associated genes. These genes included cation channel genes *Trpv1*, *Calcna1a*, *Calcna1b*, and *Calcna1c*; potassium channel gene *Kcnt1*; and sodium channel gene *Scn10a*. The stacked violin plots demonstrated that all these ion channel genes displayed higher expression in CGRP-alpha2 neurons (**Figure 26 C**).

### 3.3.4 Cell-cell interactions in aged WT DRG

Coordination of cellular activities is crucial for multicellular life and depends on cell-cell interactions between diverse cell types and tissues within an organism [133]. Consequently, the analysis and identification of intercellular interactions have become increasingly important for understating and predicting the potential cellular activities. Additionally, to our knowledge, the cell-cell interactions among DRG cell types have not been examined previously. Cell-cell interactions rely on intercellular signaling crosstalk by ligand-receptor pairs, by physical interaction via membrane proteins and by paracrine crosstalk by binding of secreted ligand to distant receptors (**Figure 27 A**). Since CGRP-alpha neurons were most abundant neuron subtypes in the aged DRG, to further understand and predict their potential functional differences and to investigate the potential intracellular signaling networks within aged DRGs, we performed putative cell-cell communication interaction analyses in an unbiased manner among CGRP-alpha subtypes and the various non-neuronal cell types within DRG using CellChat. CellChat algorithm predicts incoming (sender) and outgoing (receiver) interactions of cells by analyzing the relative likelihood of each cell type interacting with another cell type [182]. From total cell-cell interactions counts among all cell types within DRGs, we observed more cell-cell interactions of CGRP-alpha2 neurons with non-neuronal cell types compared to CGRP-alpha1 neurons, and there were no cell-cell interactions of CGRP-alpha3 neurons with non-neuronal cells (**Figure 27 B, C**). The cell-cell interaction analysis of CGRP-alpha2 neurons showed that the interaction counts of CGRP-alpha2 neurons with ECs, fibroblasts, and glial cells (SGC, nmSch and mSh) were higher than with other non-neuronal cell types. In CGRP-alpha1 neurons, the highest interaction count was observed between CGRP-alpha1 neurons and neutrophils (**Figure 27 C**).

## RESULTS

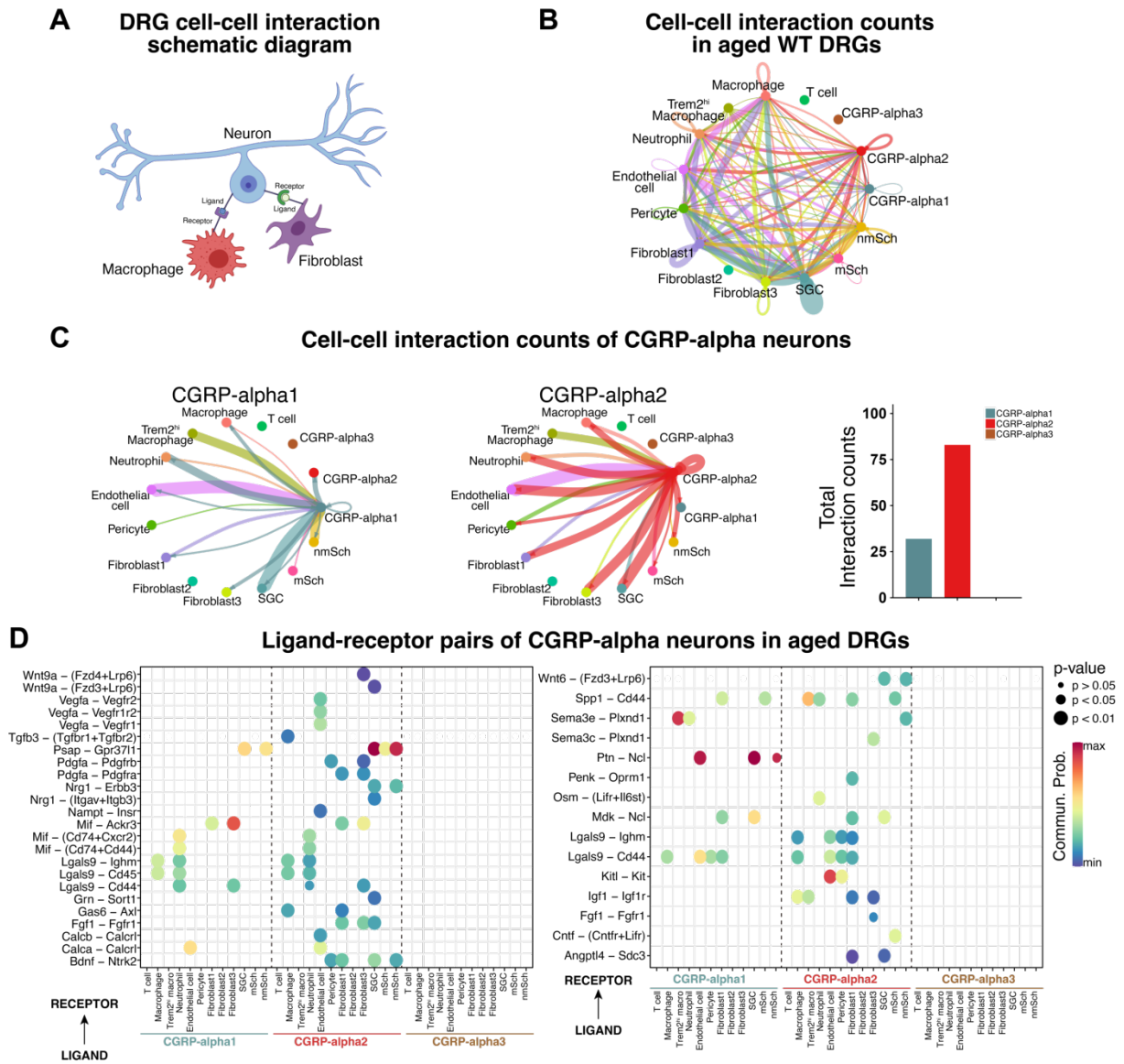


**Figure 27 Potential cell-cell communication network of CGRP-alpha subtypes with other DRG cell types.** **A**, Schematic of potential cell-cell communication interactions in aged DRGs between neurons, macrophages, and fibroblasts; **B**, Circle plot shows total cell-cell interaction counts between all aged WT DRG cell types. **C**, Circle plots show the ligand-receptor pair counts of CGRP-alpha1, CGRP-alpha2, CGRP-alpha3 neurons with non-neuronal cells in aged WT DRG. Each node represents one cell type, all nodes are colored by the same colors in UMAP, the line width between two nodes designates the ligand-receptor pair counts between two cell types. Bar plot on the right show the sum of the total interaction counts of CGRP-alpha1 and CGRP-alpha2, and similar interactions are not detected in CGRP-alpha3 neurons. **D**, Bubble plot of all significant ligand/receptor pair (left) and receptor/ligand pair (right) between corresponding CGRP-alpha neuron subtypes and other non-neuronal cells and vice-versa in aged WT DRG. The colors of the bubble represent the log-transformed expression levels of the ligand and receptors in each cell type, and the sizes of the bubbles indicate the significance of the interaction. P-values are computed using one-sided permutation test by CellChat.

Furthermore, the ligand-receptor interaction analyses were performed to construct the interaction network among CGRP-alpha subtypes and non-neuronal cell types in aged DRGs. We show that

## RESULTS

both outgoing and incoming ligand-receptor pairs were more abundant in CGRP-alpha2 neurons with non-neuronal cell types in aged DRGs compared to CGRP-alpha1 neurons (**Figure 27 D**). In the CGRP-alpha outgoing ligand-receptors, Bdnf-Ntrk2 ligand-receptor pair was detected between CGRP-alpha2 neurons and pericytes, fibroblasts, and glial cells. Since the upregulation of this ligand-receptor pair in DRGs has been reported to regulate synaptic excitability in inflammatory pain transmission [204], CGRP-alpha2 might be associated with inflammatory pain processing in DRGs. Calca/Calcb - calcitonin receptor-like (Calcrl) ligand-receptor pairs were detected in CGRP-alpha1 and CGRP-alpha2 neurons with ECs has been reported to activate the Gas/adenylyl cyclase/cAMP pathway [205]. The ligand-receptor pair Nrg1-ErbB3, which was detected in CGRP-alpha2 neurons with glial cells has been reported to be associated with nerve injury and regeneration [206]. This implies that CGRP-alpha2 neurons may associated with nerve injury and regeneration via interaction with glial cells in aged DRGs. Regarding the outgoing or incoming ligand-receptor pairs of CGRP-alpha neurons, the Wingless-related integration site signaling (Wnt) pathway Wnt6-(Fzd+Lrp6), was expressed between CGRP-alpha2 neurons with SGC and nmSch (**Figure 30 D**). This pathway had been reported to be associated with sensory neuronal pain sensitivity regulation via the noncanonical calcium pathway [207].

In summary, these results demonstrated CGRP-alpha1, CGRP-alpha2, and CGRP-alpha3 neurons were different in their transcriptomes and putative functions in aged DRGs. Among three subtypes, CGRP-alpha2 neurons were predicted to contribute more to cell-cell interactions than the other CGRP-alpha neurons.

### 3.4 Molecular changes of DRGs during atherosclerosis progression

#### 3.4.1 Changes of Apoe expression and Apoe-associated genes

As described above, we identified and characterized the cell types and their transcriptional profiles in aged WT DRGs. However, the differences in DRGs between aged WT and aged Apoe<sup>-/-</sup> mice remained unclear. Since the Apoe gene has a robust genetic link to cardiovascular disease, identifying Apoe-associated changes may help to understand the transcriptional changes in DRGs between aged WT and aged Apoe<sup>-/-</sup> mice. For this purpose, we examined the expression of the Apoe gene in both aged WT and Apoe<sup>-/-</sup> DRGs. In aged WT DRGs, the Apoe gene was expressed in immune cells, glial cells, and at a lower level in vascular cells and fibroblasts. As expected, no expression of the Apoe gene was observed in aged Apoe<sup>-/-</sup> DRGs (**Figure 31 A left**).

## RESULTS

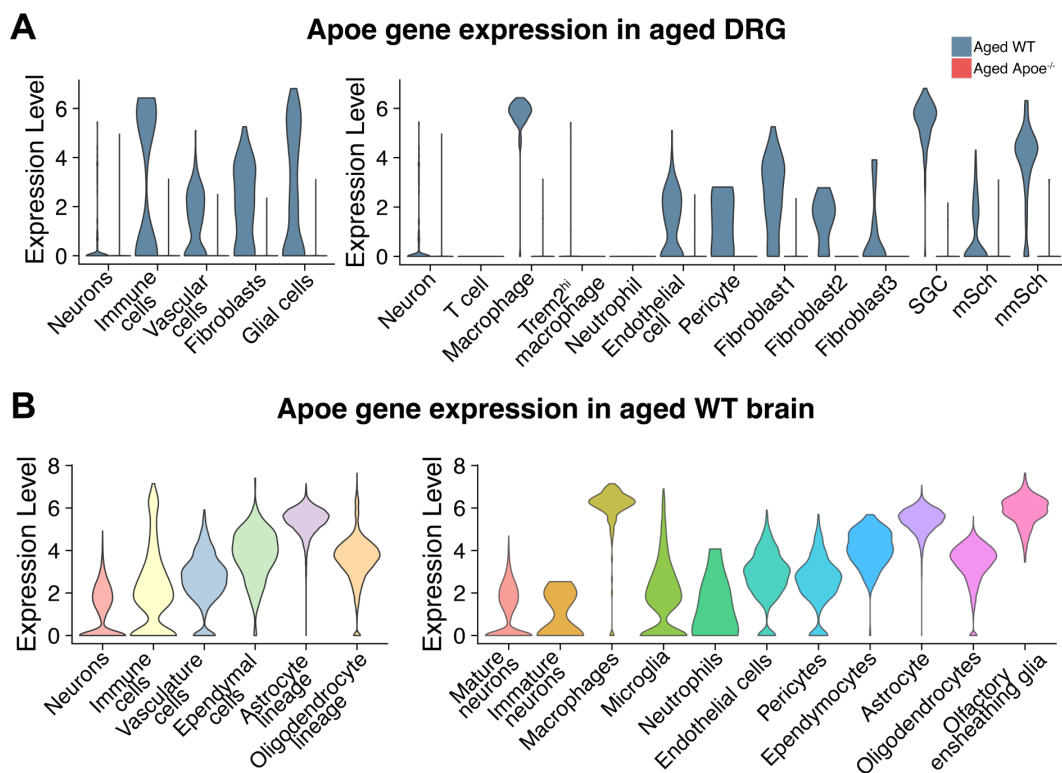


**Figure 28 Comparison of Apoe gene expression at single-cell levels from aged WT DRGs and aged WT brain.** **A**, Violin plots show Apoe gene expression patterns in aged DRG classes (left) and in each cell type (right) in aged WT versus Apoe<sup>-/-</sup>. **B**, Violin plots show Apoe gene expression patterns of aged WT brain classes (left) and in cell types (right) (GSE129788) [185]. The width of the violin plots represents the abundance of cell numbers of the class or cell type, and the violins are colored by groups.

To investigate the expression of the Apoe gene in brain cells, we examined Apoe gene expression in aged WT brain using published data (GSE129788) [185]. Similar cell types in DRGs were defined in brain scRNA-seq datasets using different names. We observed that the expression of the Apoe gene was higher in glial cells and lower in neuronal cells, other immune cells, and vascular cells (**Figure 31 B left**). Apoe was highly expressed in macrophages and SGC in WT DRGs (**Figure 31 A right**), as well as in macrophages and olfactory ensheathing glial cells (**Figure 31 B right**). These comparisons demonstrated similar Apoe expression patterns in aged DRG and brain.

To determine the role of Apoe in aged WT DRGs and to identify the genes which were altered in WT compared to Apoe<sup>-/-</sup> DRGs, correlation coefficients between these genes and Apoe in WT DRG were computed. The results demonstrated that, in aged WT DRG, the SGC marker gene *Fabp7* exhibited the highest correlation coefficient with the Apoe gene. Additionally, macrophages highly expressed genes like *Mmd2*, *Cx3cr1* and lipid metabolism-associated genes (*Apoc1*, *Apod*) displayed positive correlations with the Apoe gene. In contrast, ion channel genes, including *Trpv1*, and Trem2<sup>hi</sup> macrophage marker genes (*Cd9*, *Spp1*) were found to be negatively associated with Apoe gene in aged WT DRG (**Figure 29 A**).

## RESULTS

To determine the origin of changes observed in aged WT versus *Apoe*<sup>-/-</sup>, the score values of *Apoe* positively- or negatively-associated genes were calculated. The results indicated that *Apoe* positively-associated genes were significantly decreased in aged WT compared to *Apoe*<sup>-/-</sup> DRGs, while no significant changes were observed for negatively-associated genes (**Figure 29 A**). These results indicated that the changes in aged WT versus *Apoe*<sup>-/-</sup> DRGs might be attributed to *Apoe* positively-associated genes. To further understand the potential functions of the regulated genes, an enrichment analysis was conducted using *Apoe* gene positively- or negatively-associated genes. Bar plots revealed that *Apoe* gene positively-associated genes were related to the functions such as glial cell differentiation, regulation of glial migration, oxidoreductase activity and regulation of ion transport (**Figure 29 C**). In summary, positively-associated genes appeared to contribute at a higher proportion compared to lower expressed changes in aged *Apoe*<sup>-/-</sup> DRGs. The affected functions potentially included glial cell differentiation, ion transport, and oxidoreductase activity.

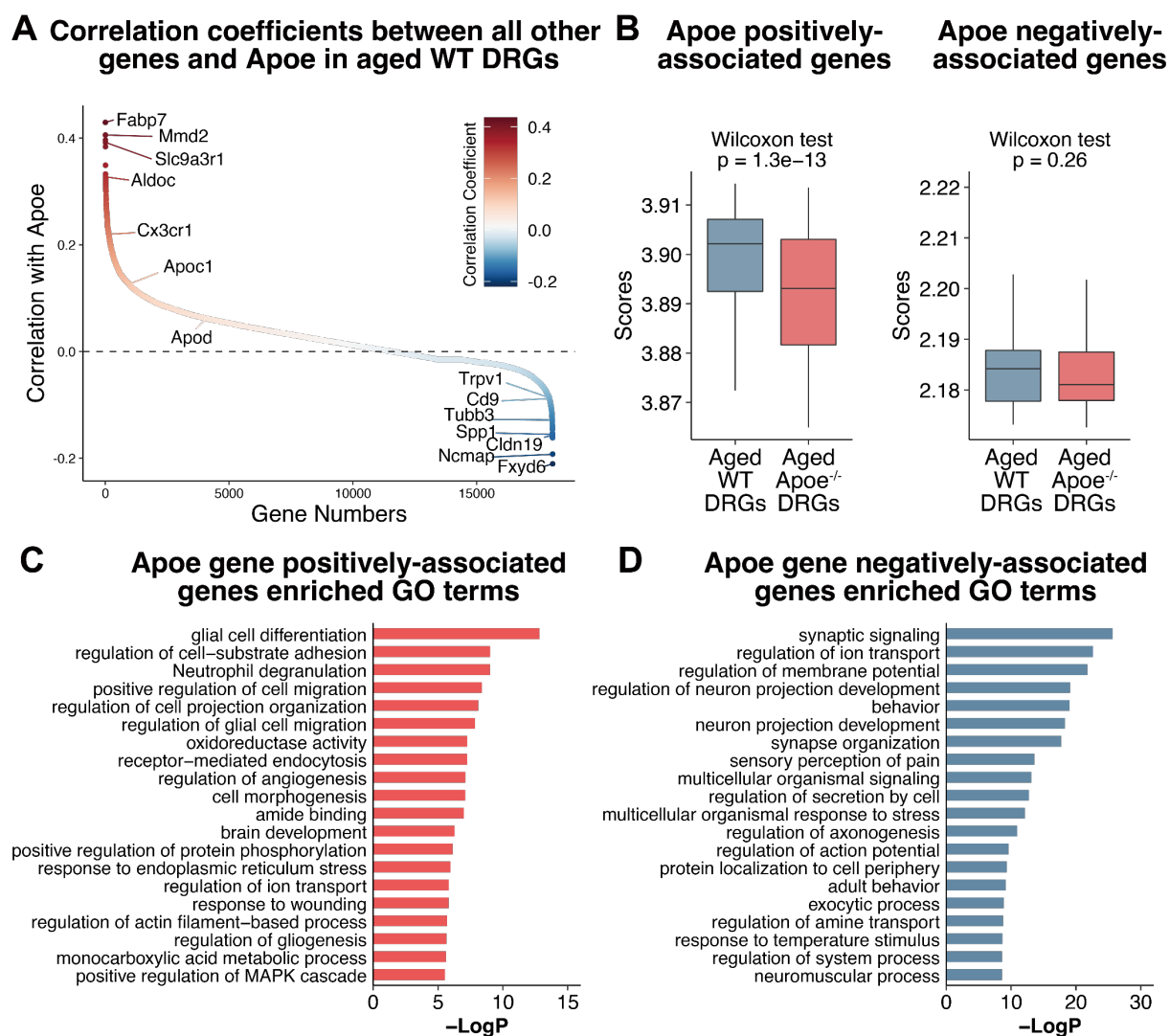


**Figure 29 Apoe positively- and negatively-associated genes in aged WT and *Apoe*<sup>-/-</sup> DRGs. A,** Dot plot show pairwise Pearson correlation of *Apoe* gene with all other genes in aged WT DRGs. Each dot designate

## RESULTS

one gene. Color of dot represents the degree of correlation coefficient. **B**, Box plots show the score values of Apoe gene positively- and negatively-associated genes in aged WT versus Apoe<sup>-/-</sup> DRGs. The significances of changes are checked using Wilcoxon rank sum test. **C**, Bar plots show the top 20 non-redundant enriched GO terms of Apoe gene positively-associated genes. **D**, Bar plots show the top 20 non-redundant enriched GO terms of Apoe gene negatively-associated genes. Ranked by negative log p-value.

### 3.4.2 Transcriptome differences in aged WT versus Apoe<sup>-/-</sup> DRGs

As demonstrated above, Apoe positively-associated genes exhibited a significant decrease in aged Apoe<sup>-/-</sup> DRGs. To further explore the transcriptional differences between the two genotypes, a comparative analysis of gene expression was conducted between aged WT and Apoe<sup>-/-</sup> DRGs. For this purpose, GSEA GO enrichment analysis was performed using all regulated genes (Log<sub>2</sub>FC > 0.25) in all DRGs between two groups. GSEA is a bulk-seq and scRNA-seq data analytical technique, to assess if a predetermined collection of genes demonstrates significant changes between a pair of biological conditions. The enrichment network map revealed that different pathway clusters were enriched in aged WT versus Apoe<sup>-/-</sup> DRGs separately. For example, the axon growth associated pathways were grouped into a cluster and were enriched in Apoe<sup>-/-</sup> DRGs, indicating the expression of axon growth-associated genes may be increased in Apoe<sup>-/-</sup> DRGs compared to WT DRGs. We also observed additional functional clusters, such as ribosomal subunits, neurotransmitters, and adaptive immune responses, to be enriched in aged Apoe<sup>-/-</sup> DRGs compared to WT DRGs. The functional clusters, such as dendritic spine maintenance, endothelial cells related functions, and vessel morphogenesis, to be enriched in aged WT DRGs compared to Apoe<sup>-/-</sup> DRGs (**Figure 30 A**). Upon examining the specific pathways in the comparison in aged WT DRGs versus Apoe<sup>-/-</sup> DRGs, such as pathway axon (GO:0030424), a negative normalized enrichment score (NES) value indicated higher expression in aged Apoe<sup>-/-</sup> DRGs, and the ranked genes were clustered in the aged Apoe<sup>-/-</sup> side (**Figure 30 C**). Consequently, comparison of the enrichment score in aged WT or Apoe<sup>-/-</sup> DRGs revealed that the pathways related to stimulus response, epithelial cell proliferation, blood vessel morphogenesis, tubular development, and transporter activity were enriched in aged WT DRGs (**Figure 30 B**). On the other hand, pathways like peptide biosynthetic processes, axon components, exocytosis, adaptive immune response, and ribosome constituents were enriched in aged Apoe<sup>-/-</sup> DRGs (**Figure 30 C**). These results highlight the potential functional differences between aged WT and aged Apoe<sup>-/-</sup> DRGs.

## RESULTS

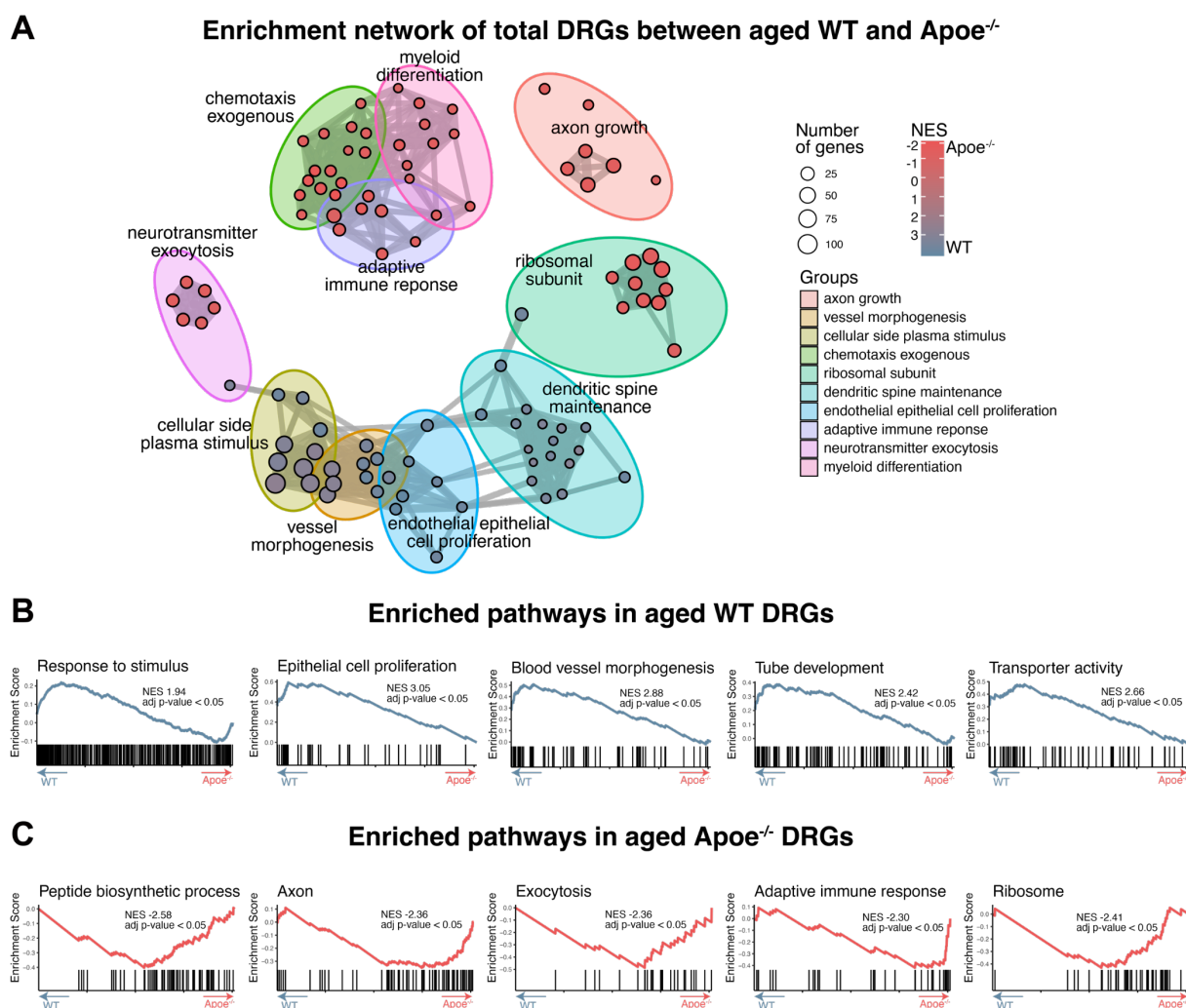


**Figure 30** GSEA enrichment analysis of aged WT and *Apoe*<sup>-/-</sup> DRG higher expressed genes. **A**, Enrichment network map of total DRG GSEAs show significantly altered pathways in aged WT versus *Apoe*<sup>-/-</sup> mice. All enriched pathways are combined and unbiasedly grouped into 10 subgroups based on expression similarities. Each dot represents one pathway, grouped pathways are circled with a distinct color. Size of vertices indicate the number of genes within each pathway. Color scale represent NES based on higher or lower expressed enrichment score in WT vs *Apoe*<sup>-/-</sup> DRGs. **B,C**, Graphical view of the enrichment plots for the key gene sets in WT and *Apoe*<sup>-/-</sup> DRGs. Positive NES value and blue arrow indicate the pathways are enriched in WT DRGs, negative NES value and red arrow indicate the pathways which are enriched in aged *Apoe*<sup>-/-</sup> DRGs. NES, normalized enrichment score; adj p-value, adjusted p-value using Benjamini-Hochberg correction.

To further investigate the changes between aged WT and *Apoe*<sup>-/-</sup> DRGs, DEGs were calculated for both aged WT and aged *Apoe*<sup>-/-</sup> DRGs. The volcano plot (**Figure 31 A, Appendix Table2**) revealed a total of 72 genes, including *Apoe*, GTP-binding gene involved in protein trafficking, ADP-ribosylation factor-like 1 (*Arl1*), [208] and AD associated gene collagen type IV alpha 1 (*Col4a1*) [209] were significantly higher expressed in aged WT DRGs. Conversely, 58 genes were significantly higher expressed in aged *Apoe*<sup>-/-</sup> DRGs, including cathepsin B gene, *Ctsb*, which was reported to be higher expressed in APOE4 knock out microglia [210], and ribosomal protein gene ribosomal protein L17 (*Rpl17*), which was reported as a vascular growth inhibitor [211].

## RESULTS

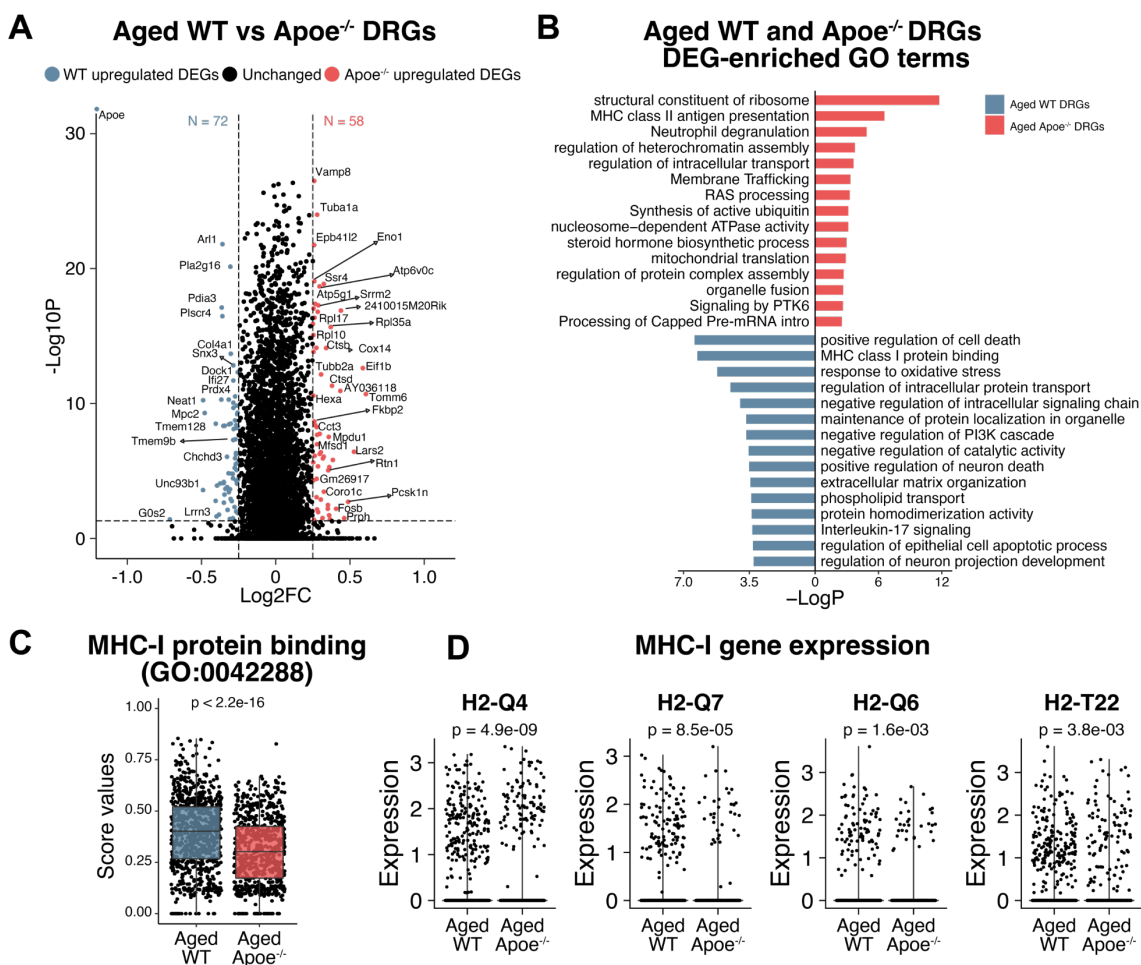


**Figure 31 Transcriptional differences between total aged WT and Apoe<sup>-/-</sup> DRGs. A**, Volcano plot depicts DEGs in aged WT versus Apoe<sup>-/-</sup> DRGs. Genes with a log<sub>2</sub>FC value > 0.25 and adjusted p-value less than 0.05 are considered as significant DEGs, red color represents the gene which is higher expressed in aged Apoe<sup>-/-</sup> DRGs, blue color represents the gene which is higher expressed in aged WT DRGs. **B**, Bar plots show the top ten non-redundant enriched GO terms of aged WT and Apoe<sup>-/-</sup> DRG significantly higher expressed genes, the GO terms are ranked by negative log p-value from highest to lowest. **C**, Box plot show score values of MHC class I protein binding-associated genes. **D**, Violin plots show the expression of MHC class I genes in aged DRGs. The significances of changes are calculated using the Wilcoxon rank sum test and adjusted for multiple comparisons using Bonferroni's correction.

To identify potential functions of these DEGs in aged WT and Apoe<sup>-/-</sup> DRGs, GO enrichment analysis was performed using DEGs from both samples (**Figure 31 B**). The bar plot demonstrated that GO terms associated with ribosomal pathways, MHC class II antigen presentation, neutrophil degranulation, and intracellular transport-related pathways were enriched in aged Apoe<sup>-/-</sup> DRGs. In aged WT DRGs, enriched GO terms included cell death-associated pathways, intracellular signal-related pathways, and MHC class I protein binding. MHC-I expression in WT DRG was in line with previous study on brain neurons in an AD model [212]. To further examine the importance of these potential biological functions, score values for MHC class I (GO:0042288) protein binding terms were

## RESULTS

calculated. Box plots revealed that MHC class I protein binding score values were significantly decreased in aged Apoe<sup>-/-</sup> DRGs including downregulation of several MHC class I genes like H2-Q4, H2-Q7, H2-Q6, H2-T22 (**Figure 34 C, D**). These findings demonstrated the differential gene expression profile between total aged WT and Apoe<sup>-/-</sup> DRGs.

### 3.4.3 Transcriptome changes of each cell type in aged WT versus Apoe<sup>-/-</sup> DRGs

The transcriptional differences in total aged WT versus Apoe<sup>-/-</sup> DRGs were examined above. To understand the underlying causes of the transcriptional differences between total aged WT versus Apoe<sup>-/-</sup> DRGs, we further analyzed each DRG cell type. We obtained a total of 735 cells in WT DRG and 828 cells in Apoe<sup>-/-</sup> DRGs. Firstly, the main cell classes were examined. We did not include the cell number in the figure because of the very limited number of cells. In aged WT versus Apoe<sup>-/-</sup> DRGs, the percentage of neurons and immune cells increased from 10.7% to 15% and from 16.5% to 21.6% respectively (**Figure 32 A**). Correspondingly, the absolute numbers for these cell types also increased from 89 to 110 for neurons and from 137 to 159 for immune cells in WT versus Apoe<sup>-/-</sup> DRGs. Meanwhile, the percentages of vascular cells in total DRG cells decreased from 20.7% to 15.3%, the percentages of glial cells in total DRG cells decreased from 41.8% to 36.7% in aged Apoe<sup>-/-</sup> DRGs compared to aged WT DRGs (**Figure 32 A**). Comparison of different cell types in aged DRGs revealed increased percentages of neurons, and Trem2<sup>hi</sup> macrophages in aged Apoe<sup>-/-</sup> DRGs compared to aged WT DRGs. Conversely, the percentages of ECs in total DRG cells were decreased, while glial cells showed a tendency to decrease in aged Apoe<sup>-/-</sup> mice (**Figure 32 B**). The observed alterations indicated an increased percentages of neurons and immune cells in aged Apoe<sup>-/-</sup> DRGs compared to aged WT DRGs. Higher immune cells in aged Apoe<sup>-/-</sup> DRG supported the observation on immune cells infiltration during atherosclerosis as shown by FACS analysis (**Figure 13**) as well as by immunostaining of DRG sections [52]. These findings also suggested a restructuring of the aged Apoe<sup>-/-</sup> DRGs during atherosclerosis progression.

## RESULTS

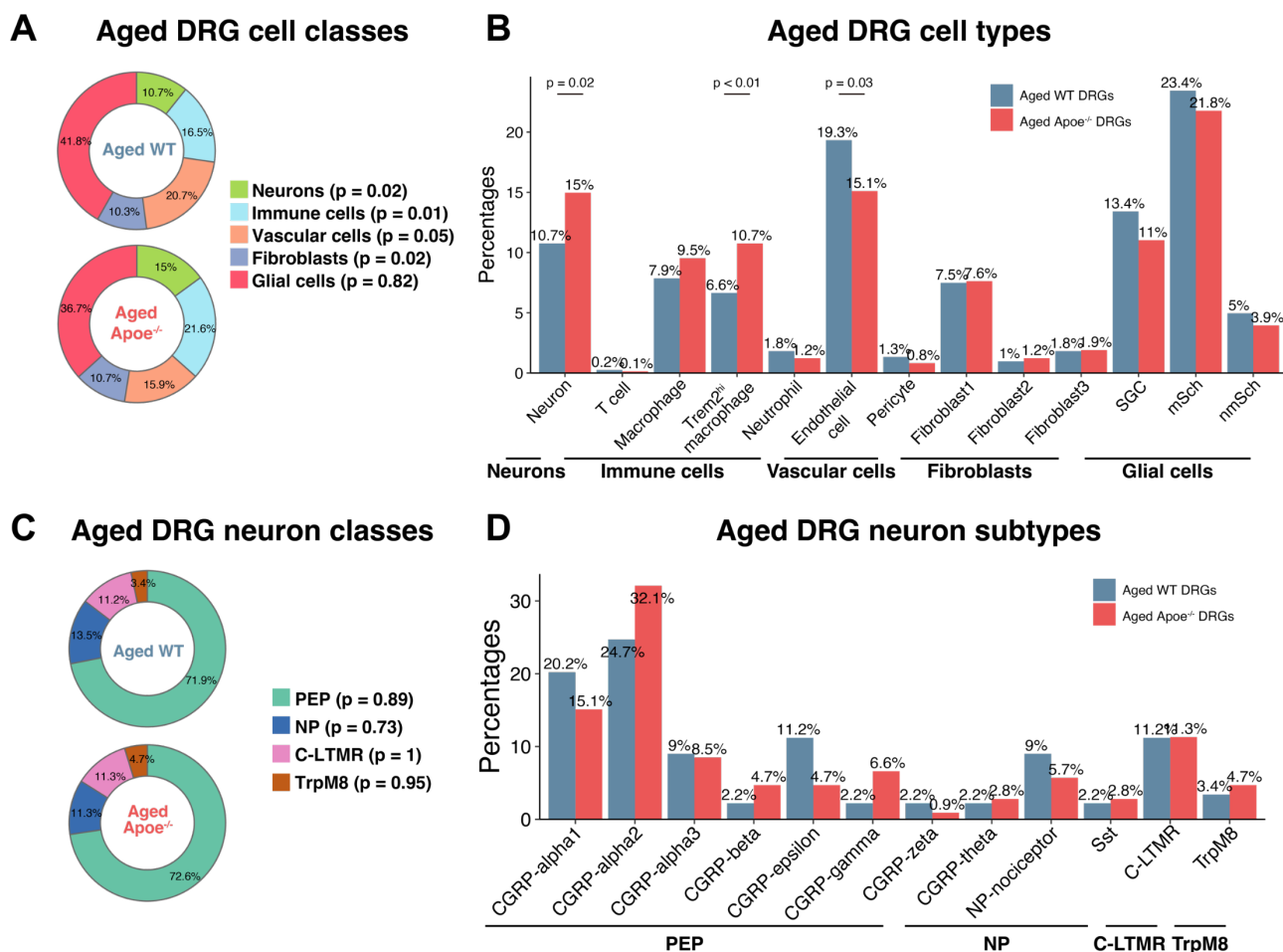


**Figure 32** The cell composition altered in aged WT versus *Apoe*<sup>-/-</sup> DRGs. **A**, Donut plots show the percentages of cell classes in aged WT and *Apoe*<sup>-/-</sup> DRGs. **B**, Bar plots show percentages of all cell types in aged WT and *Apoe*<sup>-/-</sup> DRGs. **C**, Donut plots show the percentages of neuron subtypes in aged WT and *Apoe*<sup>-/-</sup> DRGs. **D**, Bar plots show the percentages of neuron subtypes in aged WT and *Apoe*<sup>-/-</sup> DRGs. In bar plots, red color represents aged *Apoe*<sup>-/-</sup> and blue color represents aged WT mice, the numbers above the bar designate percentages. The significance in WT versus *Apoe*<sup>-/-</sup> are analyzed using Pearson's Chi-squared test and adjusted using Benjamini-Hochberg correction.

In aged DRGs, we obtained a total of 89 aged WT DRG neurons and 110 aged *Apoe*<sup>-/-</sup> DRG neurons. As the subclustering results of aged DRG neurons demonstrated, neurons in aged DRGs were categorized into four major classes and twelve subtypes (**Figure 22**). To further understand the increased percentages of total neurons in aged *Apoe*<sup>-/-</sup> DRG compared to WT DRG, we examined the changes in all neuron classes and subtypes. Donut plots revealed no apparent alterations in neuron classes between aged WT versus *Apoe*<sup>-/-</sup> (**Figure 32 C**). However, the cell numbers were increased from 22 in aged WT DRGs to 34 in aged *Apoe*<sup>-/-</sup> DRGs, the percentage of CGRP-alpha2 neurons rose from 24.7% in aged WT DRGs to 32.1% in aged *Apoe*<sup>-/-</sup> DRGs. Although the percentages of CGRP-alpha1, CGRP-epsilon, and NP-nociceptor neurons showed a tendency to decrease in aged *Apoe*<sup>-/-</sup> DRGs (**Figure 32 D**). These changes suggested the potential restructuring of neuron subtypes within the DRG during atherosclerosis progression.

## RESULTS

We next sought to understand the potential functional and transcriptional changes in each aged DRG cell type. To accomplish this, we calculated significant DEGs ( $\log_2FC > 0.25$  & adjusted p-value  $< 0.05$ ) for each cell type and all neuron subtypes in aged WT versus *Apoe*<sup>-/-</sup> DRGs. In the divergent bar plot of all aged DRG cell types, the highest number of DEGs was observed in mSch, with 239 DEGs in aged *Apoe*<sup>-/-</sup> mSch and 279 DEGs in aged WT mSch. Among the non-neuronal cells, more significant DEGs were observed in macrophages, endothelial cells (ECs), and fibroblast1 compared to other non-neuronal cells (**Figure 33 A**). The changes in gene expression profiles of neurons and macrophages were consistent with the changes in percentage in aged WT versus *Apoe*<sup>-/-</sup> mice as shown above (**Figure 32**). Among neuron subtypes, there were 104 DEGs in WT CGRP-alpha2 neurons, however only 4 DEGs were observed in *Apoe*<sup>-/-</sup> CGRP-alpha2 neurons, and very few DEGs were found in all other neuron subtypes (**Figure 33 B, Appendix Table 3**).

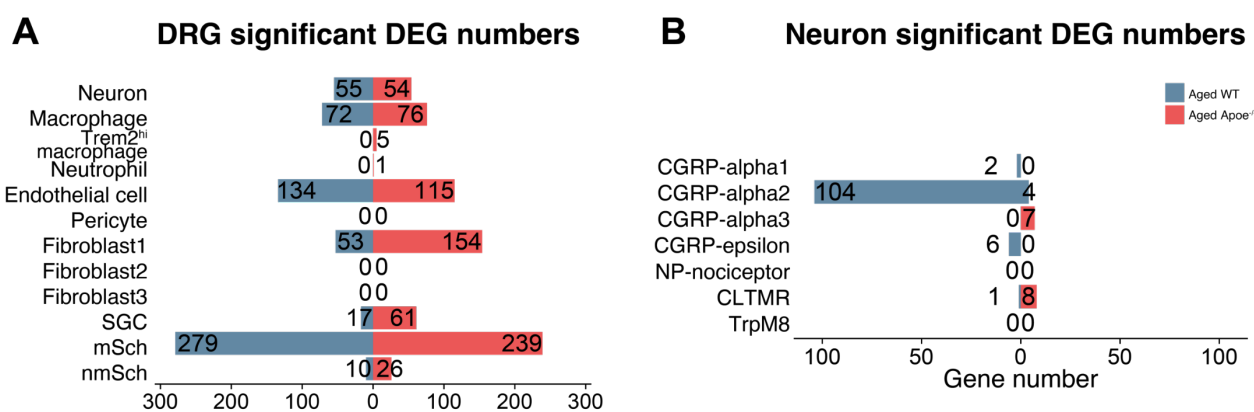


**Figure 33 Significant DEGs of aged WT and *Apoe*<sup>-/-</sup> DRG cell types.** **A**, Divergent bar plots shows significant DEGs ( $\log_2FC > 0.25$  & adjusted p-value  $< 0.05$ ) of each cell type in aged WT versus *Apoe*<sup>-/-</sup> mice. **C**, Divergent bar plots show DEGs of each neuron subtype in aged WT versus *Apoe*<sup>-/-</sup> mice. **D**, Divergent bar plots show all regulated genes of all neuron subtypes in aged WT versus *Apoe*<sup>-/-</sup> mice. The length of the bars correlate with the numbers of the significant DEGs of each cell type, the blue color designate the DEGs genes which are higher expressed in aged WT DRGs, and the red color designate the DEGs genes which are higher expressed in aged *Apoe*<sup>-/-</sup> DRGs of each cell type. The significance of DEGs are calculated using likelihood-ratio test and are adjusted using Benjamini-Hochberg correction.

Upon examining the DEGs, we also identified the enriched GO terms for each cell type using DEGs in aged WT versus *Apoe*<sup>-/-</sup> DRGs. In aged *Apoe*<sup>-/-</sup> macrophage, the TGF-beta signaling pathway, which has been observed to be enriched in brain microglia [213] and reported as essential for microglial activation [214], was highly enriched. Additionally, the pathway for negative regulation of glial cell proliferation was also notably enriched. These results suggest potential functional interactions between macrophages and glial cells in aged *Apoe*<sup>-/-</sup> mice (**Figure 34 A**). In ECs, bar plots revealed that tricarboxylic acid (TCA) cycle-associated pathways and the neurotransmitter dopamine biosynthetic pathway were enriched in aged WT DRGs. In contrast, several DNA/RNA

## RESULTS

metabolism pathways were enriched in aged *Apoe*<sup>-/-</sup> DRGs (**Figure 34 B**). In fibroblast1, a greater number of pathways were enriched in aged *Apoe*<sup>-/-</sup> versus WT DRGs, including cellular response to stress, MAPK3 activation, GTPase binding, and G protein activation. These pathways may be associated with various cellular processes such as apoptosis, stress responses, and endoplasmic reticulum activities (**Figure 34 C**). In mSch, similar pathways to those in ECs were altered, with TCA cycle-associated pathways enriched in aged WT DRGs, ribosome and mitochondria-associated pathways enriched in aged *Apoe*<sup>-/-</sup> DRGs (**Figure 37D**). For non-neuronal cells, no major enriched pathways were identified in aged WT versus *Apoe*<sup>-/-</sup> DRGs. Based on these pathway enrichment analyses, we hypothesized that the functions of the selected cell types might be altered in aged WT and *Apoe*<sup>-/-</sup> mice.

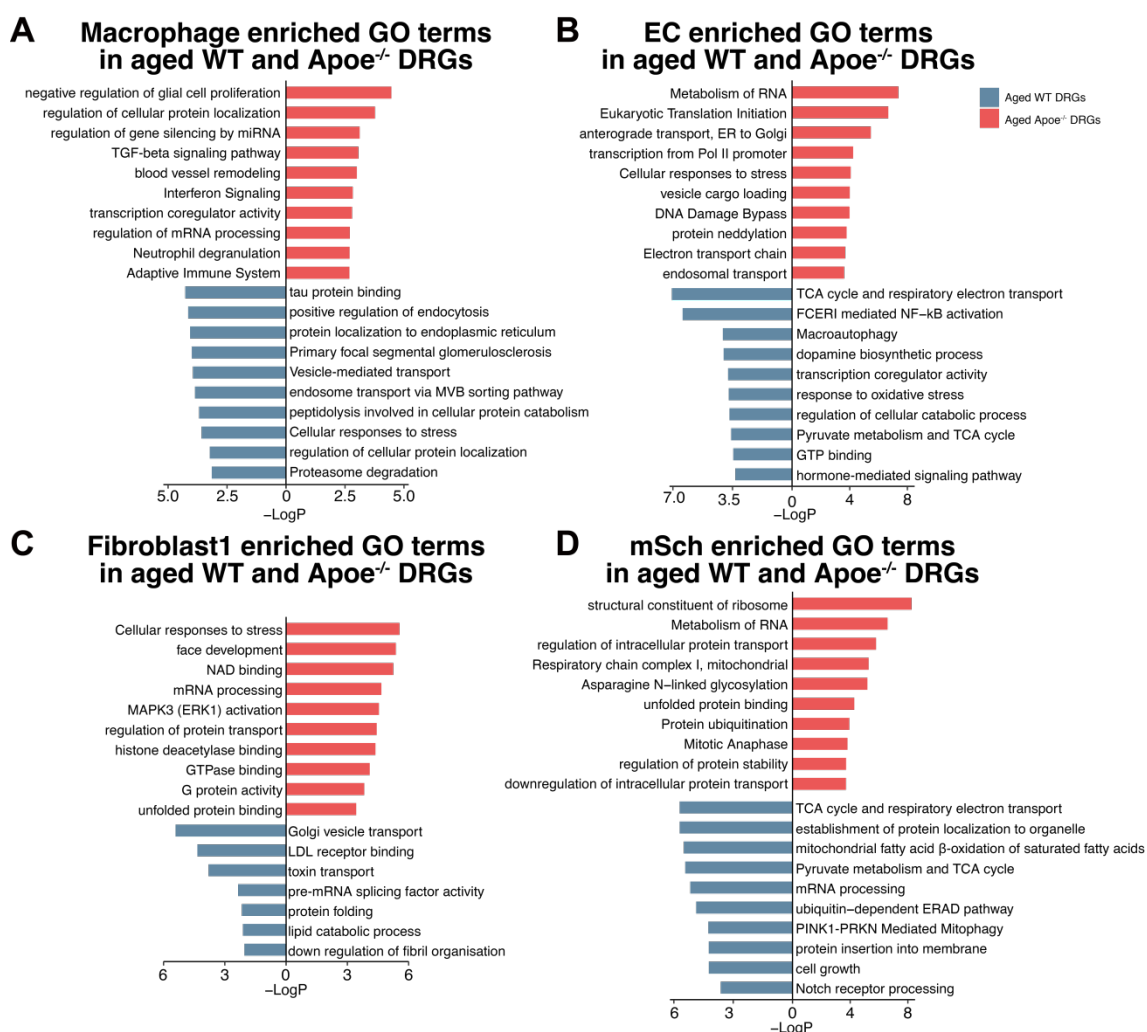


**Figure 34 Enriched GO terms of each cluster in WT and *Apoe*<sup>-/-</sup> DRGs.** Bar plots show the top non-redundant enriched GO terms of aged WT and *Apoe*<sup>-/-</sup> DEGs in different cell types: macrophage (**A**), ECs (**B**), fibroblast1 (**C**), and mSchs (**D**). Y-axis designate GO terms. X-axis numbers designate negative log p-values (-logP), and the lengths of the bars represent the negative log p-values (-logP) of enriched GO terms.

## RESULTS

### 3.4.4 CGRP-alpha2 neuron transcriptional profiles in aged WT versus *Apoe*<sup>-/-</sup> DRGs

The percentages of CGRP-alpha2 neurons were observed to increase in aged *Apoe*<sup>-/-</sup> DRGs. This finding prompted an investigation into the alterations of these neurons during the progression of atherosclerosis. To achieve this objective, we conducted GSEA on CGRP-alpha2 neurons in aged WT and *Apoe*<sup>-/-</sup> mice. Initially, all enriched pathways of CGRP-alpha2 neurons in aged WT and *Apoe*<sup>-/-</sup> mice were grouped into several clusters based on functional similarity within the enrichment network. A greater number of significantly enriched pathways were observed in aged *Apoe*<sup>-/-</sup> mice (in red) compared to WT mice (in blue) (**Figure 36 A**). To further identify the enriched pathways of CGRP-alpha2 neurons, we present several selected pathways in enrichment plots, along with their potential functions. These pathways are enriched in aged WT CGRP-alpha2 including cation binding (GO:0043169), lipid localization (GO:0010876) and protein kinase activity (GO:0004672) (**Figure 36 B**). The *Apoe* gene was associated with the pathways in CGRP-alpha2 neurons that included peptide biosynthetic process (GO:0043043), which had previously been reported to be associated with immune cells in inflammatory diseases [74], ATP synthesis-coupled electron transport (GO:0042773) which had been associated with intracellular energy metabolism [215], and myelin sheath (GO:0043209), which had been associated with glial cell activity [216] (**Figure 36 C**).

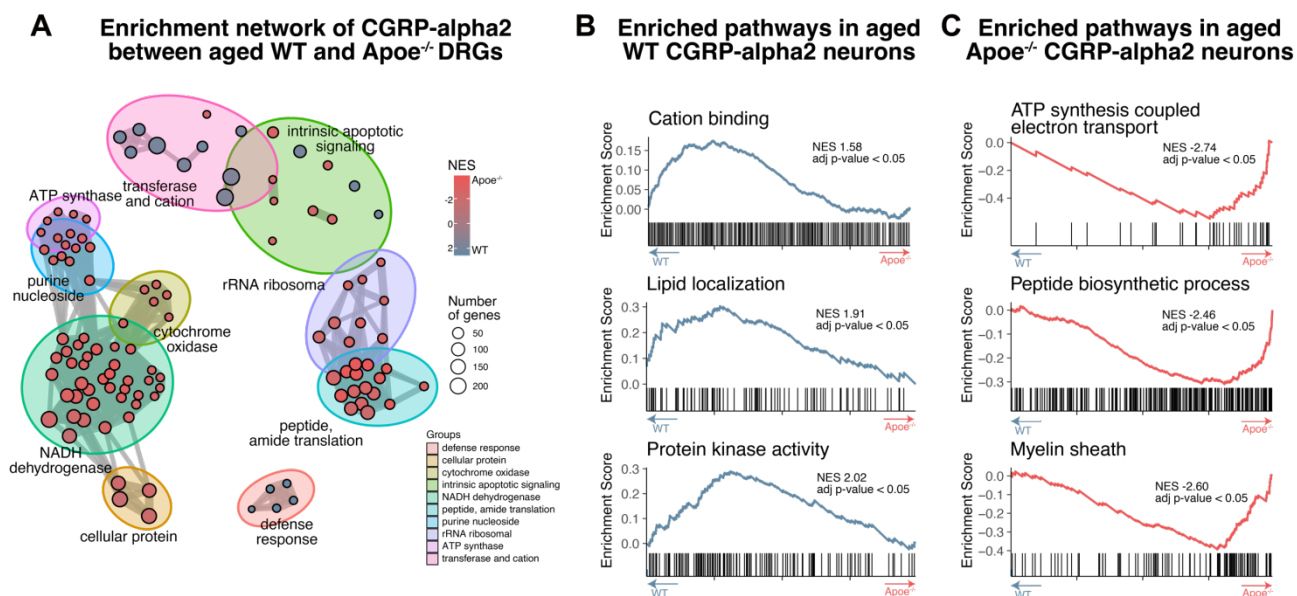


**Figure 35 GSEA enrichment analysis of aged WT versus *Apoe*<sup>-/-</sup> CGRP-alpha2 neurons.** **A**, Enrichment network map of CGRP-alpha2 neurons GSEA shows significantly altered pathways in aged WT versus *Apoe*<sup>-/-</sup> DRGs. All enriched pathways are combined and unbiasedly grouped into 10 subgroups based on expression similarities. Each group is circled with a distinct color. Sizes of vertices indicate the number of genes within each pathway. Color scale represents NES based on up or down altered enrichment score in WT vs *Apoe*<sup>-/-</sup> DRGs. **B,C**, Graphical view of the enrichment plots for the key gene sets in WT and *Apoe*<sup>-/-</sup> CGRP-alpha2 neurons. Positive NES value and blue arrow indicate the pathways that are enriched in WT CGRP-alpha2 neurons, negative NES value and red arrow indicate the pathways that are enriched in aged *Apoe*<sup>-/-</sup> CGRP-

## RESULTS

alpha2 neurons. Significances are determined using rank-sum test and are adjusted using Benjamini-Hochberg correction performed by ClusterProfiler. NES, normalized enrichment score; adj p-value, adjusted p-value using Benjamini-Hochberg correction.

### 3.4.5 Cell-cell interactions in aged WT versus Apoe<sup>-/-</sup> CGRP-alpha2 neurons

To reveal the potential neuronal changes during the progression of atherosclerosis, we examined transcriptomic profiles of the prevalent neuron subtype in both WT and Apoe<sup>-/-</sup> DRG, i.e. CGRP-alpha neurons. To predict the changes in intercellular communication among all DRGs cell types during atherosclerosis progression, we utilized CellChat, as described in the methods section, to compare differential cell-cell interactions among all cell types in aged WT versus Apoe<sup>-/-</sup> DRGs [182]. Our observations reveal an increase in the number of cell-cell interaction pairs in WT DRGs compared to Apoe<sup>-/-</sup> DRGs, particularly between CGRP-alpha2 neurons and macrophages, pericytes, and fibroblasts. Additionally, interactions between CGRP-alpha2 neurons with mSch, nmSch and fibroblast1 were also increased in aged Apoe<sup>-/-</sup> DRGs compared to WT. Subsequently, we calculated the interaction strengths by the interaction probability algorithm that was used to describe the interaction power [182, 217]. Differential interaction strengths showed that the increased cell-cell interaction probabilities in Apoe<sup>-/-</sup> DRG, in particular between CGRP-alpha2 neurons with macrophages, ECs, fibroblast3s, SGC and mSch (**Figure 36 A**). To determine potential intercellular interactions between each cell type in DRGs, we calculated the differential incoming and outgoing interaction strengths values for each cell type, as previously described [217]. The differences between outgoing and incoming interactions in aged Apoe<sup>-/-</sup> and WT DRGs highlight a positive difference for CGRP-alpha2, indicating a higher expression of interactions in aged Apoe<sup>-/-</sup> DRGs. In contrast, other cell types exhibited negative differences. The most highly expressed changes occurred in CGRP-alpha2 neurons when compared to aged WT DRGs (**Figure 36 B**). Collectively, these cell-cell interaction results of aged WT and Apoe<sup>-/-</sup> DRGs indicated that CGRP-alpha2 neurons were the primary DRG cell type that contributed to differential communication interactions. These results were consistent with the percentage increase of CGRP-alpha2 neurons in aged Apoe<sup>-/-</sup> DRGs compared to aged WT DRGs. To gain a better understanding of atherosclerosis-associated changes in aged DRGs, we will focus on the changes of CGRP-alpha2 neurons in aged WT versus Apoe<sup>-/-</sup> below.

## RESULTS

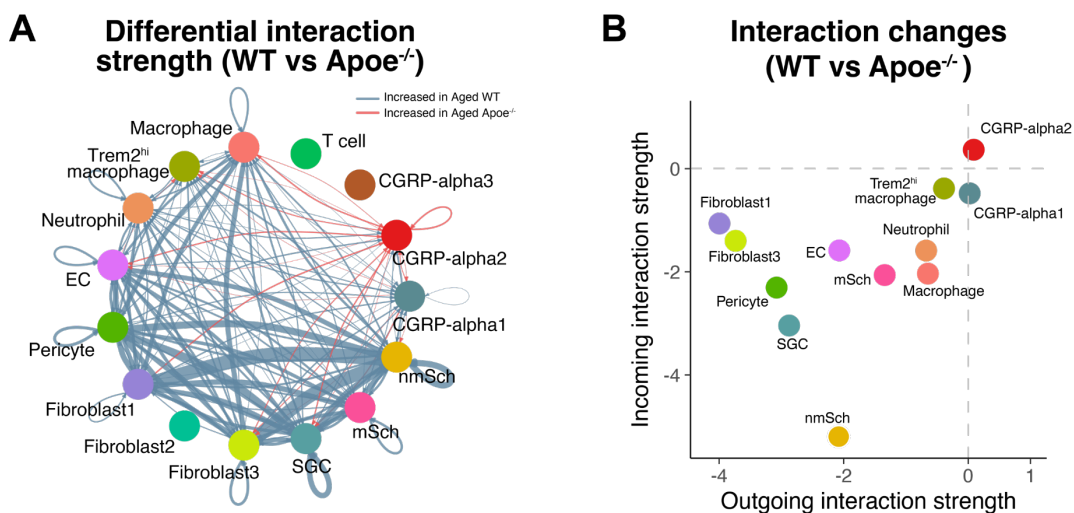


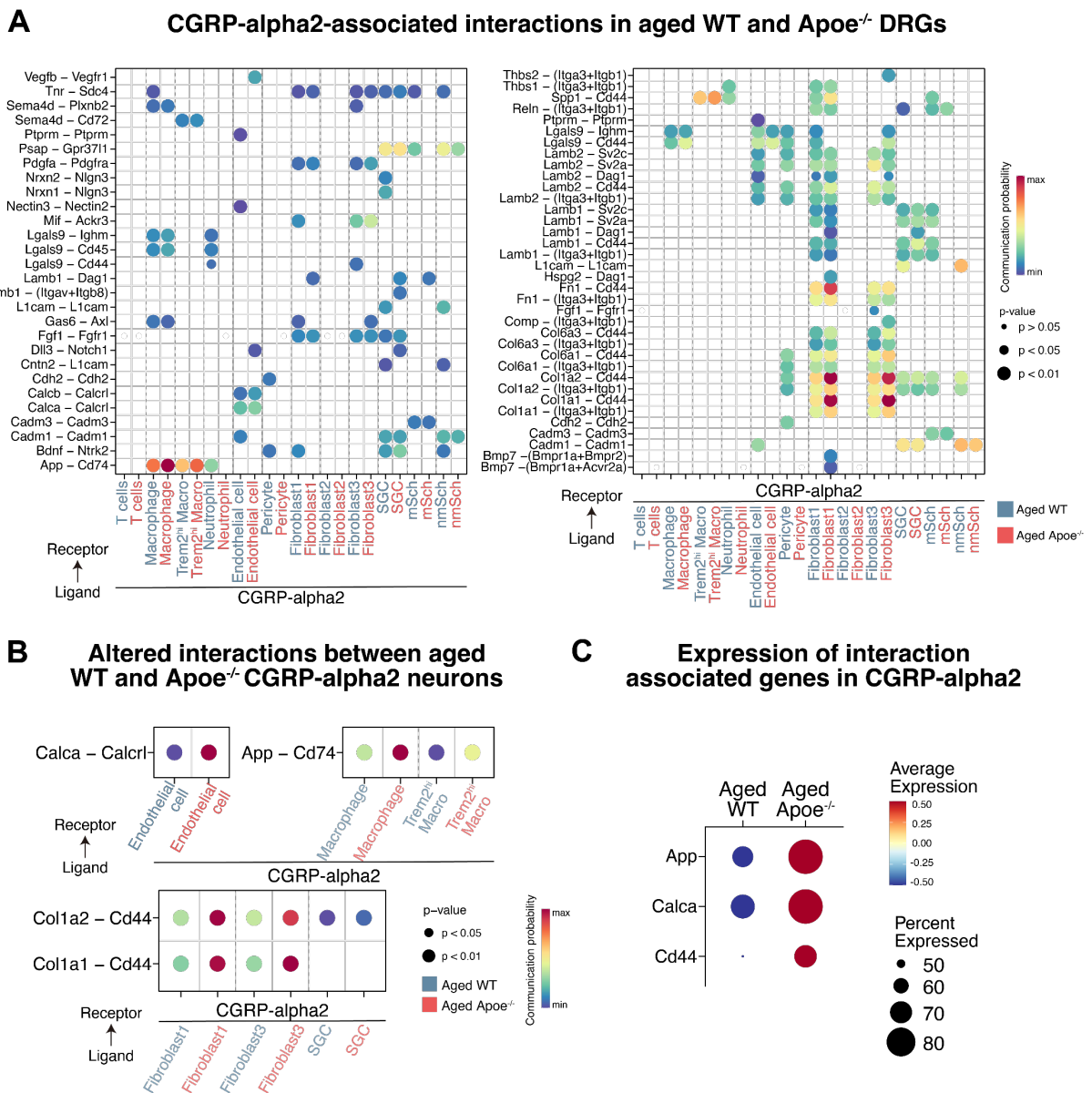
**Figure 36 Potential cell-cell interactions among all cell types in aged WT versus Apoe<sup>-/-</sup> DRGs.** **A**, Circle plots highlight the potential differential interaction strengths between aged WT and Apoe<sup>-/-</sup> DRGs. Edge weights represent the interaction counts and strength, respectively. Blue and red edges indicate potentially increased interaction in the aged WT and Apoe<sup>-/-</sup> DRGs, respectively. Vertices represent cell type. **B**, Dot plots show the comparison of major targets and source shifts between aged WT and Apoe<sup>-/-</sup> DRGs. X-axis represents the differences between outgoing interaction strengths of aged Apoe<sup>-/-</sup> DRGs and aged WT DRGs. Y-axis represents the differences between incoming interaction strengths of aged Apoe<sup>-/-</sup> DRGs and aged WT DRGs. Positive values of X-axis and Y-axis indicate increased interactions in aged Apoe<sup>-/-</sup> DRGs. P-values are computed by one-sided permutation test performed by CellChat.

To gain further insight into the alterations of CGRP-alpha2 neurons in aged WT versus Apoe<sup>-/-</sup> DRGs, we examined the putative cellular communication partners of these neurons in aged WT and Apoe<sup>-/-</sup> DRGs. In WT DRGs, several neuronal genes from CGRP-alpha2 neurons act as ligands for non-neuronal cells. Semaphorin 4d (Sema4d), a regulator of axon activity in the NS, has been reported to bind to members of the Plexin family. Additionally, Cd72 regulates neuronal development and immune responses [218]. In aged DRGs, Sema4d was predicted to act as a ligand of plexin b2 (Plxnb2) in macrophages, and as a ligand of CD72 in Trem2<sup>hi</sup> macrophages. In haematopoietic stem cells, Calca has been shown to bind to calcitonin receptor-like receptor (Calcr) and activate the G<sub>s</sub>/adenylyl cyclase/cAMP pathway [205]. Through the analysis of cell-cell interactions, we predicted that calcitonin-related polypeptide alpha and beta (Calca and Calcb) could act as ligands to bind to Calcr in ECs. Amyloid beta (A $\beta$ ) precursor protein-CD74 antigen (App-Cd74) had been reported to be associated with Alzheimer disease A $\beta$  production and inflammatory diseases [219, 220]. The App-Cd74 interaction is predicted to occur between CGRP-alpha2 neurons and immune cells, including macrophages, Trem2<sup>hi</sup> macrophages, and neutrophils. Moreover, several other neuronal genes of interest, including prosaposin (Psap), neurexin I and II (Nrxn1, Nrxn2), and L1cam, are predicted to act as ligands on non-neuronal cells. In CGRP-alpha2 neurons incoming ligand receptor pairs, laminin B1 and B2 (Lamb1, Lamb2), collagen family genes, and bone morphogenetic protein 7 (Bmp7) are predicted to be the primary potential ligands (**Figure 37 A, B**). We also

## RESULTS

examined these predicted interactions-related genes, including App, Calca, and Cd44. The expression levels of these genes and the percentage of gene-expressing cells were found to be higher in aged Apoe<sup>-/-</sup> versus WT CGRP-alpha2 neurons (**Figure 37 C**).

The data presented herein detail changes observed in entire DRGs and the putative cell-cell interactions, along with the results obtained from the enrichment analysis of CGRP-alpha2 neurons in aged WT versus Apoe<sup>-/-</sup> DRGs. The findings indicate that CGRP-alpha2 neurons exhibit potential atherosclerosis-associated functions, including peptide biosynthetic, oxidative phosphorylation, ribosome, and neurodegeneration-associated functions. Notably, the interactions involving Calca-Calcr1, App-Cd74, and Col1a2/Col1a1-Cd44 are predicted as potential principal CGRP-alpha2 neuron-related interactions. To ascertain and corroborate the relationship between CGRP-alpha2 neurons and atherosclerosis, we conducted resiniferatoxin (RTX) treatment experiments which is a powerful TRPV1 pharmaceutical that leads to apoptosis of TRPV1-expressing neurons.



## RESULTS

### Figure 37 Predicted cell-cell interactions among CGRP-alpha2 and non-neuronal cells in aged DRGs.

**A**, The left and right bubble plots depict the interaction probabilities of all significant ligand-receptor pairs sent from CGRP-alpha2 neurons or non-neuronal cell types in DRGs, respectively. Red color represents aged *Apoe*<sup>-/-</sup> DRGs, blue color represents aged WT DRGs. **B**, Bubble plots show the communication probabilities of interactions between Calca-Calcr1, App-Cd74, Col1a1/Col1a2-Cd44 between CGRP-alpha2 neurons and non-neuronal cells in aged DRGs. The communication probabilities and p-values are represented by dot colors and sizes. P-values are computed using a one-sided permutation test performed by CellChat. **C**, Bubble plot show the expression of App, Calca, and Cd44 genes in CGRP-alpha2 neurons from aged WT and *Apoe*<sup>-/-</sup> DRGs. The sizes of bubbles represent the percentage of cells expressing the marker genes in each cell type. The color depth corresponds to the average expression levels, red color designated the highest expression levels, blue color means low or no expression.

### 3.4.6 Predicted neuroimmune interactions among DRGs and ATLOs/renal lymph nodes (RLNs)

In recent years, bidirectional neuroimmune communication between the PNS and the immune system has received increasing attention as a potential mechanism for neuroimmune modulation and inflammation regulation [76, 124, 221]. These studies - while they are hypothetical in nature - are likely to understand scRNA-seq data better and guide us to perform independent studies to confirm or rule out cell-cell interaction as predicted via the algorithm. For instance, stromal cells in lymph nodes were found to exhibit the highest interaction with lymph node-innervating DRG sensory neurons and to rapidly alter their transcriptional profile upon neuronal modulation, as demonstrated by cell-cell interaction analysis and optogenetic stimulation of innervating neurons [76]. Previous data from our group indicated that atherosclerosis was associated neuritis in DRGs of aged *Apoe*<sup>-/-</sup> versus WT mice, and ATLOs expressed higher levels of neuronal genes, including neuronal receptors, compared to RLNs in WT and *Apoe*<sup>-/-</sup> mice [52].

To further investigate the potential neuroimmune interactions between neurons in DRGs with immune cells in RLNs or ATLOs, we employed the same method as previously described [76] and examined the putative cell-cell interactions among DRGs, RLNs, and ATLOs using the R toolkit CellChat [76, 182]. Cell-cell interactions were compared within all immune cells and between immune cells and neurons among three groups: WT DRGs-RLNs, *Apoe*<sup>-/-</sup> DRGs-RLNs, and *Apoe*<sup>-/-</sup> DRGs-ATLOs. We observed that interaction counts reached 1097 in *Apoe*<sup>-/-</sup> DRGs-ATLOs, while the counts were 549 in WT DRGs-RLNs and 618 in *Apoe*<sup>-/-</sup> DRGs-RLNs. These results indicated that potential interactions were 2-fold higher in *Apoe*<sup>-/-</sup> DRGs-ATLOs compared to the other two comparison groups, suggesting more potential interactions in ATLOs and between DRGs and ATLOs when compared with DRGs to RLNs (**Figure 38 A, B**). As stated above, these results require further in vivo studies including microscopic analyses to obtain initial real-time evidence.

## RESULTS

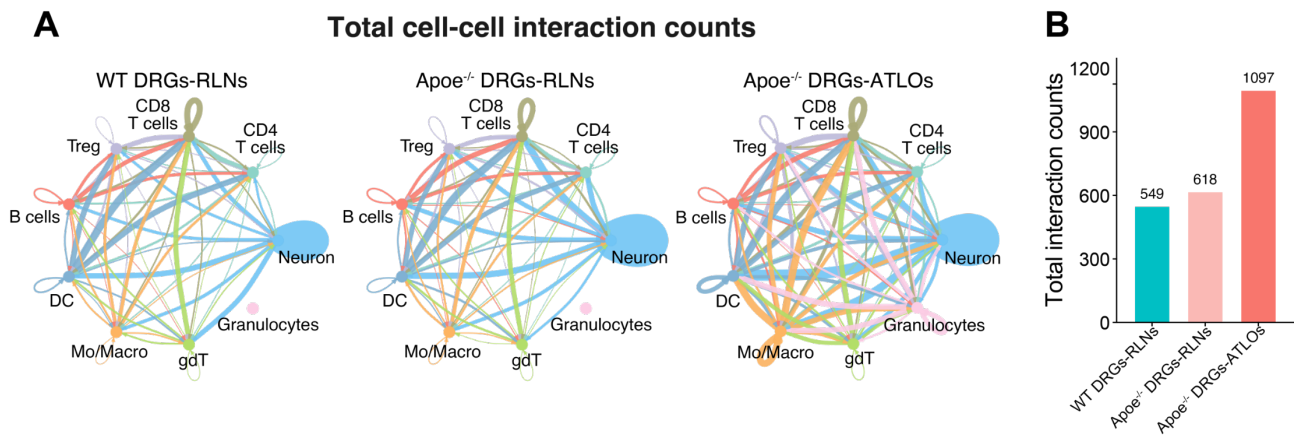


**Figure 38 Total cell-cell interaction counts are increased in Apoe<sup>-/-</sup> DRGs-ATLOs interactions. A**, Circle plot shows significant potential cell-cell interaction counts of WT DRGs-RLNs, Apoe<sup>-/-</sup> DRGs-RLNs, and Apoe<sup>-/-</sup> DRGs-ATLOs. Vertices designate cell types, the widths of edges represent interaction counts, and edge colors show the signal sender. **B**, Bar plot shows all significant cell-cell interaction counts of WT DRGs-RLNs, Apoe<sup>-/-</sup> DRGs-RLNs, and Apoe<sup>-/-</sup> DRGs-ATLOs. P-values are computed using a one-sided permutation test performed by CellChat.

To further identify potential interactions between major classes of neurons and immune cells, we assessed the putative interactions between DRG neurons and all immune cell types. Specifically, we defined the cell-cell interactions between DRG neuron classes (including PEP, NP, C-LTMR, TrpM8) and all immune cell types as putative neuroimmune interactions. By comparing outgoing and incoming neuroimmune interactions in three groups: WT DRGs-RLNs, Apoe<sup>-/-</sup> DRGs-RLNs, and Apoe<sup>-/-</sup> DRGs-ATLOs. We observed more outgoing interactions and rare incoming interactions (**Figure 39 A**). These results indicated that the majority of neuroimmune interactions originate from neurons directed toward immune cells between DRGs and RLNs or ATLOs. Furthermore, we noted an increase in the number of interaction counts, which reached 171 in the Apoe<sup>-/-</sup> DRGs-ATLOs, while the counts were 87 in WT DRGs-RLNs and 117 in Apoe<sup>-/-</sup> DRGs-RLNs. Thus, putative neuroimmune interactions were increased in Apoe<sup>-/-</sup> DRGs-ATLOs (**Figure 39 B**). We also discovered an increase in PEP neuron-associated interactions, particularly between PEP neurons and monocytes/macrophages, DCs, and granulocytes. Upon examining the distribution of neuroimmune interactions for each immune cell type, we found that CD8 T-cells, DCs, and macrophages provided more interactions than other immune cell types, indicating that these three immune cell types are the primary interaction receivers between DRGs and RLNs or ATLOs in aged mice. In the Apoe<sup>-/-</sup> DRGs-ATLOs, the interaction counts of immune cell types, including monocytes/macrophages, DCs, and granulocytes were increased.

## RESULTS

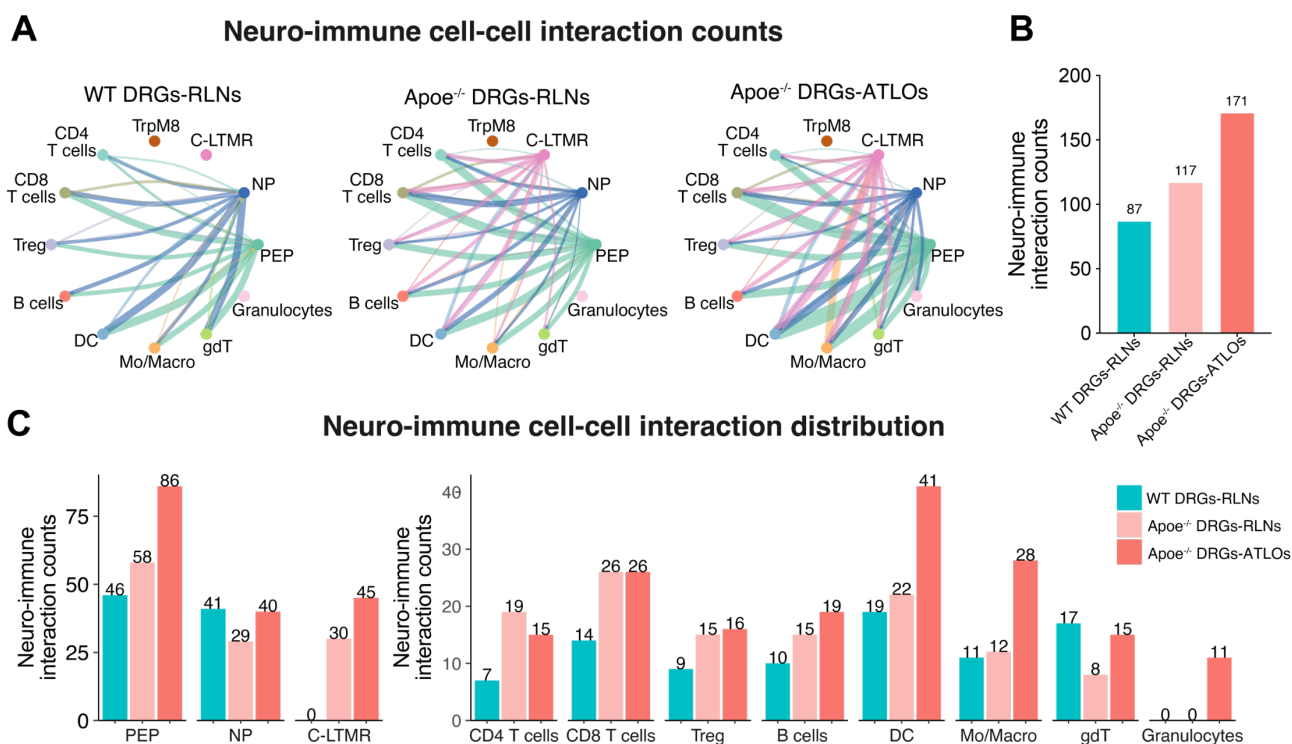


**Figure 39 Potential neuroimmune interactions between neurons in DRGs and immune cells in ATLOs/RLNs.** **A**, Circle plots show all significant outgoing and incoming neuron-immune interaction counts of the WT DRGs-RLNs, the Apoe<sup>-/-</sup> DRGs-RLNs, and the Apoe<sup>-/-</sup> DRGs-ATLOs. The cell types are represented by vertices, while the interaction counts are depicted by the edge widths. The signal sender are designated by the edge color. The significance of the interactions are determined using a permutation test performed by CellChat. **B**, Bar plot shows the total neuron-immune interaction counts of the WT DRGs-RLNs, the Apoe<sup>-/-</sup> DRGs-RLNs, and the Apoe<sup>-/-</sup> DRGs-ATLOs. **C**, Bar plots show the distribution of neuron-immune interactions in neurons and non-neuronal cells of the WT DRGs-RLNs, the Apoe<sup>-/-</sup> DRGs-RLNs, and the Apoe<sup>-/-</sup> DRGs-ATLOs.

To understand the potential mechanisms underlying enhanced neuron-immune interactions during atherosclerosis progression, we further examined PEP neuron-associated ligand-receptor pairs among WT DRGs-RLNs, Apoe<sup>-/-</sup> DRGs-RLNs, and Apoe<sup>-/-</sup> DRGs-ATLOs. Notably, several specific ligand-receptor pairs which are known to regulate neuroimmune functions were found to be higher expressed in Apoe<sup>-/-</sup> DRGs-ATLOs compared to the other two groups (**Figure 40**).

Fibroblast growth factor 1 - fibroblast growth factor receptor 1 (Fgf1-Fgfr1), a ligand-receptor pair known to affect cell proliferation in the brain and maintain somatosensory barrel cortex stellate cells dendritic complexity [222], was specifically higher expressed between PEP neurons and DCs in Apoe<sup>-/-</sup> DRGs-ATLOs. Bone marrow stromal cell antigen 2 - paired-Ig-like receptor A2 (Bst2-Pira2), another ligand-receptor pair associated with innate immune and MHC-I functions [223], was also higher expressed. Cell adhesion molecule 1 - cell adhesion molecule 1 (Cadm1-Cadm1), a pair reported can induce mast cell degranulation upon antigenic stimulation indicating its role in neuroinflammation [224], was higher expressed between PEP neurons and DCs in Apoe<sup>-/-</sup> DRGs-

## RESULTS

ATLOs. Macrophage migration inhibitory factor - Cd74 antigen (Mif-Cd74) interaction, described as essential for inflammatory and neuropathic pain responses to stress, playing a crucial role in healing and injury [225, 226], was also higher expressed. Interestingly, Cd74, the receptor of Mif and App in the interaction of *Apoe*<sup>-/-</sup> DRGs-ATLOs, was highly expressed in human atherosclerotic plaques and associated with inflammatory responses in atherosclerosis [227].

These findings suggested that the *Apoe*<sup>-/-</sup> DRGs-ATLOs showed potential increased neuroimmune interactions, particularly between PEP neurons and immune cells. Furthermore, the APP-Cd74 signaling pathway may play an important role in neuroimmune communication in *Apoe*<sup>-/-</sup> DRGs-ATLOs.

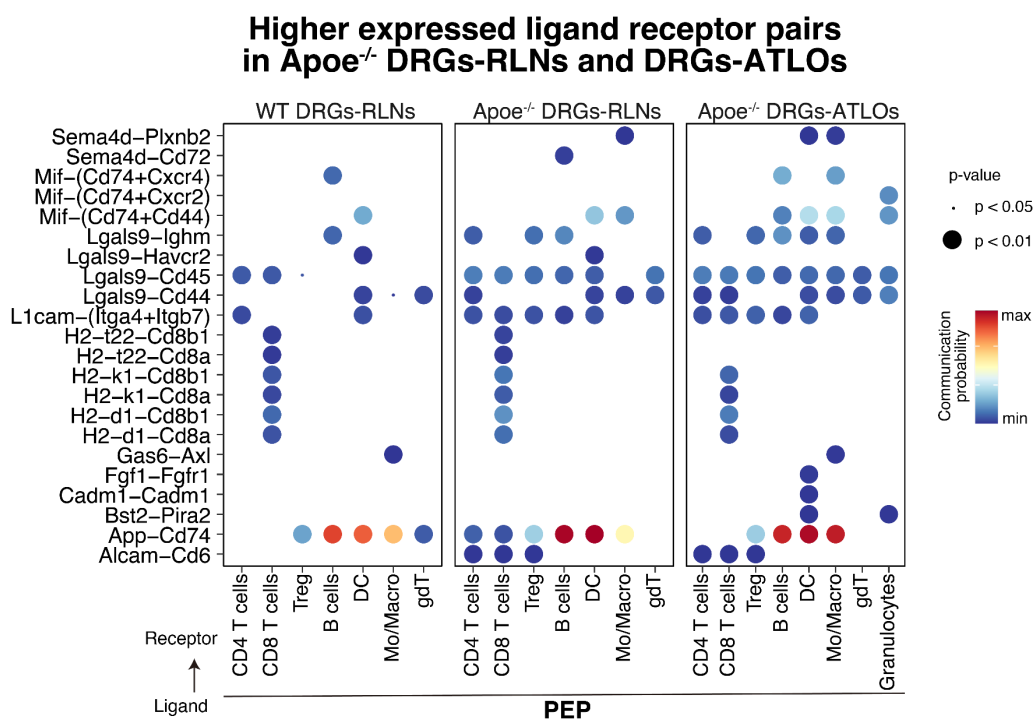


**Figure 40 Significantly higher expressed putative interactions between PEP neurons and immune cells in *Apoe*<sup>-/-</sup> DRGs-ATLOs.** Bubble plot shows the communication probability of all the significant ligand-receptor pairs that contributed to immune cells sent from PEP neurons in WT DRGs-RLNs, *Apoe*<sup>-/-</sup> DRGs-RLNs, and *Apoe*<sup>-/-</sup> DRGs-ATLOs. The dot color and size represent the communication probability and p-values respectively. The significance of the interactions are determined using a permutation test performed by CellChat.

## RESULTS

### 3.5 Effect of resiniferatoxin (RTX) treatment on CGRP-alpha2-associated changes

#### 3.5.1 Trpv1<sup>+</sup> neurons in aged DRGs

The scRNA-seq analysis comparing aged WT versus Apoe<sup>-/-</sup> DRGs demonstrated that CGRP-alpha2 neurons accounted for the majority of neuron-associated changes in aged Apoe<sup>-/-</sup> DRGs during atherosclerosis. Moreover, Trpv1, a known receptor for neuroinflammation and pain sensing, was identified to be expressed at higher levels on CGRP-alpha2 neurons. To investigate the potential contribution of CGRP-alpha2 neurons in neuroinflammation sensing during atherosclerosis, we further examined the Trpv1 expression in these neurons. Trpv1 expression was primarily detected in neurons rather than non-neuronal cells in aged DRGs. The percentages of Trpv1<sup>+</sup> neurons among all neurons in aged WT and Apoe<sup>-/-</sup> DRGs were similar (**Figure 41 A**). To further examine the distribution of Trpv1<sup>+</sup> neurons in the DRGs, we characterized the composition Trpv1<sup>+</sup> neurons. In aged DRGs, approximately 85% of Trpv1<sup>+</sup> neurons were PEP neurons among all neuron classes, and around 40% Trpv1<sup>+</sup> neurons were CGRP-alpha2 neurons among subtype of all Trpv1<sup>+</sup> neurons (**Figure 41 B**), whereas approximately 65% of CGRP-alpha2 neurons were Trpv1<sup>+</sup> (**Figure 41 A**). These results indicated that Trpv1<sup>+</sup> neurons were primarily PEP neurons and that the majority of CGRP-alpha2 neurons were Trpv1<sup>+</sup>.

## RESULTS

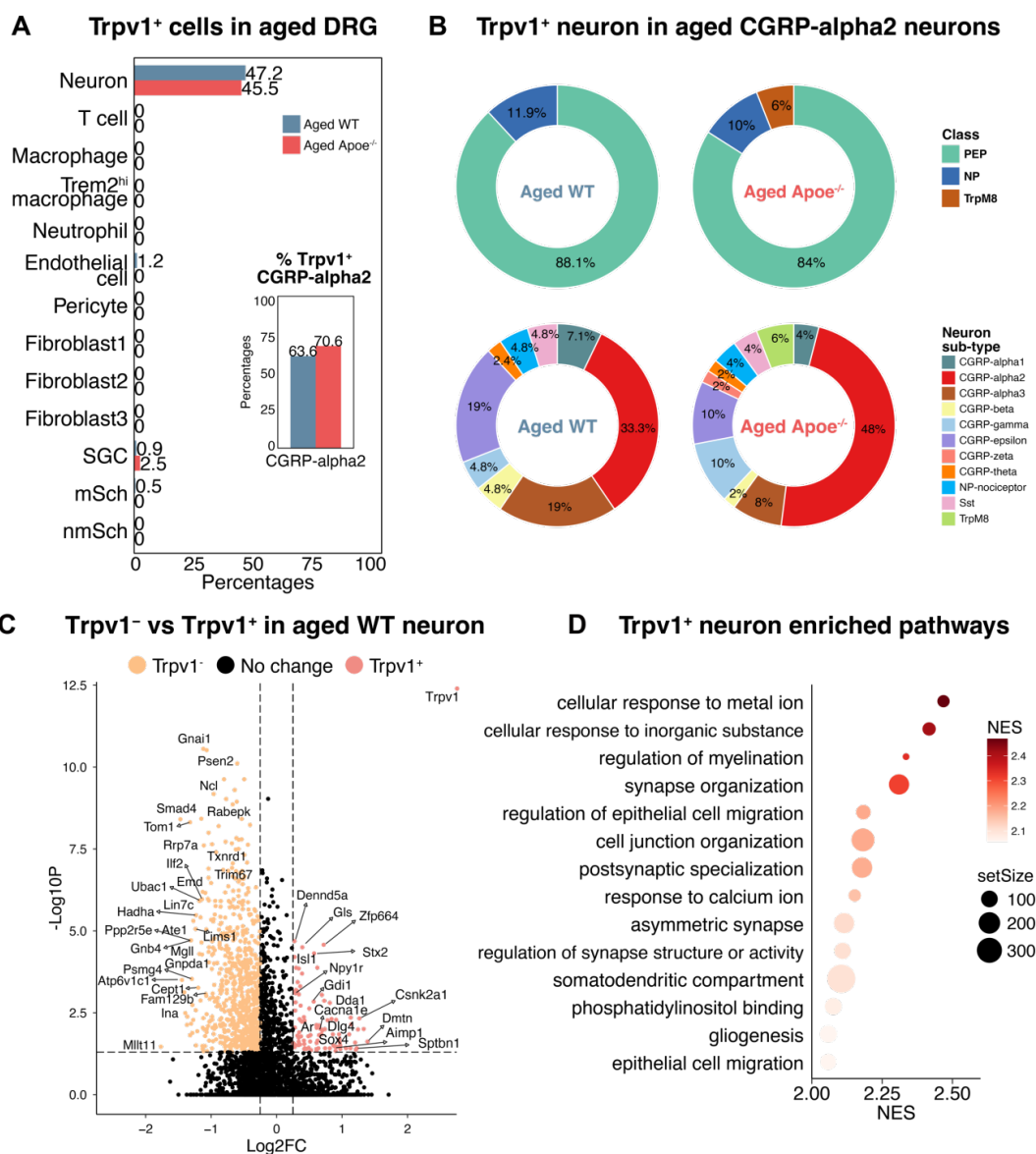


**Figure 41 Trpv1<sup>+</sup> neurons in aged DRGs.** **A**, Bar plot shows the percentages of Trpv1<sup>+</sup> cells in cell type and in CGRP-alpha2 neurons from aged DRGs. The bars are labeled as the percentages and colored by groups, with blue color representing aged WT DRGs and red color representing aged Apoe<sup>-/-</sup> DRGs. **B**, Donut plots show the distribution of neuron classes and subtypes of Trpv1<sup>+</sup> neurons among different groups. Donut blocks are colored by neuron subtypes and labeled as percentages. **C**, Volcano plots depict DEGs between Trpv1<sup>+</sup> versus Trpv1<sup>-</sup> neurons in aged WT DRGs (T6-T13). Red color represents the Trpv1<sup>+</sup> neurons with higher expressed DEGs, earthy yellow represents Trpv1<sup>-</sup> neurons with higher expressed DEGs, black represents no change in gene expression. Significances are examined using the likelihood-ratio test followed by Bonferroni correction. **D**, Bubble plot shows enriched pathways in aged WT Trpv1<sup>+</sup> neurons with bubbles representing the number of genes in the analysis and colored by NES. NES, normalized enrichment score.

To gain insight into potential impacts of Trpv1<sup>+</sup> neurons in T6-T13 DRGs, we examined the transcriptional profiles of Trpv1<sup>+</sup> PEP neurons and Trpv1<sup>-</sup> PEP neurons in aged WT DRGs. Our data show that genes associated with sensory perception of pain, including Trpv1, voltage-dependent calcium channel alpha 1e (Cacna1e) and neuropeptide Y receptor Y1 (Npy1r), were expressed at

## RESULTS

higher levels in Trpv1<sup>+</sup> neurons. We also identified genes involved in peptide hormone secretion regulation, including Islet 1 (Isl1) and the kinesin family member 5B (Kif5b). Additionally, genes associated with protein localization to membrane regulation, including ankyrin 3 epithelial (Ank3), casein kinase 2 alpha 1 polypeptide (Csnk2a1), dematin actin binding protein (Dmtn), heat shock 105kDa/110kDa protein 1 (Hsph1), were expressed at significantly higher levels in Trpv1<sup>+</sup> PEP neurons (**Figure 41 C**). GSEA show that the response to metal ion, response to calcium ion, regulation of myelination, synapse organization, and somatodendritic compartment, are enriched in Trpv1<sup>+</sup> compared to Trpv1<sup>-</sup> neurons in aged WT T6-T13 DRGs (**Figure 41 D**). In summary, these findings indicated that Trpv1<sup>+</sup> neurons are associated with the potential functions like calcium ion activities, synapse organization, and regulation of myelination in aged DRGs. These results provide important insights into the potential roles of Trpv1<sup>+</sup> neurons in the context of aging and atherosclerosis progression.

### 3.5.2 ScRNA-seq of control and RTX-treated DRGs

CGRP-alpha2 neurons were the most abundant neuron subtype in aged DRGs and contributed to the majority of higher expressed transcriptional changes during atherosclerosis. As we described above, Trpv1 was negatively-associated with the Apoe gene in aged DRGs (**Figure 29**) and Trpv1 was highly expressed in CGRP-alpha2 neurons (**Figure 25, 41**). To understand the potential roles of Trpv1<sup>+</sup> neurons during atherosclerosis progression, Trpv1<sup>+</sup> neuron ablation was established using repeated RTX injections within a 24-week time window of RTX treatment beginning at young age of 8 weeks. T6-T13 DRGs were collected thereafter for scRNA-seq analyses using the same protocol as has been used for aged DRGs scRNA-seq analyses (**Figure 42 A**). We obtained a total of 1371 control DRG cells and 2537 RTX-treated DRG cells. These 3908 total DRG cells from control and RTX-treated mice were classified into five classes and 14 cell types (**Figure 42 B**). The neuron subtype composition was determined as described above using young DRG neuronal scRNA-seq dataset as a reference [124] (**Figure 22**). Neurons from control and RTX-treated mice were classified into five classes: PEP, NP, NF, C-LTMR, TrpM8 neurons. These five classes were clustered into 12 subtypes including CGRP-alpha1, CGRP-alpha2, CGRP-alpha3, CGRP-beta, CGRP-epsilon, CGRP-zeta, CGRP-theta, NP-nociceptor, Adelta-LTMR, proprioceptors, C-LTMR, and TrpM8 (**Figure 42 C, D**).

## RESULTS

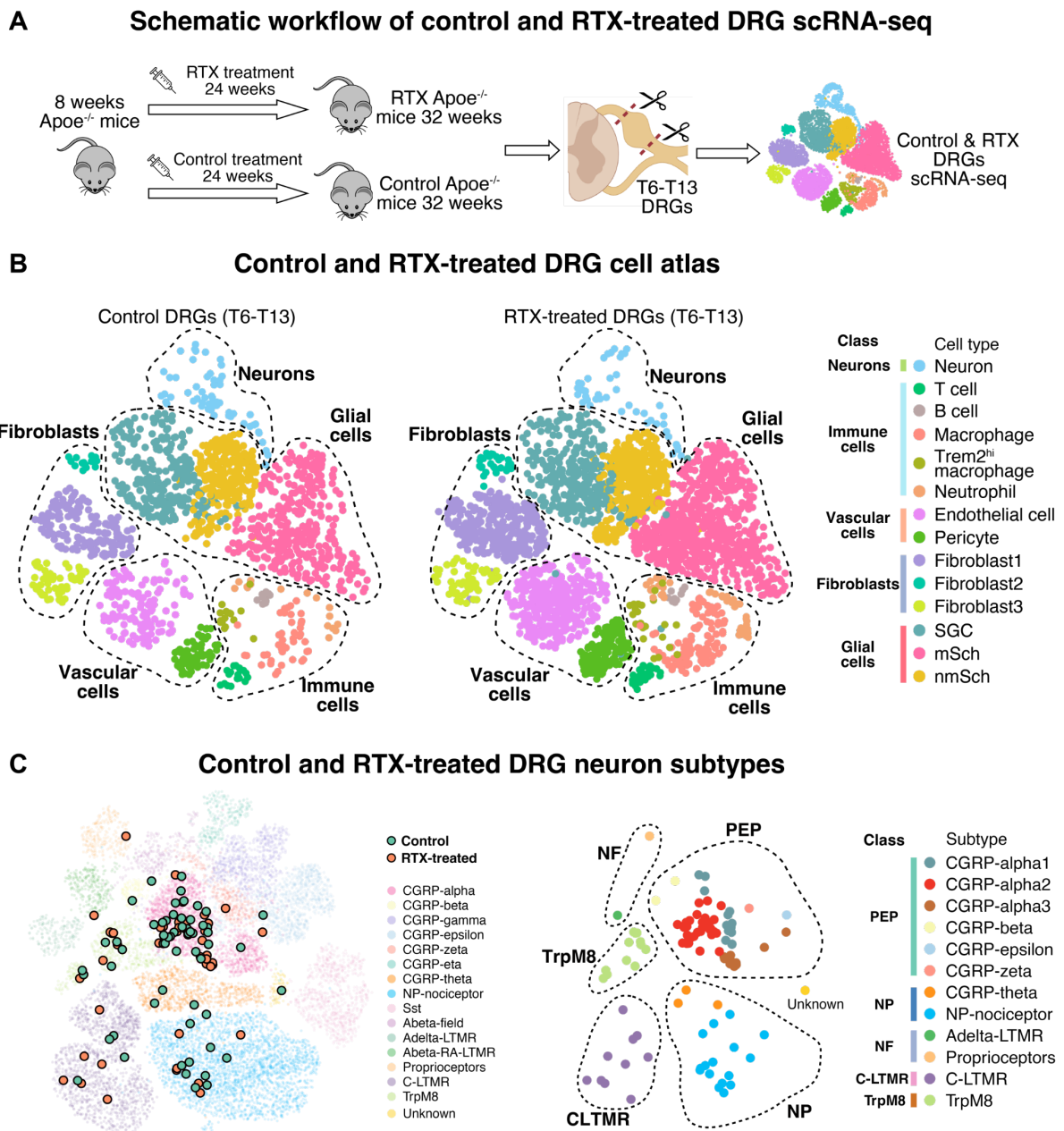


**Figure 42 ScRNA-seq of control and RTX-treated DRGs identifies cell types and neuron subtypes. A,** Schematic workflow show the DRG scRNA-seq workflow of control and RTX-treated mice using the same method described above. Mice are sacrificed after 24 weeks (mice are 32 weeks old at the end of the experiment). **B,** UMAP depicts all single-cell transcriptomes from control ( $n = 4$ ) and RTX ( $n = 6$ ) mice. Each dot represents a single cell: 3908 individual cells are obtained. Colored dots are based on scRNA-seq clustering results whereby different colors represent different cell clusters. UMAPs of control and RTX-treated DRGs are shown. Each class is circled by dashed lines. **C,** UMAP (left) shows the integrated dataset of aged  $Apoe^{-/-}$  DRG neurons, control DRG neurons, RTX-treated DRG neurons, and young DRG neurons. Young DRG neurons are set as background with higher transparency and are colored by cell types. Control DRG neurons and RTX-treated DRG neurons are highlighted by bigger sizes and black outlines with green representing control DRG neurons and orange representing RTX-treated DRG neurons. UMAP (right) shows all neuron subtypes of control and RTX-treated DRGs.

## RESULTS

### 3.5.3 Effects of RTX treatment on T6-T13 DRGs

RTX is an agonist of Trpv1, which activates the Trpv1 channel leading to neuronal death in most of the neurons. This property has been used to achieve Trpv1<sup>+</sup> ablation in mice [228-230]. To determine the effects of RTX treatment on DRG (T6-T13) neurons, Trpv1<sup>+</sup> neurons in T6-T13 DRGs were examined between control and RTX-treated mice. We obtained 1,371 cells from control DRGs and 2,537 cells from RTX-treated DRGs. Among these, there were 60 and 43 neurons, respectively, with 16 Trpv1<sup>+</sup> neurons in control DRGs and 4 Trpv1<sup>+</sup> neurons in RTX-treated DRGs. The percentage of Trpv1<sup>+</sup> neurons significantly decreased from 26.7% in control to 9.3% in RTX-treated DRGs (**Figure 43 A**). These results indicated that approximately 65% Trpv1<sup>+</sup> neurons in T6-T13 DRGs were ablated after RTX treatment. The discrepancy in percentages compared to previous publications [229, 230] might be due to the limited number of neurons studied. Further experimental evidence is needed to confirm these findings.

To further understand Trpv1<sup>+</sup> neuron in DRGs, we determined the neuron subtype composition of Trpv1<sup>+</sup> neurons in T6-T13 DRGs after control or RTX treatment. We observed that the majority of the Trpv1<sup>+</sup> neurons were PEP neurons, and CGRP-alpha2 neurons were the most abundant neuron subtype in Trpv1<sup>+</sup>-expressing neurons in both control and RTX-treated mice. After RTX treatment, approximately 50 % of the Trpv1<sup>+</sup> CGRP-alpha2 neurons were ablated (**Figure 43 B, C**). These results validated the effects of RTX treatment on Trpv1<sup>+</sup> neurons in DRGs, especially Trpv1<sup>+</sup> CGRP-alpha2 neurons.

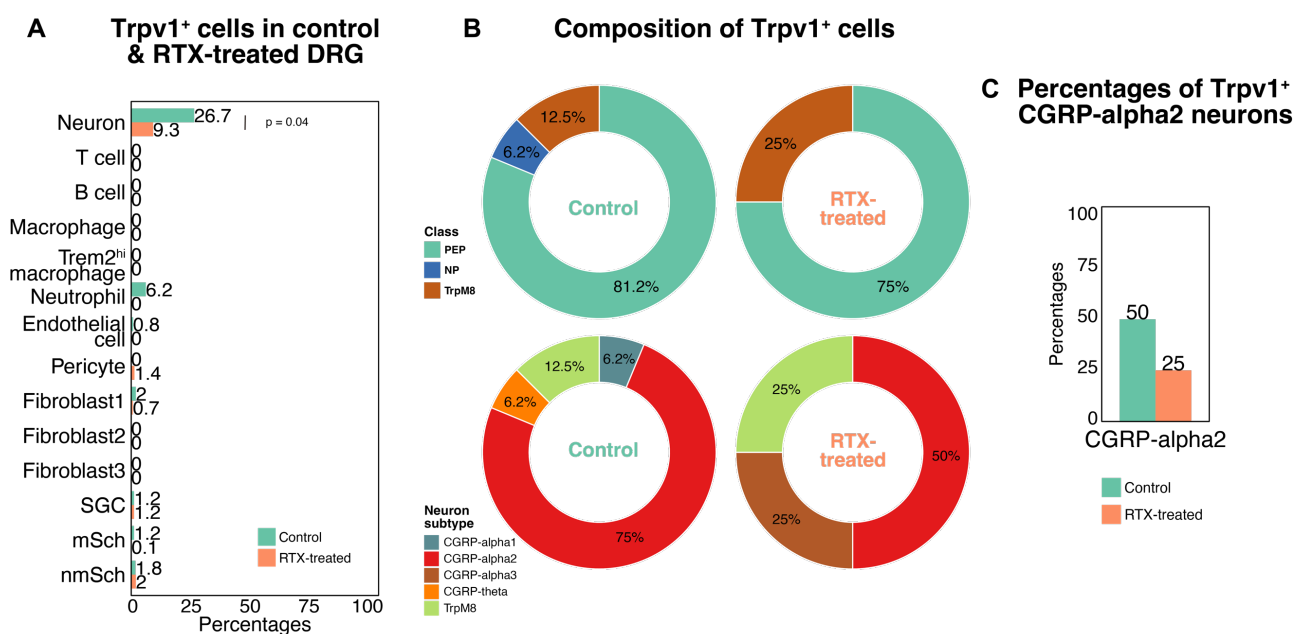
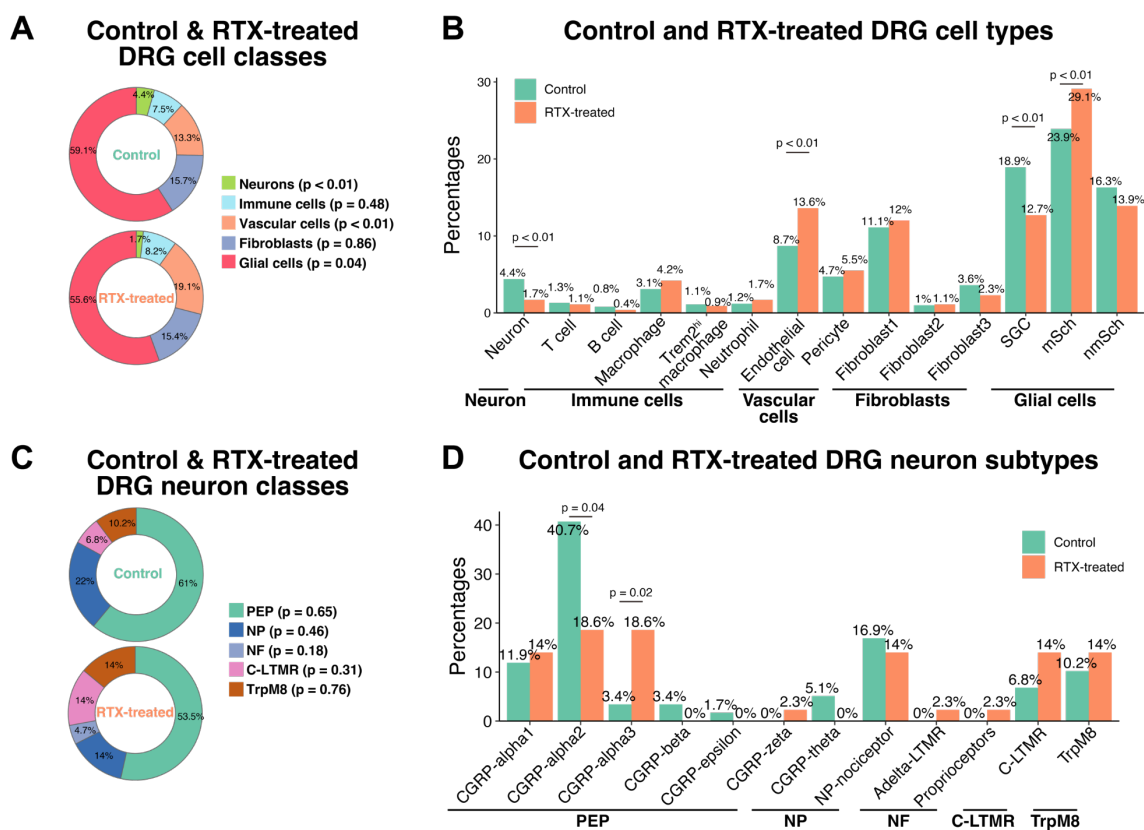


**Figure 43 Trpv1 expression in control and RTX-treated DRGs.** **A**, Bar plot shows the percentages of Trpv1<sup>+</sup> cells in each cell type in control and RTX-treated DRGs, the bar designates percentages and are colored by groups. Green represents control DRGs, orange represents RTX-treated DRGs. The significances in control

## RESULTS

versus RTX are determined by the Chi-squared test and adjusted using Benjamini-Hochberg correction. **B**, Donut plots show neuron classes and subtypes distribution of Trpv1<sup>+</sup> neurons among different groups. Donut blocks are colored by neuron subtypes and labeled as percentages and group names. **C**, Bar plots show the percentages of Trpv1<sup>+</sup> neurons among CGRP-alpha2 in control and RTX-treated mice.

We obtained a total of 1,371 control DRG cells and 2,537 RTX-treated DRG cells, as previously mentioned. These 3,908 total DRG cells from both control and RTX groups were classified into five classes and fourteen cell types. To further examine transcriptional changes following RTX treatment of T6-T13 DRGs, we determined the percentages of each DRG classe and cell type. The absolute numbers of neurons were 60 and 43 in control and RTX-treated DRGs respectively, while the percentages was decreased from 4.4% in control DRGs to 1.7% in RTX-treated DRGs. In contrast, the absolute numbers of vascular cells rose from 183 in control DRGs and reached 485 in RTX-treated DRGs, with the percentage increased from 13.3% in control DRGs to 19.1% in RTX-treated DRGs. The changes of vascular cells was particularly pronounced in ECs. Regarding glial cells, the absolute numbers increased from 810 in control DRGs to 1410 in RTX-treated DRGs, while the percentages of glial cells were similar between control and RTX-treated DRGs. However, the percentage of SGC was decreased, whereas the percentage of mSch was increased, based on the analysis of scRNA-seq data. For all other non-neuronal cell types, the percentages were similar in control and RTX-treated DRGs (**Figure 44 A, B**). These results indicated RTX treatment had a more significant impact on neurons and the prcentages of ECs, SGC and mSch. The effects of neurons were expected, but the eeffects of ECs, SGC and mSch require further biological experimental evidences for validation.



## RESULTS

**Figure 44 Cell type composition of DRGs is altered in control versus RTX-treated mice.** **A**, Donut plots show the percentages of main classes in control DRGs and RTX-treated DRGs. **B**, Bar plots show the percentages of all cell types in control and RTX mice. **C**, Donut plots show the percentages of neuron classes in control DRG and RTX mice. **D**, Bar plots show the percentages of neuron subtypes in control and RTX mice. In bar plots, orange represent DRGs of RTX-treated mice. Green represents control mice. The significance in WT versus *Apoe*<sup>-/-</sup> are analyzed using Pearson's Chi-squared test and adjusted using Benjamini-Hochberg correction. RTX-treated, resiniferatoxin-treated.

In addition to the cell types mentioned above, we further compared neuron subtypes in control and RTX-treated DRGs. The absolute numbers of PEP neurons were 36 in control DRGs and 23 in RTX-treated DRGs, while the percentages decreased from 61% in control DRGs to 53.5% in RTX-treated mice. The absolute numbers of CLTMR were 4 in control DRGs and 6 in RTX-treated mice, with the percentages increased from 6.8% in control DRGs to 14% in RTX-treated mice. Although the percentages changed based on the analysis of scRNA-seq data, the absolute numbers obtained were low and therefore further biological experimental evidence is required for validation. Upon examining neuronal subtypes, we can find that the absolute numbers of CGRP-alpha2 neuron were 24 in control DRGs and 8 in RTX-treated DRGs respectively, with the percentage significantly decreasing from 40.7% in control DRG neurons to 18.6% in RTX-treated DRG neurons. Meanwhile, the percentage of CGRP-alpha3 neurons increased from 3.4% in control DRG neurons to 18.6% in RTX-treated DRG neurons (**Figure 44 C, D**). The decrease of CGRP-alpha2 neurons might be due to the higher expression of *Trpv1* (**Figure 26 C**) and RTX treatment were *Trpv1*<sup>+</sup> neurons reside. Further transcriptional analyses of CGRP-alpha2 neurons between control and RTX-treated DRG neurons are required to further understand the effects of RTX treatment and the relationship between CGRP-alpha2 neurons and atherosclerosis.

### 3.5.4 Transcriptome changes after RTX treatment

In order to gain a better understanding of the effects of RTX treatment on DRG phenotypes, we calculated the DEGs and all regulated genes that were utilized for GSEA for each cell type in T6-T13 DRGs. The data indicated that there were few significant DEGs, including total neurons and neuron subtypes (**Figure 45, Appendix Table4**). Therefore, GSEA was conducted using all regulated genes without considering the p-values.

## RESULTS

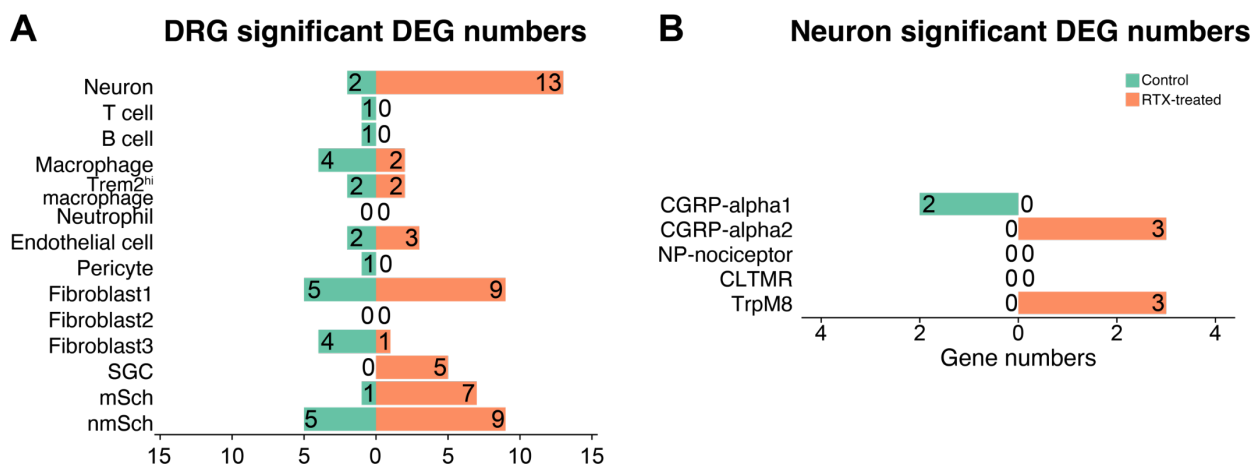


**Figure 45 Significant DEGs of control versus RTX-treated DRGs.** **A**, Divergent bar plots show significant DEGs ( $\log_2FC > 0.25$  & adjusted  $p$ -value  $< 0.05$ ) for each cell type in control versus RTX-treated DRGs. **B**, Divergent bar plots show DEGs of each neuron subtype in control versus RTX-treated DRGs. The length of the bars correlates with the numbers of significant DEGs of each cell type, with green and orange colors representing the higher expressed DEGs genes in control and RTX-treated DRGs, respectively. The significance of DEGs are calculated using likelihood-ratio test and are adjusted using Benjamini-Hochberg correction. RTX, resiniferatoxin.

To understand the potential mechanisms of action of CGRP-alpha2 neurons during atherosclerosis progression at the transcriptional level, we performed GSEA analyses using the regulated genes (**Figure 45**) of CGRP-alpha2 neurons in control versus RTX-treated mice. The enrichment network revealed that most of the enriched pathways were higher in control DRGs, while fewer pathways were enriched in RTX-treated DRGs. The function-related pathways, including neurogenesis, development, projection, and morphogenesis were higher expressed after RTX treatment (**Figure 46 A**). Notably, the peptide biosynthetic process, ATP metabolic process, and myelin sheath, which were higher expressed in CGRP-alpha2 neurons in aged *Apoe*<sup>-/-</sup> DRGs, were lower expressed in CGRP-alpha2 neurons after RTX treatment (**Figure 46 B**). Furthermore, ribosome-associated functions were lower expressed in RTX-treated CGRP-alpha2 neurons. Interestingly, function-related pathways such as presynaptic membrane, positive regulation of cell junction assembly, and neurogenesis were higher expressed after RTX treatment (**Figure 50 C**). These results suggested that RTX treatment may decrease the peptide biosynthetic process, energy and lipid metabolism of CGRP-alpha2 neurons, which were higher in aged *Apoe*<sup>-/-</sup> CGRP-alpha2 neurons. These implied that these functions might be associated with the regulatory role of CGRP-alpha2 neurons during atherosclerosis progression at transcriptional levels. Further biological experimental evidence was required to validate and support the role of CGRP-alpha2 neurons in atherosclerosis progression.

## RESULTS

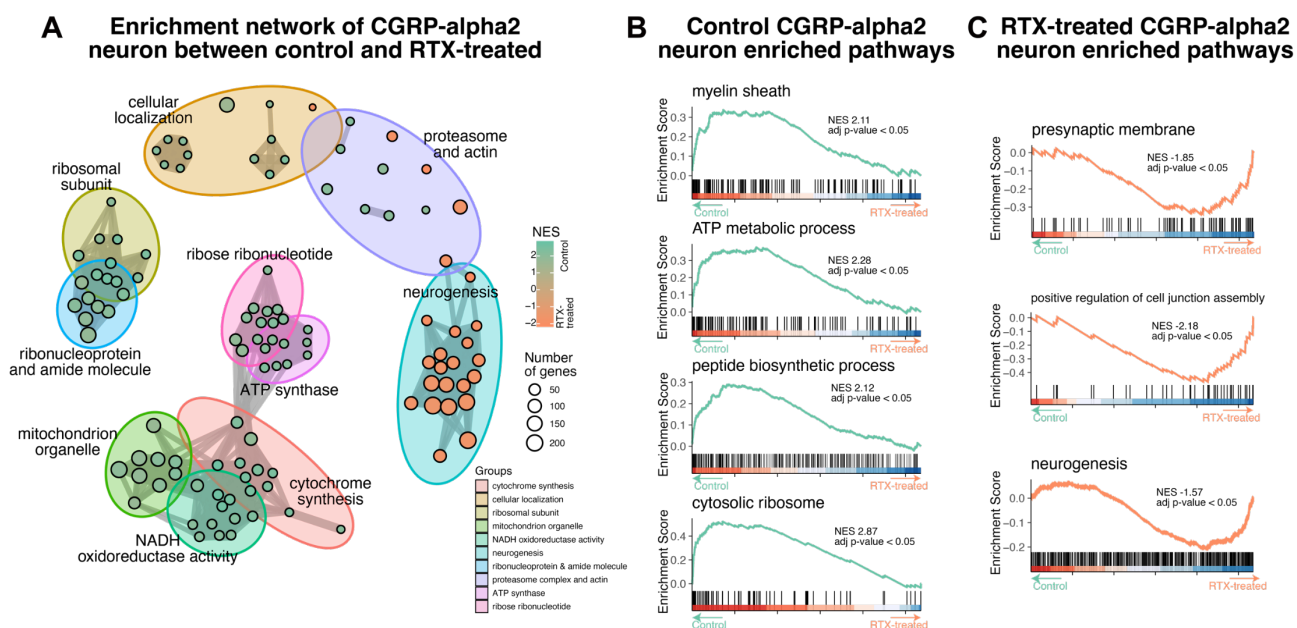


**Figure 46 GSEA identifies CGRP-alpha2 neuron changes in control versus RTX-treated DRGs. A,** The GSEA map of CGRP-alpha2 neuron shows significantly altered pathways in control versus RTX-treated DRGs. All enriched pathways are combined and unbiasedly grouped into 10 clusters based on expression similarity. Each cluster is circled with a distinct color, with the size of the vertex indicating the number of genes within each pathway. The color scale represents the adjusted p-values. **B,** Enrichment plots provide a graphical view of the enrichment score for the gene sets of cation binding, lipid localization and protein kinase activity. **C,** Enrichment plots provide a graphical view of the enrichment score for the gene sets of peptide biosynthetic process, ATP synthesis coupled electron transport, and myelin sheath. Significances are calculated using rank-sum test and adjusted using Benjamini-Hochberg correction performed by clusterProfiler. NES, normalized enrichment score; adj p-value, adjusted p-value; RTX, resiniferatoxin.

In conclusion, these findings above revealed that RTX treatment induced diverse transcriptional changes of DRG cell types, particularly in CGRP-alpha2 neurons. The potential functions, which include peptide biosynthetic process, neurodegeneration, energy and lipid metabolism, were higher expressed in aged *Apoe<sup>-/-</sup>* CGRP-alpha2 neurons and were decreased after RTX treatment. These data imply that these potential functions might be related to the regulatory role of CGRP-alpha2 neurons during atherosclerosis progression at the transcriptional level.

### 3.5.5 Potential CGRP-alpha2-associated neuroimmune pathways during atherosclerosis progression

Since CGRP-alpha2 neurons have been found to be abundant in aged mice, we hypothesized that gene expression changes were not restricted to neurons alone, and that neuron-non-neuronal cell interactions could also lead to alterations in non-neuronal gene expression patterns. To investigate these possibilities, we utilized the CellChat algorithms to examine potential cell-cell interactions

## RESULTS

within the intricately organized DRGs, which included CGRP-alpha1, CGRP-alpha2, CGRP-alpha3 neurons, and all other non-neuronal cells. The results showed that the interactions between CGRP-alpha2 neurons and non-neuronal cells were decreased after RTX treatment compared to control DRGs. Additionally, the strengths of interactions of CGRP-alpha2 neurons were diminished following RTX treatment when compared to control DRGs (**Figure 47 A**). These CGRP-alpha2 neuron-associated shifts were clearly observed in RTX-treated DRGs compared to other cell types (**Figure 47 B**). These results indicated the cell-cell interaction activities of CGRP-alpha2 neurons with non-neuronal cells were attenuated after RTX treatment.

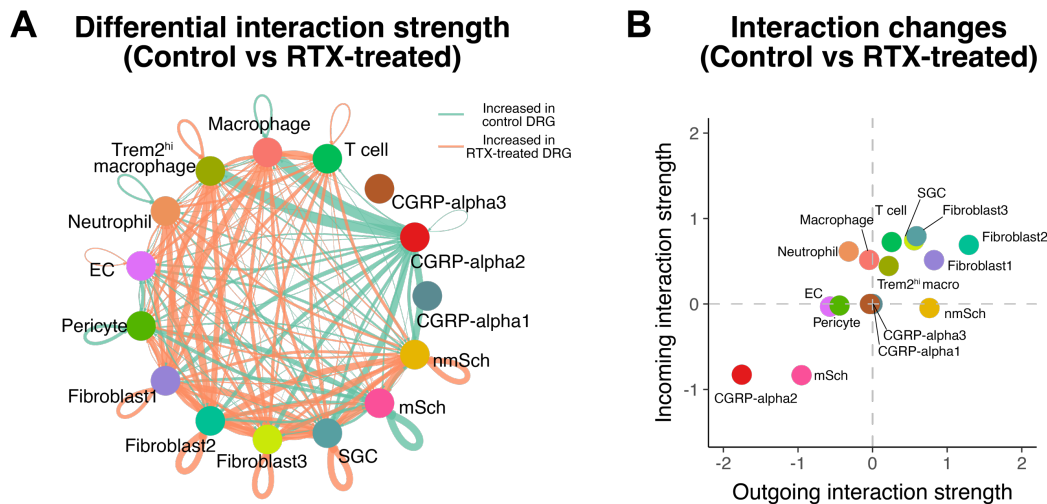
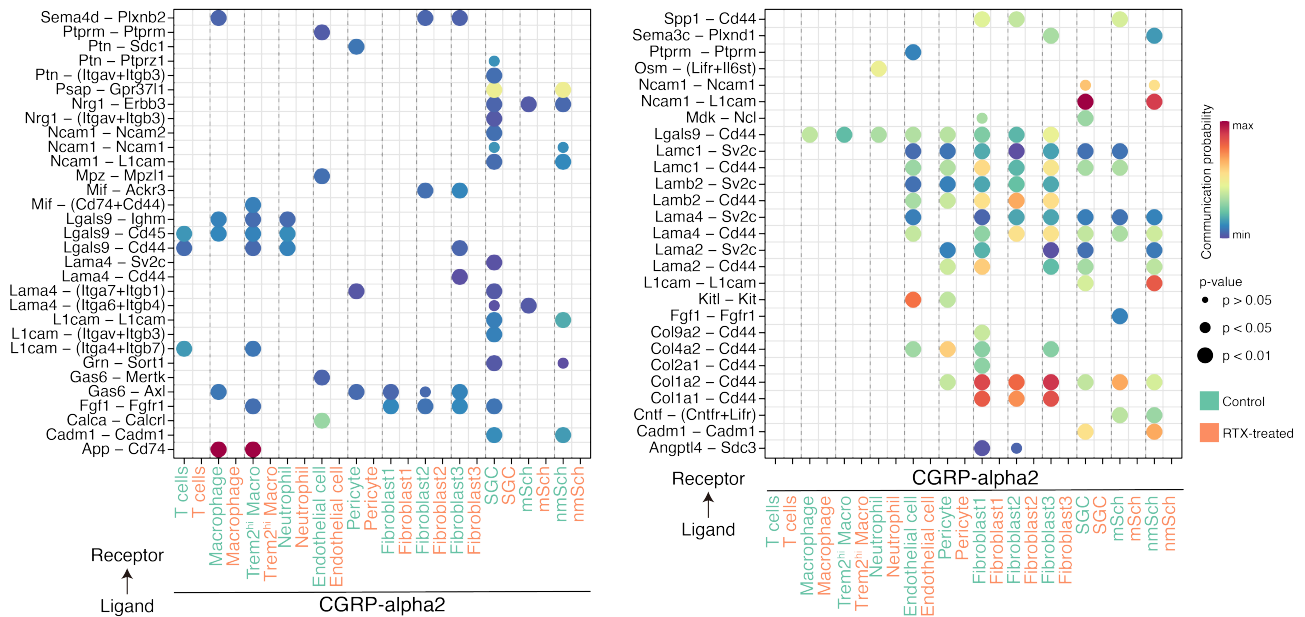


**Figure 47 Potential cell-cell interactions among all cell types in control versus RTX-treated DRGs. A,** Circle plots highlight the potential differential interaction strengths between control and RTX-treated DRGs. Edge weights represent the interaction counts and strength, respectively. Green and orange edges indicate potentially increased interaction in the control and RTX-treated DRGs respectively. Vertices represent cell type. **B,** Dot plots show the comparison of major targets and source shifts between control and RTX-treated DRGs. X-axis represents the differences between outgoing interaction strengths of RTX-treated and control mice. Y-axis represents the differences between incoming interaction strengths of RTX-treated and control mice. Positive values of X-axis and Y-axis indicate the increased incoming and outgoing interactions in RTX-treated DRGs. P-values are computed by one-sided permutation test performed by CellChat.

My colleague Ting Sun's data in her PhD thesis revealed that atherosclerotic plaque sizes were reduced after RTX treatment (Sun T, unpublished 2023), which was in line with the findings in scRNA-seq data: the percentages of CGRP-alpha2 neurons were decreased in RTX-treated DRGs, and also coincided with the attenuation of CGRP-alpha2 neuron-associated cell-cell interactions after RTX treatment. Additionally, as previously mentioned, the percentages of CGRP-alpha2 neurons were increased and the associated cell-cell interactions were enhanced during atherosclerosis in aged *Apoe*<sup>-/-</sup> mice. We hypothesize that CGRP-alpha2 neurons might be involved and play an important role during atherosclerosis progression.

## RESULTS

### A CGRP-alpha2 associated interactions in control and RTX-treated DRGs



### B The changed interactions in both Control and RTX-treated DRGs

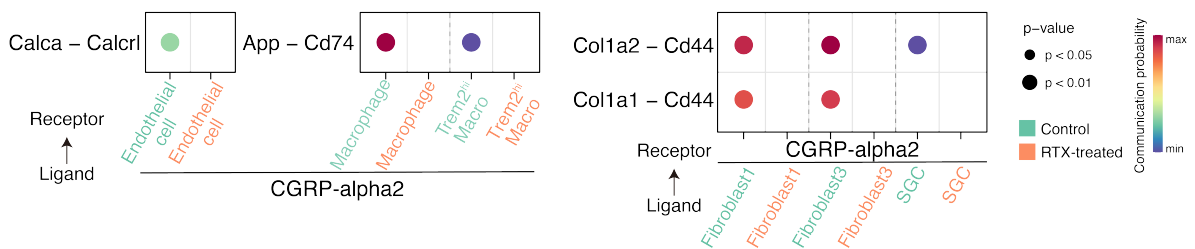


**Figure 48 CGRP-alpha2-associated interactions increased in aged *Apoe*<sup>-/-</sup> and control DRGs. A, Bubble plot of the communication probability of all significant ligand-receptor pairs in which DRG non-neuronal cells are involved. These include outgoing signals from CGRP-alpha2 neurons in control and RTX-treated mice (left). Bubble plot of the communication probability of all significant outgoing ligand-receptor pairs from DRG non-neuronal cells in control and RTX-treated mice (right). Green represents control DRGs, orange color represent DRGs from RTX-treated mice. B, Bubble plot shows the communication probability of interactions Calca-Calcr, App-Cd74, Col1a1/Col1a2-Cd44 among CGRP-alpha2 neurons and non-neuronal cells. The dot color and size represents the communication probability and p-values, respectively. P-values are computed from one-sided permutation test performed by CellChat.**

As the data presented above, CGRP-alpha2 neurons were abundant in both aged WT and *Apoe*<sup>-/-</sup> DRGs, and the majority of CGRP-alpha2 neurons expressed *Trpv1*. The cell-cell communication analysis of CGRP-alpha2 neurons in aged DRGs illustrated altered interactions, including Calca-Calcr, App-Cd74, and Col1a1/Col1a2-Cd44, which may be associated with atherosclerosis. To confirm and further understand the potential role of these cell-cell interactions in DRGs during atherosclerosis progression, we evaluated the interactions and predicted ligand-receptor pairs among CGRP-alpha2 neurons and non-neuronal cell types in both control and RTX-treated DRGs. We observed potential interactions between CGRP-alpha2 neurons and non-neuronal cell types

## RESULTS

both in control and RTX-treated DRGs: neural cell adhesion molecule 1 (Ncam1), laminin, alpha 4 (Lama4), L1cam were identified as the primary ligands of CGRP-alpha2 neurons. Ncam1/2, Cd44, and collagen family genes act as the primary receptors of CGRP-alpha2 neurons (**Figure 48 A**). These genes were associated with numerous essential functions in the NS. For instance, Ncam genes have been shown to be associated with neuronal development, synaptic plasticity, and regeneration; and the activation of Ncam gene can stimulate Ca<sup>2+</sup> influx of neurons [231]. From the ligand-receptor pairs, the interaction pairs Ncam1-Ncam1, Ncam1-Ncam2, and Ncam1-L1cam were reduced after RTX treatment. These results may indicate that RTX treatment affects these potential functions via decreasing these ligand-receptor pairs. However, more evidence is required for further validation.

To investigate the potential relationship between CGRP-alpha2 neurons and atherosclerosis, we compared the cell-cell interaction ligand-receptor pairs of control and RTX-treated DRGs with the interacting pairs of aged WT and Apoe<sup>-/-</sup> DRGs. We observed that the multiple ligand-receptor pairs that were higher aged Apoe<sup>-/-</sup> DRGs were depleted after RTX treatment including interaction of Calca-Calcr1 among CGRP-alpha2 neurons with ECs, interaction of App-Cd74 among CGRP-alpha2 neurons with macrophages and Trem2<sup>hi</sup> macrophages, and interaction of Col1a1/Col1a2-Cd44 among CGRP-alpha2 neurons with SGCs (**Figure 48 B**). In summary, these results suggested that interactions of Calca-Calcr1, App-Cd74, and Col1a1/Col1a2-Cd44 might be associated with atherosclerosis. Based on the analyses of scRNA-seq data at transcriptional levels, RTX treatment can deplete these interactions between CGRP-alpha2 neurons and non-neuronal cells in DRG, which may contribute to the pharmacological effect of RTX treatment on atherosclerotic plaque reduction.

## 4 DISCUSSION

The present study yielded several major findings: immune cells increase in WT DRGs and SCs during aging with significant changes in CD4<sup>+</sup> T<sub>EM</sub> and CD8<sup>+</sup> T<sub>EM</sub> cells; immune cells increase further in TCRb<sup>+</sup> T cells with significant changes in CD8<sup>+</sup> T<sub>EM</sub> cells in DRGs and SCs of aged Apoe<sup>-/-</sup> mice with severe atherosclerosis; using sRNA-seq, we identified five main classes and thirteen cell types in aged DRG based on their transcriptional profiles; these classes and cell types were previously reported in young DRG but were first defined in this study of aged DRGs; macrophages in aged DRG were defined as two distinct types: macrophages that were transcriptionally similar to brain macrophages, and Trem2<sup>hi</sup> macrophages; we identified ten previously reported subtypes of neurons in aged DRGs and we further divided CGRP-alpha neurons into three distinct subtypes, including CGRP-alpha1, CGRP-alpha2, and CGRP-alpha3; among these three CGRP-alpha neurons subtypes, CGRP-alpha2 neurons were more abundant and had a unique transcriptome profile compared to other neuron subtypes; modeling studies suggested that more neuroimmune cell-cell interactions may occur in aged DRGs; the changes in total DRG cells during atherosclerosis progression were observed in aged WT versus Apoe<sup>-/-</sup> mice including a decrease in Apoe<sup>-/-</sup> positively associated genes, higher expressed pathways, and alterations in DRG cell type composition; higher expressed potential cell-cell interactions were observed in aged Apoe<sup>-/-</sup> DRGs mainly in CGRP-alpha2 neurons; enhanced potential cell-cell interactions were identified in aged Apoe<sup>-/-</sup> DRGs with ATLOs when compared to Apoe<sup>-/-</sup> and WT DRG with RLN; the potential cell-cell interactions were particularly pronounced in PEP neuron-associated interactions, with App-Cd74 and Calca-Calcr1 ligand-receptor pairs between DRGs and ATLOs; depletion of Trpv1<sup>+</sup> neurons in DRGs by RTX treatment reduced the percentages CGRP-alpha2 neurons.

Our data should be viewed in the context of the relation between immune cells and brain homeostasis: Adaptive immune cells are known to be present in the CNS of both healthy individuals and patients with inflammatory and degenerative CNS diseases [232-234]. Increasing evidence indicated that the crosstalk between immune system and NS was needed to maintain brain homeostasis [138, 232-236]. Aging was identified as a major risk factor associated with NS inflammation, neurodegenerative diseases and CVDs, including atherosclerosis [52, 232, 237, 238]. Immune cell infiltration in the NS has been reported to be enhanced during aging, possibly due to disruption of the blood-tissue barrier including blood-brain barrier [232, 237]. Importantly, infiltrated cytotoxic CD8<sup>+</sup> T cells were found to cause axon degeneration during aging [233]. However, the systemic alterations of immune cells in the NS, especially in SC and DRG during aging remained unknown. Our data showed that leukocytes increased in aged DRGs and SCs including CD4 T cells, CD8 T cells, naïve T cells, T<sub>CM</sub>, T<sub>EM</sub>, SSC-A<sup>low</sup>CD11b<sup>+</sup>, and SSC-A<sup>low</sup>CD11c<sup>+</sup> myeloid cells. In the CNS, CD8<sup>+</sup> T cells had been associated with neuronal injury via secreting inflammatory cytokines [233, 239]. Moreover, CD8<sup>+</sup> T cells had been reported to increase in neurodegenerative disease-

## DISCUSSION

affected hippocampi, and the abundance of CD8<sup>+</sup> T<sub>EM</sub> were increased in blood during aging [240, 241]. Similarly, we observed an expansion of CD8<sup>+</sup> T cells infiltration during aging in the SC. During T cell aging, mitochondrial dysfunction, TCR repertoire reduction, naïve and memory T cell imbalance were suggested to explain the aging-associated changes of T cells [242]. For instance, the increase of CD8<sup>+</sup> T cells mitochondrial reactive oxygen species were found to be associated with old age [243-246]. In addition, CD8<sup>+</sup> T<sub>EM</sub> cells had been reported to transmigrate more readily across blood-brain barrier-EC than non-CD8<sup>+</sup> T<sub>EM</sub> [247]. Our data showed that naïve CD8<sup>+</sup> T cells and CD8<sup>+</sup> T<sub>CM</sub> were rare in DRGs and SC but that the number of CD8<sup>+</sup> T<sub>EM</sub> cells increased in DRGs and SCs. These results suggested that CD8<sup>+</sup> T<sub>EM</sub> might be the key T cell subpopulation in DRGs and SCs during aging. In a previous study, we observed the atherosclerosis-related inflammation of nerves and ganglia of the PNS, characterized by increased infiltration of macrophages, T cells and mast cells infiltration increased in aged Apoe<sup>-/-</sup> DRG compared to WT DRG [52]. Here, we examined leukocytes and their subpopulations in DRGs and SCs of young, adult, and aged Apoe<sup>-/-</sup> mice, as well as age-matched WT mice. The results revealed that total leukocyte infiltration in the NS increased in aged Apoe<sup>-/-</sup> compared to WT mice, especially in aged Apoe<sup>-/-</sup> mice with advanced atherosclerosis. FACS analyses of leukocyte subtypes showed that the enhanced leukocyte infiltration in the NS during atherosclerosis progression was mainly attributable to an increase of TCRb<sup>+</sup> T cells, including CD4<sup>+</sup> T cells, CD8<sup>+</sup> T cells and activated T<sub>EM</sub> cells. These results suggested that the atherosclerosis-related inflammation alterations in the NS were primarily driven by changes in CD8<sup>+</sup> T<sub>EM</sub> cells and predominantly occurred in aged mice with severe atherosclerosis rather than in young and adult mice.

Single-cell molecular profiles based on RNA, chromatin accessibility, or select protein signatures provide a more profound comprehension of cell type composition in the NS [112, 248]. Our previous study demonstrated that abdominal adventitia nociceptive afferents entered the CNS via T6-T13 DRGs and were traced to higher brain regions [52]. Transcriptomics profiles obtained using scRNA-seq demonstrated that multiple sensory neuron subsets innervate LNs, and the neurons were predominantly peptidergic nociceptors [76]. Understanding the DRG cell types could provide deeper insight into distinct DRG neuronal-related neuroimmune responses during atherosclerosis. However, the cell type composition of aged DRGs was unknown. For instance, in the mouse PNS, cells from the brachial plexus and sciatic nerves had been characterized as Schwann cells, fibroblasts, vascular cells, and hematopoietic cells using scRNA-seq [66]. In a cellular atlas of the forebrain and midbrain, brain cells were classified into 25 distinct cell types, including neurons, glial cells, vascular cells, neuroendocrine cells, ependymocytes, and immune cells [185]. In aged DRGs, we identified live DRG cells as five primary classes (neurons, immune cells, vascular cells, fibroblasts, glial cells) and thirteen cell types (neuron, T cell, macrophage, Trem2<sup>hi</sup> macrophage, neutrophil, EC, pericyte, fibroblast1, fibroblast2, fibroblast3, SGC, mSch, nmSch). Enriched GO terms for each cell type's marker genes revealed their respective transcriptional profiles and potential specialized functions.

## DISCUSSION

Based on these outcomes and the transcriptional characteristics of each cell type, we constructed an unbiased single-cell atlas of aged DRGs and demonstrated the distinct heterogeneity of aged DRGs at the single-cell resolution.

Macrophage has been shown to constitute a heterogeneous population within the NS compartments during autoimmune inflammation, exhibiting tissue-specific functions [137, 197]. CNS-associated macrophages are characterized by the high expression of marker genes including *Mrc1*, *Pf4*, *Ms4a7*, *Stab1*, and *Cbr2*, while they did not express microglia marker genes. In addition, MHC class II molecules were significantly higher expressed in CNS-associated macrophages, highlighting their critical role in antigen presentation during neuroinflammation of CNS-associated macrophages [137]. Microglia are regarded as brain tissue-resident macrophages [249] and they specifically express the marker genes including *P2ry12*, *Tmem119*, *Sparc*, and *Olfml3*. Microglia functions were associated with the secretion of proinflammatory mediators and the removal of debris, facilitating proper remyelination [137]. In the PNS, resident-macrophages from DRGs, vagal nerves, and sciatic nerves were reported to express the marker genes including *Cx3cr1*, *Csf1r*, *Cd64* and several signature genes of microglia such as *P2ry12*, *Siglech*, *Tmem119*, and *Trem2* [250]. Neuron-associated macrophages were found to express *Adgre1*, *Csf1r*, *Cx3cr1*, *Fn1* and *Ciita*. Among these marker genes, *Cx3cr1* and *Adgre1*, which encode F4/80, are expressed across all macrophage types. *Csf1r* was reported as a marker of tissue-resident macrophages, it has been reported that *Csf1r*-expressing cells were reported mainly originated from the CSF1R-expressing yolk-sac progenitors at E8.5 developmental stage [251]. *Ciita* is the transactivator of MHC class II, which was reported to be related with neuroinflammation and neurodegeneration in the NS [252], indicating the potential functions of neuron-associated macrophages. These macrophages were implicated in the uptake and degradation of norepinephrine [85]. In our study of aged DRGs, macrophages were categorized into two types: macrophage and *Trem2*<sup>hi</sup> macrophages. Integration analysis of DRG macrophages and brain macrophages revealed that the DRG macrophages exhibited the highest expression similarity with brain macrophages, rather than microglia and macrophages from lymph nodes (**Figure 20, 21**). These results suggested potential functional similarities between DRG and brain macrophages. Additionally, DRG macrophages were observed to be associated with functions such as transcripts of MHC-I and MHC-II antigen processing and phagocytosis (**Figure 21**). In the brain, microglial expression of *trem2* was related to anti-inflammatory IL-4 signaling pathways. *Trem2* knockdown in microglia led to a decrease in the expression of IL-4-induced anti-inflammatory genes, including *Arg1*, *Ap1b1*, and *Dusp4*, which were identified as M2 macrophage-like [190, 253]. *Trem2* deficiency in macrophages impaired energy pathways and lower expressed ATP levels, demonstrating that *Trem2* was associated with energy metabolism [196]. Our scRNA-seq data of *Trem2*<sup>hi</sup> macrophage presented consistent findings regarding anti-inflammatory and energy metabolism functions in aged DRGs (**Figure 20, 21**). Further research is needed to elucidate the distinct characteristics of the two macrophage types in aged DRGs.

## DISCUSSION

DRG neurons were the primary sensory neurons in DRGs [112, 119, 123, 124, 254]. DRG neurons have been classified into four main categories: PEP neurons, NP neurons, NF neurons and TH neurons [119]. Within our DRG scRNA-seq datasets, young WT DRG neurons were divided into fifteen cell types [124] (**Figure 7, 22, 23**). Kupari et al. [126] observed that CGRP-alpha, CGRP-beta, CGRP-gamma, and CGRP-epsilon in the young DRG neurons could be grouped into a single class, aligning with the PEP1 cluster in a reported scRNA-seq dataset including CGRP-zeta and CGRP-eta in the young DRG scRNA-seq neurons dataset corresponded to the PEP2 cluster in the scRNA-seq dataset clustering results of Usoskin et al. [126]. These findings suggested that the same neuron subtype might have distinct designations in studies utilizing different clustering criteria, yet the transcriptional profiles remained consistent between studies investigating the same neuron subtype. Furthermore, different DRG scRNA-seq datasets demonstrated that DRG neuronal marker expression remained consistent across different ages [76, 119, 124]. Consequently, determining the neuron compositions of aged DRGs at single-cell resolution was feasible despite low cell numbers based on previously reported DRG neuron scRNA-seq studies, even though cell type compositions had not been previously investigated in aged DRG. In our study, we first classified all cell types in aged DRGs, then performed neuron subclustering steps to reveal detailed neuron subtype information. Due to the limited number of aged DRG neurons, accurately distinguishing them into distinct neuron subtypes was challenging. We employed a well-established neuron subclustering method from the literature to obtain precise information on neuron subtypes [76]. Five neuron main classes, which have been reported (including PEP, NP, C-LTMR, TrpM8), and ten previously reported neuron subtypes (CGRP-alpha, CGRP-beta, CGRP-gamma, CGRP-epsilon, CGRP-zeta, Adelta-LTMR, CLTMR, CGRP-theta, NP-nociceptor, Sst, and TrpM8.) were defined in aged DRGs. The clustering results were validated by comparing gene expression similarities with reported young DRG neuron scRNA-seq datasets, which was previously confirmed using RNA fluorescent in situ hybridization [124]. In addition, we further classified the CGRP-alpha into three novel subtypes: CGRP-alpha1, CGRP-alpha2, and CGRP-alpha3 neurons, based on the transcriptional profiles in aged DRGs, differed from the young DRG neuron scRNA-seq dataset (**Figure 22, 25, 26, 27**). These findings enabled us to construct DRG neuronal atlases, presenting the transcriptional profiles of DRG neurons at single-cell resolution. Additionally, our results also offered valuable insights for further exploring the alterations in DRG neurons during aging and under other disease conditions.

Throughout the development of atherosclerosis, neuroimmune cardiovascular interactions form a structural artery-brain connection. This link has been established as abdominal adventitia nociceptive afferents that reach the CNS through the T6-T13 DRGs and subsequently extend to more advanced brain regions [52]. Our comprehensive investigations, including FACS analyses, have shed light on immune cells in the NS. Furthermore, scRNA-seq data obtained from both aged WT and Apoe<sup>-/-</sup> DRGs have facilitated the exploration of transcriptional alterations during

## DISCUSSION

atherosclerosis progression at an unparalleled single-cell resolution. This in-depth approach enables a more profound understanding of the molecular mechanisms and dynamic changes that occur within DRGs as related to atherosclerosis.

To determine potential atherosclerosis-related transcriptional alterations within DRGs, we initially computed Apoe-associated genes and observed a decrease in the expression of Apoe positively associated genes during atherosclerosis progression. The comparison of DRG transcriptomes and GSEA showed that transcripts related to functions such as ribosome, immunity, axon growth, and neurotransmitter exocytosis, were higher or lower expressed in aged WT versus Apoe<sup>-/-</sup> DRGs (**Figure 29, 30**). As Apoe positively- and negatively-associated genes were relatively highly expressed in macrophages and neurons, we hypothesize that the transcriptional alterations mainly occurred in macrophages and neurons.

In aged DRGs, we observed upregulation in the percentages of neurons and macrophages. Among neuron subtypes, the most significant changes were an increase in CGRP-alpha2 neurons and a decrease in CGRP-alpha1 neurons. Furthermore, the cell-cell communications among CGRP-alpha neurons and all non-neuronal cells confirmed that CGRP-alpha2 neurons were responsible for the majority of higher expressed alterations in aged Apoe<sup>-/-</sup> DRGs (**Figure 30-33**). These findings strongly suggest an association between CGRP-alpha2 neurons and atherosclerosis in aged DRGs. As previously described, CGRP-alpha2 neurons were an abundant subtype in aged DRGs, exhibiting specificity in ion channel genes, neurotransmitter receptors, and GPCR genes. GSEA results demonstrated that functions such as cation binding, peptide biosynthetic processes, and ATP synthase were altered during atherosclerosis progression in aged DRGs. Furthermore, the analysis of cell-cell interaction pairs indicated that the altered functions of CGRP-alpha2 might be associated with the genes App, Calca, and Cd44 (**Figure 35-37**). The cell-cell communication analysis between DRGs and ATLO or control tissue RLN revealed that our study corroborated the connections between DRGs and atherosclerosis. Our modeling data support the hypothesis that PEP neurons contribute to the majority of cell-cell interactions during atherosclerosis progression, with interactions such as APP-Cd74 possibly being significant (**Figure 38, 39, 40**). Collectively, these findings outlined the transcriptional changes in DRGs during atherosclerosis progression and underscored the crucial role of CGRP-alpha2 in the progression of atherosclerosis.

Trpv1<sup>+</sup> neurons represent a subtype of DRG sensory neurons that are implicated in various physiological and pathological processes such as nociception, pain perception, immune responses, and inflammation. Our scRNA-seq data demonstrated a high expression of Trpv1 in CGRP-alpha2 neurons (**Figure 26, 41**). The utilization of RTX to ablate Trpv1<sup>+</sup> neurons has emerged as a valuable approach to study effects of Trpv1<sup>+</sup> neurons in different biological contexts [229, 230, 255, 256]. In order to gain a deeper understanding of the functions of neurons in DRGs, particularly those of

## DISCUSSION

CGRP- $\alpha$ 2 neurons, during the progression of atherosclerosis, we employed RTX to selectively ablate Trpv1<sup>+</sup> neurons. Following the ablation of Trpv1<sup>+</sup> neurons, we conducted scRNA-seq analysis of T6-T13 DRG cells to further elucidate the molecular and functional consequences of Trpv1<sup>+</sup> neuron ablation (**Figure 42**). The results from this analysis form a blueprint to further provide new insights into the intricate relationships between sensory neurons and the development of atherosclerosis.

Our scRNA-seq data substantiated that Trpv1 was expressed in DRG neurons and the majority of the Trpv1<sup>+</sup> neurons in DRGs were ablated after RTX treatment (**Figure 43**). The most prominent change in DRG neuronal subtypes showed a decline of CGRP- $\alpha$ 2 neurons after RTX treatment. The results of cell-cell communication modeling revealed a reduction in CGRP- $\alpha$ 2-associated interactions subsequent to RTX treatment. GSEA data pointed to metabolic functions, such as ATP metabolic processes, peptide biosynthetic processes, and ribosome regulation, being affected post-RTX treatment. These functions were also modulated in aged WT compared to Apoe<sup>-/-</sup> DRGs, indicating that the ablation of Trpv1<sup>+</sup> neurons in DRG might also eliminate several CGRP- $\alpha$ 2-specific functions altered during atherosclerosis progression. In summary, scRNA-seq data of control and RTX treated DRGs supported several new concepts: **(i)** Trpv1 was primarily expressed in neurons in DRGs, CGRP- $\alpha$ 2 neurons were the most abundant neuron subtype in all Trpv1<sup>+</sup> neurons; **(ii)** RTX treatment can effectively ablate the Trpv1<sup>+</sup> neuron in DRGs, particularly CGRP- $\alpha$ 2 neurons; and **(iii)** CGRP- $\alpha$ 2 neurons-associated cell-cell communications and specific function are decreased after RTX treatment, and these potential functions might be related to atherosclerosis within DRGs.

### 4.1 Outlook

This thesis systemically analyzed the alterations of immune cell infiltration within the NS during aging and during atherosclerosis progression. It provides a principal blueprint to define the role of specific components of the PNS in regulating atherosclerosis progression and pointed to a role of specific immune cells including T cells and macrophages.

Despite constructing the aged DRG atlas at single-cell resolutions and providing a transcriptional survey of aged DRGs during atherosclerosis, it is essential to validate these scRNA-seq findings, including the clustering results and neuroimmune cell-cell communication modeling data. For instance, RNA-fluorescence in situ hybridization is needed to confirm the atlas. Furthermore, due to the limited cell numbers analyzed, certain conclusions cannot be definitively drawn from the current data. Also, this study lacks validation of our findings in human DRG samples during atherosclerosis, and it is crucial to design further experiments to investigate the functional effects within DRGs during atherosclerosis progression.

## **DISCUSSION**

This thesis will form the basis to address the following major questions in future studies: (i) employ RNA-fluorescence in situ hybridization to validate the neuronal subtype of CGRP-alpha2 neurons; (ii) investigate the functions of CGRP-alpha2 neuron-associated interactions and genes; (iii) examine the roles of non-neuronal cell changes, excluding neurons and macrophages, in DRGs during atherosclerosis progression; (iv) explore the connections between DRGs and aorta cell types, including endothelial cells (ECs), smooth muscle cells, and fibroblasts.

## REFERENCES

## REFERENCES

1. Roth, G.A., et al., *Global burden of cardiovascular diseases and risk factors, 1990–2019: update from the GBD 2019 study*. Journal of the American College of Cardiology, 2020. **76**(25): p. 2982-3021.
2. Disease, G.B.D., I. Injury, and C. Prevalence, *Global, regional, and national incidence, prevalence, and years lived with disability for 354 diseases and injuries for 195 countries and territories, 1990-2017: a systematic analysis for the Global Burden of Disease Study 2017*. Lancet, 2018. **392**(10159): p. 1789-1858.
3. Gistera, A. and G.K. Hansson, *The immunology of atherosclerosis*. Nat Rev Nephrol, 2017. **13**(6): p. 368-380.
4. Mohanta, S.K., et al., *Artery Tertiary Lymphoid Organs Contribute to Innate and Adaptive Immune Responses in Advanced Mouse Atherosclerosis*. Circ Res, 2014. **114**(11): p. 1772-1787.
5. Moos, M.P., et al., *The lamina adventitia is the major site of immune cell accumulation in standard chow-fed apolipoprotein E-deficient mice*. Arterioscler Thromb Vasc Biol, 2005. **25**(11): p. 2386-91.
6. Kasikara, C., et al., *The role of non-resolving inflammation in atherosclerosis*. J Clin Invest, 2018. **128**(7): p. 2713-2723.
7. Back, M., et al., *Inflammation and its resolution in atherosclerosis: mediators and therapeutic opportunities*. Nat Rev Cardiol, 2019. **16**(7): p. 389-406.
8. Galkina, E. and K. Ley, *Immune and inflammatory mechanisms of atherosclerosis (\*)*. Annu Rev Immunol, 2009. **27**: p. 165-97.
9. Glass, C.K. and J.L. Witztum, *Atherosclerosis. the road ahead*. Cell, 2001. **104**(4): p. 503-16.
10. Cottet, J. and M. Lenoir, *Two thousand years of historical study on the words atheroma, atheromatosis, atherosclerosis, arteriosclerosis*. Bulletin de L'academie Nationale de Medecine, 1992. **176**(9): p. 1385-90; discussion 1390.
11. Ross, R., J. Glomset, and L. Harker, *Response to injury and atherogenesis*. Am J Pathol, 1977. **86**(3): p. 675-84.
12. Hansson, G.K. and A. Hermansson, *The immune system in atherosclerosis*. Nat Immunol, 2011. **12**(3): p. 204-12.
13. Weih, F., et al., *Control of dichotomic innate and adaptive immune responses by artery tertiary lymphoid organs in atherosclerosis*. Front Physiol, 2012. **3**: p. 226.
14. Nakashima, Y., et al., *ApoE-deficient mice develop lesions of all phases of atherosclerosis throughout the arterial tree*. Arterioscler Thromb, 1994. **14**(1): p. 133-40.
15. Hansson, G.K., *Inflammation, atherosclerosis, and coronary artery disease*. N Engl J Med, 2005. **352**(16): p. 1685-95.
16. Grabner, R., et al., *Lymphotoxin beta receptor signaling promotes tertiary lymphoid organogenesis in the aorta adventitia of aged ApoE<sup>-/-</sup> mice*. J Exp Med, 2009. **206**(1): p. 233-48.
17. Binder, C.J., et al., *Innate and acquired immunity in atherogenesis*. Nat Med, 2002. **8**(11): p. 1218-26.
18. Ross, R., *Atherosclerosis--an inflammatory disease*. N Engl J Med, 1999. **340**(2): p. 115-26.
19. Moore, K.J. and I. Tabas, *Macrophages in the pathogenesis of atherosclerosis*. Cell, 2011. **145**(3): p. 341-55.
20. Libby, P., A.H. Lichtman, and G.K. Hansson, *Immune effector mechanisms implicated in atherosclerosis: from mice to humans*. Immunity, 2013. **38**(6): p. 1092-104.
21. Libby, P., *Mechanisms of acute coronary syndromes and their implications for therapy*. N Engl J Med, 2013. **368**(21): p. 2004-13.
22. Hansson, G.K. and P. Libby, *The immune response in atherosclerosis: a double-edged sword*. Nat Rev Immunol, 2006. **6**(7): p. 508-19.
23. Weber, C., A. Zernecke, and P. Libby, *The multifaceted contributions of leukocyte subsets to atherosclerosis: lessons from mouse models*. Nat Rev Immunol, 2008. **8**(10): p. 802-15.

## REFERENCES

24. Libby, P., *Inflammation in atherosclerosis*. Nature, 2002. **420**(6917): p. 868-74.
25. Weber, C. and H. Noels, *Atherosclerosis: current pathogenesis and therapeutic options*. Nat Med, 2011. **17**(11): p. 1410-22.
26. Lutgens, E., et al., *Atherosclerotic plaque rupture: local or systemic process?* Arterioscler Thromb Vasc Biol, 2003. **23**(12): p. 2123-30.
27. Libby, P., et al., *Atherosclerosis*. Nat Rev Dis Primers, 2019. **5**(1): p. 56.
28. Wolf, D. and K. Ley, *Immunity and Inflammation in Atherosclerosis*. Circ Res, 2019. **124**(2): p. 315-327.
29. Subramanian, M., et al., *Treg-mediated suppression of atherosclerosis requires MYD88 signaling in DCs*. J Clin Invest, 2013. **123**(1): p. 179-88.
30. Zhou, X., et al., *Adoptive transfer of CD4+ T cells reactive to modified low-density lipoprotein aggravates atherosclerosis*. Arterioscler Thromb Vasc Biol, 2006. **26**(4): p. 864-70.
31. Ammirati, E., et al., *Effector Memory T cells Are Associated With Atherosclerosis in Humans and Animal Models*. J Am Heart Assoc, 2012. **1**(1): p. 27-41.
32. Murray, P.J. and T.A. Wynn, *Protective and pathogenic functions of macrophage subsets*. Nat Rev Immunol, 2011. **11**(11): p. 723-37.
33. Butcher, M.J. and E.V. Galkina, *Phenotypic and functional heterogeneity of macrophages and dendritic cell subsets in the healthy and atherosclerosis-prone aorta*. Front Physiol, 2012. **3**: p. 44.
34. Mueller, K., *Inflammation. Inflammation's yin-yang. Introduction*. Science, 2013. **339**(6116): p. 155.
35. Saigusa, R., H. Winkels, and K. Ley, *T cell subsets and functions in atherosclerosis*. Nat Rev Cardiol, 2020. **17**(7): p. 387-401.
36. Sage, A.P., et al., *The role of B cells in atherosclerosis*. Nat Rev Cardiol, 2019. **16**(3): p. 180-196.
37. Fani, L., et al., *The association of innate and adaptive immunity, subclinical atherosclerosis, and cardiovascular disease in the Rotterdam Study: A prospective cohort study*. PLoS Med, 2020. **17**(5): p. e1003115.
38. He, S., et al., *Gut intraepithelial T cells calibrate metabolism and accelerate cardiovascular disease*. Nature, 2019. **566**(7742): p. 115-119.
39. Cochain, C., et al., *Single-Cell RNA-Seq Reveals the Transcriptional Landscape and Heterogeneity of Aortic Macrophages in Murine Atherosclerosis*. Circ Res, 2018. **122**(12): p. 1661-1674.
40. Winkels, H., et al., *Atlas of the Immune Cell Repertoire in Mouse Atherosclerosis Defined by Single-Cell RNA-Sequencing and Mass Cytometry*. Circ Res, 2018. **122**(12): p. 1675-1688.
41. Yin, C., et al., *Artery Tertiary Lymphoid Organs: Powerhouses of Atherosclerosis Immunity*. Frontiers in immunology, 2016. **7**: p. 387.
42. van Gils, J.M., et al., *The neuroimmune guidance cue netrin-1 promotes atherosclerosis by inhibiting the emigration of macrophages from plaques*. Nat Immunol, 2012. **13**(2): p. 136-43.
43. van Gils, J.M., et al., *Endothelial expression of guidance cues in vessel wall homeostasis dysregulation under proatherosclerotic conditions*. Arterioscler Thromb Vasc Biol, 2013. **33**(5): p. 911-9.
44. Wanschel, A., et al., *Neuroimmune guidance cue Semaphorin 3E is expressed in atherosclerotic plaques and regulates macrophage retention*. Arterioscler Thromb Vasc Biol, 2013. **33**(5): p. 886-93.
45. Yukawa, K., et al., *Deletion of Sema4D gene reduces intimal neovascularization and plaque growth in apolipoprotein E-deficient mice*. Int J Mol Med, 2010. **26**(1): p. 39-44.
46. Randolph, G.J. and E.L. Gautier, *Emerging roles of neural guidance molecules in atherosclerosis: sorting out the complexity*. Arterioscler Thromb Vasc Biol, 2013. **33**(5): p. 882-3.
47. Funk, S.D. and A.W. Orr, *Ephs and ephrins resurface in inflammation, immunity, and atherosclerosis*. Pharmacol Res, 2013. **67**(1): p. 42-52.

## REFERENCES

48. Majesky, M.W., et al., *The adventitia: a dynamic interface containing resident progenitor cells*. *Arterioscler Thromb Vasc Biol*, 2011. **31**(7): p. 1530-9.
49. Stenmark, K.R., et al., *The adventitia: essential regulator of vascular wall structure and function*. *Annu Rev Physiol*, 2013. **75**: p. 23-47.
50. Houtkamp, M.A., et al., *Adventitial infiltrates associated with advanced atherosclerotic plaques: structural organization suggests generation of local humoral immune responses*. *J Pathol*, 2001. **193**(2): p. 263-9.
51. Moreno, P.R., et al., *Intimomedial interface damage and adventitial inflammation is increased beneath disrupted atherosclerosis in the aorta: implications for plaque vulnerability*. *Circulation*, 2002. **105**(21): p. 2504-11.
52. Mohanta, S.K., et al., *Neuroimmune cardiovascular interfaces control atherosclerosis*. *Nature*, 2022. **605**(7908): p. 152-159.
53. Costa, M., S.J. Brookes, and G.W. Hennig, *Anatomy and physiology of the enteric nervous system*. *Gut*, 2000. **47 Suppl 4**: p. iv15-9; discussion iv26.
54. Zeng, H. and J.R. Sanes, *Neuronal cell-type classification: challenges, opportunities and the path forward*. *Nat Rev Neurosci*, 2017. **18**(9): p. 530-546.
55. Kastriti, M.E. and I. Adameyko, *Specification, plasticity and evolutionary origin of peripheral glial cells*. *Curr Opin Neurobiol*, 2017. **47**: p. 196-202.
56. Jessen, K.R., *Glial cells*. *The international journal of biochemistry & cell biology*, 2004. **36**(10): p. 1861-1867.
57. Jessen, K.R. and R. Mirsky, *The origin and development of glial cells in peripheral nerves*. *Nat Rev Neurosci*, 2005. **6**(9): p. 671-82.
58. Lavdas, A.A. and R. Matsas, *Schwann Cell Morphology*, in *Encyclopedia of Neuroscience*, L.R. Squire, Editor. 2009, Academic Press: Oxford. p. 475-484.
59. Boerboom, A., et al., *Molecular Mechanisms Involved in Schwann Cell Plasticity*. *Front Mol Neurosci*, 2017. **10**: p. 38.
60. Hanani, M. and D.C. Spray, *Emerging importance of satellite glia in nervous system function and dysfunction*. *Nat Rev Neurosci*, 2020. **21**(9): p. 485-498.
61. Pannese, E., *Biology and pathology of perineuronal satellite cells in sensory ganglia*, in *Biology and Pathology of Perineuronal Satellite Cells in Sensory Ganglia*. 2018, Springer. p. 1-63.
62. Afroz, S., et al., *CGRP Induces Differential Regulation of Cytokines from Satellite Glial Cells in Trigeminal Ganglia and Orofacial Nociception*. *International Journal of Molecular Sciences*, 2019. **20**(3): p. 711.
63. Mitterreiter, J.G., et al., *Satellite glial cells in human trigeminal ganglia have a broad expression of functional Toll-like receptors*. *Eur J Immunol*, 2017. **47**(7): p. 1181-1187.
64. Takeda, M., M. Takahashi, and S. Matsumoto, *Contribution of the activation of satellite glia in sensory ganglia to pathological pain*. *Neurosci Biobehav Rev*, 2009. **33**(6): p. 784-92.
65. Weick, M., et al., *P2 receptors in satellite glial cells in trigeminal ganglia of mice*. *Neuroscience*, 2003. **120**(4): p. 969-77.
66. Wolbert, J., et al., *Redefining the heterogeneity of peripheral nerve cells in health and autoimmunity*. *Proc Natl Acad Sci U S A*, 2020. **117**(17): p. 9466-9476.
67. Keeler, A.B., et al., *A developmental atlas of somatosensory diversification and maturation in the dorsal root ganglia by single-cell mass cytometry*. *Nature Neuroscience*, 2022. **25**(11): p. 1543-1558.
68. Compston, A. and A. Coles, *Multiple sclerosis*. *Lancet*, 2008. **372**(9648): p. 1502-17.
69. Marin, I. and J. Kipnis, *Learning and memory ... and the immune system*. *Learn Mem*, 2013. **20**(10): p. 601-6.
70. Muller, N. and M.J. Schwarz, *Immune System and Schizophrenia*. *Curr Immunol Rev*, 2010. **6**(3): p. 213-220.
71. Heppner, F.L., R.M. Ransohoff, and B. Becher, *Immune attack: the role of inflammation in Alzheimer disease*. *Nat Rev Neurosci*, 2015. **16**(6): p. 358-72.

## REFERENCES

72. Yin, C., et al., *ApoE attenuates unresolvable inflammation by complex formation with activated CIq*. Nature Medicine, 2019. **25**(3): p. 496-506.
73. Wong, C.H., et al., *Functional innervation of hepatic iNKT cells is immunosuppressive following stroke*. Science, 2011. **334**(6052): p. 101-5.
74. Udit, S., K. Blake, and I.M. Chiu, *Somatosensory and autonomic neuronal regulation of the immune response*. Nature Reviews Neuroscience, 2022: p. 1-15.
75. Chiu, I.M., et al., *Bacteria activate sensory neurons that modulate pain and inflammation*. Nature, 2013. **501**(7465): p. 52-7.
76. Huang, S., et al., *Lymph nodes are innervated by a unique population of sensory neurons with immunomodulatory potential*. Cell, 2021. **184**(2): p. 441-459.e25.
77. Pinho-Ribeiro, F.A., W.A. Verri, Jr., and I.M. Chiu, *Nociceptor Sensory Neuron-Immune Interactions in Pain and Inflammation*. Trends Immunol, 2017. **38**(1): p. 5-19.
78. Chiu, I.M., C.A. von Hehn, and C.J. Woolf, *Neurogenic inflammation and the peripheral nervous system in host defense and immunopathology*. Nat Neurosci, 2012. **15**(8): p. 1063-7.
79. Lai, N.Y., K. Mills, and I.M. Chiu, *Sensory neuron regulation of gastrointestinal inflammation and bacterial host defence*. J Intern Med, 2017. **282**(1): p. 5-23.
80. Mazzone, S.B. and B.J. Udem, *Vagal Afferent Innervation of the Airways in Health and Disease*. Physiol Rev, 2016. **96**(3): p. 975-1024.
81. Pavlov, V.A., S.S. Chavan, and K.J. Tracey, *Molecular and Functional Neuroscience in Immunity*. Annu Rev Immunol, 2018. **36**: p. 783-812.
82. Calvillo, L., et al., *Neuroimmune crosstalk in the pathophysiology of hypertension*. Nature Reviews Cardiology, 2019. **16**(8): p. 476-490.
83. Scanzano, A. and M. Cosentino, *Adrenergic regulation of innate immunity: a review*. Front Pharmacol, 2015. **6**: p. 171.
84. Loza, M.J., et al., *beta-Agonist enhances type 2 T-cell survival and accumulation*. J Allergy Clin Immunol, 2007. **119**(1): p. 235-44.
85. Pirzgalska, R.M., et al., *Sympathetic neuron-associated macrophages contribute to obesity by importing and metabolizing norepinephrine*. Nat Med, 2017. **23**(11): p. 1309-1318.
86. Tracey, K.J., *Neurons Are the Inflammatory Problem*. Cell, 2018. **173**(5): p. 1066-1068.
87. Tracey, K.J., *The inflammatory reflex*. Nature, 2002. **420**(6917): p. 853-9.
88. Schiller, M., T.L. Ben-Shanan, and A. Rolls, *Neuronal regulation of immunity: why, how and where?* Nature Reviews Immunology, 2021. **21**(1): p. 20-36.
89. Tracey, K.J., *Reflex control of immunity*. Nat Rev Immunol, 2009. **9**(6): p. 418-28.
90. Baral, P., et al., *Nociceptor sensory neurons suppress neutrophil and gammadelta T cell responses in bacterial lung infections and lethal pneumonia*. Nat Med, 2018. **24**(4): p. 417-426.
91. Kihara, N., et al., *Vanilloid receptor-1 containing primary sensory neurones mediate dextran sulphate sodium induced colitis in rats*. Gut, 2003. **52**(5): p. 713-9.
92. Pinho-Ribeiro, F.A., et al., *Blocking Neuronal Signaling to Immune Cells Treats Streptococcal Invasive Infection*. Cell, 2018. **173**(5): p. 1083-1097 e22.
93. Parati, G. and M. Esler, *The human sympathetic nervous system: its relevance in hypertension and heart failure*. Eur Heart J, 2012. **33**(9): p. 1058-66.
94. Navar, L.G., *Counterpoint: Activation of the intrarenal renin-angiotensin system is the dominant contributor to systemic hypertension*. J Appl Physiol (1985), 2010. **109**(6): p. 1998-2000; discussion 2015.
95. Avolio, E., et al., *Role of Brain Neuroinflammatory Factors on Hypertension in the Spontaneously Hypertensive Rat*. Neuroscience, 2018. **375**: p. 158-168.
96. Eze, U.C., et al., *Single-cell atlas of early human brain development highlights heterogeneity of human neuroepithelial cells and early radial glia*. Nature Neuroscience, 2021. **24**(4): p. 584-594.
97. Ranzoni, A.M., et al., *Integrative Single-Cell RNA-Seq and ATAC-Seq Analysis of Human Developmental Hematopoiesis*. Cell Stem Cell, 2021. **28**(3): p. 472-487.e7.

## REFERENCES

98. Tang, F., et al., *mRNA-Seq whole-transcriptome analysis of a single cell*. Nat Methods, 2009. **6**(5): p. 377-82.
99. Svensson, V., R. Vento-Tormo, and S.A. Teichmann, *Exponential scaling of single-cell RNA-seq in the past decade*. Nat Protoc, 2018. **13**(4): p. 599-604.
100. Reuter, J.A., D.V. Spacek, and M.P. Snyder, *High-throughput sequencing technologies*. Mol Cell, 2015. **58**(4): p. 586-97.
101. Islam, S., et al., *Characterization of the single-cell transcriptional landscape by highly multiplex RNA-seq*. Genome Res, 2011. **21**(7): p. 1160-7.
102. Soumillon, M., et al., *Characterization of directed differentiation by high-throughput single-cell RNA-Seq*. BioRxiv, 2014: p. 003236.
103. Ramskold, D., et al., *Full-length mRNA-Seq from single-cell levels of RNA and individual circulating tumor cells*. Nat Biotechnol, 2012. **30**(8): p. 777-82.
104. Picelli, S., et al., *Smart-seq2 for sensitive full-length transcriptome profiling in single cells*. Nat Methods, 2013. **10**(11): p. 1096-8.
105. Macosko, E.Z., et al., *Highly Parallel Genome-wide Expression Profiling of Individual Cells Using Nanoliter Droplets*. Cell, 2015. **161**(5): p. 1202-14.
106. Zheng, G.X., et al., *Haplotyping germline and cancer genomes with high-throughput linked-read sequencing*. Nat Biotechnol, 2016. **34**(3): p. 303-11.
107. Bagnoli, J.W., et al., *Sensitive and powerful single-cell RNA sequencing using mcSCR-seq*. Nature Communications, 2018. **9**(1): p. 2937.
108. Zappia, L., B. Phipson, and A. Oshlack, *Exploring the single-cell RNA-seq analysis landscape with the scRNA-tools database*. PLoS Comput Biol, 2018. **14**(6): p. e1006245.
109. Lun, A., D. McCarthy, and J. Marioni, *A step-by-step workflow for low-level analysis of single-cell RNA-seq data with Bioconductor*. F1000Research, 2016. **5**(2122): p. 2122.
110. Perraudeau, F., et al., *Bioconductor workflow for single-cell RNA sequencing: Normalization, dimensionality reduction, clustering, and lineage inference*. F1000Research, 2017. **6**(1158): p. 1158.
111. Stuart, T., et al., *Comprehensive Integration of Single-Cell Data*. Cell, 2019. **177**(7): p. 1888-1902 e21.
112. Zeisel, A., et al., *Molecular Architecture of the Mouse Nervous System*. Cell, 2018. **174**(4): p. 999-1014 e22.
113. Toma, J.S., et al., *Peripheral Nerve Single-Cell Analysis Identifies Mesenchymal Ligands that Promote Axonal Growth*. eNeuro, 2020. **7**(3): p. ENEURO.0066-20.2020.
114. Lawson, S.N. and P.J. Waddell, *Soma neurofilament immunoreactivity is related to cell size and fibre conduction velocity in rat primary sensory neurons*. J Physiol, 1991. **435**: p. 41-63.
115. Ernfors, P., K.F. Lee, and R. Jaenisch, *Mice lacking brain-derived neurotrophic factor develop with sensory deficits*. Nature, 1994. **368**(6467): p. 147-50.
116. Rees, C.L., C.M. White, and G.A. Ascoli, *Neurochemical Markers in the Mammalian Brain: Structure, Roles in Synaptic Communication, and Pharmacological Relevance*. Curr Med Chem, 2017. **24**(28): p. 3077-3103.
117. Beyene, A.G., S.J. Yang, and M.P. Landry, *Review Article: Tools and trends for probing brain neurochemistry*. J Vac Sci Technol A, 2019. **37**(4): p. 040802.
118. Spencer, N.J. and H. Hu, *Enteric nervous system: sensory transduction, neural circuits and gastrointestinal motility*. Nat Rev Gastroenterol Hepatol, 2020. **17**(6): p. 338-351.
119. Usoskin, D., et al., *Unbiased classification of sensory neuron types by large-scale single-cell RNA sequencing*. Nature Neuroscience, 2015. **18**(1): p. 145-153.
120. Wiesenfeld-Hallin, Z., et al., *Immunoreactive calcitonin gene-related peptide and substance P coexist in sensory neurons to the spinal cord and interact in spinal behavioral responses of the rat*. Neurosci Lett, 1984. **52**(1-2): p. 199-204.
121. Silverman, J.D. and L. Kruger, *Acid phosphatase as a selective marker for a class of small sensory ganglion cells in several mammals: spinal cord distribution, histochemical properties,*

## REFERENCES

- and relation to fluoride-resistant acid phosphatase (FRAP) of rodents.* Somatosens Res, 1988. **5**(3): p. 219-46.
122. Kashiba, H., Y. Uchida, and E. Senba, *Difference in binding by isolectin B4 to trkA and c-ret mRNA-expressing neurons in rat sensory ganglia.* Brain Res Mol Brain Res, 2001. **95**(1-2): p. 18-26.
123. Li, C.L., et al., *Somatosensory neuron types identified by high-coverage single-cell RNA-sequencing and functional heterogeneity.* Cell Res, 2016. **26**(8): p. 967.
124. Sharma, N., et al., *The emergence of transcriptional identity in somatosensory neurons.* Nature, 2020. **577**(7790): p. 392-398.
125. Emery, E.C. and P. Ernfors, *Dorsal Root Ganglion Neuron Types and Their Functional Specialization*, in *The Oxford Handbook of the Neurobiology of Pain*, J.N. Wood, Editor. 2020, Oxford University Press. p. 128-155.
126. Kupari, J., et al., *Single cell transcriptomics of primate sensory neurons identifies cell types associated with chronic pain.* Nature communications, 2021. **12**(1): p. 1-15.
127. Wirka, R.C., et al., *Atheroprotective roles of smooth muscle cell phenotypic modulation and the TCF21 disease gene as revealed by single-cell analysis.* Nat Med, 2019. **25**(8): p. 1280-1289.
128. Asp, M., et al., *A Spatiotemporal Organ-Wide Gene Expression and Cell Atlas of the Developing Human Heart.* Cell, 2019. **179**(7): p. 1647-1660 e19.
129. Efremova, M., et al., *CellPhoneDB: inferring cell-cell communication from combined expression of multi-subunit ligand-receptor complexes.* Nat Protoc, 2020. **15**(4): p. 1484-1506.
130. Chen, Y.-P., et al., *Single-cell transcriptomics reveals regulators underlying immune cell diversity and immune subtypes associated with prognosis in nasopharyngeal carcinoma.* Cell Research, 2020. **30**(11): p. 1024-1042.
131. Wang, S., et al., *Single cell transcriptomics of human epidermis identifies basal stem cell transition states.* Nat Commun, 2020. **11**(1): p. 4239.
132. Skelly, D.A., et al., *Single-Cell Transcriptional Profiling Reveals Cellular Diversity and Intercommunication in the Mouse Heart.* Cell Rep, 2018. **22**(3): p. 600-610.
133. Armingol, E., et al., *Deciphering cell-cell interactions and communication from gene expression.* Nat Rev Genet, 2021. **22**(2): p. 71-88.
134. Papalexi, E. and R. Satija, *Single-cell RNA sequencing to explore immune cell heterogeneity.* Nat Rev Immunol, 2018. **18**(1): p. 35-45.
135. Jordão, M.J.C., et al., *Single-cell profiling identifies myeloid cell subsets with distinct fates during neuroinflammation.* Science, 2019. **363**(6425): p. eaat7554.
136. Masuda, T., et al., *Spatial and temporal heterogeneity of mouse and human microglia at single-cell resolution.* Nature, 2019. **566**(7744): p. 388-392.
137. Jordao, M.J.C., et al., *Single-cell profiling identifies myeloid cell subsets with distinct fates during neuroinflammation.* Science, 2019. **363**(6425).
138. Hu, D., et al., *Artery Tertiary Lymphoid Organs Control Aorta Immunity and Protect against Atherosclerosis via Vascular Smooth Muscle Cell Lymphotoxin  $\beta$  Receptors.* Immunity, 2015. **42**(6): p. 1100-15.
139. Wang, Z., et al., *Pairing of single-cell RNA analysis and T cell antigen receptor profiling indicates breakdown of T cell tolerance checkpoints in atherosclerosis.* Nature Cardiovascular Research, 2023. **2**(3): p. 290-306.
140. Dang, M.T., F. Mafra, and M. Haldar, *Isolation of myeloid cells from mouse brain tumors for single-cell RNA-seq analysis.* STAR Protocols, 2021. **2**(4): p. 100957.
141. Lee, J.-K. and M.G. Tansey, *Microglia Isolation from Adult Mouse Brain*, in *Microglia: Methods and Protocols*, B. Joseph and J.L. Venero, Editors. 2013, Humana Press: Totowa, NJ. p. 17-23.
142. MacKay, H., et al., *DNA methylation in AgRP neurons regulates voluntary exercise behavior in mice.* Nature communications, 2019. **10**(1): p. 1-11.

## REFERENCES

143. Matson, K.J.E., et al., *Single cell atlas of spinal cord injury in mice reveals a pro-regenerative signature in spinocerebellar neurons*. Nature Communications, 2022. **13**(1): p. 5628.
144. Polioudakis, D., et al., *A Single-Cell Transcriptomic Atlas of Human Neocortical Development during Mid-gestation*. Neuron, 2019. **103**(5): p. 785-801 e8.
145. Kalish, B.T., et al., *Single-cell transcriptomics of the developing lateral geniculate nucleus reveals insights into circuit assembly and refinement*. Proceedings of the National Academy of Sciences, 2018. **115**(5): p. E1051-E1060.
146. Dell'Anno, M.T., et al., *Human neuroepithelial stem cell regional specificity enables spinal cord repair through a relay circuit*. Nature communications, 2018. **9**(1): p. 1-15.
147. Renthall, W., et al., *Transcriptional Reprogramming of Distinct Peripheral Sensory Neuron Subtypes after Axonal Injury*. Neuron, 2020. **108**(1): p. 128-144 e9.
148. Schörnig, M., et al., *Comparison of induced neurons reveals slower structural and functional maturation in humans than in apes*. Elife, 2021. **10**: p. e59323.
149. Eschweiler, S., et al., *Intratumoral follicular regulatory T cells curtail anti-PD-1 treatment efficacy*. Nature Immunology, 2021: p. 1-12.
150. Niehaus, J.K., et al., *Spinal macrophages resolve nociceptive hypersensitivity after peripheral injury*. Neuron, 2021. **109**(8): p. 1274-1282. e6.
151. Willemsen, L. and M.P. de Winther, *Macrophage subsets in atherosclerosis as defined by single-cell technologies*. J Pathol, 2020. **250**(5): p. 705-714.
152. Yu, X., A. Basbaum, and Z. Guan, *Contribution of colony-stimulating factor 1 to neuropathic pain*. Pain reports, 2021. **6**(1): p. e883.
153. Yu, X., et al., *Dorsal root ganglion macrophages contribute to both the initiation and persistence of neuropathic pain*. Nat Commun, 2020. **11**(1): p. 264.
154. Ochocka, N., et al., *Single-cell RNA sequencing reveals functional heterogeneity of glioma-associated brain macrophages*. Nature communications, 2021. **12**(1): p. 1-14.
155. Zhang, L., et al., *Single-cell analyses inform mechanisms of myeloid-targeted therapies in colon cancer*. Cell, 2020. **181**(2): p. 442-459. e29.
156. Ryckman, C., et al., *Proinflammatory activities of S100: proteins S100A8, S100A9, and S100A8/A9 induce neutrophil chemotaxis and adhesion*. The Journal of Immunology, 2003. **170**(6): p. 3233-3242.
157. Xie, X., et al., *Single-cell transcriptome profiling reveals neutrophil heterogeneity in homeostasis and infection*. Nature Immunology, 2020. **21**(9): p. 1119-1133.
158. Calcagno, D.M., et al., *SiglecF(HI) Marks Late-Stage Neutrophils of the Infarcted Heart: A Single-Cell Transcriptomic Analysis of Neutrophil Diversification*. J Am Heart Assoc, 2021. **10**(4): p. e019019.
159. Vafadarnejad, E., et al., *Dynamics of Cardiac Neutrophil Diversity in Murine Myocardial Infarction*. Circ Res, 2020. **127**(9): p. e232-e249.
160. Grieshaber-Bouyer, R., et al., *The neutrotime transcriptional signature defines a single continuum of neutrophils across biological compartments*. Nature communications, 2021. **12**(1): p. 1-21.
161. Megat, S., et al., *Nociceptor translational profiling reveals the Ragulator-Rag GTPase complex as a critical generator of neuropathic pain*. Journal of Neuroscience, 2019. **39**(3): p. 393-411.
162. Mapps, A.A., et al., *Diversity of satellite glia in sympathetic and sensory ganglia*. Cell Rep, 2022. **38**(5): p. 110328.
163. Faal, T., et al., *Induction of mesoderm and neural crest-derived pericytes from human pluripotent stem cells to study blood-brain barrier interactions*. Stem cell reports, 2019. **12**(3): p. 451-460.
164. Habib, N., et al., *Disease-associated astrocytes in Alzheimer's disease and aging*. Nat Neurosci, 2020. **23**(6): p. 701-706.
165. Vanlandewijck, M., et al., *A molecular atlas of cell types and zonation in the brain vasculature*. Nature, 2018. **554**(7693): p. 475-480.

## REFERENCES

166. He, L., et al., *Single-cell RNA sequencing of mouse brain and lung vascular and vessel-associated cell types*. Scientific data, 2018. **5**(1): p. 1-11.
167. Kuppe, C., et al., *Decoding myofibroblast origins in human kidney fibrosis*. Nature, 2021. **589**(7841): p. 281-286.
168. Stebbins, M.J., et al., *Human pluripotent stem cell-derived brain pericyte-like cells induce blood-brain barrier properties*. Science advances, 2019. **5**(3): p. eaau7375.
169. Cho, H., et al., *Pericyte-specific expression of Rgs5: implications for PDGF and EDG receptor signaling during vascular maturation*. The FASEB journal, 2003. **17**(3): p. 1-17.
170. Ayloo, S., et al., *Pericyte-to-endothelial cell signaling via vitronectin-integrin regulates blood-CNS barrier*. Neuron, 2022. **110**(10): p. 1641-1655 e6.
171. Muhl, L., et al., *Single-cell analysis uncovers fibroblast heterogeneity and criteria for fibroblast and mural cell identification and discrimination*. Nat Commun, 2020. **11**(1): p. 3953.
172. Kim, N., et al., *Single-cell RNA sequencing demonstrates the molecular and cellular reprogramming of metastatic lung adenocarcinoma*. Nat Commun, 2020. **11**(1): p. 2285.
173. Singhmar, P., et al., *The fibroblast-derived protein P116 controls neuropathic pain*. Proc Natl Acad Sci U S A, 2020. **117**(10): p. 5463-5471.
174. Xie, T., et al., *Single-Cell Deconvolution of Fibroblast Heterogeneity in Mouse Pulmonary Fibrosis*. Cell Rep, 2018. **22**(13): p. 3625-3640.
175. Avraham, O., et al., *Satellite glial cells promote regenerative growth in sensory neurons*. Nat Commun, 2020. **11**(1): p. 4891.
176. Avraham, O., et al., *Profiling sensory neuron microenvironment after peripheral and central axon injury reveals key pathways for neural repair*. Elife, 2021. **10**: p. e68457.
177. Tasdemir-Yilmaz, O.E., et al., *Diversity of developing peripheral glia revealed by single-cell RNA sequencing*. Dev Cell, 2021. **56**(17): p. 2516-2535 e8.
178. Inak, G., et al., *Defective metabolic programming impairs early neuronal morphogenesis in neural cultures and an organoid model of Leigh syndrome*. Nature Communications, 2021. **12**(1): p. 1929.
179. Lucas, T.A., L. Zhu, and M.S. Buckwalter, *Spleen glia are a transcriptionally unique glial subtype interposed between immune cells and sympathetic axons*. Glia, 2021. **69**(7): p. 1799-1815.
180. Kegel, L., et al., *Functional phylogenetic analysis of LGI proteins identifies an interaction motif crucial for myelination*. Development, 2014. **141**(8): p. 1749-1756.
181. Andreatta, M. and S.J. Carmona, *UCell: Robust and scalable single-cell gene signature scoring*. Computational and Structural Biotechnology Journal, 2021. **19**: p. 3796-3798.
182. Jin, S., et al., *Inference and analysis of cell-cell communication using CellChat*. Nature communications, 2021. **12**(1): p. 1088.
183. Hao, Y., et al., *Integrated analysis of multimodal single-cell data*. Cell, 2021. **184**(13): p. 3573-3587 e29.
184. Galow, A.-M., et al., *Quality control in scRNA-Seq can discriminate pacemaker cells: the mtRNA bias*. Cellular and Molecular Life Sciences, 2021. **78**(19): p. 6585-6592.
185. Ximerakis, M., et al., *Single-cell transcriptomic profiling of the aging mouse brain*. Nat Neurosci, 2019. **22**(10): p. 1696-1708.
186. Wang, K., et al., *Single-cell transcriptomic analysis of somatosensory neurons uncovers temporal development of neuropathic pain*. Cell Research, 2021. **31**(8): p. 904-918.
187. Zhou, Y., et al., *Metascape provides a biologist-oriented resource for the analysis of systems-level datasets*. Nat Commun, 2019. **10**(1): p. 1523.
188. Jung, S.-H., et al., *Spatiotemporal dynamics of macrophage heterogeneity and a potential function of Trem2hi macrophages in infarcted hearts*. Nature Communications, 2022. **13**(1): p. 4580.
189. Willemsen, L. and M.P. de Winther, *Macrophage subsets in atherosclerosis as defined by single-cell technologies*. The Journal of Pathology, 2020. **250**(5): p. 705-714.

## REFERENCES

190. Liu, W., et al., *Trem2 promotes anti-inflammatory responses in microglia and is suppressed under pro-inflammatory conditions*. Human molecular genetics, 2020. **29**(19): p. 3224-3248.
191. Jung, S.-H., et al., *Spatiotemporal dynamics of macrophage heterogeneity and a potential function of Trem2hi macrophages in infarcted hearts*. Nature communications, 2022. **13**(1): p. 1-15.
192. de Araujo, R., et al., *Fibroblast Growth Factors: A Controlling Mechanism of Skin Aging*. Skin Pharmacol Physiol, 2019. **32**(5): p. 275-282.
193. Sarker, F.A., et al., *Forcing a growth factor response – tissue-stiffness modulation of integrin signaling and crosstalk with growth factor receptors*. Journal of Cell Science, 2020. **133**(23): p. jcs242461.
194. Skaper, S.D., *Nerve growth factor: a neuroimmune crosstalk mediator for all seasons*. Immunology, 2017. **151**(1): p. 1-15.
195. Vance, J.E., R.B. Campenot, and D.E. Vance, *The synthesis and transport of lipids for axonal growth and nerve regeneration*. Biochimica et Biophysica Acta (BBA)-Molecular and Cell Biology of Lipids, 2000. **1486**(1): p. 84-96.
196. Ulland, T.K., et al., *TREM2 maintains microglial metabolic fitness in Alzheimer's disease*. Cell, 2017. **170**(4): p. 649-663. e13.
197. Davies, L.C., et al., *Tissue-resident macrophages*. Nat Immunol, 2013. **14**(10): p. 986-95.
198. Lavin, Y., et al., *Tissue-resident macrophage enhancer landscapes are shaped by the local microenvironment*. Cell, 2014. **159**(6): p. 1312-1326.
199. Zigmond, R.E. and F.D. Echevarria, *Macrophage biology in the peripheral nervous system after injury*. Progress in neurobiology, 2019. **173**: p. 102-121.
200. Udit, S., K. Blake, and I.M. Chiu, *Somatosensory and autonomic neuronal regulation of the immune response*. Nature Reviews Neuroscience, 2022. **23**(3): p. 157-171.
201. Manville, R.W., M. Papanikolaou, and G.W. Abbott, *Direct neurotransmitter activation of voltage-gated potassium channels*. Nature Communications, 2018. **9**(1): p. 1847.
202. Lovinger, D.M., et al., *Local modulation by presynaptic receptors controls neuronal communication and behaviour*. Nature Reviews Neuroscience, 2022. **23**(4): p. 191-203.
203. Wu, H., et al., *Distinct subtypes of proprioceptive dorsal root ganglion neurons regulate adaptive proprioception in mice*. Nature communications, 2021. **12**(1): p. 1-13.
204. Lin, Y.-T., et al., *Up-regulation of dorsal root ganglia BDNF and trkB receptor in inflammatory pain: an in vivo and in vitro study*. Journal of neuroinflammation, 2011. **8**(1): p. 1-22.
205. Gao, X., et al., *Nociceptive nerves regulate haematopoietic stem cell mobilization*. Nature, 2021. **589**(7843): p. 591-596.
206. Mizobuchi, S., et al., *Spinal nerve injury causes upregulation of ErbB2 and ErbB3 receptors in rat dorsal root ganglia*. J Pain Res, 2013. **6**: p. 87-94.
207. Simonetti, M., et al., *Wnt-Fzd signaling sensitizes peripheral sensory neurons via distinct noncanonical pathways*. Neuron, 2014. **83**(1): p. 104-21.
208. Hesse, D., et al., *Hepatic trans-Golgi action coordinated by the GTPase ARFRP1 is crucial for lipoprotein lipidation and assembly*. Journal of Lipid Research, 2014. **55**(1): p. 41-52.
209. Xiao, X., et al., *The role of vascular dementia associated genes in patients with Alzheimer's disease: A large case-control study in the Chinese population*. CNS Neuroscience & Therapeutics, 2021. **27**(12): p. 1531-1539.
210. Koutsodendris, N., et al., *Neuronal APOE4 removal protects against tau-mediated gliosis, neurodegeneration and myelin deficits*. Nature Aging, 2023. **3**(3): p. 275-296.
211. Smolock, E.M., et al., *Ribosomal Protein L17, RpL17, is an Inhibitor of Vascular Smooth Muscle Growth and Carotid Intima Formation*. Circulation, 2012. **126**(20): p. 2418-2427.
212. Zalocusky, K.A., et al., *Neuronal ApoE upregulates MHC-I expression to drive selective neurodegeneration in Alzheimer's disease*. Nature Neuroscience, 2021. **24**(6): p. 786-798.
213. Yang, A.C., et al., *A human brain vascular atlas reveals diverse mediators of Alzheimer's risk*. Nature, 2022. **603**(7903): p. 885-892.

## REFERENCES

214. Zöllner, T., et al., *Silencing of TGF $\beta$  signalling in microglia results in impaired homeostasis*. Nature communications, 2018. **9**(1): p. 4011.
215. Baker, S.A. and J. Rutter, *Metabolites as signalling molecules*. Nature Reviews Molecular Cell Biology, 2023: p. 1-20.
216. Taveggia, C., M.L. Feltri, and L. Wrabetz, *Signals to promote myelin formation and repair*. Nat Rev Neurol, 2010. **6**(5): p. 276-87.
217. Hill, M.C., et al., *Integrated multi-omic characterization of congenital heart disease*. Nature, 2022. **608**(7921): p. 181-191.
218. Smith, E.P., et al., *Expression of neuroimmune semaphorins 4A and 4D and their receptors in the lung is enhanced by allergen and vascular endothelial growth factor*. BMC immunology, 2011. **12**(1): p. 1-15.
219. Farr, L., et al., *CD74 Signaling Links Inflammation to Intestinal Epithelial Cell Regeneration and Promotes Mucosal Healing*. Cell Mol Gastroenterol Hepatol, 2020. **10**(1): p. 101-112.
220. Matsuda, S., Y. Matsuda, and L. D'Adamio, *CD74 interacts with APP and suppresses the production of A $\beta$* . Mol Neurodegener, 2009. **4**(1): p. 41.
221. Baral, P., S. Udit, and I.M. Chiu, *Pain and immunity: implications for host defence*. Nat Rev Immunol, 2019. **19**(7): p. 433-447.
222. Huang, J.-Y., M.L. Miskus, and H.-C. Lu, *FGF-FGFR mediates the activity-dependent dendritogenesis of layer IV neurons during barrel formation*. Journal of Neuroscience, 2017. **37**(50): p. 12094-12105.
223. Cao, W., et al., *Regulation of TLR7/9 responses in plasmacytoid dendritic cells by BST2 and ILT7 receptor interaction*. J Exp Med, 2009. **206**(7): p. 1603-14.
224. Magadmi, R., et al., *Secretion of mast cell inflammatory mediators is enhanced by CADMI-dependent adhesion to sensory neurons*. Frontiers in cellular neuroscience, 2019: p. 262.
225. Farr, L., S. Ghosh, and S. Moonah, *Role of MIF Cytokine/CD74 Receptor Pathway in Protecting Against Injury and Promoting Repair*. Front Immunol, 2020. **11**: p. 1273.
226. Alexander, J.K., et al., *Macrophage migration inhibitory factor (MIF) is essential for inflammatory and neuropathic pain and enhances pain in response to stress*. Experimental neurology, 2012. **236**(2): p. 351-362.
227. Martin-Ventura, J.L., et al., *Increased CD74 expression in human atherosclerotic plaques: contribution to inflammatory responses in vascular cells*. Cardiovasc Res, 2009. **83**(3): p. 586-94.
228. Cao, E., et al., *TRPV1 structures in distinct conformations reveal activation mechanisms*. Nature, 2013. **504**(7478): p. 113-118.
229. Donnelly, C.R., et al., *STING controls nociception via type I interferon signalling in sensory neurons*. Nature, 2021. **591**(7849): p. 275-280.
230. Cohen, J.A., et al., *Cutaneous TRPV1+ neurons trigger protective innate type 17 anticipatory immunity*. Cell, 2019. **178**(4): p. 919-932. e14.
231. Amores-Bonet, L., et al., *Interactions between the Polysialylated Neural Cell Adhesion Molecule and the Transient Receptor Potential Canonical Channels 1, 4, and 5 Induce Entry of Ca<sup>2+</sup> into Neurons*. International Journal of Molecular Sciences, 2022. **23**(17): p. 10027.
232. Mayne, K., et al., *Aging and Neurodegenerative Disease: Is the Adaptive Immune System a Friend or Foe?* Frontiers in aging neuroscience, 2020. **12**: p. 305.
233. Groh, J., et al., *Accumulation of cytotoxic T cells in the aged CNS leads to axon degeneration and contributes to cognitive and motor decline*. Nature Aging, 2021. **1**(4): p. 357-367.
234. Negrodo, P.N. and A. Brunet, *Unwanted help from T cells in the aging central nervous system*. Nature Aging, 2021. **1**(4): p. 330-331.
235. Ellwardt, E., et al., *Understanding the role of T cells in CNS homeostasis*. Trends in immunology, 2016. **37**(2): p. 154-165.
236. Wang, J.C. and M. Bennett, *Aging and atherosclerosis: mechanisms, functional consequences, and potential therapeutics for cellular senescence*. Circulation research, 2012. **111**(2): p. 245-259.

## REFERENCES

237. Montagne, A., et al., *Blood-brain barrier breakdown in the aging human hippocampus*. *Neuron*, 2015. **85**(2): p. 296-302.
238. Ritzel, R.M., et al., *Age-associated resident memory CD8 T cells in the central nervous system are primed to potentiate inflammation after ischemic brain injury*. *The Journal of Immunology*, 2016. **196**(8): p. 3318-3330.
239. Rustenhoven, J., et al., *Functional characterization of the dural sinuses as a neuroimmune interface*. *Cell*, 2021. **184**(4): p. 1000-1016. e27.
240. Gate, D., et al., *Clonally expanded CD8 T cells patrol the cerebrospinal fluid in Alzheimer's disease*. *Nature*, 2020. **577**(7790): p. 399-404.
241. Mogilenko, D.A., I. Shchukina, and M.N. Artyomov, *Immune ageing at single-cell resolution*. *Nature Reviews Immunology*, 2021: p. 1-15.
242. Mittelbrunn, M. and G. Kroemer, *Hallmarks of T cell aging*. *Nat Immunol*, 2021. **22**(6): p. 687-698.
243. Sanderson, S.L. and A.K. Simon, *In aged primary T cells, mitochondrial stress contributes to telomere attrition measured by a novel imaging flow cytometry assay*. *Aging cell*, 2017. **16**(6): p. 1234-1243.
244. Quinn, K.M., et al., *Age-related decline in primary CD8+ T cell responses is associated with the development of senescence in virtual memory CD8+ T cells*. *Cell Reports*, 2018. **23**(12): p. 3512-3524.
245. Chiu, B.-C., et al., *Cutting edge: Central memory CD8 T cells in aged mice are virtual memory cells*. *The Journal of Immunology*, 2013. **191**(12): p. 5793-5796.
246. Martin, M.D. and V.P. Badovinac, *Defining Memory CD8 T Cell*. *Front Immunol*, 2018. **9**: p. 2692.
247. Ifergan, I., et al., *Central nervous system recruitment of effector memory CD8+ T lymphocytes during neuroinflammation is dependent on  $\alpha 4$  integrin*. *Brain*, 2011. **134**(12): p. 3560-3577.
248. Haniffa, M., et al., *A roadmap for the human developmental cell atlas*. *Nature*, 2021. **597**(7875): p. 196-205.
249. Bennett, M.L. and F.C. Bennett, *The influence of environment and origin on brain resident macrophages and implications for therapy*. *Nat Neurosci*, 2020. **23**(2): p. 157-166.
250. Wang, P.L., et al., *Peripheral nerve resident macrophages share tissue-specific programming and features of activated microglia*. *Nat Commun*, 2020. **11**(1): p. 2552.
251. Wu, Y. and K.K. Hirschi, *Tissue-Resident Macrophage Development and Function*. *Frontiers in Cell and Developmental Biology*, 2021. **8**.
252. Williams, G.P., et al., *Targeting of the class II transactivator attenuates inflammation and neurodegeneration in an alpha-synuclein model of Parkinson's disease*. *Journal of Neuroinflammation*, 2018. **15**(1): p. 244.
253. Xue, F. and H. Du, *TREM2 mediates microglial anti-inflammatory activations in Alzheimer's disease: lessons learned from transcriptomics*. *Cells*, 2021. **10**(2): p. 321.
254. Nguyen, M.Q., et al., *Single-nucleus transcriptomic analysis of human dorsal root ganglion neurons*. *Elife*, 2021. **10**: p. e71752.
255. Chu, C., D. Artis, and I.M. Chiu, *Neuro-immune Interactions in the Tissues*. *Immunity*, 2020. **52**(3): p. 464-474.
256. Juárez-Contreras, R., et al., *TRPV1 Channel: A Noxious Signal Transducer That Affects Mitochondrial Function*. *International Journal of Molecular Sciences*, 2020. **21**(23): p. 8882.

## APPENDIX

### APPENDIX

**Table1 The top 50 marker genes of each cell type in aged DRGs.** Data were calculated by the R package Seurat FindAllMarkers function. Top 50 marker genes (ranked by p\_adj\_val) are shown. p\_val: p-value; avg\_log2FC: log2 fold-change of the average expression between the cell type and all other cells in DRG; pct.1: the percentage of cells where the feature is detected in the first group; pct.2: the percentage of cells where the feature is detected in the second group; p\_val\_adj: adjusted p value.

Cell type	Gene	Gene full name	p_val	avg_log2 FC	pct.1	pct.2	p_val_adj
Neuron	Snhg11	small nucleolar RNA host gene 11	4E-232	5,229332	0,889	0,039	1,4E-227
	Stmn2	stathmin-like 2	4,4E-218	4,539549	0,91	0,056	1,5E-213
	Prph	peripherin	2,7E-215	3,855332	0,834	0,036	8,9E-211
	Elavl4	ELAV like RNA binding protein 4	2,4E-213	2,698181	0,739	0,013	8E-209
	Tac1	tachykinin 1	1,8E-212	4,271231	0,789	0,025	6,2E-208
	Syt4	synaptotagmin IV	7,8E-208	3,177005	0,739	0,017	2,6E-203
	Tubb3	tubulin, beta 3 class III	6,2E-207	4,138112	0,829	0,04	2,1E-202
	Nrxn1	neurexin I	7,2E-205	2,56451	0,688	0,009	2,4E-200
	Pirt	phosphoinositide-interacting regulator of transient receptor potential channels	8,4E-203	2,81968	0,704	0,012	2,8E-198
	Gng3	guanine nucleotide binding protein (G protein), gamma 3	2,7E-199	3,880235	0,774	0,029	9,1E-195
	Fgf13	fibroblast growth factor 13	8,3E-194	2,993406	0,749	0,027	2,8E-189
	Stmn3	stathmin-like 3	1,8E-191	3,862066	0,789	0,039	6,1E-187
	Cadps	Ca2+-dependent secretion activator	2,3E-191	2,124653	0,663	0,01	7,7E-187
	Ctnna2	catenin (cadherin associated protein), alpha 2	1E-190	1,72042	0,618	0,004	3,5E-186
	Elavl3	ELAV like RNA binding protein 3	1,5E-189	1,941093	0,618	0,004	5E-185
	Scn10a	sodium channel, voltage-gated, type X, alpha	1,7E-184	2,224115	0,608	0,005	5,8E-180
	Miat	myocardial infarction associated transcript (non-protein coding)	6,5E-184	2,200097	0,593	0,003	2,2E-179
	Dpp6	dipeptidylpeptidase 6	6,9E-184	1,73624	0,598	0,004	2,3E-179
	Add2	adducin 2 (beta)	4,8E-183	1,988131	0,633	0,01	1,6E-178
	Trim36	tripartite motif-containing 36	2,4E-182	1,676449	0,608	0,006	8E-178
	Pclo	piccolo (presynaptic cytomatrix protein)	2,7E-182	2,228155	0,683	0,018	8,9E-178
	Isl1	ISL1 transcription factor, LIM/homeodomain	1,4E-181	1,536545	0,593	0,004	4,8E-177
	Myt1l	myelin transcription factor 1-like	2,5E-180	1,846866	0,603	0,006	8,4E-176
	Meg3	maternally expressed 3	9,8E-180	5,764007	0,889	0,095	3,3E-175
	Nefl	neurofilament, light polypeptide	1,5E-179	3,113195	0,734	0,034	4,9E-175
	Bex2	brain expressed X-linked 2	8,3E-179	2,712541	0,628	0,011	2,8E-174
	Ppp1r1c	protein phosphatase 1, regulatory inhibitor subunit 1C	2,8E-177	2,043414	0,653	0,016	9,2E-173
	Scn9a	sodium channel, voltage-gated, type IX, alpha	3,2E-177	2,370348	0,658	0,017	1,1E-172
	Snap25	synaptosomal-associated protein 25	1,1E-175	2,700233	0,724	0,034	3,7E-171
	Rab3c	RAB3C, member RAS oncogene family	6,9E-175	1,797747	0,603	0,008	2,3E-170
	Nap1l5	nucleosome assembly protein 1-like 5	1,2E-174	2,251184	0,653	0,018	3,9E-170
	Peg3	paternally expressed 3	4,8E-174	2,721648	0,693	0,028	1,6E-169
	Rbfox3	RNA binding protein, fox-1 homolog (C. elegans) 3	9,7E-174	1,56956	0,563	0,003	3,2E-169
	Cacna1b	calcium channel, voltage-dependent, N type, alpha 1B subunit	6,4E-172	1,556186	0,558	0,003	2,1E-167
	Scn11a	sodium channel, voltage-gated, type XI, alpha	7,5E-172	2,114449	0,588	0,007	2,5E-167
	Kif5a	kinesin family member 5A	4,3E-170	2,474533	0,688	0,028	1,4E-165
	Syt1	synaptotagmin I	8,6E-170	1,916588	0,603	0,011	2,9E-165

## APPENDIX

	Uchl1	ubiquitin carboxy-terminal hydrolase L1	7,5E-169	4,555207	0,91	0,117	2,5E-164
	Nrsn1	neurensin 1	1,5E-168	2,029708	0,563	0,005	5E-164
	Plekha6	pleckstrin homology domain containing, family A member 6	2,9E-168	1,863109	0,613	0,013	9,9E-164
	Celf4	CUGBP, Elav-like family member 4	7,9E-167	2,900292	0,678	0,03	2,7E-162
	Nefm	neurofilament, medium polypeptide	3,2E-166	2,923315	0,663	0,025	1,1E-161
	Cyfp2	cytoplasmic FMR1 interacting protein 2	2,4E-165	2,279455	0,683	0,03	8,1E-161
	Ndr4	N-myc downstream regulated gene 4	1,3E-164	2,831221	0,709	0,038	4,5E-160
	Paccin1	protein kinase C and casein kinase substrate in neurons 1	2,6E-164	1,463646	0,543	0,004	8,8E-160
	Gal	galanin and GMAP prepropeptide	9,9E-164	3,510159	0,558	0,007	3,3E-159
	Epb4113	erythrocyte membrane protein band 4.1 like 3	2,4E-163	2,249306	0,678	0,031	8,1E-159
	Nacad	NAC alpha domain containing	2,1E-161	1,183843	0,523	0,002	7E-157
	Gnal	guanine nucleotide binding protein, alpha stimulating, olfactory type	3E-161	1,800096	0,573	0,01	1E-156
	Ptprcap	protein tyrosine phosphatase, receptor type, C polypeptide-associated protein	8,4E-257	3,851169	1	0,001	2,8E-252
	Ncr1	natural cytotoxicity triggering receptor 1	5,9E-115	3,594735	0,333	0	2E-110
	Cxcr6	chemokine (C-X-C motif) receptor 6	5,9E-115	3,594735	0,333	0	2E-110
	Cd7	CD7 antigen	5,9E-115	3,594735	0,333	0	2E-110
	Cd3e	CD3 antigen, epsilon polypeptide	5,9E-115	3,27509	0,333	0	2E-110
	Trbc2	T cell receptor beta, constant 2	5,9E-115	2,935259	0,333	0	2E-110
	Klrb1c	killer cell lectin-like receptor subfamily B member 1C	5,9E-115	2,935259	0,333	0	2E-110
	Klrc2	killer cell lectin-like receptor subfamily C, member 2	5,9E-115	2,935259	0,333	0	2E-110
	Krt83	keratin 83	5,9E-115	2,935259	0,333	0	2E-110
	Cd2	CD2 antigen	5,9E-115	2,50798	0,333	0	2E-110
	Xcl1	chemokine (C motif) ligand 1	5,9E-115	2,441649	0,333	0	2E-110
	Zfp683	zinc finger protein 683	5,9E-115	2,441649	0,333	0	2E-110
	Gimap3	GTPase, IMAP family member 3	5,9E-115	2,441649	0,333	0	2E-110
	Cd247	CD247 antigen	5,9E-115	2,416915	0,333	0	2E-110
	Cldn13	claudin 13	5,9E-115	2,416915	0,333	0	2E-110
	Cd3d	CD3 antigen, delta polypeptide	5,9E-115	2,416915	0,333	0	2E-110
	Gm19585	predicted gene, 19585	5,9E-115	2,416915	0,333	0	2E-110
	Sh2d2a	SH2 domain containing 2A	5,9E-115	1,685407	0,333	0	2E-110
	Gimap7	GTPase, IMAP family member 7	5,9E-115	1,685407	0,333	0	2E-110
	Gm33104	predicted gene, 33104	5,9E-115	1,685407	0,333	0	2E-110
	Trdv2-2	T cell receptor delta variable 2-2	5,9E-115	1,685407	0,333	0	2E-110
	Ccr8	chemokine (C-C motif) receptor 8	5,9E-115	1,685407	0,333	0	2E-110
	Il2rb	interleukin 2 receptor, beta chain	5,9E-115	1,685407	0,333	0	2E-110
	Gstp3	glutathione S-transferase pi 3	5,9E-115	1,685407	0,333	0	2E-110
	Ms4a4b	membrane-spanning 4-domains, subfamily A, member 4B	5,9E-115	1,685407	0,333	0	2E-110
	Tnfrsf18	tumor necrosis factor receptor superfamily, member 18	1,67E-66	3,817936	0,667	0,003	5,61E-62
	Skap1	src family associated phosphoprotein 1	2,61E-58	2,441409	0,333	0,001	8,73E-54
	Txk	TXK tyrosine kinase	2,61E-58	2,441332	0,333	0,001	8,73E-54
	Ctsw	cathepsin W	2,61E-58	2,439533	0,333	0,001	8,73E-54
	Klrd1	killer cell lectin-like receptor, subfamily D, member 1	2,61E-58	2,437227	0,333	0,001	8,73E-54
	Lat	linker for activation of T cells	2,61E-58	1,685077	0,333	0,001	8,73E-54
	Tbx21	T-box 21	2,61E-58	1,684554	0,333	0,001	8,73E-54
	Cd160	CD160 antigen	2,61E-58	1,684544	0,333	0,001	8,73E-54
	Gm19385	predicted gene, 19385	2,61E-58	1,683673	0,333	0,001	8,73E-54
	Lax1	lymphocyte transmembrane adaptor 1	2,61E-58	1,683274	0,333	0,001	8,73E-54
	Slc27a6	solute carrier family 27 (fatty acid transporter), member 6	2,61E-58	1,68242	0,333	0,001	8,73E-54

## APPENDIX

	B93003 6N10Ri k	RIKEN cDNA B930036N10 gene	2,61E-58	1,682385	0,333	0,001	8,73E-54
	Gm170 39	predicted gene 17039	2,61E-58	1,681208	0,333	0,001	8,73E-54
	Il4i1	interleukin 4 induced 1	5,68E-43	3,816141	0,667	0,006	1,9E-38
	Ltb	lymphotoxin B	2,16E-39	3,582585	0,333	0,001	7,25E-35
	Pla2g4f	phospholipase A2, group IVF	2,16E-39	2,409717	0,333	0,001	7,25E-35
	Cd96	CD96 antigen	2,16E-39	1,684852	0,333	0,001	7,25E-35
	Tlr12	toll-like receptor 12	2,16E-39	1,680624	0,333	0,001	7,25E-35
	Kcne3	potassium voltage-gated channel, Isk-related subfamily, gene 3	6,5E-30	2,415708	0,333	0,002	2,18E-25
	Stat4	signal transducer and activator of transcription 4	7,69E-30	2,40334	0,333	0,002	2,58E-25
	Il7r	interleukin 7 receptor	2,46E-26	3,331801	0,667	0,01	8,24E-22
	Dkk1	dickkopf-like 1	3,24E-24	2,505192	0,333	0,003	1,09E-19
Macro phage	Mrc1	mannose receptor, C type 1	3,8E-285	4,029387	0,919	0,008	1,3E-280
	Csf1r	colony stimulating factor 1 receptor	2,3E-267	3,980926	0,963	0,019	7,6E-263
	Pf4	platelet factor 4	3,5E-267	4,958835	0,896	0,011	1,2E-262
	Cbr2	carbonyl reductase 2	5,2E-259	3,814379	0,8	0,003	1,7E-254
	F13a1	coagulation factor XIII, A1 subunit	2,2E-252	3,381175	0,793	0,004	7,4E-248
	Cx3cr1	chemokine (C-X3-C motif) receptor 1	4,5E-239	3,240768	0,83	0,011	1,5E-234
	Hpgd	hydroxyprostaglandin dehydrogenase 15 (NAD)	2,7E-216	3,157416	0,822	0,02	9,1E-212
	Adgre1	adhesion G protein-coupled receptor E1	3,7E-212	2,772506	0,793	0,016	1,2E-207
	Pld4	phospholipase D family, member 4	9,6E-209	2,699658	0,763	0,014	3,2E-204
	C1qc	complement component 1, q subcomponent, C chain	4E-208	4,380659	0,985	0,058	1,3E-203
	C1qa	complement component 1, q subcomponent, alpha polypeptide	3,3E-202	4,413634	1	0,067	1,1E-197
	Stab1	stabilin 1	8,5E-202	3,360004	0,837	0,031	2,9E-197
	Cd163	CD163 antigen	5E-196	2,7889	0,615	0,002	1,7E-191
	Ms4a4a	membrane-spanning 4-domains, subfamily A, member 4A	4,4E-193	2,822583	0,652	0,006	1,5E-188
	Fcgr3	Fc receptor, IgG, low affinity III	4,9E-187	2,906972	0,881	0,039	1,6E-182
	C1qb	complement component 1, q subcomponent, beta polypeptide	8,3E-183	3,615601	0,993	0,069	2,8E-178
	Gpr34	G protein-coupled receptor 34	1E-182	2,08774	0,57	0,001	3,5E-178
	Ms4a6b	membrane-spanning 4-domains, subfamily A, member 6B	1,3E-179	2,25959	0,652	0,011	4,5E-175
	Ltc4s	leukotriene C4 synthase	7,7E-177	2,309331	0,615	0,008	2,6E-172
	Fcgr2b	Fc receptor, IgG, low affinity IIb	5,3E-174	2,37999	0,778	0,029	1,8E-169
	Ccl8	chemokine (C-C motif) ligand 8	1,9E-173	4,142306	0,57	0,004	6,4E-169
	P2ry6	pyrimidinergic receptor P2Y, G-protein coupled, 6	2E-172	2,207649	0,659	0,014	6,8E-168
	C3ar1	complement component 3a receptor 1	6,6E-172	2,192366	0,741	0,024	2,2E-167
	Aif1	allograft inflammatory factor 1	2,3E-167	2,257425	0,696	0,021	7,7E-163
	Lyz2	lysozyme 2	1,2E-164	3,672772	1	0,094	4E-160
	Trf	transferrin	1,8E-164	2,778344	0,911	0,067	6,1E-160
	Clec4a1	C-type lectin domain family 4, member a1	1,4E-162	2,066142	0,578	0,008	4,8E-158
	Dab2	disabled 2, mitogen-responsive phosphoprotein	6,7E-162	2,942537	0,8	0,048	2,2E-157
	Ctss	cathepsin S	1,9E-157	2,786368	0,993	0,085	6,3E-153
	Gpr183	G protein-coupled receptor 183	5,1E-156	1,986679	0,548	0,007	1,7E-151
	H2-Ab1	histocompatibility 2, class II antigen A, beta 1	2,5E-155	3,887941	0,83	0,055	8,4E-151
	Cd36	CD36 molecule	1,1E-153	2,518382	0,63	0,019	3,7E-149
Trem2	triggering receptor expressed on myeloid cells 2	4,2E-152	2,099002	0,77	0,037	1,4E-147	
Tyrobp	TYRO protein tyrosine kinase binding protein	1E-151	2,916727	0,956	0,085	3,4E-147	
Laptm5	lysosomal-associated protein transmembrane 5	1,5E-151	2,369794	0,881	0,06	5E-147	
Ms4a7	membrane-spanning 4-domains, subfamily A, member 7	1,8E-150	2,323355	0,889	0,06	6E-146	

**APPENDIX**

	Ms4a6c	membrane-spanning 4-domains, subfamily A, member 6C	1,5E-149	2,103653	0,681	0,026	4,9E-145
	Ly86	lymphocyte antigen 86	9,1E-149	2,490441	0,8	0,05	3,1E-144
	Unc93b 1	unc-93 homolog B1, TLR signaling regulator	9,6E-147	2,935343	0,911	0,097	3,2E-142
	H2-DMa	histocompatibility 2, class II, locus DMa	1,3E-146	2,438202	0,726	0,039	4,2E-142
	Ptpn18	protein tyrosine phosphatase, non-receptor type 18	1,2E-142	2,366744	0,785	0,054	3,9E-138
	H2-Aa	histocompatibility 2, class II antigen A, alpha	3,3E-142	3,64252	0,807	0,058	1,1E-137
	Clec4a3	C-type lectin domain family 4, member a3	2,4E-141	1,635252	0,541	0,011	8E-137
	Lilra5	leukocyte immunoglobulin-like receptor, subfamily A (with TM domain), member 5	1,4E-139	1,691956	0,459	0,003	4,7E-135
	Cd300d3	CD300 molecule like family member D3	1E-137	1,682448	0,444	0,002	3,4E-133
	H2-Eb1	histocompatibility 2, class II antigen E beta	1,5E-137	3,704677	0,77	0,054	5E-133
	Mgl2	macrophage galactose N-acetyl-galactosamine specific lectin 2	2,1E-137	2,258382	0,511	0,009	6,9E-133
	Fcgr1	Fc receptor, IgG, high affinity I	1,1E-136	1,844236	0,533	0,011	3,7E-132
	Spi1	spleen focus forming virus (SFFV) proviral integration oncogene	5,3E-134	1,896389	0,63	0,026	1,8E-129
	Fcer1g	Fc receptor, IgE, high affinity I, gamma polypeptide	4,6E-128	3,563757	0,903	0,111	1,5E-123
	Cd72	CD72 antigen	7,23E-98	3,537531	0,403	0,012	2,42E-93
	Ctss	cathepsin S	4,31E-97	3,150197	0,784	0,106	1,44E-92
	Rgs1	regulator of G-protein signaling 1	2,48E-85	3,00047	0,336	0,008	8,32E-81
	Tyrobp	TYRO protein tyrosine kinase binding protein	2,47E-84	2,724579	0,746	0,106	8,28E-80
	Lgals3	lectin, galactose binding, soluble 3	1,54E-83	4,128879	0,769	0,155	5,16E-79
	Cd52	CD52 antigen	5,7E-79	3,405833	0,612	0,08	1,91E-74
	Cd68	CD68 antigen	8,96E-78	3,479634	0,619	0,087	3E-73
	Ms4a7	membrane-spanning 4-domains, subfamily A, member 7	1,19E-71	3,318992	0,604	0,087	3,98E-67
	C1qb	complement component 1, q subcomponent, beta polypeptide	5,14E-71	2,743883	0,672	0,099	1,72E-66
	Lyz2	lysozyme 2	4,67E-68	2,509119	0,724	0,12	1,57E-63
	Tmsb4x	thymosin, beta 4, X chromosome	2,05E-67	2,38094	1	0,868	6,88E-63
	Cd74	CD74 antigen (invariant polypeptide of major histocompatibility complex, class II antigen-associated)	5,27E-66	2,963885	0,672	0,115	1,76E-61
	Ftl1	ferritin light polypeptide 1	1,14E-61	2,631477	0,985	0,84	3,81E-57
	Fth1	ferritin heavy polypeptide 1	8,05E-61	2,410972	1	0,954	2,7E-56
	Actb	actin, beta	1,56E-60	2,249453	0,978	0,912	5,21E-56
	Cxcl2	chemokine (C-X-C motif) ligand 2	1,61E-60	3,269357	0,299	0,014	5,41E-56
	Lcp1	lymphocyte cytosolic protein 1	4,26E-56	3,099248	0,604	0,13	1,43E-51
	Ccl4	chemokine (C-C motif) ligand 4	1,27E-55	3,336896	0,254	0,01	4,26E-51
	C1qa	complement component 1, q subcomponent, alpha polypeptide	1,85E-54	1,859805	0,634	0,102	6,19E-50
	Fxyd5	FXYD domain-containing ion transport regulator 5	2,07E-51	2,961803	0,776	0,313	6,93E-47
	Sh3bgrl 3	SH3 domain binding glutamic acid-rich protein-like 3	3,9E-51	2,642842	0,866	0,495	1,31E-46
	Il1b	interleukin 1 beta	1,26E-50	3,224756	0,261	0,014	4,22E-46
	Cyba	cytochrome b-245, alpha polypeptide	9,41E-50	3,059767	0,754	0,303	3,15E-45
	Laptm5	lysosomal-associated protein transmembrane 5	2,33E-49	2,760744	0,515	0,094	7,79E-45
	Dpep2	dipeptidase 2	1,31E-47	1,980582	0,187	0,004	4,4E-43
	C1qc	complement component 1, q subcomponent, C chain	3,1E-45	1,804314	0,567	0,098	1,04E-40
	Zmynd1 5	zinc finger, MYND-type containing 15	2,04E-43	2,59412	0,201	0,008	6,82E-39
	Alox5ap	arachidonate 5-lipoxygenase activating protein	1,23E-42	2,6809	0,463	0,088	4,11E-38
	Bcl2a1b	B cell leukemia/lymphoma 2 related protein A1b	2,65E-41	2,954177	0,381	0,058	8,87E-37
Trem 2 <sup>hi</sup> Macrophage							

## APPENDIX

	Spp1	secreted phosphoprotein 1	3,52E-41	4,129062	0,507	0,116	1,18E-36
	Slamf7	SLAM family member 7	5,37E-41	2,215639	0,246	0,018	1,8E-36
	Lsp1	lymphocyte specific 1	6,13E-41	2,84176	0,388	0,061	2,05E-36
	Pfn1	profilin 1	6,36E-40	2,346587	0,843	0,664	2,13E-35
	Glipr1	GLI pathogenesis-related 1 (glioma)	1,17E-38	2,372816	0,224	0,015	3,92E-34
	Ctsb	cathepsin B	1,86E-38	2,818988	0,836	0,601	6,22E-34
	Slamf9	SLAM family member 9	3,72E-38	2,667316	0,284	0,031	1,25E-33
	H2-Aa	histocompatibility 2, class II antigen A, alpha	7,48E-38	2,706645	0,463	0,091	2,5E-33
	Mmp12	matrix metalloproteinase 12	5,97E-37	2,479674	0,134	0,002	2E-32
	Wfdc17	WAP four-disulfide core domain 17	2,12E-36	2,889934	0,336	0,05	7,11E-32
	Ctsh	cathepsin H	1,4E-35	2,591988	0,507	0,136	4,68E-31
	Eef1a1	eukaryotic translation elongation factor 1 alpha 1	2,44E-35	1,201898	0,97	0,927	8,18E-31
	Coro1a	coronin, actin binding protein 1A	2,65E-34	2,846969	0,478	0,127	8,87E-30
	Tnf	tumor necrosis factor	2,32E-33	1,838232	0,149	0,006	7,79E-29
	Rpsa	ribosomal protein SA	4,33E-32	1,386832	0,91	0,855	1,45E-27
	Bcl2a1d	B cell leukemia/lymphoma 2 related protein A1d	1,5E-31	1,851867	0,157	0,008	5,03E-27
	Rac2	Rac family small GTPase 2	4,56E-31	2,419609	0,306	0,049	1,53E-26
	Lilrb4a	leukocyte immunoglobulin-like receptor, subfamily B, member 4A	1,03E-30	2,253079	0,231	0,025	3,45E-26
	Cytip	cytohesin 1 interacting protein	1,41E-30	1,678235	0,119	0,003	4,73E-26
	Slpi	secretory leukocyte peptidase inhibitor	1,1E-209	6,580817	0,75	0,003	3,5E-205
	S100a8	S100 calcium binding protein A8 (calgranulin A)	2,3E-115	8,461385	0,375	0,001	7,7E-111
	Retnlg	resistin like gamma	4,6E-114	6,744098	0,333	0	1,6E-109
	Hp	haptoglobin	4,6E-114	2,582164	0,333	0	1,6E-109
	Wfdc21	WAP four-disulfide core domain 21	5,6E-100	3,281479	0,292	0	1,86E-95
	Mmp8	matrix metalloproteinase 8	5,6E-100	2,867474	0,292	0	1,86E-95
	Ly6c2	lymphocyte antigen 6 complex, locus C2	4,72E-91	2,480689	0,333	0,001	1,58E-86
	Sell	selectin, lymphocyte	6,46E-86	1,459062	0,25	0	2,17E-81
	Cxcr2	chemokine (C-X-C motif) receptor 2	7,31E-72	1,932485	0,208	0	2,45E-67
	Padi4	peptidyl arginine deiminase, type IV	7,31E-72	1,097767	0,208	0	2,45E-67
	Mcemp1	mast cell expressed membrane protein 1	2,72E-71	2,253513	0,375	0,005	9,11E-67
	S100a9	S100 calcium binding protein A9 (calgranulin B)	7,53E-68	8,494203	0,417	0,007	2,52E-63
	Clec4e	C-type lectin domain family 4, member e	6,2E-67	3,452465	0,417	0,007	2,08E-62
	Il1r2	interleukin 1 receptor, type II	2,07E-60	2,579683	0,333	0,005	6,93E-56
	Pclaf	PCNA clamp associated factor	7,5E-60	1,380304	0,208	0,001	2,51E-55
	Mmp9	matrix metalloproteinase 9	2,68E-58	2,820382	0,292	0,003	8,97E-54
Neutr ophil	Ighv1-53	immunoglobulin heavy variable 1-53	8,09E-58	5,732643	0,167	0	2,71E-53
	Igkc	immunoglobulin kappa constant	8,09E-58	4,637685	0,167	0	2,71E-53
	Iglv1	immunoglobulin lambda variable 1	8,09E-58	2,689746	0,167	0	2,71E-53
	Trem1	triggering receptor expressed on myeloid cells 1	8,09E-58	2,075876	0,167	0	2,71E-53
	Slc7a11	solute carrier family 7 (cationic amino acid transporter, y+ system), member 11	3,33E-57	2,610019	0,25	0,002	1,12E-52
	Ngp	neutrophilic granule protein	2,38E-46	4,922155	0,167	0,001	7,96E-42
	Cd177	CD177 antigen	2,38E-46	1,769995	0,167	0,001	7,96E-42
	Ccnb2	cyclin B2	2,38E-46	0,689944	0,167	0,001	7,96E-42
	Clec4d	C-type lectin domain family 4, member d	1,42E-45	3,168137	0,458	0,017	4,75E-41
	Cxcl2	chemokine (C-X-C motif) ligand 2	3,46E-45	4,273461	0,583	0,03	1,16E-40
	Arg1	arginase, liver	5,83E-45	3,318447	0,208	0,002	1,95E-40
	Igkv3-5	immunoglobulin kappa chain variable 3-5	8,88E-44	8,947174	0,125	0	2,97E-39
	Mzb1	marginal zone B and B1 cell-specific protein 1	8,88E-44	1,232692	0,125	0	2,97E-39
	Gm5150	predicted gene 5150	8,88E-44	1,200157	0,125	0	2,97E-39
	Il18rap	interleukin 18 receptor accessory protein	8,88E-44	1,018238	0,125	0	2,97E-39
	Nfe2	nuclear factor, erythroid derived 2	8,88E-44	0,607379	0,125	0	2,97E-39

**APPENDIX**

	Pram1	PML-RAR alpha-regulated adaptor molecule 1	8,88E-44	0,459033	0,125	0	2,97E-39
	Pbk	PDZ binding kinase	8,88E-44	0,257366	0,125	0	2,97E-39
	Acod1	aconitate decarboxylase 1	1,41E-38	2,021763	0,167	0,001	4,72E-34
	Napsa	napsin A aspartic peptidase	5,22E-34	1,642256	0,333	0,012	1,75E-29
	Hdc	histidine decarboxylase	2,97E-33	2,646921	0,292	0,009	9,95E-29
	Hcar2	hydroxycarboxylic acid receptor 2	4,41E-33	1,543088	0,167	0,002	1,48E-28
	Igkv3-2	immunoglobulin kappa variable 3-2	5,36E-33	9,062741	0,125	0,001	1,79E-28
	Ube2c	ubiquitin-conjugating enzyme E2C	5,36E-33	0,947264	0,125	0,001	1,79E-28
	Aurkb	aurora kinase B	5,36E-33	0,317365	0,125	0,001	1,79E-28
	Trem12	triggering receptor expressed on myeloid cells-like 2	6,07E-33	0,419568	0,125	0,001	2,03E-28
	Bub1	BUB1, mitotic checkpoint serine/threonine kinase	6,47E-33	0,54002	0,125	0,001	2,17E-28
	Trem3	triggering receptor expressed on myeloid cells 3	6,47E-33	0,427323	0,125	0,001	2,17E-28
	Ccl6	chemokine (C-C motif) ligand 6	2,54E-30	4,321491	0,583	0,049	8,5E-26
	Top2a	topoisomerase (DNA) II alpha	4,04E-29	1,065808	0,167	0,003	1,35E-24
	Flt1	FMS-like tyrosine kinase 1	1,6E-283	4,076717	0,875	0,003	5,5E-279
	Esam	endothelial cell-specific adhesion molecule	4,7E-277	3,783846	0,871	0,007	1,6E-272
	Cldn5	claudin 5	3,7E-273	4,620588	0,852	0,005	1,2E-268
	Ly6c1	lymphocyte antigen 6 complex, locus C1	3,1E-266	5,611642	0,923	0,034	1E-261
	Emcn	endomucin	3,2E-261	3,510204	0,823	0,005	1,1E-256
	Cyrr1	cysteine and tyrosine-rich protein 1	5,3E-231	2,793432	0,738	0,004	1,8E-226
	Ly6a	lymphocyte antigen 6 complex, locus A	5,4E-230	4,154424	0,93	0,07	1,8E-225
	Abcb1a	ATP-binding cassette, sub-family B (MDR/TAP), member 1A	4,3E-227	3,132789	0,76	0,012	1,4E-222
	Pecam1	platelet/endothelial cell adhesion molecule 1	5,1E-226	2,860255	0,716	0,002	1,7E-221
	Cxcl12	chemokine (C-X-C motif) ligand 12	6,7E-226	4,958199	0,86	0,049	2,2E-221
	Ctla2a	cytotoxic T lymphocyte-associated protein 2 alpha	5E-222	3,641056	0,742	0,012	1,7E-217
	Sox17	SRY (sex determining region Y)-box 17	3,6E-221	2,86813	0,705	0,003	1,2E-216
	Egfl7	EGF-like domain 7	3,4E-220	3,691037	0,889	0,07	1,1E-215
	Slco1a4	solute carrier organic anion transporter family, member 1a4	2,8E-215	3,066003	0,694	0,004	9,3E-211
	C130074G19Rik	RIKEN cDNA C130074G19 gene	1,6E-208	2,773527	0,683	0,006	5,5E-204
	Abcg2	ATP binding cassette subfamily G member 2 (Junior blood group)	9,7E-203	3,623041	0,852	0,074	3,3E-198
	Adgrl4	adhesion G protein-coupled receptor L4	3,9E-200	2,542006	0,635	0,001	1,3E-195
	Pcp4l1	Purkinje cell protein 4-like 1	1,8E-199	3,311931	0,856	0,075	5,9E-195
	Cdh5	cadherin 5	3,4E-196	2,397145	0,653	0,006	1,1E-191
	Eng	endoglin	3,2E-194	2,719641	0,734	0,03	1,1E-189
	Mmrn2	multimerin 2	1,4E-190	2,342963	0,613	0,002	4,6E-186
	Igfbp7	insulin-like growth factor binding protein 7	2,1E-188	4,312363	0,937	0,15	7E-184
	Tmem204	transmembrane protein 204	1,4E-186	2,35315	0,627	0,007	4,7E-182
	Cavin2	caveolae associated 2	3E-184	2,547805	0,668	0,018	1E-179
	Sox18	SRY (sex determining region Y)-box 18	1,8E-182	2,222519	0,605	0,005	5,9E-178
	Adgrf5	adhesion G protein-coupled receptor F5	9E-182	2,479763	0,631	0,012	3E-177
	Tm4sf1	transmembrane 4 superfamily member 1	2,6E-181	3,221828	0,841	0,087	8,8E-177
	Gimap6	GTPase, IMAP family member 6	7,8E-178	2,349868	0,624	0,012	2,6E-173
	Prom1	prominin 1	1,3E-170	2,231199	0,565	0,004	4,2E-166
	Sema7a	sema domain, immunoglobulin domain (Ig), and GPI membrane anchor, (semaphorin) 7A	5,1E-170	2,300461	0,62	0,017	1,7E-165
	Ptprb	protein tyrosine phosphatase, receptor type, B	4E-165	2,397895	0,587	0,012	1,3E-160
	Slc7a5	solute carrier family 7 (cationic amino acid transporter, y+ system), member 5	2,1E-164	2,624074	0,675	0,039	7E-160
	Spock2	sparc/osteonectin, cwcv and kazal-like domains proteoglycan 2	8,5E-164	3,484334	0,86	0,139	2,8E-159

## APPENDIX

	Tinagl1	tubulointerstitial nephritis antigen-like 1	1,5E-163	2,37093	0,613	0,018	5E-159
	Icam2	intercellular adhesion molecule 2	1,4E-161	1,938461	0,546	0,005	4,8E-157
	Podxl	podocalyxin-like	3,6E-160	2,190348	0,542	0,005	1,2E-155
	Kdr	kinase insert domain protein receptor	1,2E-149	2,134174	0,52	0,007	3,9E-145
	Ly6e	lymphocyte antigen 6 complex, locus E	3,3E-149	2,919522	0,959	0,245	1,1E-144
	Mfsd2a	MFSD2 lysolipid transporter A, lysophospholipid	1,2E-147	2,866319	0,705	0,067	4E-143
	Tie1	tyrosine kinase with immunoglobulin-like and EGF-like domains 1	3E-147	1,789964	0,483	0,002	1E-142
	Ushbp1	USH1 protein network component harmonin binding protein 1	7,1E-147	1,779599	0,483	0,002	2,4E-142
	Kank3	KN motif and ankyrin repeat domains 3	1,3E-146	2,040892	0,609	0,033	4,3E-142
	Tsc22d1	TSC22 domain family, member 1	7,9E-145	3,234284	0,827	0,161	2,7E-140
	Tmem88	transmembrane protein 88	5,8E-143	1,805392	0,48	0,003	1,9E-138
	Rsad2	radical S-adenosyl methionine domain containing 2	4E-140	2,551629	0,52	0,014	1,4E-135
	Id1	inhibitor of DNA binding 1, HLH protein	3E-138	2,533023	0,646	0,054	1E-133
	Kitl	kit ligand	1,4E-137	2,3218	0,638	0,053	4,8E-133
	Cd34	CD34 antigen	1,8E-137	2,305573	0,771	0,091	6,2E-133
Pericyte	Ndufa4l2	Ndufa4, mitochondrial complex associated like 2	1,4E-162	4,043137	0,882	0,008	4,6E-158
	Kcnj8	potassium inwardly-rectifying channel, subfamily J, member 8	2,3E-128	3,398476	0,647	0,005	7,6E-124
	Notch3	notch 3	3,2E-128	3,264884	0,647	0,005	1,1E-123
	Gucy1b1	guanylate cyclase 1, soluble, beta 1	6E-118	3,22257	0,765	0,01	2E-113
	Higd1b	HIG1 domain family, member 1B	2,8E-112	2,954877	0,588	0,005	9,5E-108
	Slc38a11	solute carrier family 38, member 11	8,8E-110	1,965796	0,412	0,001	3E-105
	Gucy1a1	guanylate cyclase 1, soluble, alpha 1	5,8E-106	2,974006	0,647	0,008	1,9E-101
	Mnd1	meiotic nuclear divisions 1	6,94E-91	2,85215	0,647	0,01	2,33E-86
	Aspn	asporin	2,02E-79	3,418274	0,765	0,019	6,77E-75
	Agtr1a	angiotensin II receptor, type 1a	4,06E-75	2,878434	0,588	0,011	1,36E-70
	Rgs5	regulator of G-protein signaling 5	4,52E-75	6,002829	1	0,042	1,51E-70
	Lamc3	laminin gamma 3	3,04E-72	2,908155	0,588	0,012	1,02E-67
	Carmn	cardiac mesoderm enhancer-associated non-coding RNA	4,89E-66	2,915166	0,412	0,005	1,64E-61
	Colec11	collectin sub-family member 11	3,99E-65	1,490624	0,235	0,001	1,34E-60
	Myh11	myosin, heavy polypeptide 11, smooth muscle	2,08E-64	1,969898	0,471	0,008	6,97E-60
	Tacr3	tachykinin receptor 3	2,45E-61	1,024396	0,176	0	8,21E-57
	Des	desmin	4,91E-59	3,206897	0,471	0,009	1,64E-54
	Vstm4	V-set and transmembrane domain containing 4	2,95E-58	2,859031	0,706	0,025	9,9E-54
	Ifitm1	interferon induced transmembrane protein 1	1,17E-52	3,91497	0,824	0,041	3,91E-48
	Abcc9	ATP-binding cassette, sub-family C (CFTR/MRP), member 9	5,98E-52	1,793107	0,353	0,005	2E-47
	Ace2	angiotensin I converting enzyme (peptidyl-dipeptidase A) 2	7,08E-51	1,648104	0,294	0,003	2,37E-46
	Cox4i2	cytochrome c oxidase subunit 4I2	1,41E-48	3,244646	0,647	0,026	4,72E-44
	Ddit4l	DNA-damage-inducible transcript 4-like	3,7E-48	2,927553	0,588	0,021	1,24E-43
	Pde5a	phosphodiesterase 5A, cGMP-specific	6,59E-48	2,202371	0,471	0,012	2,21E-43
	Vtn	vitronectin	1,82E-46	4,182079	0,765	0,041	6,09E-42
	Kbtbd13	kelch repeat and BTB (POZ) domain containing 13	3,28E-46	1,378571	0,176	0,001	1,1E-41
	Gabbr1	gamma-aminobutyric acid (GABA) C receptor, subunit rho 1	3,28E-46	1,142541	0,176	0,001	1,1E-41
	Slc2a4	solute carrier family 2 (facilitated glucose transporter), member 4	4,27E-46	1,0687	0,176	0,001	1,43E-41
	Kcne4	potassium voltage-gated channel, Isk-related subfamily, gene 4	1,74E-45	1,803964	0,353	0,006	5,83E-41

**APPENDIX**

	Slc30a10	solute carrier family 30, member 10	1,88E-41	1,200157	0,118	0	6,31E-37
	Pde3a	phosphodiesterase 3A, cGMP inhibited	5,76E-41	2,148162	0,412	0,011	1,93E-36
	Wdr86	WD repeat domain 86	7,14E-41	1,23521	0,235	0,003	2,39E-36
	Ednra	endothelin receptor type A	1,22E-36	2,043056	0,353	0,009	4,07E-32
	Steap4	STEAP family member 4	2,76E-36	2,849191	0,647	0,037	9,24E-32
	Rem1	rad and gem related GTP binding protein 1	5,3E-35	2,24004	0,471	0,019	1,77E-30
	Ano1	anoctamin 1, calcium activated chloride channel	9,38E-33	1,294261	0,235	0,004	3,14E-28
	Nrip2	nuclear receptor interacting protein 2	1,82E-32	2,070066	0,471	0,021	6,09E-28
	Cyp4b1	cytochrome P450, family 4, subfamily b, polypeptide 1	4,7E-32	2,64717	0,412	0,016	1,57E-27
	Aoc3	amine oxidase, copper containing 3	4,64E-31	1,354247	0,176	0,002	1,56E-26
	Nfatc4	nuclear factor of activated T cells, cytoplasmic, calcineurin dependent 4	4,64E-31	0,869156	0,176	0,002	1,56E-26
	Tpm2	tropomyosin 2, beta	1,18E-29	2,740251	0,647	0,047	3,97E-25
	Il2ra	interleukin 2 receptor, alpha chain	1,44E-29	1,013829	0,235	0,005	4,82E-25
	Hspa1l	heat shock protein 1-like	5,84E-28	0,701877	0,118	0,001	1,96E-23
	Myl9	myosin, light polypeptide 9, regulatory	2,26E-27	4,323165	0,941	0,13	7,58E-23
	Pdgfrb	platelet derived growth factor receptor, beta polypeptide	5,88E-27	2,202623	0,588	0,043	1,97E-22
	Adra2a	adrenergic receptor, alpha 2a	5,91E-27	1,925853	0,294	0,009	1,98E-22
	Rasl11a	RAS-like, family 11, member A	8,27E-27	2,626881	0,471	0,027	2,77E-22
	Ccl11	chemokine (C-C motif) ligand 11	1,2E-217	4,225622	0,797	0,015	3,9E-213
	Smoc2	SPARC related modular calcium binding 2	3E-205	3,299034	0,78	0,017	1E-200
	Gpc3	glypican 3	5,1E-204	4,139103	0,805	0,021	1,7E-199
	Lum	lumican	8,5E-197	5,306821	0,907	0,045	2,9E-192
	Vit	vitrin	6,5E-186	2,912615	0,703	0,015	2,2E-181
	Mmp2	matrix metalloproteinase 2	1E-179	3,355165	0,72	0,019	3,3E-175
	Col1a1	collagen, type I, alpha 1	3,9E-177	3,487572	0,822	0,034	1,3E-172
	Cdkn2a	cyclin dependent kinase inhibitor 2A	7E-177	2,406993	0,559	0,002	2,3E-172
	Dcn	decorin	3,9E-175	5,813101	0,983	0,084	1,3E-170
	Myoc	myocilin	3,3E-172	3,82782	0,653	0,012	1,1E-167
	Igfbp6	insulin-like growth factor binding protein 6	2,1E-158	2,989478	0,847	0,046	7E-154
	Crispld2	cysteine-rich secretory protein LCCL domain containing 2	1,8E-157	2,672094	0,568	0,008	6,2E-153
	Prelp	proline arginine-rich end leucine-rich repeat	5,3E-152	2,259941	0,644	0,019	1,8E-147
	Foxs1	forkhead box S1	3,3E-150	2,861837	0,568	0,011	1,1E-145
	Enpp2	ectonucleotide pyrophosphatase/phosphodiesterase 2	1,4E-148	2,993339	0,703	0,032	4,6E-144
	Islr	immunoglobulin superfamily containing leucine-rich repeat	5,1E-140	2,447426	0,737	0,039	1,7E-135
	Thy1	thymus cell antigen 1, theta	6,6E-139	2,98546	0,636	0,026	2,2E-134
	Abi3bp	ABI family member 3 binding protein	2,8E-137	2,729899	0,729	0,044	9,3E-133
	C1s1	complement component 1, s subcomponent 1	1,9E-132	2,121698	0,653	0,029	6,4E-128
	Fn1	fibronectin 1	3,2E-131	4,511757	0,754	0,049	1,1E-126
	Aebp1	AE binding protein 1	2,5E-128	3,089259	0,737	0,052	8,5E-124
	Pdgfra	platelet derived growth factor receptor, alpha polypeptide	2,3E-125	2,121759	0,551	0,018	7,8E-121
	Pcolce	procollagen C-endopeptidase enhancer protein	1,6E-124	3,112376	0,839	0,082	5,5E-120
	Col6a1	collagen, type VI, alpha 1	1,5E-123	2,286171	0,619	0,029	5,1E-119
	Angptl7	angiopoietin-like 7	2,4E-120	3,428738	0,407	0,003	8,1E-116
	Cpxm1	carboxypeptidase X 1 (M14 family)	5,4E-119	1,88712	0,517	0,017	1,8E-114
	Vcan	versican	1,2E-115	2,117361	0,492	0,015	3,9E-111
	Col6a2	collagen, type VI, alpha 2	6,1E-113	2,291211	0,644	0,042	2E-108
	Ebf2	early B cell factor 2	1,7E-110	1,877129	0,508	0,019	5,8E-106
	Dpep1	dipeptidase 1	1E-106	1,885262	0,381	0,005	3,5E-102
	Col3a1	collagen, type III, alpha 1	1,4E-106	2,770466	0,737	0,068	4,6E-102
	Ecm1	extracellular matrix protein 1	1,7E-106	3,336245	0,822	0,107	5,6E-102
	Thbs1	thrombospondin 1	3,4E-106	2,350069	0,475	0,015	1,1E-101

Fibro  
blast1

## APPENDIX

	Scara5	scavenger receptor class A, member 5	1,7E-104	1,425529	0,424	0,01	5,6E-100
	Osr2	odd-skipped related 2	1,5E-102	1,301338	0,339	0,002	5,02E-98
	Il33	interleukin 33	1,1E-100	1,864045	0,407	0,01	3,52E-96
	Abca6	ATP-binding cassette, sub-family A (ABC1), member 6	2,1E-99	2,336808	0,593	0,043	6,97E-95
	Nupr1	nuclear protein transcription regulator 1	4,8E-99	2,927357	0,669	0,055	1,62E-94
	Serpinf1	serine (or cysteine) peptidase inhibitor, clade F, member 1	1,24E-97	2,364692	0,712	0,072	4,17E-93
	Col15a1	collagen, type XV, alpha 1	1,25E-95	2,747896	0,678	0,067	4,19E-91
	Podn	podocan	4,38E-95	1,338206	0,339	0,004	1,47E-90
	Ccl7	chemokine (C-C motif) ligand 7	5,13E-92	2,532217	0,517	0,03	1,72E-87
	Col2a1	collagen, type II, alpha 1	1,44E-91	4,213063	0,314	0,003	4,82E-87
	Serping1	serine (or cysteine) peptidase inhibitor, clade G, member 1	4,67E-90	2,686136	0,805	0,12	1,56E-85
	Cp	ceruloplasmin	7,9E-89	2,942647	0,814	0,139	2,65E-84
	Sox9	SRY (sex determining region Y)-box 9	8,74E-88	1,520019	0,356	0,008	2,93E-83
	Htra3	HtrA serine peptidase 3	3,32E-87	1,534149	0,415	0,016	1,11E-82
	Pamr1	peptidase domain containing associated with muscle regeneration 1	1,48E-84	1,34933	0,314	0,005	4,97E-80
	Apod	apolipoprotein D	1,39E-83	6,885639	0,89	0,244	4,66E-79
Fibro blast2	Cldn22	claudin 22	5,7E-141	1,427914	0,412	0	1,9E-136
	Lypd2	Ly6/Plaur domain containing 2	3,1E-137	3,476876	0,706	0,006	1E-132
	Slc6a13	solute carrier family 6 (neurotransmitter transporter, GABA), member 13	2,4E-118	2,989807	0,588	0,005	8,2E-114
	Kcnj13	potassium inwardly-rectifying channel, subfamily J, member 13	8E-110	1,761137	0,412	0,001	2,7E-105
	Stra6	stimulated by retinoic acid gene 6	6,4E-102	2,453648	0,529	0,005	2,13E-97
	Slc6a20a	solute carrier family 6 (neurotransmitter transporter), member 20A	2,2E-84	0,950701	0,294	0,001	7,39E-80
	Thbs4	thrombospondin 4	3,31E-69	2,155761	0,647	0,016	1,11E-64
	Mpzl2	myelin protein zero-like 2	2,19E-54	1,361925	0,235	0,001	7,33E-50
	Ccdc3	coiled-coil domain containing 3	1,51E-53	1,905061	0,471	0,01	5,06E-49
	Klf5	Kruppel-like transcription factor 5	1,53E-53	2,813907	0,765	0,034	5,13E-49
	Cldn1	claudin 1	5,73E-52	3,571253	0,824	0,041	1,92E-47
	Wfdc1	WAP four-disulfide core domain 1	7,73E-50	2,26001	0,765	0,036	2,59E-45
	Lbp	lipopolysaccharide binding protein	2,65E-48	3,163212	0,824	0,045	8,88E-44
	Lamc2	laminin, gamma 2	3,58E-46	0,557521	0,176	0,001	1,2E-41
	Islr	immunoglobulin superfamily containing leucine-rich repeat	1,11E-43	4,121769	1	0,082	3,72E-39
	Tnnt3	troponin T3, skeletal, fast	1,88E-41	0,661771	0,118	0	6,31E-37
	Slc30a2	solute carrier family 30 (zinc transporter), member 2	1,88E-41	0,383517	0,118	0	6,31E-37
	Slc6a12	solute carrier family 6 (neurotransmitter transporter, betaine/GABA), member 12	1,88E-41	0,337717	0,118	0	6,31E-37
	Gjb2	gap junction protein, beta 2	7,14E-41	1,015637	0,235	0,003	2,39E-36
	Igfbp6	insulin-like growth factor binding protein 6	6,99E-39	4,69986	1	0,097	2,34E-34
	Wnt10a	wingless-type MMTV integration site family, member 10A	1,82E-36	0,872179	0,235	0,003	6,1E-32
	Cldn11	claudin 11	4,79E-36	1,960771	0,353	0,009	1,6E-31
	Chrdl1	chordin-like 1	1,07E-35	0,988061	0,353	0,009	3,58E-31
	Itgb7	integrin beta 7	1,02E-33	1,216396	0,294	0,006	3,42E-29
	Perp	PERP, TP53 apoptosis effector	4,2E-33	1,059661	0,353	0,01	1,41E-28
	Prelp	proline arginine-rich end leucine-rich repeat	1,12E-32	2,341347	0,765	0,058	3,76E-28
	Gm11627	predicted gene 11627	1,06E-31	1,155018	0,294	0,007	3,54E-27
	Foxc1	forkhead box C1	1,2E-30	1,743068	0,471	0,022	4,01E-26
	Gli1	GLI-Kruppel family member GLI1	2,64E-30	1,35852	0,353	0,012	8,84E-26
	Ecm2	extracellular matrix protein 2, female organ and adipocyte specific	2,4E-28	2,460262	0,765	0,071	8,05E-24
	Nbl1	NBL1, DAN family BMP antagonist	4,51E-28	4,175074	1	0,152	1,51E-23
	Mlxipl	MLX interacting protein-like	5,84E-28	0,742949	0,118	0,001	1,96E-23

## APPENDIX

	Gm46332	predicted gene, 46332	5,84E-28	0,559345	0,118	0,001	1,96E-23
	Slc9a2	solute carrier family 9 (sodium/hydrogen exchanger), member 2	5,84E-28	0,348374	0,118	0,001	1,96E-23
	Adra1b	adrenergic receptor, alpha 1b	6,32E-28	0,629134	0,118	0,001	2,12E-23
	Syt1	synaptotagmin-like 1	6,32E-28	0,521925	0,118	0,001	2,12E-23
	Slc13a4	solute carrier family 13 (sodium/sulfate symporters), member 4	7,75E-28	0,809613	0,294	0,008	2,6E-23
	Dleu7	deleted in lymphocytic leukemia, 7	2,56E-27	0,793588	0,235	0,005	8,58E-23
	Mustn1	musculoskeletal, embryonic nuclear protein 1	2,96E-27	1,97182	0,647	0,05	9,92E-23
	Crabp2	cellular retinoic acid binding protein II	6,09E-27	1,92293	0,294	0,009	2,04E-22
	Smoc2	SPARC related modular calcium binding 2	6,11E-27	2,00882	0,765	0,067	2,05E-22
	Nrtn	neurturin	1,23E-26	0,59057	0,176	0,003	4,14E-22
	Itgbl1	integrin, beta-like 1	1,68E-25	1,624731	0,471	0,027	5,64E-21
	Wnt6	wingless-type MMTV integration site family, member 6	1,85E-25	2,164659	0,824	0,091	6,19E-21
	Tbx15	T-box 15	2,95E-25	0,773356	0,235	0,006	9,89E-21
	C2	complement component 2 (within H-2S)	3,05E-25	1,812014	0,471	0,028	1,02E-20
	Scara3	scavenger receptor class A, member 3	5,49E-24	1,905499	0,588	0,048	1,84E-19
	Serping1	serine (or cysteine) peptidase inhibitor, clade G, member 1	6,68E-24	3,272003	1	0,163	2,24E-19
	Efnb3	ephrin B3	1,99E-23	0,963093	0,176	0,003	6,67E-19
	Dact1	dishevelled-binding antagonist of beta-catenin 1	2,13E-23	1,220893	0,353	0,016	7,15E-19
Fibro blast3	Tspan11	tetraspanin 11	7,8E-144	2,129063	0,483	0,001	2,6E-139
	Clec3b	C-type lectin domain family 3, member b	4,5E-131	5,101185	0,793	0,016	1,5E-126
	Pi16	peptidase inhibitor 16	3,8E-125	5,066991	0,655	0,01	1,3E-120
	Fbln1	fibulin 1	1,15E-97	2,90073	0,517	0,008	3,84E-93
	Aspn	asporin	5,5E-97	2,983364	0,655	0,016	1,84E-92
	Svep1	sushi, von Willebrand factor type A, EGF and pentraxin domain containing 1	2,57E-83	1,901207	0,379	0,004	8,61E-79
	Sfrp4	secreted frizzled-related protein 4	2,93E-82	4,632029	0,655	0,022	9,83E-78
	Dpt	dermatopontin	1,53E-76	2,093077	0,414	0,007	5,11E-72
	Osr1	odd-skipped related transcription factor 1	2,43E-64	1,351464	0,241	0,001	8,15E-60
	Fndc1	fibronectin type III domain containing 1	3,78E-63	1,330163	0,31	0,004	1,27E-58
	Angptl1	angiopoietin-like 1	1,18E-61	2,908938	0,69	0,037	3,94E-57
	Gdf10	growth differentiation factor 10	9,1E-58	1,215224	0,241	0,002	3,05E-53
	Prrx1	paired related homeobox 1	2,24E-56	2,050918	0,621	0,031	7,5E-52
	Zic1	zinc finger protein of the cerebellum 1	1,98E-52	1,535072	0,448	0,016	6,63E-48
	Has1	hyaluronan synthase 1	1,07E-49	1,160922	0,172	0,001	3,58E-45
	Lbp	lipopolysaccharide binding protein	2,7E-49	2,639533	0,655	0,042	9,05E-45
	Igfbp6	insulin-like growth factor binding protein 6	2,07E-48	3,821113	0,897	0,092	6,95E-44
	Cd248	CD248 antigen, endosialin	2,67E-48	2,835857	0,552	0,029	8,96E-44
	Prg4	proteoglycan 4 (megakaryocyte stimulating factor, articular superficial zone protein)	1,03E-47	1,331972	0,241	0,003	3,46E-43
	Gas1	growth arrest specific 1	3,68E-46	1,80595	0,414	0,016	1,23E-41
	Igfbp5	insulin-like growth factor binding protein 5	1,69E-44	5,160091	0,862	0,099	5,68E-40
	Col1a1	collagen, type I, alpha 1	7,54E-44	2,832087	0,828	0,08	2,52E-39
	Fbln7	fibulin 7	8,49E-43	1,546233	0,345	0,011	2,84E-38
	Ltbp4	latent transforming growth factor beta binding protein 4	8,25E-41	2,417448	0,793	0,081	2,76E-36
	Serpinf1	serine (or cysteine) peptidase inhibitor, clade F, member 1	1,33E-40	3,445237	0,862	0,106	4,45E-36
	Mgp	matrix Gla protein	1,53E-40	2,950333	0,897	0,108	5,12E-36
	Col6a2	collagen, type VI, alpha 2	1,7E-40	2,600158	0,759	0,075	5,68E-36
	Pcolce	procollagen C-endopeptidase enhancer protein	2,85E-39	2,963355	0,931	0,125	9,54E-35
Lrrn4cl	LRRN4 C-terminal like	1,9E-37	1,320437	0,31	0,01	6,38E-33	
Mmp23	matrix metalloproteinase 23	3,05E-37	1,281575	0,276	0,008	1,02E-32	
Dcn	decorin	1,64E-36	2,317205	1	0,136	5,5E-32	

## APPENDIX

	Krtdap	keratinocyte differentiation associated protein	2,04E-36	1,027502	0,103	0	6,85E-32
	Dio2	deiodinase, iodothyronine, type II	2,04E-36	0,775559	0,103	0	6,85E-32
	Itih2	inter-alpha trypsin inhibitor, heavy chain 2	2,04E-36	0,321362	0,103	0	6,85E-32
	Col3a1	collagen, type III, alpha 1	3,63E-36	3,233633	0,828	0,105	1,22E-31
	Col14a1	collagen, type XIV, alpha 1	8,54E-36	2,374199	0,517	0,037	2,86E-31
	Lypd2	Ly6/Plaur domain containing 2	2,7E-35	2,295794	0,276	0,008	9,05E-31
	Serping1	serine (or cysteine) peptidase inhibitor, clade G, member 1	1,05E-34	3,439147	0,931	0,158	3,53E-30
	Lepr	leptin receptor	1,73E-34	1,354087	0,345	0,015	5,79E-30
	Islr	immunoglobulin superfamily containing leucine-rich repeat	3,23E-34	1,671577	0,759	0,08	1,08E-29
	C1qtnf7	C1q and tumor necrosis factor related protein 7	7,72E-34	1,138509	0,379	0,02	2,59E-29
	Pcolce2	procollagen C-endopeptidase enhancer 2	7,94E-34	1,371589	0,276	0,009	2,66E-29
	Mmp2	matrix metalloproteinase 2	2,86E-33	1,826201	0,655	0,061	9,57E-29
	Ackr3	atypical chemokine receptor 3	3,73E-33	2,802067	0,621	0,063	1,25E-28
	Loxl1	lysyl oxidase-like 1	3,85E-33	1,550254	0,379	0,02	1,29E-28
	Nell2	NEL-like 2	4,7E-33	0,764381	0,172	0,003	1,57E-28
	Ccdc80	coiled-coil domain containing 80	5,16E-33	2,128772	0,31	0,012	1,73E-28
	Mustn1	musculoskeletal, embryonic nuclear protein 1	1,61E-32	2,105826	0,552	0,047	5,4E-28
	Col6a5	collagen, type VI, alpha 5	4,05E-32	1,121643	0,138	0,001	1,36E-27
	Gfpt2	glutamine fructose-6-phosphate transaminase 2	5,13E-32	1,835684	0,414	0,025	1,72E-27
SGC	Fabp7	fatty acid binding protein 7, brain	2,6E-219	4,955093	0,943	0,062	8,5E-215
	Mmd2	monocyte to macrophage differentiation-associated 2	1,9E-205	2,984254	0,802	0,031	6,5E-201
	Ednrb	endothelin receptor type B	8,2E-181	3,333901	0,911	0,089	2,8E-176
	Bcan	brevican	1,1E-169	2,637159	0,667	0,024	3,8E-165
	Ptprz1	protein tyrosine phosphatase, receptor type Z, polypeptide 1	1,1E-143	2,575579	0,646	0,036	3,8E-139
	Acsbg1	acyl-CoA synthetase bubblegum family member 1	1,2E-132	2,367399	0,599	0,033	4,1E-128
	Fbln5	fibulin 5	1E-131	2,580832	0,766	0,087	3,5E-127
	Aldoc	aldolase C, fructose-bisphosphate	3,8E-128	2,336239	0,625	0,044	1,3E-123
	Prss35	protease, serine 35	1,3E-127	1,946295	0,583	0,032	4,3E-123
	Lgr5	leucine rich repeat containing G protein coupled receptor 5	1E-112	1,444212	0,422	0,009	3,4E-108
	Lpar1	lysophosphatidic acid receptor 1	1E-112	2,39793	0,828	0,154	3,4E-108
	Cnmd	chondromodulin	5,7E-112	2,019963	0,469	0,019	1,9E-107
	Lrrtm1	leucine rich repeat transmembrane neuronal 1	8,6E-112	1,620106	0,443	0,014	2,9E-107
	Ncam1	neural cell adhesion molecule 1	2,2E-111	2,320398	0,812	0,14	7,3E-107
	Gpr3711	G protein-coupled receptor 37-like 1	1,4E-110	2,260713	0,818	0,133	4,8E-106
	Ttyh1	tweety family member 1	2,1E-106	1,991694	0,719	0,093	7E-102
	Fbln2	fibulin 2	2,9E-105	2,167491	0,661	0,082	9,6E-101
	Kcnj10	potassium inwardly-rectifying channel, subfamily J, member 10	1,5E-102	1,732937	0,505	0,033	5,02E-98
	Dbi	diazepam binding inhibitor	4,89E-98	3,201866	0,99	0,564	1,64E-93
	Tspan7	tetraspanin 7	2,96E-94	1,906462	0,745	0,126	9,92E-90
	Matn4	matrilin 4	4,39E-93	1,563426	0,438	0,023	1,47E-88
	Itgb8	integrin beta 8	1,33E-91	2,027023	0,714	0,114	4,44E-87
	Hey2	hairly/enhancer-of-split related with YRPW motif 2	3,21E-91	1,603666	0,469	0,034	1,08E-86
	Ptn	pleiotrophin	4,12E-91	2,15289	0,948	0,263	1,38E-86
	Cmtm5	CKLF-like MARVEL transmembrane domain containing 5	5,02E-91	1,951119	0,859	0,188	1,68E-86
	Gpm6b	glycoprotein m6b	1E-90	2,162688	0,932	0,292	3,37E-86
	Ntrk2	neurotrophic tyrosine kinase, receptor, type 2	1,13E-88	1,953687	0,682	0,112	3,78E-84
Abca8a	ATP-binding cassette, sub-family A (ABC1), member 8a	1,22E-88	1,891079	0,792	0,153	4,09E-84	

## APPENDIX

	Aspa	aspartoacylase	4,79E-85	1,719944	0,755	0,141	1,6E-80
	Vldlr	very low density lipoprotein receptor	3,14E-84	1,459624	0,443	0,033	1,05E-79
	Scd1	stearoyl-Coenzyme A desaturase 1	2,04E-83	2,371411	0,786	0,206	6,85E-79
	Kcnn4	potassium intermediate/small conductance calcium-activated channel, subfamily N, member 4	1,07E-78	1,244895	0,453	0,039	3,57E-74
	Cyp2j6	cytochrome P450, family 2, subfamily j, polypeptide 6	1,25E-78	1,695529	0,677	0,124	4,2E-74
	Sostdc1	sclerostin domain containing 1	1,12E-76	1,788517	0,745	0,146	3,75E-72
	290005 2N01Ri k	RIKEN cDNA 2900052N01 gene	1,76E-76	1,866383	0,318	0,012	5,89E-72
	Wnt6	wingless-type MMTV integration site family, member 6	3,68E-75	1,328728	0,469	0,047	1,23E-70
	Slc35f1	solute carrier family 35, member F1	5,53E-75	1,241027	0,401	0,029	1,85E-70
	S1pr3	sphingosine-1-phosphate receptor 3	6,36E-75	1,772091	0,536	0,075	2,13E-70
	Pmepa 1	prostate transmembrane protein, androgen induced 1	2,72E-74	1,875911	0,609	0,101	9,11E-70
	Tmod2	tropomodulin 2	1,87E-73	1,849229	0,823	0,257	6,27E-69
	Kif21a	kinesin family member 21A	2,21E-73	1,789265	0,818	0,22	7,4E-69
	Slc43a3	solute carrier family 43, member 3	2,87E-73	1,678511	0,531	0,074	9,62E-69
	Atp1b2	ATPase, Na <sup>+</sup> /K <sup>+</sup> transporting, beta 2 polypeptide	3,06E-72	1,356693	0,557	0,078	1,02E-67
	Fads2	fatty acid desaturase 2	9,89E-72	1,561086	0,562	0,088	3,32E-67
	Sod3	superoxide dismutase 3, extracellular	1,63E-71	1,610287	0,594	0,093	5,45E-67
	Scg3	secretogranin III	4,99E-70	1,632223	0,562	0,093	1,67E-65
	Atp1a2	ATPase, Na <sup>+</sup> /K <sup>+</sup> transporting, alpha 2 polypeptide	5,83E-70	1,711674	0,906	0,289	1,95E-65
mSch	Ncmap	noncompact myelin associated protein	1,3E-275	4,62566	0,907	0,022	4,4E-271
	Fxyd3	FXYD domain-containing ion transport regulator 3	1,3E-242	4,529923	0,91	0,066	4,3E-238
	Cldn19	claudin 19	3,7E-229	3,457252	0,799	0,023	1,2E-224
	Mpz	myelin protein zero	9,8E-227	5,925712	0,992	0,21	3,3E-222
	Mbp	myelin basic protein	3,4E-217	5,037589	0,989	0,243	1,1E-212
	Prx	periaxin	2,4E-214	3,378357	0,743	0,017	7,9E-210
	Fxyd6	FXYD domain-containing ion transport regulator 6	5E-197	3,720815	0,873	0,12	1,7E-192
	Cryab	crystallin, alpha B	7,3E-193	3,777361	0,977	0,313	2,5E-188
	Pmp22	peripheral myelin protein 22	3,8E-188	4,389086	0,986	0,422	1,3E-183
	Bcas1	brain enriched myelin associated protein 1	3,7E-170	2,85917	0,636	0,023	1,2E-165
	Mt3	metallothionein 3	1,5E-166	3,26505	0,932	0,236	5,1E-162
	Cnp	2',3'-cyclic nucleotide 3' phosphodiesterase	1,8E-166	3,223771	0,932	0,273	6E-162
	Fam178 b	family with sequence similarity 178, member B	2,8E-163	2,975773	0,596	0,017	9,2E-159
	Gatm	glycine amidinotransferase (L-arginine:glycine amidinotransferase)	6,7E-162	3,026977	0,955	0,285	2,2E-157
	Plip	plasma membrane proteolipid	4,1E-160	3,199076	0,763	0,11	1,4E-155
	Ndrp1	N-myc downstream regulated gene 1	9,5E-153	2,737282	0,944	0,404	3,2E-148
	Kcna1	potassium voltage-gated channel, shaker-related subfamily, member 1	4,9E-150	2,580262	0,819	0,136	1,6E-145
	Mal	myelin and lymphocyte protein, T cell differentiation protein	5,1E-146	2,63848	0,921	0,324	1,7E-141
	Emid1	EMI domain containing 1	4,3E-144	2,717846	0,559	0,022	1,4E-139
	Slc36a2	solute carrier family 36 (proton/amino acid symporter), member 2	2,4E-138	2,380497	0,477	0,002	8E-134
	Plekhb1	pleckstrin homology domain containing, family B (evectins) member 1	3,4E-138	2,668031	0,845	0,218	1,1E-133
	Mag	myelin-associated glycoprotein	1,6E-134	2,411307	0,54	0,022	5,5E-130
	Plp1	proteolipid protein (myelin) 1	2,4E-134	2,079834	0,972	0,237	8,2E-130
	Cdkn1a	cyclin dependent kinase inhibitor 1A (P21)	1,4E-133	2,672446	0,828	0,213	4,8E-129
	Cd9	CD9 antigen	1,7E-128	2,170084	0,975	0,663	5,8E-124
	Ugt8a	UDP galactosyltransferase 8A	4,1E-128	2,409139	0,497	0,018	1,4E-123
	Secisbp 2l	SECIS binding protein 2-like	3,3E-127	2,88683	0,799	0,239	1,1E-122

## APPENDIX

	Fa2h	fatty acid 2-hydroxylase	1,6E-123	2,203308	0,452	0,008	5,2E-119
	Sema3b	sema domain, immunoglobulin domain (Ig), short basic domain, secreted, (semaphorin) 3B	1,1E-121	2,47935	0,78	0,185	3,7E-117
	Eif1	eukaryotic translation initiation factor 1	1,1E-119	1,622775	0,98	0,822	3,7E-115
	S100b	S100 protein, beta polypeptide, neural	1,2E-117	2,645204	0,78	0,203	4E-113
	Sfrp5	secreted frizzled-related sequence protein 5	3,6E-114	2,301973	0,732	0,139	1,2E-109
	Ldhb	lactate dehydrogenase B	2,3E-112	2,283524	0,831	0,282	7,7E-108
	Gldn	gliomedin	2E-111	2,03389	0,427	0,012	6,8E-107
	Ogn	osteoglycin	6E-111	2,529528	0,655	0,112	2E-106
	Art3	ADP-ribosyltransferase 3	2,4E-108	2,18408	0,785	0,214	7,9E-104
	Rasal2	RAS protein activator like 2	1,4E-106	2,586082	0,655	0,141	4,7E-102
	Egfl8	EGF-like domain 8	2,1E-104	2,565338	0,655	0,132	6,9E-100
	Drp2	dystrophin related protein 2	7,7E-104	2,371452	0,458	0,031	2,6E-99
	Dusp15	dual specificity phosphatase-like 15	5,1E-103	2,284646	0,514	0,057	1,72E-98
	Cuedc2	CUE domain containing 2	6,62E-97	2,596764	0,791	0,358	2,22E-92
	Gjb1	gap junction protein, beta 1	5,03E-94	1,894769	0,364	0,01	1,69E-89
	Gypc	glycophorin C	4,36E-93	2,130803	0,466	0,047	1,46E-88
	Mlip	muscular LMNA-interacting protein	2,36E-91	1,871913	0,37	0,014	7,92E-87
	Limch1	LIM and calponin homology domains 1	6,69E-84	2,160613	0,624	0,16	2,24E-79
	Aif1l	allograft inflammatory factor 1-like	7,6E-79	2,003988	0,489	0,083	2,55E-74
	S100a6	S100 calcium binding protein A6 (calcyclin)	9,55E-79	1,269498	0,975	0,572	3,2E-74
	Arhgap19	Rho GTPase activating protein 19	1,58E-76	1,918757	0,356	0,026	5,29E-72
	Dynll1	dynein light chain LC8-type 1	6,45E-76	1,575284	0,898	0,643	2,16E-71
	Chl1	cell adhesion molecule L1-like	1,5E-43	2,944358	0,614	0,101	5,02E-39
	Entpd2	ectonucleoside triphosphate diphosphohydrolase 2	3,58E-39	2,944317	0,671	0,137	1,2E-34
	Klk8	kallikrein related-peptidase 8	6,7E-37	1,096888	0,143	0,002	2,24E-32
	Cdh19	cadherin 19, type 2	1,15E-36	2,462895	0,629	0,126	3,86E-32
	Lgi4	leucine-rich repeat LGI family, member 4	2,36E-30	2,375689	0,571	0,122	7,91E-26
	Rasgef1c	RasGEF domain family, member 1C	5,34E-30	1,277254	0,214	0,013	1,79E-25
	Scn7a	sodium channel, voltage-gated, type VII, alpha	1,92E-24	3,28676	0,486	0,113	6,44E-20
	Dbi	diazepam binding inhibitor	2,04E-24	2,07434	0,929	0,601	6,82E-20
	Kcna1	potassium voltage-gated channel, shaker-related subfamily, member 1	2,88E-24	1,950675	0,786	0,268	9,66E-20
	Fxyd1	FXVD domain-containing ion transport regulator 1	8,31E-24	2,189428	0,8	0,379	2,78E-19
	Gas7	growth arrest specific 7	1,01E-23	2,057091	0,543	0,138	3,39E-19
	Gpnmb	glycoprotein (transmembrane) nmb	4,85E-23	1,177397	0,257	0,027	1,63E-18
	Mrgprf	MAS-related GPR, member F	1,83E-20	1,165232	0,157	0,011	6,11E-16
	Rxrg	retinoid X receptor gamma	3,29E-20	1,910422	0,343	0,062	1,1E-15
	Itgb4	integrin beta 4	1,17E-19	1,996628	0,357	0,067	3,93E-15
	Col27a1	collagen, type XXVII, alpha 1	1,26E-19	1,648134	0,3	0,047	4,23E-15
	Cmtm5	CKLF-like MARVEL transmembrane domain containing 5	6,18E-19	1,80981	0,671	0,252	2,07E-14
	Rarres2	retinoic acid receptor responder (tazarotene induced) 2	1,25E-18	1,762248	0,586	0,194	4,19E-14
	Matn2	matrilin 2	1,47E-18	1,855425	0,557	0,178	4,91E-14
	Cyp2j9	cytochrome P450, family 2, subfamily j, polypeptide 9	9,39E-18	1,730588	0,543	0,17	3,15E-13
	Stard13	StAR-related lipid transfer (START) domain containing 13	3,2E-17	2,047646	0,486	0,149	1,07E-12
	Aspa	aspartoacylase	4,77E-17	1,882204	0,571	0,2	1,6E-12
	Gpr3711	G protein-coupled receptor 37-like 1	6,69E-17	1,690299	0,571	0,2	2,24E-12
	Abca8b	ATP-binding cassette, sub-family A (ABC1), member 8b	1,11E-16	1,877357	0,414	0,108	3,71E-12
	Gpm6b	glycoprotein m6b	4,15E-16	1,293338	0,8	0,35	1,39E-11
	Art3	ADP-ribosyltransferase 3	4,88E-16	1,487621	0,729	0,326	1,63E-11
nmSc h							

## APPENDIX

Prnp	prion protein	4,88E-16	2,204264	0,743	0,451	1,64E-11
ErbB3	erb-b2 receptor tyrosine kinase 3	7,58E-16	1,518987	0,4	0,1	2,54E-11
Sema3e	sema domain, immunoglobulin domain (Ig), short basic domain, secreted, (semaphorin) 3E	1,15E-15	1,084661	0,2	0,026	3,87E-11
Ntng1	netrin G1	2,87E-15	1,517346	0,157	0,016	9,63E-11
Gm29683	predicted gene, 29683	4,08E-15	1,008289	0,171	0,019	1,37E-10
C4b	complement component 4B (Chido blood group)	8,67E-15	2,050313	0,357	0,088	2,9E-10
Cldn11	claudin 11	9,17E-15	1,161857	0,114	0,008	3,07E-10
Frmd5	FERM domain containing 5	2,06E-14	0,619359	0,1	0,006	6,89E-10
Cd59a	CD59a antigen	7,24E-14	1,708437	0,686	0,355	2,42E-09
Vim	vimentin	1,18E-13	1,0054	0,971	0,794	3,95E-09
Zeb2	zinc finger E-box binding homeobox 2	1,21E-13	1,692971	0,686	0,366	4,07E-09
Csm1	CUB and Sushi multiple domains 1	2,4E-13	1,765317	0,386	0,113	8,03E-09
Ncam1	neural cell adhesion molecule 1	3,58E-13	1,623108	0,529	0,208	1,2E-08
Olfml2b	olfactomedin-like 2B	3,9E-13	1,232345	0,257	0,052	1,31E-08
Ank3	ankyrin 3, epithelial	9,63E-13	1,907616	0,486	0,189	3,23E-08
Ptn	pleiotrophin	1,6E-12	1,177827	0,729	0,329	5,35E-08
Abca8a	ATP-binding cassette, sub-family A (ABC1), member 8a	2,17E-12	1,805675	0,529	0,218	7,27E-08
Pdlim4	PDZ and LIM domain 4	3,79E-12	1,704092	0,486	0,186	1,27E-07
Kcna6	potassium voltage-gated channel, shaker-related, subfamily, member 6	5,22E-12	1,566892	0,371	0,113	1,75E-07
Plce1	phospholipase C, epsilon 1	6,73E-12	2,000554	0,286	0,072	2,26E-07
Tmod2	tropomodulin 2	1,12E-11	1,733562	0,629	0,313	3,76E-07
Sox10	SRY (sex determining region Y)-box 10	1,35E-11	1,381065	0,586	0,246	4,52E-07
Asap2	ArfGAP with SH3 domain, ankyrin repeat and PH domain 2	2,65E-11	1,220022	0,314	0,086	8,86E-07
Matn4	matrilin 4	3,68E-11	1,24134	0,271	0,065	1,23E-06

## APPENDIX

**Table2 The DEGs of total DRGs in aged WT versus Apoe<sup>-/-</sup> DRGs.** Data were calculated by the R package Seurat FindMarkers function in; only the significant DEGs are shown (avg\_log2FC > 0.25 or avg\_log2FC < -0.25 and p\_adj\_val < 0.05). The positive avg\_log2FC designates genes upregulated in aged WT DRGs. The negative avg\_log2FC represents genes upregulated in aged Apoe<sup>-/-</sup> DRGs. p\_val: p value; avg\_log2FC: log2 fold-change of the average expression between the two groups; pct.1: the percentage of cells where the feature is detected in the first group; pct.2: the percentage of cells where the feature is detected in the second group; p\_val\_adj: adjusted p value.

Gene	Gene full name	p_val	avg_log2FC	pct.1	pct.2	p_val_adj
Apoe	apolipoprotein E	2,4E-133	5,643835	0,583	0,057	8,1E-129
G0s2	G0/G1 switch gene 2	1,17E-06	0,713531	0,128	0,056	0,039104
Gpcpd1	glycerophosphocholine phosphodiesterase 1	7,79E-09	0,489803	0,274	0,144	0,000261
Neat1	nuclear paraspeckle assembly transcript 1 (non-protein coding)	1,71E-15	0,489169	0,443	0,253	5,71E-11
Ddit4	DNA-damage-inducible transcript 4	1,51E-14	0,47873	0,405	0,222	5,07E-10
H2-Q6	histocompatibility 2, Q region locus 6	4,91E-08	0,405003	0,112	0,042	0,001645
Klf2	Kruppel-like transcription factor 2 (lung)	9,43E-14	0,403972	0,309	0,163	3,16E-09
Sparcl1	SPARC-like 1	6,98E-07	0,398551	0,442	0,312	0,023388
Epas1	endothelial PAS domain protein 1	3,63E-09	0,39543	0,262	0,139	0,000122
Prnp	prion protein	5,18E-07	0,382253	0,531	0,389	0,01736
H2-Q7	histocompatibility 2, Q region locus 7	2,52E-09	0,374317	0,141	0,049	8,45E-05
Hist1h2bc	/	1,54E-15	0,3666	0,501	0,302	5,15E-11
Pdia3	protein disulfide isomerase associated 3	2,31E-22	0,363779	0,635	0,39	7,75E-18
Plscr4	phospholipid scramblase 4	1,01E-21	0,359401	0,225	0,073	3,38E-17
Arl1	ADP-ribosylation factor-like 1	4,63E-27	0,358861	0,42	0,193	1,55E-22
Lims2	LIM and senescent cell antigen like domains 2	1,38E-13	0,352627	0,133	0,031	4,61E-09
Ttyh1	tweety family member 1	2,38E-09	0,350676	0,222	0,112	7,99E-05
Sgms1	sphingomyelin synthase 1	1,98E-09	0,349997	0,24	0,122	6,62E-05
Cdc40	cell division cycle 40	6,69E-08	0,349524	0,163	0,068	0,00224
Net1	neuroepithelial cell transforming gene 1	1,69E-08	0,345436	0,159	0,067	0,000566
Hspa5	heat shock protein 5	1,35E-13	0,344535	0,633	0,439	4,51E-09
Sostdc1	sclerostin domain containing 1	6,33E-09	0,339473	0,275	0,156	0,000212
Ndrgr1	N-myc downstream regulated gene 1	2,66E-11	0,328105	0,609	0,433	8,92E-07
Cdkn1b	cyclin dependent kinase inhibitor 1B	4,68E-09	0,327249	0,335	0,199	0,000157
Eps8l2	EPS8-like 2	2,3E-07	0,324427	0,111	0,037	0,007709
Snx16	sorting nexin 16	6,41E-09	0,319976	0,188	0,09	0,000215
Prex2	phosphatidylinositol-3,4,5-trisphosphate-dependent Rac exchange factor 2	4,46E-10	0,317365	0,176	0,072	1,49E-05
Cav2	caveolin 2	1,54E-15	0,3165	0,268	0,124	5,16E-11
Art3	ADP-ribosyltransferase 3	1,12E-08	0,316022	0,411	0,268	0,000376
Gng12	guanine nucleotide binding protein (G protein), gamma 12	1,06E-13	0,315436	0,22	0,09	3,56E-09
Acsbg1	acyl-CoA synthetase bubblegum family member 1	1,07E-06	0,308593	0,138	0,063	0,035713
Plscr1	phospholipid scramblase 1	6,7E-09	0,30774	0,12	0,041	0,000225
Pla2g16	/	2,17E-25	0,305854	0,436	0,222	7,26E-21
Dbi	diazepam binding inhibitor	3,56E-08	0,304105	0,685	0,539	0,001191
Hsp90b1	heat shock protein 90, beta (Grp94), member 1	9,24E-14	0,303184	0,75	0,561	3,1E-09
Col4a1	collagen, type IV, alpha 1	6,15E-19	0,302621	0,273	0,117	2,06E-14
Ppp1r14c	protein phosphatase 1, regulatory inhibitor subunit 14C	4,75E-10	0,296347	0,156	0,06	1,59E-05
Itch	itchy, E3 ubiquitin protein ligase	5,06E-08	0,296042	0,232	0,121	0,001695
Rbpms	RNA binding protein gene with multiple splicing	4,97E-10	0,28978	0,153	0,061	1,67E-05
Grrp1	/	9,5E-07	0,2886	0,134	0,067	0,031822

## APPENDIX

Serpine2	serine (or cysteine) peptidase inhibitor, clade E, member 2	1,05E-09	0,287839	0,417	0,275	3,52E-05
Tmem9b	TMEM9 domain family, member B	1,5E-12	0,286317	0,332	0,184	5,03E-08
Mpc2	mitochondrial pyruvate carrier 2	2,64E-15	0,285598	0,423	0,244	8,85E-11
Dock1	dedicator of cytokinesis 1	5,92E-17	0,285521	0,181	0,059	1,98E-12
Snx3	sorting nexin 3	4,45E-18	0,285518	0,607	0,395	1,49E-13
Aspa	aspartoacylase	6,29E-15	0,285338	0,284	0,14	2,11E-10
Sorcs1	sortilin-related VPS10 domain containing receptor 1	2,32E-13	0,283608	0,194	0,079	7,78E-09
Pik3ip1	phosphoinositide-3-kinase interacting protein 1	1,41E-07	0,277319	0,221	0,117	0,004721
Lrrn3	leucine rich repeat protein 3, neuronal	1,47E-06	0,276751	0,13	0,057	0,049409
Adamts5	a disintegrin-like and metallopeptidase (reprolysin type) with thrombospondin type 1 motif, 5 (aggrecanase-2)	1,76E-10	0,276192	0,187	0,086	5,9E-06
Scarb2	scavenger receptor class B, member 2	5,4E-14	0,273693	0,312	0,158	1,81E-09
Lpar1	lysophosphatidic acid receptor 1	3,4E-11	0,27364	0,298	0,167	1,14E-06
Prdx4	peroxiredoxin 4	9E-16	0,27342	0,28	0,135	3,01E-11
Tmem128	transmembrane protein 128	1,35E-12	0,271259	0,244	0,118	4,53E-08
Cd38	CD38 antigen	9,35E-11	0,269313	0,116	0,033	3,13E-06
Mpv17	MpV17 mitochondrial inner membrane protein	1,4E-11	0,267413	0,252	0,125	4,69E-07
Ramp2	receptor (calcitonin) activity modifying protein 2	1,77E-11	0,267277	0,366	0,229	5,92E-07
H2-D1	histocompatibility 2, D region locus 1	3,02E-07	0,266402	0,687	0,554	0,010124
Pin4	peptidyl-prolyl cis/trans isomerase, NIMA-interacting, 4 (parvulin)	1,53E-09	0,265933	0,237	0,121	5,12E-05
Slc44a1	solute carrier family 44, member 1	1,2E-13	0,265817	0,362	0,204	4,01E-09
Ifi203	interferon activated gene 203	2,51E-10	0,265095	0,174	0,076	8,4E-06
Marc2	/	4,29E-15	0,262234	0,396	0,223	1,44E-10
Cd59a	CD59a antigen	1,97E-13	0,261667	0,449	0,28	6,6E-09
Chchd3	coiled-coil-helix-coiled-coil-helix domain containing 3	1,46E-11	0,261448	0,222	0,105	4,91E-07
Psm1	proteasome subunit alpha 1	2,64E-09	0,261149	0,302	0,171	8,84E-05
Ugdh	UDP-glucose dehydrogenase	7,93E-11	0,260242	0,186	0,078	2,66E-06
Vwa1	von Willebrand factor A domain containing 1	1,84E-14	0,259742	0,463	0,284	6,15E-10
Itih5	inter-alpha-trypsin inhibitor, heavy chain 5	1,45E-14	0,257	0,371	0,212	4,85E-10
Fut8	fucosyltransferase 8	1,47E-13	0,256258	0,269	0,133	4,91E-09
Ttc17	tetratricopeptide repeat domain 17	3,92E-07	0,256214	0,112	0,044	0,013126
Ifi27	interferon, alpha-inducible protein 27	1,44E-17	0,255601	0,533	0,337	4,82E-13
B4galt4	UDP-Gal:betaGlcNAc beta 1,4-galactosyltransferase, polypeptide 4	1,26E-09	0,253022	0,123	0,042	4,22E-05
Mrpl52	mitochondrial ribosomal protein L52	3,82E-21	-0,25003	0,458	0,351	1,28E-16
Trim28	tripartite motif-containing 28	6,9E-11	-0,25245	0,168	0,132	2,31E-06
Unc93b1	unc-93 homolog B1, TLR signaling regulator	1,51E-09	-0,25271	0,192	0,139	5,06E-05
Tshz2	teashirt zinc finger family member 2	7,88E-16	-0,25285	0,257	0,219	2,64E-11
Rpl10	ribosomal protein L10	2,56E-20	-0,25346	0,577	0,452	8,57E-16
Cox14	cytochrome c oxidase assembly protein 14	4,37E-19	-0,25406	0,318	0,227	1,46E-14
Rpl17	ribosomal protein L17	2,7E-22	-0,25477	0,688	0,566	9,06E-18
Bin1	bridging integrator 1	1,24E-06	-0,25748	0,174	0,159	0,041459
Epb4112	erythrocyte membrane protein band 4.1 like 2	5,37E-27	-0,25807	0,25	0,143	1,8E-22
Vamp8	vesicle-associated membrane protein 8	9,57E-32	-0,25924	0,394	0,245	3,21E-27
Eno1	enolase 1, alpha non-neuron	2,6E-24	-0,25954	0,615	0,469	8,71E-20
Fkbp2	FK506 binding protein 2	6,39E-14	-0,25963	0,388	0,306	2,14E-09
Trmt112	tRNA methyltransferase 11-2	1,3E-21	-0,26113	0,43	0,313	4,36E-17
Lsm7	LSM7 homolog, U6 small nuclear RNA and mRNA degradation associated	2,25E-11	-0,26223	0,3	0,245	7,55E-07
Atp5g1	ATP synthase, H+ transporting, mitochondrial F0 complex, subunit C1 (subunit 9)	1,24E-22	-0,26591	0,465	0,346	4,15E-18

## APPENDIX

Cct3	chaperonin containing Tcp1, subunit 3 (gamma)	1,23E-13	-0,26658	0,273	0,205	4,11E-09
S100a10	S100 calcium binding protein A10 (calpactin)	2,23E-19	-0,27356	0,482	0,362	7,49E-15
Cotl1	coactosin-like 1 (Dictyostelium)	2,63E-08	-0,27482	0,185	0,141	0,00088
Gm26917	/	1,14E-09	-0,27515	0,333	0,212	3,84E-05
Stxbp6	syntaxin binding protein 6 (amisyn)	1,65E-13	-0,27522	0,143	0,105	5,54E-09
Mfsd1	major facilitator superfamily domain containing 1	3,13E-12	-0,27774	0,146	0,102	1,05E-07
Nagk	N-acetylglucosamine kinase	6,25E-13	-0,27828	0,199	0,146	2,09E-08
Ftl1-ps1	ferritin light polypeptide 1, pseudogene 1	2,14E-07	-0,27854	0,394	0,335	0,007154
Tuba1a	tubulin, alpha 1A	3,03E-29	-0,27875	0,674	0,49	1,01E-24
Tpr	translocated promoter region, nuclear basket protein	4,76E-22	-0,28254	0,39	0,282	1,6E-17
Chd3	chromodomain helicase DNA binding protein 3	1,36E-10	-0,28426	0,198	0,163	4,54E-06
Ppp5c	protein phosphatase 5, catalytic subunit	3,34E-07	-0,28535	0,141	0,141	0,011201
Srrm2	serine/arginine repetitive matrix 2	1,59E-22	-0,28646	0,527	0,397	5,32E-18
Atp6v0c	ATPase, H+ transporting, lysosomal V0 subunit C	6,26E-24	-0,29497	0,696	0,548	2,1E-19
Maf	MAF bZIP transcription factor	5,32E-13	-0,29573	0,335	0,269	1,78E-08
Abhd17a	abhydrolase domain containing 17A	1,64E-11	-0,2961	0,192	0,171	5,51E-07
Socs3	suppressor of cytokine signaling 3	3,93E-08	-0,30322	0,174	0,133	0,001316
Ccdc12	coiled-coil domain containing 12	1,24E-11	-0,30336	0,225	0,177	4,14E-07
Tubb2a	tubulin, beta 2A class IIA	2,09E-17	-0,30528	0,337	0,246	7E-13
Arglu1	arginine and glutamate rich 1	9,31E-07	-0,31486	0,197	0,174	0,031186
Ftl1	ferritin light polypeptide 1	3,5E-11	-0,31764	0,894	0,807	1,17E-06
Cstb	cystatin B	2,61E-11	-0,32295	0,376	0,29	8,74E-07
Ssr4	signal sequence receptor, delta	4,11E-24	-0,32378	0,431	0,305	1,38E-19
Coro1c	coronin, actin binding protein 1C	1,04E-08	-0,32389	0,128	0,127	0,000347
Eif1b	eukaryotic translation initiation factor 1B	2,29E-19	-0,33941	0,335	0,261	7,68E-15
Apobec1	apolipoprotein B mRNA editing enzyme, catalytic polypeptide 1	1,9E-07	-0,35063	0,105	0,078	0,006367
Gngt2	guanine nucleotide binding protein (G protein), gamma transducing activity polypeptide 2	1E-07	-0,35157	0,107	0,087	0,003359
Rtn1	reticulum 1	2,68E-10	-0,35383	0,202	0,173	8,98E-06
Mpdu1	mannose-P-dolichol utilization defect 1	8,93E-13	-0,35732	0,146	0,116	2,99E-08
Ptpn18	protein tyrosine phosphatase, non-receptor type 18	5,72E-07	-0,35936	0,123	0,11	0,019161
Uchl1	ubiquitin carboxy-terminal hydrolase L1	1,56E-10	-0,36072	0,243	0,189	5,23E-06
Fosb	FBJ osteosarcoma oncogene B	1,15E-06	-0,36541	0,106	0,087	0,038488
Rpl35a	ribosomal protein L35A	6,41E-21	-0,37008	0,775	0,686	2,15E-16
Ctsd	cathepsin D	1,44E-16	-0,37893	0,65	0,522	4,82E-12
Rab3a	RAB3A, member RAS oncogene family	4,56E-11	-0,38464	0,15	0,125	1,53E-06
Trf	transferrin	1,89E-07	-0,40667	0,143	0,136	0,006329
Hexa	hexosaminidase A	3,47E-16	-0,43472	0,324	0,25	1,16E-11
Prph	peripherin	9,37E-07	-0,46102	0,14	0,135	0,0314
Pcsk1n	proprotein convertase subtilisin/kexin type 1 inhibitor	5,86E-08	-0,48762	0,182	0,178	0,001962
Lars2	leucyl-tRNA synthetase, mitochondrial	1,12E-11	-0,52708	0,697	0,654	3,76E-07
AY036118	cDNA sequence AY036118	7,14E-18	-0,58654	0,622	0,566	2,39E-13
Tomm6	translocase of outer mitochondrial membrane 6	5,98E-16	-0,60733	0,19	0,23	2E-11

## APPENDIX

**Table3 The DEGs of each cell type in aged WT versus ApoE<sup>-/-</sup> DRGs.** Data were calculated by the R package Seurat FindMarkers function. The significant DEGs are shown (avg\_log2FC > 0.25 or avg\_log2FC < -0.25 and p\_adj\_val < 0.05). The positive avg\_log2FC designates genes upregulated in aged WT DRGs. The negative avg\_log2FC represents genes upregulated in aged ApoE<sup>-/-</sup> DRGs. p\_val: p value; avg\_log2FC: log fold-change of the average expression between the two groups; pct.1: the percentage of cells where the feature is detected in the first group; pct.2: the percentage of cells where the feature is detected in the second group; p\_val\_adj: adjusted p value.

Cell type	Gene	Gene full name	p_val	avg_log2FC	pct.1	pct.2	p_val_adj
Neuro n	Prepl	prolyl endopeptidase-like	3,31E-07	0,600155	0,393	0,355	0,011104
	Poldip3	polymerase (DNA-directed), delta interacting protein 3	4,85E-07	0,558133	0,371	0,236	0,016238
	Smarcc1	SWI/SNF related, matrix associated, actin dependent regulator of chromatin, subfamily c, member 1	1,17E-06	0,476091	0,292	0,327	0,03907
	Hnrnp3	heterogeneous nuclear ribonucleoprotein H3	7,06E-07	0,442356	0,36	0,4	0,023668
	Pcdh10	protocadherin 10	4,49E-07	0,413495	0,225	0,209	0,015033
	Fam174b	family with sequence similarity 174, member B	1,23E-06	0,402641	0,202	0,182	0,041366
	Rwdd1	RWD domain containing 1	3,3E-07	0,394387	0,292	0,409	0,011045
	Ampd2	adenosine monophosphate deaminase 2	1,37E-06	0,385771	0,303	0,3	0,045861
	Rfc2	replication factor C (activator 1) 2	1,27E-06	0,381606	0,281	0,191	0,042418
	Supt3	SPT3, SAGA and STAGA complex component	1,06E-06	0,379935	0,225	0,273	0,035462
	Prps1	phosphoribosyl pyrophosphate synthetase 1	3,6E-07	0,324432	0,213	0,255	0,012064
	Rnf113a2	ring finger protein 113A2	3,85E-07	0,320074	0,124	0,127	0,012908
	Bud31	BUD31 homolog	6,16E-07	0,312627	0,213	0,227	0,02065
	Bcs1l	BCS1-like (yeast)	3,68E-07	0,31166	0,135	0,145	0,012335
	Kbtbd3	kelch repeat and BTB (POZ) domain containing 3	4,17E-07	0,297447	0,247	0,255	0,01397
	Skiv2l2	/	5,95E-07	0,293488	0,292	0,264	0,019933
	Fem1a	fem 1 homolog a	3,77E-07	0,291156	0,18	0,182	0,012616
	Rae1	ribonucleic acid export 1	1,33E-06	0,286538	0,292	0,227	0,044428
	Klhl22	kelch-like 22	1,01E-06	0,281489	0,191	0,2	0,033835
	Timm8a1	translocase of inner mitochondrial membrane 8A1	4,09E-07	0,267047	0,169	0,127	0,013688
	Timm44	translocase of inner mitochondrial membrane 44	3,17E-07	-0,25302	0,303	0,282	0,010634
	Ecd	ecdysoneless cell cycle regulator	5,82E-07	-0,2581	0,225	0,236	0,019507
	Capn10	calpain 10	5,71E-07	-0,29729	0,236	0,236	0,019134
	Gt(ROSA)26Sor	gene trap ROSA 26, Philippe Soriano	2,8E-07	-0,30064	0,202	0,273	0,009387
	Rcc2	regulator of chromosome condensation 2	3,32E-07	-0,30115	0,247	0,218	0,011127
	Tmem222	transmembrane protein 222	6,98E-07	-0,30195	0,169	0,282	0,023374
	Frat2	frequently rearranged in advanced T cell lymphomas 2	2,52E-07	-0,3053	0,135	0,164	0,008435
	Tcaim	T cell activation inhibitor, mitochondrial	6E-07	-0,30691	0,258	0,245	0,020107
	Spsb2	splA/ryanodine receptor domain and SOCS box containing 2	3,2E-07	-0,31263	0,124	0,182	0,010724
	Rps6kl1	ribosomal protein S6 kinase-like 1	3,57E-07	-0,31275	0,191	0,2	0,011969
	Utp14a	UTP14A small subunit processome component	4,76E-07	-0,32398	0,146	0,2	0,015948
	Mcm3ap	minichromosome maintenance complex component 3 associated protein	3,12E-07	-0,40938	0,157	0,209	0,010437
Ccdc107	coiled-coil domain containing 107	7,5E-07	-0,43044	0,315	0,391	0,025115	

**APPENDIX**

	Cdk4	cyclin dependent kinase 4	9,06E-07	-0,44278	0,236	0,309	0,030354
	Nme3	NME/NM23 nucleoside diphosphate kinase 3	7,04E-07	-0,47224	0,112	0,209	0,023586
	Ythdf2	YTH N6-methyladenosine RNA binding protein 2	2,46E-07	-0,47228	0,292	0,364	0,008254
	Tbc1d8	TBC1 domain family, member 8	5,49E-07	-0,4885	0,258	0,327	0,018408
	Sec11a	SEC11 homolog A, signal peptidase complex subunit	2,85E-07	-0,54366	0,258	0,345	0,009559
	Tshz3	teashirt zinc finger family member 3	2,35E-07	-0,59143	0,27	0,3	0,007858
	Vkorc1	vitamin K epoxide reductase complex, subunit 1	1,3E-06	-0,67904	0,191	0,336	0,043436
Macro phage	Skap2	src family associated phosphoprotein 2	4,65E-07	0,748886	0,446	0,071	0,015565
	Pcnp	PEST proteolytic signal containing nuclear protein	6,78E-07	0,733693	0,308	0,029	0,02272
	Rac3	Rac family small GTPase 3	1,25E-06	0,696239	0,415	0,071	0,041722
	Blnk	B cell linker	1,24E-06	0,688645	0,523	0,143	0,041673
	Fcho2	FCH domain only 2	6,19E-07	0,665661	0,554	0,157	0,020745
	Itgb1	integrin beta 1 (fibronectin receptor beta)	7,38E-07	0,604095	0,708	0,343	0,024737
	Mtdh	metadherin	1,04E-06	0,569766	0,662	0,243	0,034956
	Ifi203	interferon activated gene 203	7,09E-07	0,56357	0,554	0,171	0,023745
	Blvra	biliverdin reductase A	6,57E-07	0,55924	0,431	0,1	0,022017
	Ywhaz	tyrosine 3-monooxygenase/tryptophan 5-monooxygenase activation protein, zeta polypeptide	4,86E-07	0,514413	0,8	0,371	0,016283
	Snx8	sorting nexin 8	1,23E-06	0,504822	0,462	0,129	0,041046
	Rer1	retention in endoplasmic reticulum sorting receptor 1	6,59E-07	0,475308	0,615	0,243	0,022079
	Hdlbp	high density lipoprotein (HDL) binding protein	6,38E-07	0,437456	0,415	0,1	0,021388
	Cd151	CD151 antigen	5,94E-07	0,358975	0,431	0,114	0,01989
	Xbp1	X-box binding protein 1	1,05E-06	0,355425	0,523	0,186	0,035198
	Smdt1	single-pass membrane protein with aspartate rich tail 1	9,86E-07	0,340845	0,662	0,3	0,033048
	Csnk1a 1	casein kinase 1, alpha 1	1,02E-06	0,322939	0,492	0,186	0,034112
	Tln1	talin 1	6,69E-07	0,316067	0,754	0,414	0,022396
	Nme2	NME/NM23 nucleoside diphosphate kinase 2	5,16E-07	0,302652	0,723	0,357	0,017286
	Thoc7	THO complex 7	8,83E-07	0,259722	0,231	0,071	0,029581
	Larp7	La ribonucleoprotein 7, transcriptional regulator	1,06E-06	-0,26676	0,108	0,1	0,035522
	Ik	IK cytokine	1,24E-06	-0,30311	0,292	0,143	0,041445
	Rtcb	RNA 2',3'-cyclic phosphate and 5'-OH ligase	1,05E-06	-0,31311	0,4	0,3	0,035022
	Npepl1	aminopeptidase-like 1	1,19E-06	-0,31323	0,215	0,114	0,039703
	Eif4g2	eukaryotic translation initiation factor 4, gamma 2	5,96E-07	-0,33297	0,508	0,343	0,01998
	Stard9	START domain containing 9	6,52E-07	-0,34036	0,246	0,143	0,021842
	Ddx5	DEAD box helicase 5	7,27E-07	-0,37268	0,8	0,6	0,024353
	Pias1	protein inhibitor of activated STAT 1	8E-07	-0,38312	0,292	0,186	0,026801
	Tfe3	transcription factor E3	6,3E-07	-0,38332	0,292	0,171	0,021093
	Lrp1	low density lipoprotein receptor-related protein 1	6,44E-07	-0,40733	0,538	0,386	0,021582
	Necap2	NECAP endocytosis associated 2	5,28E-07	-0,4218	0,477	0,314	0,017691
	Ywhab	tyrosine 3-monooxygenase/tryptophan 5-monooxygenase activation protein, beta polypeptide	4,79E-07	-0,45098	0,523	0,386	0,016038
	Foxn3	forkhead box N3	8,95E-07	-0,46333	0,354	0,257	0,029996
	Ube2l3	ubiquitin-conjugating enzyme E2L 3	1,09E-06	-0,47054	0,323	0,229	0,036573
	Idh2	isocitrate dehydrogenase 2 (NADP+), mitochondrial	1,31E-06	-0,48096	0,477	0,329	0,043938
	Coro7	coronin 7	1,35E-06	-0,50287	0,154	0,071	0,04509
Prex1	phosphatidylinositol-3,4,5-trisphosphate-dependent Rac exchange factor 1	1,25E-06	-0,51154	0,338	0,214	0,041728	

**APPENDIX**

	Hist1h2ap		9,19E-07	-0,58358	0,185	0,114	0,030775	
	H2afy		9,51E-07	-0,76171	0,292	0,314	0,031861	
	Ski	ski sarcoma viral oncogene homolog (avian)	9,18E-07	-0,93943	0,2	0,229	0,03077	
Trem <sub>2</sub> <sup>hi</sup> Macro phage	Lamp1	lysosomal-associated membrane protein 1	5,75E-07	-0,25715	0,327	0,215	0,019252	
	P2rx4	purinergic receptor P2X, ligand-gated ion channel 4	1,45E-07	-0,26145	0,109	0,063	0,004848	
	Ccdc12	coiled-coil domain containing 12	2,62E-08	-1,29814	0,145	0,19	0,000878	
	Kmt2e	lysine (K)-specific methyltransferase 2E	2,23E-08	-1,4522	0,073	0,114	0,000747	
	Eif3d	eukaryotic translation initiation factor 3, subunit D	6,94E-07	-1,48728	0,036	0,114	0,023243	
Neutrophil	Cfdp1	craniofacial development protein 1	6,31E-07	-2,0352	0,133	0,222	0,021137	
EC	Cldnd1	claudin domain containing 1	1,04E-06	0,569483	0,281	0,054	0,03484	
	Pa2g4	proliferation-associated 2G4	1,06E-06	0,568071	0,438	0,162	0,035457	
	Mrps33	mitochondrial ribosomal protein S33	1,46E-06	0,566112	0,438	0,171	0,048837	
	Gch1	GTP cyclohydrolase 1	1,23E-06	0,529953	0,325	0,081	0,041327	
	Cd38	CD38 antigen	1,13E-06	0,516091	0,362	0,108	0,037798	
	Col4a1	collagen, type IV, alpha 1	1,44E-06	0,493165	0,475	0,189	0,048208	
	Ndufs6	NADH:ubiquinone oxidoreductase core subunit S6	9,83E-07	0,472145	0,375	0,117	0,032932	
	Rtl8b	retrotransposon Gag like 8B	9,91E-07	0,43742	0,537	0,243	0,033213	
	Ctsz	cathepsin Z	1,1E-06	0,424853	0,619	0,324	0,036823	
	Ifi35	interferon-induced protein 35	1,19E-06	0,396561	0,556	0,27	0,039748	
	Mllt6	myeloid/lymphoid or mixed-lineage leukemia; translocated to, 6	1,03E-06	0,3941	0,188	0,036	0,034621	
	Lmbrd1	LMBR1 domain containing 1	1,31E-06	0,382432	0,35	0,126	0,04383	
	Aes		1,46E-06	0,379861	0,662	0,36	0,048838	
		Psm8	proteasome (prosome, macropain) subunit, beta type 8 (large multifunctional peptidase 7)	1,11E-06	0,3779	0,7	0,396	0,037128
		Slc48a1	solute carrier family 48 (heme transporter), member 1	1,09E-06	0,368775	0,4	0,144	0,036392
		Nucks1	nuclear casein kinase and cyclin-dependent kinase substrate 1	1,15E-06	0,350096	0,412	0,162	0,03845
		Atp2b1	ATPase, Ca <sup>++</sup> transporting, plasma membrane 1	1,16E-06	0,339327	0,306	0,09	0,038758
		Cisd2	CDGSH iron sulfur domain 2	1,08E-06	0,31962	0,281	0,072	0,03604
		Secisbp2l	SECIS binding protein 2-like	1,43E-06	0,299165	0,281	0,072	0,047818
		Dram2	DNA-damage regulated autophagy modulator 2	1,27E-06	0,266715	0,425	0,18	0,042621
		Aff4	AF4/FMR2 family, member 4	1,11E-06	-0,25344	0,269	0,144	0,037064
		Gpr4	G protein-coupled receptor 4	1,04E-06	-0,27334	0,281	0,189	0,034868
		Acadm	acyl-Coenzyme A dehydrogenase, medium chain	1,3E-06	-0,2763	0,144	0,09	0,043704
		Itgb3bp	integrin beta 3 binding protein (beta3-endonexin)	8,94E-07	-0,27792	0,131	0,072	0,029953
		Bet1l	Bet1 golgi vesicular membrane trafficking protein like	1E-06	-0,28748	0,156	0,099	0,033534
		Mvb12a	multivesicular body subunit 12A	1,13E-06	-0,28801	0,275	0,18	0,037786
		Tmem70	transmembrane protein 70	1,33E-06	-0,28993	0,188	0,099	0,044618
		Trp53	transformation related protein 53	1,04E-06	-0,29887	0,244	0,171	0,034919
		Clpp	caseinolytic mitochondrial matrix peptidase proteolytic subunit	6,08E-07	-0,30778	0,194	0,117	0,02038
		Ndufa2	NADH:ubiquinone oxidoreductase subunit A2	6,2E-07	-0,33897	0,581	0,45	0,020774
		Rps12-ps3	ribosomal protein S12, pseudogene 3	6,24E-07	-0,35878	0,238	0,18	0,020895
		Tspan3	tetraspanin 3	7,81E-07	-0,39445	0,238	0,171	0,02615
		Tmed7	transmembrane p24 trafficking protein 7	7,29E-07	-0,39985	0,275	0,18	0,024436
	Phax	phosphorylated adaptor for RNA export	6,38E-07	-0,40396	0,194	0,135	0,021372	

**APPENDIX**

	Ehd4	EH-domain containing 4	1,08E-06	-0,44258	0,519	0,396	0,03626
	Abi3	ABI family member 3	6,28E-07	-0,447	0,238	0,189	0,02105
	Wdr43	WD repeat domain 43	8,48E-07	-0,47382	0,156	0,135	0,028418
	Polr2k	polymerase (RNA) II (DNA directed) polypeptide K	1,41E-06	-0,52636	0,294	0,234	0,047368
	Stox2	storkhead box 2	1,29E-06	-0,53274	0,131	0,09	0,043242
	Ube2m	ubiquitin-conjugating enzyme E2M	1,45E-06	-0,55773	0,106	0,108	0,048539
Fibro blast1	Fam102 b		1,41E-06	0,932313	0,548	0,125	0,047363
	Hmgn2	high mobility group nucleosomal binding domain 2	6,74E-07	0,925939	0,516	0,089	0,022591
	Sf3b1	splicing factor 3b, subunit 1	1,44E-06	0,708384	0,516	0,143	0,048259
	Eef1b2	eukaryotic translation elongation factor 1 beta 2	7,96E-07	0,662869	0,839	0,393	0,026657
	S1pr2	sphingosine-1-phosphate receptor 2	1,3E-06	0,558488	0,258	0,036	0,0434
	Gnb1	guanine nucleotide binding protein (G protein), beta 1	4,65E-07	0,551704	0,516	0,107	0,015586
	Mbd3	methyl-CpG binding domain protein 3	9,17E-07	0,548923	0,452	0,089	0,030728
	Cenpx	centromere protein X	1,02E-06	0,533776	0,435	0,071	0,034304
	Atxn7l3 b	ataxin 7-like 3B	8,78E-07	0,524602	0,468	0,107	0,029403
	Hnrnpdl	heterogeneous nuclear ribonucleoprotein D-like	1,42E-06	0,501491	0,468	0,089	0,04753
	Psip1	PC4 and SFRS1 interacting protein 1	9,46E-07	0,47972	0,71	0,268	0,031689
	Snw1	SNW domain containing 1	9,14E-07	0,429447	0,435	0,089	0,030626
	Rbx1	ring-box 1	5,1E-07	0,372221	0,677	0,25	0,017101
	Fkbp2	FK506 binding protein 2	6,68E-07	0,329954	0,597	0,196	0,022389
	D8Ertd7 38e	DNA segment, Chr 8, ERATO Doi 738, expressed	9,99E-07	0,323528	0,629	0,268	0,033483
	Serpinb 6a	serine (or cysteine) peptidase inhibitor, clade B, member 6a	6,12E-07	0,306451	0,823	0,393	0,020508
	Cct8	chaperonin containing Tcp1, subunit 8 (theta)	1,38E-06	0,305905	0,5	0,161	0,046382
	Pfdn2	prefoldin 2	4,55E-07	0,300961	0,435	0,089	0,015259
	Dnm1	dynamamin 1	5,6E-07	0,295613	0,581	0,196	0,01875
	Ndufa1 1	NADH:ubiquinone oxidoreductase subunit A11	1,07E-06	0,281433	0,629	0,232	0,035946
	Homer2	homer scaffolding protein 2	1,23E-06	-0,25067	0,129	0,036	0,04134
	Tmbim4	transmembrane BAX inhibitor motif containing 4	1,02E-06	-0,26041	0,435	0,214	0,034032
	Trmt11 2	tRNA methyltransferase 11-2	1,41E-06	-0,27407	0,532	0,286	0,047116
	Gm300 25	predicted gene, 30025	1,31E-06	-0,30637	0,113	0,089	0,043943
	Ubl5	ubiquitin-like 5	1,48E-06	-0,31264	0,677	0,411	0,049574
	Mia2	MIA SH3 domain ER export factor 2	1,43E-06	-0,31606	0,177	0,107	0,047812
	Tsen34	tRNA splicing endonuclease subunit 34	1,24E-06	-0,36772	0,435	0,25	0,041692
	H1f0	H1.0 linker histone	1,49E-06	-0,37517	0,339	0,196	0,049927
	Bri3	brain protein I3	9,84E-07	-0,3881	0,597	0,357	0,032965
	Stk25	serine/threonine kinase 25 (yeast)	1,47E-06	-0,39227	0,226	0,125	0,049242
	Map2k1	mitogen-activated protein kinase kinase 1	1,17E-06	-0,39817	0,258	0,143	0,039232
	Selenos	selenoprotein S	9,97E-07	-0,46604	0,677	0,429	0,033409
	Map7d2	MAP7 domain containing 2	1,41E-06	-0,47414	0,177	0,071	0,04732
	Tmx2	thioredoxin-related transmembrane protein 2	1,2E-06	-0,48101	0,306	0,143	0,040074
	Pkn2	protein kinase N2	1,46E-06	-0,50864	0,371	0,196	0,049053
	Sumo2	small ubiquitin-like modifier 2	1,41E-06	-0,51	0,806	0,589	0,047341
	Cbx5	chromobox 5	1,19E-06	-0,53089	0,323	0,179	0,039909
	Ipo5	importin 5	1,36E-06	-0,53682	0,145	0,089	0,045564
	Ddb1	damage specific DNA binding protein 1	1,45E-06	-0,55716	0,242	0,089	0,048499
	Asah1	N-acylsphingosine amidohydrolase 1	1,3E-06	-0,58641	0,339	0,232	0,043475
SGC	Apoe	apolipoprotein E	1,63E-75	7,420746	0,991	0,185	5,47E-71

**APPENDIX**

	Chd2	chromodomain helicase DNA binding protein 2	2,38E-07	0,594377	0,252	0,012	0,007985
	Sdhd	succinate dehydrogenase complex, subunit D, integral membrane protein	6,03E-08	0,463463	0,459	0,136	0,00202
	Spag9	sperm associated antigen 9	1,21E-07	0,460699	0,568	0,21	0,004042
	Slc27a1	solute carrier family 27 (fatty acid transporter), member 1	7,44E-07	0,450966	0,703	0,346	0,024942
	Snx16	sorting nexin 16	1,11E-06	0,450682	0,369	0,099	0,037287
	Ccni	cyclin I	8,39E-07	0,394845	0,514	0,185	0,028124
	Cops4	COP9 signalosome subunit 4	1,01E-06	0,377146	0,315	0,074	0,033952
	Ctsf	cathepsin F	1,33E-07	0,369399	0,27	0,037	0,004456
	Commd 8	COMM domain containing 8	8,84E-07	0,354989	0,279	0,049	0,029605
	9530077C05Rik		6,84E-07	0,325048	0,126	0,025	0,022914
	Srrm1	serine/arginine repetitive matrix 1	3,46E-07	0,323107	0,45	0,148	0,011578
	Gsk3b	glycogen synthase kinase 3 beta	4,03E-07	0,315541	0,505	0,235	0,013492
	S100a1 6	S100 calcium binding protein A16	5,96E-07	0,289387	0,721	0,383	0,019982
	Acaa1a	acetyl-Coenzyme A acyltransferase 1A	3,68E-07	0,278158	0,514	0,21	0,012342
	Nars	asparaginyl-tRNA synthetase	7,77E-07	0,259804	0,45	0,173	0,026029
	Otub1	OTU domain, ubiquitin aldehyde binding 1	3,34E-07	0,257763	0,342	0,111	0,011186
	Mrps12	mitochondrial ribosomal protein S12	6,9E-07	-0,25827	0,333	0,21	0,023125
	Phb2	prohibitin 2	1,13E-06	-0,29349	0,378	0,247	0,037824
	Rere	arginine glutamic acid dipeptide (RE) repeats	1,28E-06	-0,30947	0,189	0,136	0,043002
	Ndufb7	NADH:ubiquinone oxidoreductase subunit B7	9,19E-07	-0,34077	0,604	0,444	0,030792
	Ndufv1	NADH:ubiquinone oxidoreductase core subunit V1	1,09E-06	-0,35795	0,459	0,321	0,03639
	Tomm2 0	translocase of outer mitochondrial membrane 20	9,57E-07	-0,36309	0,459	0,358	0,03206
	Yipf5	Yip1 domain family, member 5	1,38E-06	-0,39019	0,279	0,21	0,046372
	Isoc1	isochorismatase domain containing 1	1,48E-06	-0,4057	0,189	0,148	0,049582
	HnrnpH 2	heterogeneous nuclear ribonucleoprotein H2	1,26E-06	-0,43365	0,369	0,296	0,042122
	Sh3d19	SH3 domain protein D19	1E-06	-0,44607	0,351	0,272	0,033497
	Gpr137	G protein-coupled receptor 137	7,44E-07	-0,47953	0,252	0,21	0,024935
	Dctn2	dynactin 2	1,43E-06	-0,48013	0,595	0,506	0,047795
	Klhl24	kelch-like 24	1,05E-06	-0,49551	0,18	0,123	0,035045
	Suclg1	succinate-CoA ligase, GDP-forming, alpha subunit	1,43E-06	-0,55838	0,324	0,309	0,048074
	Cltb	clathrin, light polypeptide (Lcb)	1,21E-06	-0,57292	0,505	0,469	0,040611
	2900097C17Rik		8,97E-07	-0,62263	0,288	0,296	0,030046
	Nfe2l1	nuclear factor, erythroid derived 2,-like 1	1,34E-06	-0,62671	0,225	0,247	0,044725
	Hint2	histidine triad nucleotide binding protein 2	1,08E-06	-0,69467	0,18	0,247	0,036292
	Park7	Parkinson disease (autosomal recessive, early onset) 7	1,29E-06	-0,70896	0,541	0,605	0,04322
	Ank2	ankyrin 2, brain	8,38E-07	-1,24367	0,225	0,21	0,028076
mSch	Dcaf8	DDB1 and CUL4 associated factor 8	8,34E-07	0,745417	0,165	0,019	0,027934
	Cntf	ciliary neurotrophic factor	7,83E-07	0,60247	0,392	0,188	0,026218
	Zfp91	zinc finger protein 91	1,18E-06	0,426269	0,206	0,056	0,039445
	Sh3tc2	SH3 domain and tetratricopeptide repeats 2	1,35E-06	0,423658	0,103	0,013	0,045199
	Suclg1	succinate-CoA ligase, GDP-forming, alpha subunit	6,57E-07	0,412373	0,17	0,038	0,022007
	Srsf6	serine and arginine-rich splicing factor 6	7,79E-07	0,376709	0,175	0,038	0,026114
	Ccnh	cyclin H	1,1E-06	0,352391	0,155	0,031	0,036701
	Dtx3	deltex 3, E3 ubiquitin ligase	9,62E-07	0,351876	0,196	0,056	0,032219
	Nrcam	neuronal cell adhesion molecule	1,25E-06	0,342786	0,119	0,025	0,041937
	Glrx2	glutaredoxin 2 (thioltransferase)	1,41E-06	0,330789	0,129	0,019	0,047318
	3830406C13Rik		9,42E-07	0,325195	0,201	0,056	0,031564
	Stag1	stromal antigen 1	1,03E-06	0,323683	0,144	0,038	0,034433

**APPENDIX**

	Anxa7	annexin A7	1,1E-06	0,32054	0,206	0,062	0,036714
	Mpp6		9,78E-07	0,315196	0,474	0,262	0,032771
	Eif3i	eukaryotic translation initiation factor 3, subunit I	8,37E-07	0,29677	0,258	0,106	0,028039
	Tfdp2	transcription factor Dp 2	1,41E-06	0,288815	0,165	0,044	0,047223
	Pitpnb	phosphatidylinositol transfer protein, beta	8,05E-07	0,278645	0,144	0,031	0,026956
	Pdgfc	platelet-derived growth factor, C polypeptide	7,28E-07	0,273969	0,119	0,025	0,024384
	Dnajb12	DnaJ heat shock protein family (Hsp40) member B12	1,01E-06	0,272757	0,201	0,069	0,033681
	Creg1	cellular repressor of E1A-stimulated genes 1	1E-06	0,251699	0,144	0,05	0,033573
	Oat	ornithine aminotransferase	1,28E-06	-0,25137	0,201	0,138	0,042926
	Ddx50	DEXD box helicase 50	1,33E-06	-0,28103	0,149	0,1	0,044614
	Rab24	RAB24, member RAS oncogene family	1,06E-06	-0,28459	0,149	0,1	0,035508
	Dnajc7	DnaJ heat shock protein family (Hsp40) member C7	8,74E-07	-0,28906	0,247	0,181	0,029286
	Mrpl54	mitochondrial ribosomal protein L54	7,39E-07	-0,29063	0,155	0,1	0,024765
	Drap1	Dr1 associated protein 1 (negative cofactor 2 alpha)	7,74E-07	-0,29623	0,222	0,15	0,025921
	Sfrp5	secreted frizzled-related sequence protein 5	1,32E-06	-0,3034	0,789	0,662	0,044305
	Strap	serine/threonine kinase receptor associated protein	6,53E-07	-0,30445	0,18	0,131	0,021874
	Cerk	ceramide kinase	1,43E-06	-0,33542	0,124	0,094	0,048067
	Cops5	COP9 signalosome subunit 5	1,11E-06	-0,33669	0,134	0,1	0,037275
	Gtf2b	general transcription factor IIB	6,14E-07	-0,34958	0,108	0,088	0,02058
	Manf	mesencephalic astrocyte-derived neurotrophic factor	7,61E-07	-0,35856	0,16	0,119	0,025497
	Bace2	beta-site APP-cleaving enzyme 2	1,09E-06	-0,3691	0,129	0,1	0,036676
	Smarca4	SWI/SNF related, matrix associated, actin dependent regulator of chromatin, subfamily a, member 4	1,33E-06	-0,3744	0,108	0,081	0,044648
	Ctnnd1	catenin (cadherin associated protein), delta 1	1,06E-06	-0,41716	0,113	0,094	0,035365
	Os9	amplified in osteosarcoma	9,98E-07	-0,42375	0,165	0,144	0,033419
	Mfap1a	microfibrillar-associated protein 1A	1,37E-06	-0,51854	0,108	0,088	0,046017
	Jun	jun proto-oncogene	1,14E-06	-0,52302	0,454	0,431	0,038303
	Mpdu1	mannose-P-dolichol utilization defect 1	7,73E-07	-0,67711	0,072	0,106	0,025895
	Tomm6	translocase of outer mitochondrial membrane 6	8E-07	-0,73539	0,144	0,169	0,026785
nmSc h	Apoe	apolipoprotein E	1,29E-14	5,295844	0,902	0,069	4,32E-10
	Rpl3	ribosomal protein L3	1,71E-07	1,152837	0,854	0,207	0,005718
	1810037117Rik	RIKEN cDNA 1810037117 gene	1,17E-08	1,010243	0,585	0,069	0,000391
	Kmt2e	lysine (K)-specific methyltransferase 2E	6,22E-10	0,771619	0,659	0,103	2,09E-05
	Dazap2	DAZ associated protein 2	2,06E-07	0,625946	0,415	0,069	0,006913
	Eif4a2	eukaryotic translation initiation factor 4A2	1,13E-06	0,601426	0,488	0,103	0,037831
	Rabac1	Rab acceptor 1 (prenylated)	1,02E-06	0,531587	0,732	0,241	0,03407
	Prss23	protease, serine 23	4,15E-08	0,523107	0,366	0,103	0,001389
	Ubxn4	UBX domain protein 4	1,39E-07	0,463891	0,439	0,069	0,00467
	Sf3b1	splicing factor 3b, subunit 1	6,41E-07	0,388916	0,463	0,103	0,021468
	Cct5	chaperonin containing Tcp1, subunit 5 (epsilon)	6,7E-07	-0,26267	0,317	0,103	0,022444
	Wdr1	WD repeat domain 1	3,95E-07	-0,27697	0,341	0,103	0,013242
	Hnrnmpm	heterogeneous nuclear ribonucleoprotein M	2,88E-07	-0,33103	0,195	0,069	0,009636
	Rbm39	RNA binding motif protein 39	2,72E-07	-0,37084	0,707	0,414	0,009108
	Cyfp1	cytoplasmic FMR1 interacting protein 1	3,62E-07	-0,43021	0,39	0,172	0,01212
	Lman2	lectin, mannose-binding 2	1,17E-06	-0,48962	0,171	0,069	0,039122
	Tmem33	transmembrane protein 33	6,79E-07	-0,49708	0,268	0,103	0,022736
	Ociad1	OCIA domain containing 1	5,07E-07	-0,5111	0,39	0,138	0,016994

## APPENDIX

Nr2f1	nuclear receptor subfamily 2, group F, member 1	8,44E-07	-0,51704	0,317	0,138	0,028283
Mga	MAX gene associated	1,1E-06	-0,55771	0,171	0,069	0,036721
Ndufb9	NADH:ubiquinone oxidoreductase subunit B9	7,06E-07	-0,58733	0,561	0,241	0,023661
Cpne8	copine VIII	1,77E-07	-0,62778	0,366	0,172	0,00594
Surf4	surfeit gene 4	4,2E-07	-0,62955	0,122	0,069	0,01408
Cdc42se2	CDC42 small effector 2	2,11E-07	-0,70845	0,122	0,069	0,007067
Map1lc3b	microtubule-associated protein 1 light chain 3 beta	1,64E-07	-0,8278	0,415	0,241	0,005507
Sh3glb1	SH3-domain GRB2-like B1 (endophilin)	9,17E-07	-0,84894	0,463	0,276	0,03072
Krtcap2	keratinocyte associated protein 2	1,24E-06	-1,25043	0,463	0,379	0,041705
Mea1	male enhanced antigen 1	7,75E-07	-1,30699	0,244	0,207	0,025947
Nfic	nuclear factor I/C	1,23E-06	-1,3353	0,39	0,31	0,041217
Cnbp	cellular nucleic acid binding protein	2,6E-07	-1,35912	0,537	0,483	0,008719

## APPENDIX

**Table4 The DEGs of each cell type in control versus RTX-treated DRGs.** Data were calculated by the R package Seurat FindMarkers function. The significant DEGs are shown (avg\_log2FC > 0.25 or avg\_log2FC < -0.25 and p\_adj\_val < 0.05). The positive avg\_log2FC designates genes upregulated in control DRGs. The negative avg\_log2FC represents genes upregulated in RTX-treated DRGs. p\_val: p value; avg\_logFC: log fold-chage of the average expression between the two groups; pct.1: the percentage of cells where the feature is detected in the first group; pct.2: the percentage of cells where the feature is detected in the second group; p\_val\_adj: adjusted p value.

Cell type	Gene	Gene full name	p_val	avg_log2 FC	pct.1	pct.2	p_val_adj
Neuron	Picalm	phosphatidylinositol binding clathrin assembly protein	1,43E-07	1,040383	0,283	0,116	0,004777
	Hnrnpc	heterogeneous nuclear ribonucleoprotein C	1E-06	0,806576	0,233	0,14	0,03365
	Gpr158	G protein-coupled receptor 158	6,46E-07	-0,34665	0,133	0,047	0,021643
	Gla	galactosidase, alpha	3,04E-07	-0,4566	0,117	0,07	0,010191
	Polk	polymerase (DNA directed), kappa	1,15E-06	-0,46817	0,133	0,116	0,038513
	Crls1	cardiolipin synthase 1	2,68E-07	-0,51252	0,117	0,093	0,008973
	Mib1	MIB E3 ubiquitin protein ligase 1	1,21E-06	-0,52515	0,183	0,186	0,040649
	Necap2	NECAP endocytosis associated 2	8,66E-07	-0,55305	0,1	0,07	0,029011
	Cep85l	centrosomal protein 85-like	8,65E-07	-0,61225	0,117	0,14	0,028968
	Stard9	START domain containing 9	1,33E-06	-0,62605	0,117	0,186	0,044426
	Hif1an	hypoxia-inducible factor 1, alpha subunit inhibitor	1,23E-07	-0,72398	0,133	0,093	0,004133
	Tax1bp3	Tax1 (human T cell leukemia virus type I) binding protein 3	1,15E-06	-0,81937	0,133	0,163	0,038668
	Gid4	GID complex subunit 4, VID24 homolog	3,97E-07	-0,85795	0,133	0,186	0,013302
	Dnaja4	DnaJ heat shock protein family (Hsp40) member A4	1,18E-07	-1,09193	0,1	0,14	0,003962
Aspa	aspartoacylase	2,14E-07	-1,18983	0,067	0,163	0,007166	
Tcell	Zfp451	zinc finger protein 451	5,71E-07	0,561025	0,111	0,074	0,019122
Bcell	Gtf2f1	general transcription factor IIF, polypeptide 1	6,94E-07	0,303906	0,182	0,222	0,023264
Macrophage	Anapc13	anaphase promoting complex subunit 13	3,11E-08	0,804417	0,279	0,302	0,001043
	Prmt2	protein arginine N-methyltransferase 2	9,32E-07	0,79983	0,209	0,16	0,03123
	Smpdl3b	sphingomyelin phosphodiesterase, acid-like 3B	1,24E-06	0,66421	0,209	0,132	0,041668
	Atg5	autophagy related 5	2,98E-07	0,341609	0,14	0,217	0,009998
	Nrp2	neuropilin 2	9,13E-07	-0,6619	0,047	0,208	0,030594
	Bax	BCL2-associated X protein	6,56E-08	-0,77052	0,279	0,453	0,002197
Trem2 <sup>hi</sup> Macrophage	Bcl11a	B cell CLL/lymphoma 11A (zinc finger protein)	1,34E-06	0,972267	0,133	0,167	0,044782
	Sec24b	SEC24 homolog B, COPII coat complex component	2,39E-07	0,943374	0,2	0,208	0,00802
	Tmpo	thymopoietin	6,69E-07	-0,78712	0,267	0,5	0,022396
	Haa0	3-hydroxyanthranilate 3,4-dioxygenase	8,01E-07	-0,86535	0,2	0,333	0,026849
EC	Calca	calcitonin/calcitonin-related polypeptide, alpha	1,06E-07	0,99443	0,143	0,014	0,003559
	Spock2	sparc/osteonectin, cwcv and kazal-like domains proteoglycan 2	8,5E-08	0,54759	0,798	0,818	0,002847
	Rrp15	ribosomal RNA processing 15 homolog	1,11E-06	-0,36984	0,017	0,118	0,037324
	Tmem176a	transmembrane protein 176A	3,64E-07	-1,05996	0,202	0,477	0,012185
	Lcn2	lipocalin 2	2,4E-07	-1,58498	0,109	0,37	0,008043
Pericyte	Csk	c-src tyrosine kinase	4,65E-07	1,203741	0,422	0,144	0,015578
Fibroblast1	Hsd11b1	hydroxysteroid 11-beta dehydrogenase 1	9,78E-07	0,660417	0,316	0,21	0,032766
	Rps29	ribosomal protein S29	1,06E-08	0,486774	0,849	0,839	0,000354

## APPENDIX

	Rps28	ribosomal protein S28	1,25E-06	0,46745	0,816	0,793	0,042037
	Rpl36	ribosomal protein L36	6,33E-07	0,390619	0,836	0,774	0,0212
	Eif3d	eukaryotic translation initiation factor 3, subunit D	5,32E-07	0,339125	0,243	0,259	0,017816
	Mettl3	methyltransferase 3, N6-adenosine-methyltransferase complex catalytic subunit	5,2E-07	-0,29739	0,086	0,121	0,017423
	C3	complement component 3	7,4E-08	-0,41017	0,02	0,167	0,002479
	Ahsa2	AHA1, activator of heat shock protein ATPase 2	1,08E-06	-0,45056	0,033	0,193	0,03627
	Hsph1	heat shock 105kDa/110kDa protein 1	3,62E-08	-0,60582	0,072	0,259	0,001211
	Hspa8	heat shock protein 8	1,42E-07	-0,6075	0,724	0,826	0,00475
	Dnajb9	DnaJ heat shock protein family (Hsp40) member B9	5,55E-08	-0,66481	0,184	0,38	0,001858
	Dnaja1	DnaJ heat shock protein family (Hsp40) member A1	1E-07	-0,7848	0,401	0,656	0,003358
	Hspa5	heat shock protein 5	4,85E-18	-0,98466	0,743	0,823	1,62E-13
	Hspb1	heat shock protein 1	2,79E-07	-1,15752	0,309	0,541	0,009345
Fibro blast3	Tbc1d23	TBC1 domain family, member 23	9,52E-07	0,544779	0,184	0,136	0,031884
	Smchd1	SMC hinge domain containing 1	9,59E-07	0,383926	0,286	0,305	0,032139
	Pcsk5	proprotein convertase subtilisin/kexin type 5	1,11E-06	0,356144	0,286	0,458	0,037276
	Prxl2b	peroxiredoxin like 2B	7,74E-07	0,303251	0,061	0,153	0,02594
	Hspa8	heat shock protein 8	2,92E-08	-1,11725	0,776	0,864	0,000977
SGC	Dcn	decorin	3,45E-08	-0,38973	0,216	0,439	0,001155
	Hsp90a a1	heat shock protein 90, alpha (cytosolic), class A member 1	1,01E-06	-0,62408	0,425	0,62	0,033884
	Hspa8	heat shock protein 8	1,99E-08	-0,65018	0,757	0,835	0,000668
	Hspa5	heat shock protein 5	1,02E-08	-0,81407	0,506	0,667	0,000342
	Serpinh1	serine (or cysteine) peptidase inhibitor, clade H, member 1	3,94E-14	-0,92694	0,544	0,763	1,32E-09
mSch	Calca	calcitonin/calcitonin-related polypeptide, alpha	1,6E-09	0,935367	0,171	0,047	5,35E-05
	Hsp90a b1	heat shock protein 90 alpha (cytosolic), class B member 1	1,28E-07	-0,35692	0,826	0,826	0,004305
	Dynll1	dynein light chain LC8-type 1	3,97E-08	-0,39915	0,774	0,765	0,001329
	Ogn	osteoglycin	1,31E-06	-0,51117	0,734	0,826	0,043905
	Serpinh1	serine (or cysteine) peptidase inhibitor, clade H, member 1	2,41E-08	-0,55838	0,416	0,486	0,000806
	Hspa8	heat shock protein 8	2,4E-11	-0,56464	0,615	0,67	8,05E-07
	Hspa5	heat shock protein 5	1,44E-06	-0,63725	0,346	0,449	0,048375
	Apod	apolipoprotein D	7,73E-14	-0,94445	0,609	0,798	2,59E-09
nmSc h	Ifi2712a	interferon, alpha-inducible protein 27 like 2A	2,33E-07	1,483032	0,366	0,236	0,007806
	Calca	calcitonin/calcitonin-related polypeptide, alpha	9,33E-15	1,076457	0,205	0,014	3,13E-10
	AY036118	cDNA sequence AY036118	4,87E-07	0,870682	0,58	0,44	0,016309
	Atf3	activating transcription factor 3	1,99E-07	0,653956	0,219	0,341	0,006675
	mt-Co2	mitochondrially encoded cytochrome c oxidase II	4,66E-07	0,274458	0,946	0,96	0,015613
	Hsp90a b1	heat shock protein 90 alpha (cytosolic), class B member 1	1,32E-07	-0,49345	0,853	0,852	0,004428
	Hspa8	heat shock protein 8	2,38E-08	-0,58314	0,701	0,753	0,000797
	Cryab	crystallin, alpha B	3,23E-09	-0,64201	0,812	0,849	0,000108
	Hspa5	heat shock protein 5	3,17E-07	-0,78561	0,491	0,653	0,010607
	Apod	apolipoprotein D	3,04E-09	-0,78848	0,509	0,756	0,000102
	Col3a1	collagen, type III, alpha 1	7,24E-07	-0,80758	0,375	0,56	0,024247
	Serpinh1	serine (or cysteine) peptidase inhibitor, clade H, member 1	3,03E-10	-0,80925	0,598	0,744	1,01E-05
	Dcn	decorin	2,56E-08	-0,96858	0,223	0,44	0,000858
	Hspb1	heat shock protein 1	2,31E-12	-1,35415	0,17	0,449	7,74E-08

## ACKNOWLEDGEMENTS

### ACKNOWLEDGEMENTS

I would like to convey my profound appreciation to those who have supported me throughout my seven-year doctoral journey at the IPEK Institute, University of Munich.

First and foremost, I extend my deepest thanks to my advisor, Prof. Andreas Habenicht, for his steadfast guidance, support, and encouragement. His expertise, motivation, and perceptive feedback have been instrumental in shaping my research and academic progress. I am truly thankful for the opportunity to learn and develop under his supervision.

I am equally grateful to my co-advisor, Dr. Mohanta Sarajo, for his invaluable assistance, constructive criticism, and constant encouragement. His expertise, dedication, and willingness to provide guidance have greatly contributed to my research endeavors and personal growth.

I acknowledge Prof. Dr. Wolfgang Enard for being a member of my thesis advisory committee and providing valuable advice on learning and analyzing scRNA-seq data. I also appreciate the generous assistance of Prof. Changjun Yin, who supported me throughout my entire PhD journey. I wish to acknowledge Prof. Desheng Hu, who kindly instructed me in FACS technology. I would like to thank Prof. Dr. Donato Santovito for his valuable guidance on statistical perspectives.

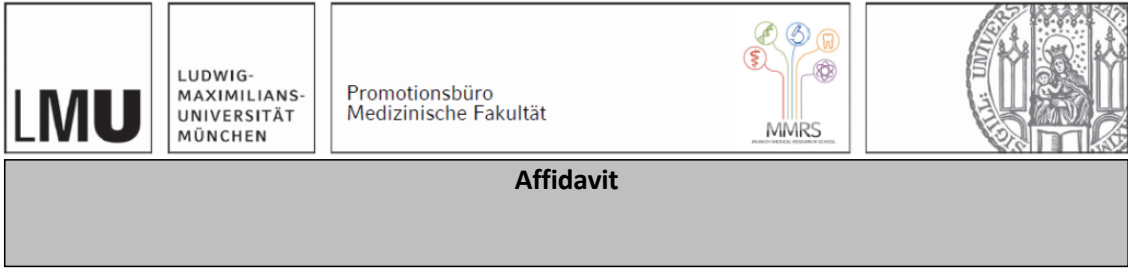
I extend my wholehearted appreciation to my colleagues, including Xi Zhang, Dr. Zhihua Wang, Dr. Yuanfang Li, Dr. Zhe Ma, Dr. Chuankai Zhang, Ting Sun, Yutao Li, Rui Su, Mingyang Hong, Xinyi Deng, Mohammad Rafiee Monjezi, Yixin Zhang for their camaraderie, collaboration, and shared wisdom. Additionally, I thank the colleagues at the IPEK Institute, including Dr. Michael Hristov, Dr. rer. nat. Xavier Blanchet, Dr. Rundan Duan, Dr. Katrin Nitz, Dr. Michael Lacy, Dr. Yi Yan, Dr. Maria Aslani, Sabine Streicher, Claudia Geissler, Yvonne Jansen, and Sigrid Unterlugauer, for their help and support. I am also thankful to my friend Chang Pan, who motivated me to persist through challenges, and Yitao Shang, who encouraged me to pursue opportunities for studying abroad. The engaging and nurturing atmosphere they cultivated made my doctoral experience both enriching and enjoyable. Their support was crucial to the successful completion of my PhD.

Lastly, I express my gratitude to my parents and brother for their unwavering belief in me, support, and encouragement. They have been my pillars of strength, inspiring and motivating me throughout this journey.

In conclusion, I dedicate this work to all those who have supported, inspired, and encouraged me during my pursuit of a PhD. My time at the IPEK Institute has provided me with invaluable opportunities, knowledge, and experiences, for which I am forever grateful.

AFFIDAVIT

AFFIDAVIT



Affidavit

Shu Lu

Surname, first name

Goethestr.72

Street

80336, Munich, Germany

Zip code, town, country

I hereby declare, that the submitted thesis entitled:

**Single-cell Transcriptome Analyses of Dorsal Root Ganglia in Aged Hyperlipidemic Mice**

.....

is my own work. I have only used the sources indicated and have not made unauthorised use of services of a third party. Where the work of others has been quoted or reproduced, the source is always given.

I further declare that the dissertation presented here has not been submitted in the same or similar form to any other institution for the purpose of obtaining an academic degree.

Munich, 05.05.2023

place, date

Shu Lu

Signature doctoral candidate

CONFIRMATION OF CONGRUENCY

CONFIRMATION OF CONGRUENCY

	LUDWIG- MAXIMILIANS- UNIVERSITÄT MÜNCHEN	Promotionsbüro Medizinische Fakultät		
<b>Confirmation of congruency between printed and electronic version of the doctoral thesis</b>				

Shu Lu

\_\_\_\_\_  
Surname, first name

Goethestr.72

\_\_\_\_\_  
Street

80336, Munich, Germany

\_\_\_\_\_  
Zip code, town, country

I hereby declare, that the submitted thesis entitled:

**Single-cell Transcriptome Analyses of Dorsal Root Ganglia in Aged  
Hyperlipidemic Mice**

.....

is congruent with the printed version both in content and format.

Munich, 05.05.2023

\_\_\_\_\_  
place, date

Shu Lu

\_\_\_\_\_  
Signature doctoral candidate

## LIST OF PUBLICATIONS

### LIST OF PUBLICATIONS

- Mohanta Sarajo K., Li Peng, Yuanfang Li, **Shu Lu**, Ting Sun, Lorenzo Carnevale, Marialuisa Perrotta et al. "Neuroimmune cardiovascular interfaces control atherosclerosis." **Nature** 605, no. 7908 (2022): 152-159.
- Wang Zhihua\*, Xi Zhang\*, **Shu Lu\***, Chuankai Zhang, Zhe Ma, Rui Su, Yuanfang Li et al. "Pairing of single-cell RNA analysis and T cell antigen receptor profiling indicates breakdown of T cell tolerance checkpoints in atherosclerosis". **Nat Cardiovasc Res** (2023): 290–306.\*equal first author.
- Zhang Xi, Zhihua Wang, Chuankai Zhang, Yutao Li, **Shu Lu**, Sabine Steffens, Sarajo Mohanta, Christian Weber, Andreas Habenicht, and Changjun Yin. "Laser capture microdissection-based mRNA expression microarrays and single-cell RNA sequencing in atherosclerosis research." **Methods Mol Biol** 2419 (2022): 715-726.
- Wang Zhihua, Xi Zhang, Chuankai Zhang, Yutao Li, **Shu Lu**, Sarajo Mohanta, Christian Weber, Andreas Habenicht, and Changjun Yin. "Combined single-cell RNA and single-cell  $\alpha/\beta$  T cell receptor sequencing of the arterial wall in atherosclerosis." **Methods Mol Biol** 2419 (2022): 727-746.
- Sun Ting, Yuanfang Li, Benjamin Förstera, Karen Stanic, **Shu Lu**, Sabine Steffens, Changjun Yin et al. "Tissue Clearing Approaches in Atherosclerosis." **Methods Mol Biol** 2419 (2022): 747-763.
- **Shu Lu**, Ming-Shan Wang, Pei-Jie Chen, Qiang Ren, and Peiming Bai. "miRNA-186 inhibits prostate cancer cell proliferation and tumor growth by targeting YY1 and CDK6." **Experimental and therapeutic medicine** 13, no. 6 (2017): 3309-3314.
- Liu, Chunlan, **Shu Lu**, Limin Yang, Peijie Chen, Peiming Bai, and Qiuquan Wang. "Near-infrared neodymium tag for quantifying targeted biomarker and counting its host circulating tumor cells." **Analytical Chemistry** 89, no. 17 (2017): 9239-9246.
- Wang, Mingshan, Chaoli Duan, Qiang Ren, Peijie Chen, **Shu Lu**, Shuchao Ye, Jiawei Wang, and Peiming Bai. "Expression of COUP-TF2 in bladder carcinoma and effect of the microenvironment of bladder cancer on endothelial cells." **Int J Clin Exp Pathol** 10, no. 5 (2017): 5506-13.